Shining New Light on Water Electrolysis: Probing Electrolytic Water Splitting on Au and Pt with Micron Spatial and Femtosecond Temporal Resolution

Gregor Zwaschka

Dissertation

zur Erlangung des Grades
eines Doktors der
Naturwissenschaften (Dr. rer. nat.)

an der Fakultät für Physik
der Freien Universität Berlin

vorgelegt von
Gregor Zwaschka

Berlin 2020

Erstgutachter: Prof. Dr. Martin Wolf
Zweitgutachter: Prof. Dr. Joachim Heberle
Tag der Disputation: 25.11.2020

Diese Arbeit entstand im Zeitraum von Mai 2016 bis Juli 2020 in der Arbeitsgruppe von Prof. Dr. Kramer Campen am Fritz-Haber-Institut der Max-Planck-Gesellschaft, Abteilung Physikalische Chemie, unter der Leitung von Prof. Dr. Martin Wolf.

Berlin, Juli 2020

Contents

List of Figures

List of Tables

Deutsche Kurzfassung

Eine Energieversorgung basierend auf H_2, das durch Wasserelektrolyse gewonnen wird, ist die vermutlich beste Antwort auf den anthropogenen Klimawandel. Bisweilen hindert uns ein unvollständiges Verständnis der an der Elektrolyse beteiligten elektrochemischen Reaktionen am Bau idealer Elektrolyseure. Verbesserungsbedarf gibt es insbesondere bei den Katalysatoren, auf denen die beteiligten Reaktionen ablaufen. In dieser Arbeit adressiere ich wichtige offene Fragen bezüglich der reduktiven und oxidativen Hälften der Wasserelektrolyse, der hydrogen evolution reaction (HER) und der oxygen evolution reaction (OER), auf Pt und Au. Frühere Arbeiten demonstrieren, dass die Rate dieser Reaktionen von Elektrolyt- und Elektrodenzusammensetzung und -struktur abhängt. Pt wurde für die HER wegen seiner einmaligen Kombination von Aktivität und Stabilität ausgewählt; Au ist ein nützliches Modellsystem für die OER.

Ich habe die HER auf Pt Einkristallen und einer Mikroelektrode elektrochemisch und mittels Summenfrequenzspektroskopie (SFS) in Gegenwart und Abwesenheit einer gepulsten, ultrakurzen nahinfrarot-Perturbation, die Ladungstransfer und die HER auf einer Femtosekunden-Zeitskala auslöst, untersucht. Aus den gewonnenen Resultaten lassen sich folgende Schlüsse ziehen: i) Dass das HER Reaktionsintermediat, monokoordiniertes Pt-H, in einem Gleichgewicht existiert mit zwei- und dreifach koordiniertem Pt-H und einem solvatisierten Proton (womöglich Oxonium) an der Grenzfläche, das in Kontakt mit Pt steht. ii) Dass Ladungstransfer von Pt zur Flüssigphase nur dann auf einer ultrakurzen Zeitskala möglich ist, wenn Elektrolyt und Adsorbate eine spezielle Anordnung einnehmen, die diesen erlaubt. iii) Dass die HER durch eine Veränderung der Grenzfläche ermöglicht wird, die zu einer Erhöhung der H-Mobilität auf einer sub-Pikosekunden-Zeitskala führt, wenn das Potenzial bei dem sie auf Pt beginnt angenähert wird. Dies geschieht vermutlich durch eine Änderung der H-Bindungsenergien zu verschiedenen Adsorptionsplätzen und der Elektrolytstruktur an der Grenzfläche.

Die Oxidation der Oberfläche (OF) ist eine Voraussetzung für die OER und eine Funktion ihrer Struktur. Im Rahmen dieser Arbeit untersuche ich räumliche Heterogenität von OF-Oxidation und OER Aktivität auf poly- und nanokristallinem Au mittels second harmonic (SH)-Mikroskopie. Ich zeige, dass man mit dem Signal der nichtoxidierten OF Rekonstruktionsmuster während Oxidation und Reduktion vorhersagen kann. Die OER Aktivität ist sehr lokal und beschränkt sich auf zwei unterschiedliche Arten von strukturellen Defekten. Der Erste ist stabil gegenüber Rekonstruktion von OF-Atomen und erstreckt sich in das Elektrodenvolumen, der Zweite, ein reiner OF-Defekt, nicht. Im Rahmen dieser Dissertation gewonnene Erkenntnisse über die OER auf Pt legen nahe, dass höhere Oxidationsstufen von Pt ($>$ +II) nicht OER-aktiv sind.

Abschließend wurde die Adsorption von Anionen von H_2SO_4 und $HClO_4$ auf einer Pt(111)-Elektrode mittels SFS untersucht, da Anionenadsorption die HER und OER beeinflussen. SO_4^{2-} (*nicht* HSO_4^-) wurde als das Adsorbat in H_2SO_4 ausgemacht. Die Potenzialabhängigkeit der optischen Antwort von SO_4^{2-} adsorbiert auf Pt(111) wurde durch ein Modell quantitativ erklärt. ClO_4^-–Adsorption wurde nur beobachtet, wenn die OF bereits mit OH bedeckt war, nicht aber auf dem blanken Metall. Es wurden zwei ClO_4^-–Subpopulationen, entgegen nur einer bei SO_4^{2-}, beobachtet.

Auf die in dieser Arbeit gewonnenen Erkenntnisse und verwendeten Methoden aufbauend könnten in Zukunft effizientere Katalysatoren für die Wasserelektrolyse geschaffen werden.

Abstract

An energy economy based on H_2 from water electrolysis is perhaps the most promising answer to man-made climate change. So far an incomplete understanding of the interfacial electrochemistry of water electrolysis prevents us from building the best water splitting devices possible. In particular the catalysts on which the involved reactions occur offer room for improvement. In this thesis, I adress urgent open questions regarding both the reductive and oxidative half-cell reactions of water electrolysis, the hydrogen evolution reaction (HER) and the oxygen evolution reaction (OER), respectively, on Pt and Au. Prior work clarifies that the rate of these reactions depends on all aspects of the interface: electrolyte and electrode composition and structure. Pt was chosen for investigating the HER because of its unique combination of activity and stability; Au is a useful model system for OER electrocatalysis.

On Pt single crystals and a microelectrode, I have investigated the HER and adsorbed H, Pt-H, electrochemically and by sum frequency generation (SFG) spectroscopy in the presence and absence of a pulsed, ultrashort near-IR perturbation that triggers charge transfer and the HER on a femtosecond timescale. The HER reaction intermediate, monocoordinated Pt-H, is concluded to exist in an equilibrium with two- and threefold coordinated Pt-H and a solvated interfacial proton (possibly an oxonium ion) that is in contact with the Pt surface. I find that charge transfer from Pt to the liquid side is only possible on femtosecond timescales if interfacial electrolyte and adsorbates are in a particular goldilocks structure. It is further concluded that the HER on Pt is enabled when approaching its onset potential by a change in the interphase that increases the mobility of adsorbed H on subpicosecond timescales, possibly by a change in H adsorption energies in different sites and in interfacial solvent structure.

Surface oxidation is a prerequisite for the OER and a function of surface structure. Here I investigate the spatial heterogeneity of surface electrooxidation and OER activity on poly- and nanocrystalline Au electrodes by second harmonic (SH) microscopy. I show that the SH signal of the unoxidized surface can be used to predict patterns in surface reconstruction that occurs during potential cycling. I find that OER activity is highly local and bound to two distinctive types of defects. The first is stable with respect to surface atom reconstruction and extends into the bulk, while the second, a pure surface defect, is not. From work on the OER on Pt conducted within the scope of this thesis, I conclude that higher oxidation states of Pt ($>$ +II) are not OER active.

Finally, the adsorption of H_2SO_4 and $HClO_4$ derived anions to a Pt(111) electrode was studied by SFG, as anion adsorption influences HER and OER. SO_4^{2-} (and *not* HSO_4^-) was identified as the adsorbate in H_2SO_4. The potential dependence of the optical response of SO_4^{2-} adsorbed on Pt(111) was quantitatively explained by a microscopic model. ClO_4^- adsorption was only observed after Pt(111) had been covered by OH at higher potentials, but not on the bare metal. Also, two distinct ClO_4^- subpopulations, compared to only one for SO_4^{2-}, were found.

The insights gained within the scope of this thesis and the employed methods may assist us in building better catalysts for water electrolysis in the future.

Chapter 1

Towards H_2 from H_2O Electrolysis as Carbon Neutral Fuel: Obstacles and Advances

From the action potential in our nerve fibers [1] (the basis of our own consciousness) to the erosion and sedimentation shaping the face of the earth [2], to food processing (e.g. coffee extraction [3]) and the corrosion of our cars [4], interfacial processes are ubiquitous and fundamental to every aspect of life. There is thus a clear incentive to better understand many of these processes. Yet, only very few interfacial processes are understood on a molecular level and improvement is mostly limited to empirical trial and error and has not reached the desired level of knowledge based design.

Our lack of understanding of interfacial processes is, in part, a consequence of the involved length and timescales: in most, actions on the fs to ps timescale (like electron transfer [5], solvent reorganization [6] and fast chemical reactions [7, 8]) are connected in ways difficult to discern to actions on µs to ms timescales (like mass transport, i.e., diffusion and convection). If such processes with actions on various timescales are probed, the time resolution of the probe will be critical [9]. If it is too coarse, the very fast actions will be obfuscated. On the contrary, a very high time resolution (e.g. fs) is impractical for monitoring dynamics that are substantially slower (e.g. µs). Similarly, only in exceptions are interfaces and the occuring processes spatially homogeneous (e.g., of single crystals and self-assembled monolayers, which often also have a degree of heterogeneity through defects and domains, respectively), most show heterogeneity on vastly differing length scales. For example, the reactivity of metals is a direct function of the metal's atomic structure on the Å scale [10]. However, apart from single crystals, real metal surfaces typically consist of µm sized grains that expose differently structured surface atom arrangements [11]. These grains are often not homogeneous either, they may show domains where the surface atom arrangement has been reconstructed and towards their edges (the *grain boundaries*) surface strain may stabilize atomic structures that are not stable in the centre of the grain [12]. These grain boundaries and their behavior are further a function of the neighboring grains' atomic structure [13]. This implies that reactivity will strongly vary as a function of

position on such metal surfaces and that different reactions will happen at different surface atoms. It is apparent that spatially averaged signals from such samples with heterogeneity on a length scale smaller than the probe spot may be too complicated to understand. Consequently, either local probes, or homogeneous samples, emulating a subsystem of the real interface, must be employed. Such model systems should be simple enough to understand, while still capturing the physics of the real interface.

Unfortunately, in many cases the frontier of science is not already concerned with bridging the involved, separated length and timescales, because characterization at the individual levels (e.g., investigation of either very fast, or slower processes) is challenging enough. Consequently, further method development is required. This is not a trivial endeavor, as different interfaces and questions require different tools.

One area in which such progress is needed most pressingly is interfacial electrochemistry for energy conversion and storage. This field will play a key role in our fight against man-made climate change by providing means i) for storing excessive renewable energy during the peak hours of production (and thereby ensuring a continuous and reliable power supply) [14] and, ii) to create carbon-neutral fuels and to convert these back to energy to power e.g. vehicles [15]. The perhaps most attractive alternative to fossil fuels is H_2 from water electrolysis where the needed energy input comes from renewable sources [16]. In this scenario, H_2O is split into H_2 and O_2 in an electrolyzer when excess renewable energy is available and later, when energy is required, combined back to water (and energy) in a fuel cell. H_2 has some advantages over candidate fuels such as methanol and ethanol, like unlimited supply of a cheap and ubiquitous resource and an already somewhat matured technology [17] and infrastructure [18] and, additionally, hydrogen is not poisonous[1]. Most researchers who study water electrolysis approach building electrolyzers (the devices that perform water electrolysis) as an empirical problem in device design and materials choice. However, decades of work in this field have not yielded a clearly optimal device design [19, 20, 21]. Such an optimal design has not been achieved yet, because building the best possible water splitting device requires understanding of two very complex interfacial processes: the cathodic (reductive) and anodic (oxidative) half-cell reactions of water splitting, the hydrogen evolution reaction (HER) and the oxygen evolution reaction (OER). Water electrolysis can be performed under varying conditions (e.g., pH and temperature) and consequently different technical solutions exist that have certain advantages and disadvantages. The two prevalent types of water electrolysis, alkaline water electrolysis and polymer eletrolyte membrane (PEM, which is sometimes also used for "proton exchange membrane") electrolysis, are compared in Figure 1.1.

The advantages of alkaline water electrolysis are that it is a mature, relatively cheap technology (abundant iron group elements are used as catalysts) with long-term stability [19, 21]. On the flip side, alkaline water electrolysis suffers from low current densities (due to high ohmic losses because of the diaphragm and liquid electrolyte), low operating pressures (therefore requiring bulky stack designs and additional compression of the product gases for

[1] One disadvantage of hydrogen is that it is a gas, necessitating compression for efficient transportation and storage. The formation of explosive gas mixtures also needs to be avoided.

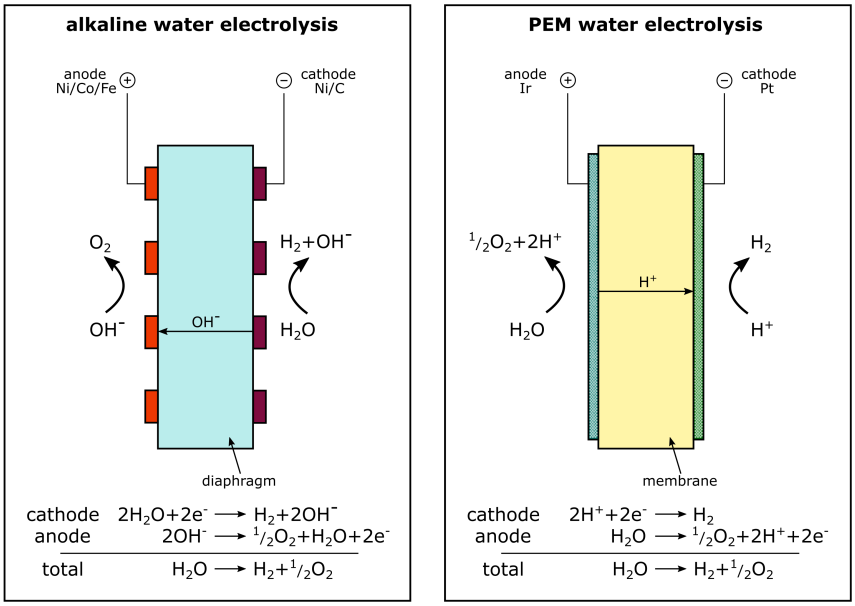

Figure 1.1: Schematic of alkaline electrolysis vs. polymer exchange membrane electrolysis together with the electrode processes.

storage and transport), low partial load range and a slow system response (disadvantageous especially if the electrolyzer is to be operated with the naturally fluctuating power of renewable sources) and crossover of gases through the diaphragm (reducing efficiency and possibly requiring an additional gas purification step) [19, 17, 21].

PEM water electrolysis overcomes these issues by usage of a proton conducting membrane in acidic electrolyte. In PEM electrolysis, high current densities, a good partial load range and a fast system response is achievable and high purity product gases are obtained [20, 21]. The makeup of PEM electrolyzers further allows operation under high pressures and a compact stack design. On the downside the PEM design is more expensive due to the corrosive, acidic environment which requires the use of Pt group electrocatalysts (the only active *and* stable catalysts under these conditions) and Ti (which is more corrosion resistant than alternatives like stainless steel, aluminum, or carbon based materials) for current collectors [19]. Due to these measures, the lifetime of PEM and alkaline electrolyzers is comparable [21]. In summary, PEM water electrolysis bears great potential, but is not economically viable yet due to the use of multiple expensive components.

The membrane electrode assembly that contains the electrocatalysts and the PEM makes up $\sim 1/4$ of the cost of an electrolyzer stack [22]; making this element more cost efficient would greatly contribute to the economic success of PEM water electrolysis and to our efforts in the fight against climate change. This endeavor is typically pursued in one of two ways: By i) replacing the precious metal catalyst with a cheaper, more abundant alternative [14]; ii) creating nanoparticle based catalysts that preserve the activity and stability of more extended phases at a fraction of their cost [23].

Both approaches would profit from a thorough understanding of the electrode reactions

and their mechanisms on the noble metal electrocatalysts. Pt and Ir (as IrO_2) have an extraordinary combination of activity and stability for the HER and OER in acidic solution [24, 25, 14], respectively. It is perhaps surprising that Pt and Ir are still used as electrocatalysts in PEM electrolysis, as they were already used in the first PEM electrolyzer design introduced by General Electric in the 1960s [26]. So far no better catalysts have been discovered because of i) the outstanding properties of these two materials for catalyzing the respective chemistries and ii) the fact that despite decades of study the reaction mechanisms of HER and OER are still only poorly understood and as a consequence it is not clear, *why* Pt and Ir are good electrocatalysts for the respective chemistries. Understanding the reactions mechanisms would help with finding better and cheaper catalysts.

Gaining such insight has proven challenging. One major obstacle is the collection of meaningful experimental observables of the electrochemical interface. The most commonly recorded signal in electrochemistry is the current itself, which, unfortunately, is a superposition of all occuring current-drawing processes and provides only indirect access to reaction mechanisms via the analysis of Tafel slopes (see discussion in the next chapter). In theory, structural probes can provide the necessary information to resolve a reaction mechanism, but this proves to be a formidable task already on well defined single crystals in ultra-high vacuum (UHV) [10] where electrons can be used as a convenient probe for the surface geometric and electronic structure [27]. However, even under UHV, determining a reaction mechanism is only possible in the rare scenario that the investigated reaction has long lived reaction intermediates (with respect to the time it takes to detect these). However, many studies of molecular adsorbates on metals or semiconductors in UHV have demonstrated that elemental reaction steps like charge transfer can occur on fs timescales [28]. A thorough comprehension of the reaction mechanism also requires characterization of the intermediates involved in these fast processes. Additionally, unravelling a reaction mechanism is substantially more complicated under ambient conditions at the solid/liquid interface because electrons can no longer be used as probes and the preparation *and* preservation of well defined and clean surfaces is not as straightforward as in UHV[2]. This is reflected in the fact that even for a relatively simple reaction like the HER (see section 2.2) on the probably most studied surface in electrochemistry, Pt, no agreed upon reaction mechanism exists that could explain the empirically observed dependencies of the reaction on parameters such as pH and surface atomic structure [30, 31, 24].

With the intent to gain mechanistic insight, I have studied the HER and related processes on various Pt electrodes in this thesis. I employed vibrationally resonant sum frequency generation (SFG) spectroscopy on well defined Pt(111) and Pt(110) single crystals to study the potential and surface structure dependent behavior of the reaction intermediate and other adsorbates. Electron transfer and the surface dynamics of the reaction intermediate and other adsorbates were investigated by triggering charge transfer and the HER with fs optical pulses, either collecting the photocurrent, or the fs resolved SFG signal

[2]It is for this reason that UHV surface scientists rejected interfacial electrochemistry as a proper scientific discipline up to the point where in situ scanning tunelling microscopy (STM) could unambiguously prove that single crystalline surface order can also be achieved under ambient conditions [29].

as a response. This allowed unprecedented insight into the behavior of the Pt/electrolyte interface during and after charge transfer: under which conditions charge transfer is possible and the rate limiting process for the HER. The time resolved SFG + fs optical trigger measurements further suggested that the HER is enabled, when the bias is tuned towards the reactions onset potential, by a change in the interface that increases the mobility of adsorbed H on a sub-ps timescale.

The OER, on virtually all materials, occurs on oxidized surfaces [32]. On metal substrates, on which the oxidized surface catalyzes the reaction, surface oxidation continues during the reaction and the oxide evolves with time [33]. Given the differences in local environment of polycrystalline metals discussed above (grains of different surface crystallographic orientation, surface reconstruction and grain boundaries), one might expect surface oxidation and therefore OER activity to be strongly spatially heterogeneous. In this thesis, I have investigated the spatial heterogeneity of surface electrooxidation, surface reconstruction during potential cycling and OER activity on a polycrystalline gold electrode that has tens of µm big grains, and a nanocrystalline electrode that is composed of tens of nm big clusters by second harmonic microscopy (SHM). The results demonstrate that the SH signal at potentials below surface oxidation can be used to predict areas that are particularly prone to surface reconstruction (and likely corrosion) at higher, oxidative, potentials. They further demonstrate that OER activity is highly local and bound to two types of defects, one that is stable with respect to surface reconstruction that extends into the bulk of the electrode and another one that is not: a pure surface defect. Furthermore, the relationship between metal oxidation state and OER activity was investigated on a Pt microelectrode with and without the presence of pulsed ultrashort near-IR radiation. Here, I conclude that on Pt higher valent oxidation states ($>$ +II) are not catalytically active for the OER.

Finally, the adsorption of sulfuric and perchloric acid derived anions on a Pt(111) electrode was studied by SFG. Anion adsorption is an electrode process that does not show up in the reaction mechanism of either HER, or OER, but substantially influences these and is therefore of major importance [34, 35, 36, 37]. For the adsorption of sulfuric acid derived anions, isotope exchange and SFG measurements clarify the long discussed question of the chemical nature of the adsorbate: it is sulfate (SO_4^{2-}) and not bisulfate (HSO_4^-). Furthermore, a microscopic model of the SFG response of sulfate adsorbed to Pt(111) was devised that quantitatively explains the potential dependent optical response on a physical basis. Lastly, the adsorption of perchlorate, an anion that behaves considerably different than sulfate [38, 39], on Pt(111) was studied by SFG. It was concluded that perchlorate does not interact with the bare Pt(111) surface, but with adsorbed OH and that two different subpopulations of interfacial perchlorate exist as soon as the surface is OH covered.

Before the actual experiments will be discussed in chapters 4 - 6, the reader will be given an introduction to electrochemistry and the necessary background in water splitting chemistry on Pt and Au in chapter 2 and the optical tools that were employed in this thesis in capter 3.

Chapter 2

Water Reduction on Pt Model Catalysts: Background, State of the Art and Beyond

In this chapter the fundamentals necessary to understand electrochemical processes like water reduction and popular electrochemical methods that will be important in the following will be introduced.

2.1 A Short Background in Electrochemistry

2.1.1 Introduction to Important Concepts and Methods

In electrochemistry the interrelation of electrical and chemical effects is studied [40]. The majority of electrochemical studies, probably, is concerned with i) chemical processes producing electrical energy, or ii) chemical reactions driven by an electric current[1]. In i), an exergonic chemical reaction of a reactant in the electrolyte or on the electrode that involves charge transfer to or from the electrode produces a current that can be used in external devices. Battery, or fuel cell powered vehicles are one example of how i) is used. In ii), an endergonic chemical reaction of a reactant in the electrolyte or on the electrode that involves charge transfer to or from the electrode is driven by supplying a current. Charging a battery, of producing H_2 and O_2 via water electrolysis are examples for ii).

The basis for either process, i) and ii), can be illustrated in a gedanken experiment in which we immerse a piece of metal M in an aqueous solution containing the metal's ions M^{z+} (an assembly called "half-cell", or electrode). Initially, the system is not in equilibrium. However, because the metal ions have different chemical potentials in the crystal lattice (m) and in solution (s) $\mu_{M^{z+}}^{(m/s)}$, metal ions will either go into solution (and electrons will accumulate at the metal surface, charging it negatively), or be reduced and incorporated into the metal lattice ("metal plating", resulting in a positive charging of the

[1] Other notable electrochemical phenomena are corrosion and electrophoresis.

metal through electron consumption) until the rates for metal dissolution and plating are identical and equilibrium is reached. This situation is illustrated in Figure 2.1:

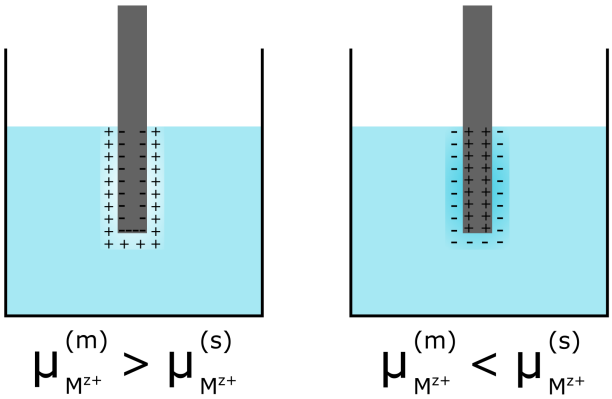

Figure 2.1: Illustration of Galvani potentials and voltage at the metal/solution interface. Whether metal ions go into solution, or are incorporated into the metal lattice depends on the relative sizes of the ions chemical potential in either phase.

The driving force for the phase transition of metal ions from solution to the crystal lattice can be written as

$$\Delta G = \mu^{(m)}_{M^{z+}} - \mu^{(s)}_{M^{z+}} < 0 \tag{2.1}$$

In this case, the equilibrium is not characterized by $\Delta G = 0$ because as the equilibrium is approached an electric field builds up at the interface (by accumulation of ions/electrons) and the ions have to be moved against this field, requiring additional electric work. The accumulation of ions/electrons at either side of the interface results in the build-up of the so-called "Galvani potential" ϕ, an electrostatic potential on each side of the interface. The potential difference across the interface is accordingly called "Galvani potential difference", or "Galvani voltage". Neither Galvani potentials, nor voltage are measurable [41]. Taking this into account, we write the equilibrium condition as

$$(\mu^{(m)}_{M^{z+}} - \mu^{(s)}_{M^{z+}}) + zF(\phi_{(m)} - \phi_{(s)}) = 0 \tag{2.2}$$

or

$$\mu^{(m)}_{M^{z+}} + zF\phi_{(m)} = \mu^{(s)}_{M^{z+}} + zF\phi_{(s)} \tag{2.3}$$

where F is Faraday's constant. The left (right) side of the equation defines the *electrochemical potential* of the ion in the metal (solution) $\mu^*_i = \mu_i + z_i F\phi$. The equilibrium is reached once the electrochemical potentials of M^{z+} in metal and solution are identical. As for conventional chemical equilibria this does not imply that ions do not move across the interface any longer, just that the rates in both directions are equal.

The charge on the metal and on the solution side of the interface is identical in magnitude and opposite in sign $q^m = -q^s$: the two phases of the interface behave like a capacitor. While the charge on the metal results from a deficiency or excess of electrons, the charge on the solution side is a consequence of the relative abundance of either cations or anions in the vicinity of the metal surface. The interfacial charge further acts on and orients the dipoles of solvent molecules nearby. The assembly of the two charged layers and the oriented dipoles is called the "electrical double layer (EDL)".

The solution side of the EDL is considered to consist of multiple layers. The first layer of solution phase species from the metal surface contains ions and solvent molecules in direct contact with the metal electrode. These entities are considered to be "specifically adsorbed"; specifically adsorbed ions form a chemical bond with the electrode surface. "Specifically" denotes that the interaction between electrode and adsorbate (a chemical bond) depends on the chemical properties of both. The plane that can be drawn through the centres of the members of the first adsorbate layer is called the "inner Helmholtz plane (IHP)". The electric potential is considered to change linearly from the metal surface to the IHP and a majority of the entire change in electric potential occurs here in concentrated electrolyte solutions (but not in dilute solutions), leading to strong electic fields on the order of 10^9 V/m. A second plane, the so-called "outer Helmholtz plane (OHP)", is defined by the distance of closest approach of the solvated counterions to the specifically adsorbed ions. In the absence of specifically adsorbing ions, the OHP is defined by the distance of closest approach of fully solvated ions to the surface. The solvated counterions only interact electrostatically with the metal surface and are not in direct contact. Because this interaction is independent of the chemical properties of the counterions (only the charge matters), they are considered to be "nonspecifically adsorbed". Due to thermal motion, the distribution of nonspecifically adsorbed ions (the excess of the corresponding charge) extends into the bulk solution and can be described by a Boltzmann distribution. Inside this so-called "diffuse layer" the electric potential decreases exponentially according to a Poisson-Boltzmann distribution. In bulk the concentrations of ions and counterions are identical and the electric potential is constant. The EDL of a metal electrode in contact with an aqueous electrolyte is illustrated in Figure 2.2:

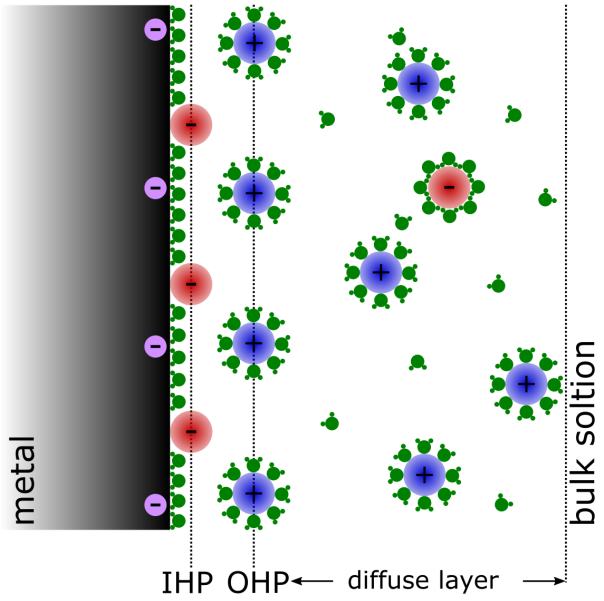

Figure 2.2: Illustration of the electrical double layer with specifically adsorbed anions in the inner Helmholtz plane and nonspecifically adsorbed cations in the outer Helmholtz plane and the diffuse layer.

As mentioned above, the actual potential distribution can not be measured experimentally and theoretical work suggests that in many cases a continuum-description is insufficient [42]. Experimentally accessible is only the difference in Galvani potentials when two electrodes are connected to what is considered an electrochemical cell. This difference is called "cell potential". Figure 2.3 displays a cartoon representation of an experimental setup that allows for such a measurement.

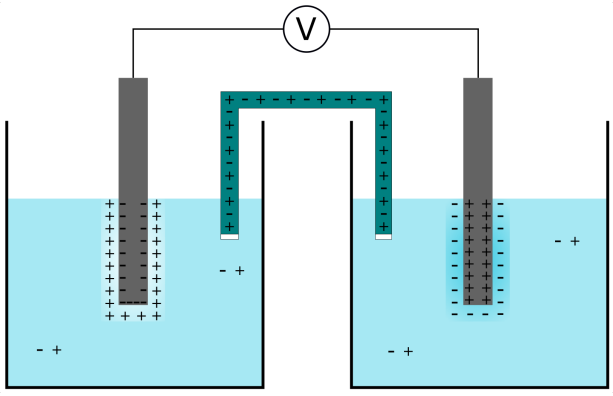

Figure 2.3: Illustration of electrochemical cell that consists of two half-cells/electrodes. While the metals are in electrical contact via a high resistivity voltmeter, the solutions are connected via a salt bridge.

The metals are in electrical contact via a high resistivity voltmeter and the solutions are connected by a salt bridge. The salt bridge typically is a U shaped tube that has glass frits on both ends, filled with a saturated salt solution (e.g. KCl). It ensures a slow exchange of ions between the two solutions in order to maintain electroneutrality inside the circuit.

This setup allows for the measurement of an electrode's potential with respect to another electrode and forms the basis for the galvanic series: a ranking of the elements (and all possible element combinations, i.e. molecules, alloys, etc.) according to their standard electrode potential, i.e. their oxidation/reduction potentials (representing their "nobility", or lack thereof) with respect to a common reference. The electrode whose potential we are interested in is called the "working electrode". The electrode that is used as reference is accordingly called the "reference electrode". The primary reference electrode is the standard hydrogen electrode (SHE) which is defined as 0 V. The SHE is defined by the equilibrium potential of the reaction $H_2 \rightleftharpoons 2H^+ + 2e^-$ at a Pt electrode in H_2 saturated acid solution with a proton activity of 1. In electrochemistry, potentials are always quoted with respect to a given reference electrode, for example: "0.5 V vs. SHE". If the SHE is used to measure the electrode potential of a material in a solution that has a proton activity different from 1, a pH-dependent potential shift of -0.059 V x pH unit arises according to the Nernst equation:

$$E = E^0 + \frac{RT}{zF} ln \frac{a_{ox}}{a_{red}} \tag{2.4}$$

Here E is the measured electrode potential and E^0 is the standard electrode potential that is measured under standard conditions: when the activities of oxidized and reduced reactant, a_i, are identical. z denotes the amount of electrons consumed, or produced per reactant entity. The remaining terms have their usual meaning. In the case of the SHE, a_{ox}/a_{red} describes proton/H_2 activity. To avoid the confusion arising from a pH dependent potential scale, potentials are quoted vs. the reversible hydrogen electrode (RHE) in this work. The RHE's electrolyte is a H_2 saturated pendant to the electrolyte in which the working electrode is immersed and therefore no correction for a pH dependent reference scale has to be done.

The cell potential can be manipulated by either varying the composition of the metal electrode or electrolyte, or by replacing the voltmeter by an external voltage source and applying a bias. If the composition of the reference electrode is fixed, any changes in the measured cell potential can be ascribed to the working electrode. However, this implies that the reference electrode has to be operated under little to no current flow in such a two electrode setup, because a current drawing process at the working electrode leads to a counter-process at the reference electrode in which the same amount of charge, but with opposite sign, is involved. This would change the composition of the reference electrode and therefore influence the reference potential. In turn, the measured potential could therefore not be straightforwardly ascribed to the working electrode. This problem is circumvented by introducing a third electrode, the counter (or auxiliary) electrode. In this three electrode setup, the potential is applied between working and reference electrode, but the current is

flowing between working and counter electrode. This approach allows the precise control (or measurement) of the working electrode potential even under conditions of current flow. The following discussion assumes a three electrode setup.

Using an external voltage source to control the potential of the working electrode effectively controls the chemical potential (energy) of the electrons within the working electrode [43]. Applying a negative (positive) potential raises (lowers) the electrons energy (more precisely, it raises (lowers) the Fermi level of the working electrode with respect to the Fermi level of the counter electrode). Raising the electron energy sufficiently high (by applying a negative bias) enables electron transfer from the metal electrode to vacant electronic states of solution phase species close to the metal surface and a negative (by convention) reduction current is measured. If the electron energy (Fermi level) is lowered far enough (by applying a positive bias to the working electrode), electron transfer from an occupied electronic state of a solution phase species close to the metal surface to unoccupied states of the electrode may occur and a positive (by convention) oxidation current is measured. Reduction and oxidation refers to the solution phase species here, not the metal. This situation is depicted in Figure 2.4:

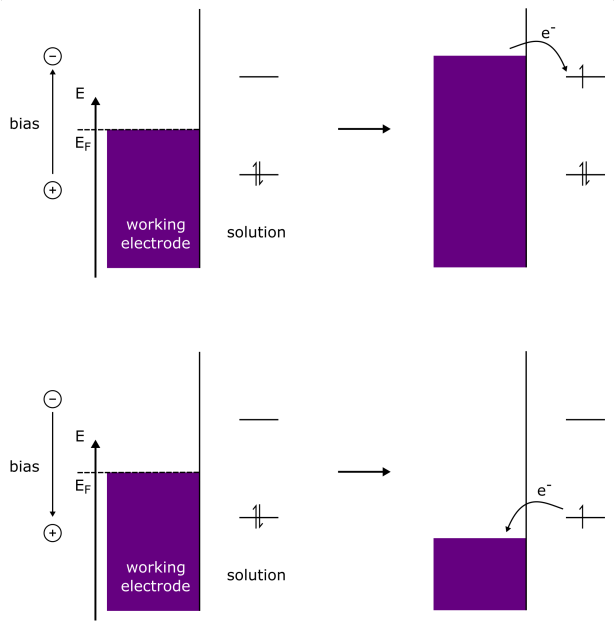

Figure 2.4: Tuning the electrode potential and inducing charge transfer. E_F denotes the position of the Fermi level.

The measured current is stoichiometrically related to the occuring chemical processes at the interface and can be used as a diagnostic means to investigate these. The most popular and perhaps most insightful (electrochemical) way to learn about interfacial electrochemistry is voltammetry: we plot the measured current as a function of varying externally applied potential (with respect to the reference electrode). The resulting current vs. potential curves are called voltammograms and contain, depending on the studied system and

potential range, information about reorientation of molecules in the EDL, adsorption and desorption (sorption) of ionic species to or from the electrode, surface oxidation and/or reduction and oxidation/reduction of solution phase species. Specific insight into the kinetics of electrode processes such as ion sorption and surface oxidation/reduction can be obtained by continuously varying the potential in a cyclic fashion (with linear voltage ramps up and down). This method is accordingly called "cylic voltammetry" and the obtained current vs. potential curves are called cyclic voltammograms (CVs). A generic CV in aqueous electrolyte with the current in black is plotted in Figure 2.5:

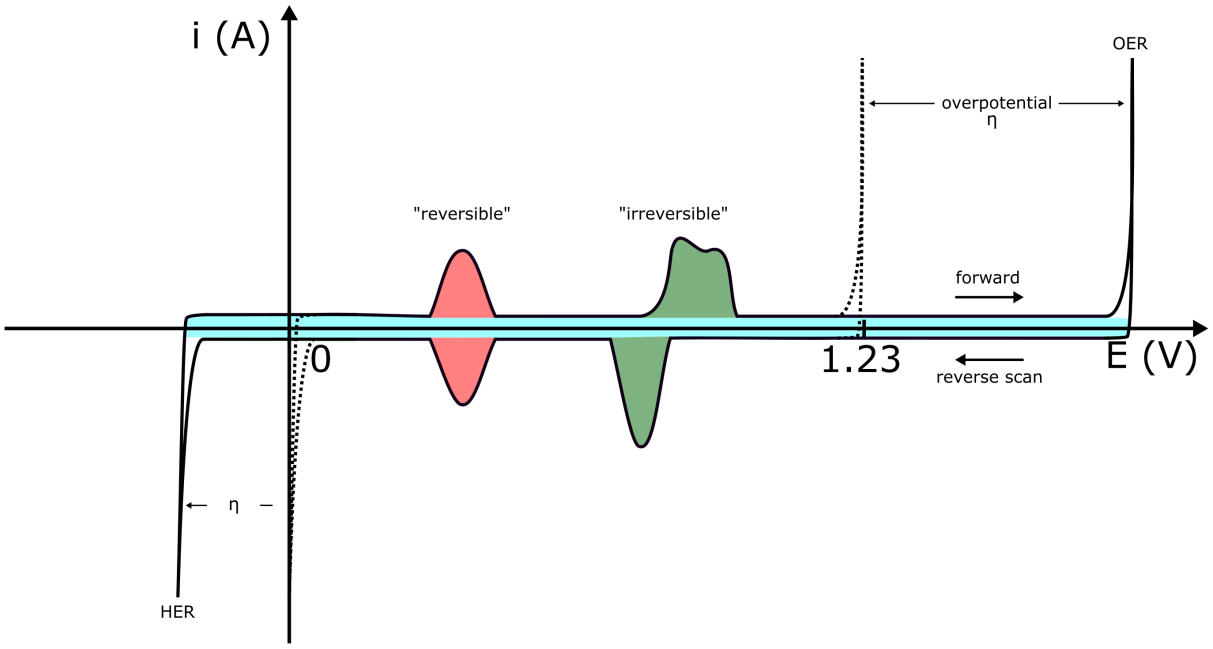

Figure 2.5: A generic CV demonstrating some fundamental capabilities of cyclic voltammetry. The turquois bar represents the EDL capacitance, the red/green peaks represent the kinetically reversible/irreversible adsorption/desorption of ions to the electrode and the current peaks HER/OER denote the cathodic/anodic half cell reactions of water splitting, the hydrogen and oxygen evolution reaction, respectively. The dotted HER/OER current peaks show the potentials at which the respective reactions would occur without activation barriers (1.23 V is the thermodynamic stability window of water). Due to nonzero activation barriers, the reactions only start at more cathodic/anodic potentials. The difference between the potential at which the reaction should occur based on thermodynamics and the potential at which it actually occurs is denoted "overpotential" η.

The linear ramp increasing the potential is called the "forward scan", the ramp decreasing the potential is accordingly called the "reverse scan". The turquoise bar represents the EDL capacitance: tuning the potential results in a varying interfacial electric field that in turn reorients and polarizes interfacial dipoles (e.g. water), leading to a capacitive current.

Ion sorption results in peak pairs, one peak for the adsorption and one for the desorption. The charge in both peaks is identical and determined by the valence of the ion (that need not be integer, as discussed in detail in section 4.2) and its coverage. The red peak pair represents (kinetically) reversible ion sorption: the adsorption/desorption kinetics are fast with respect to the rate of the potential sweep (scanning speed, typically tens of mV per second) and consequently both peaks appear at the same potential. An example of such behavior is the formation of an underpotential deposited (UPD) layer of H on Pt group metals, or the sorption of sulfate on Pt and Au [24]. The green peak pair represents (kinetically) irreversible ion sorption: the kinetics of the adsorption/desorption process, or of follow-up transformations of the adsorbate and/or surface, are slow with respect to the scanning speed. As a consequence the peak potentials in both scanning directions are not identical; the peak shape may also differ. Mass transport limitations to and from the working electrode may also result in an asymmetry of the peak potentials. A typical example of this behavior is oxide formation and reduction on Au or Pt [24]. This electrochemical definition of "irreversible" differs from the typical chemical notion of irreversibility, which describes a scenario in which a reaction equilibrium is heavily product-sided because at least one of the products leaves the phase in which the reaction is going on, or because the Gibbs free energy of the reaction ΔG is very big. The dotted current spikes at 0 and 1.23 V indicate the potential at which the HER and OER, respectively, would occur from a thermodynamic point of view (the thermodynamic stability window of water is 1.23 V). In reality, however, activation barriers exist and shift the onset for the HER cathodically (towards increasingly negative potentials) and anodically (towards increasingly positive potentials) for the OER. The difference between onset potential based on thermodynamics and actual onset potential is denoted "overpotential" η. In the absence of mass transport limitations, the overpotential is a kinetic limitation and can be overcome by a suitable catalyst.

As previously mentioned, the collected current is stoichiometrically related to the ongoing electrochemical process. This can be used for mechanistic investigations and extraction of kinetic parameters for reactions like the HER/OER. Such insight can only be achieved by a quantitative understanding of the current - voltage relationship. The change in current with varied applied bias was first empirically described by Tafel in 1905 [44], who found a logarithmic relationship:

$$\eta = a + b \cdot logj \tag{2.5}$$

where η is the applied overpotential ($\eta = E - E_0$, the difference between the electrode potential and the standard/equilibrium potential of the reaction under investigation) and j is the measured current density. The parameters a and b are called "exchange current density" and "Tafel slope" and are often mentioned together as "Tafel parameters". The exchange current density can be thought of as intrinsic reaction rate, a measure for the speed of the reaction at the equilibrium potential (the potential at which thermodynamics predicts the reaction to occur) when the forward and backward reaction are equally fast and no current is measured. In a $logj$ vs. η plot (known as a "Tafel plot") the exchange current

density is obtained by extrapolating the linear segment of the curve and taking the intercept with the y-axis (x and y axes intercept at the equilibrium potential where $\eta = 0$ mV). The Tafel slope describes how strongly the current varies with applied overpotential and is directly obtained from the linear segment of a Tafel plot. It is typically given in mV needed to achieve a tenfold higher current ("mV/decade"). The Tafel parameters are convenient for characterization and comparison of electrocatalysts: an ideal electrocatalyst for a given reaction has a high exchange current density and a low Tafel slope. Importantly, the Tafel slope is a function of the reaction mechanism. The mechanism of an electrochemical reaction can be inferred by measuring a Tafel slope and comparing it to a Tafel slope that is calculated from a kinetic model of the reaction following a certain mechanistic path.

Such kinetic models are typically constructued from one step, one electron processes (two electron processes like $M^{n+} + 2e^- \rightleftharpoons M^{(n-2)+}$ are always a sequence of one electron processes [40]) of the kind

$$O + e^- \rightleftharpoons R \tag{2.6}$$

where species O is reduced by a single electron to R in the forward reaction with rate constant k_f and k_b is the rate constant of the back reaction. The complete current - potential relationship is obtained from the rate expressions of forward and backward reactions under consideration of transition state theory (in which Arrhenius behavior is assumed):

$$j = FAk^0[C_O(0,t)e^{-\alpha f(E-E_0)} - C_R(0,t)e^{(1-\alpha)f(E-E_0)}] \tag{2.7}$$

Here F is Faraday's constant, A is the electrode's surface area and k^0 is the rate constant at the reaction's equilibrium potential when $k_f = k_b = k^0$. $C_{O/R}(0,t)$ is O/R's concentration as a function of distance from the surface (0 implies that we are evaluating the surface concentration, i.e., the coverage) and time. f=F/RT (where R is the universal gas constant and T is temperature) and α is the so-called transfer coefficient, a measure for the symmetry of the reactions activation barrier. Its value depends on the position of the transition state with respect to the educt and product states on the reaction coordinate and ranges from 0 - 1. α is larger than 0.5 if the transition state is closer to O on the reaction coordinate and smaller than 0.5, if it is closer to R. Typically, α is approximated by 0.5 (i.e. a symmetric transition state) [40]. The first term in brackets describes the cathodic contribution to the current, the second the anodic. The description of electrode reactions according to equation 2.7, in honor of the pioneers in this field, is referred to as "Butler-Volmer" kinetics [45, 46].

Equation 2.7 is more conveniently written in terms of the exchange current density j_0 (that was earlier, during the discussion of the Tafel equation 2.5, which has its own historical convention, denoted as a) and the reaction's overpotential:

$$j = j_0 \left[\frac{C_O(0,t)}{C_O^*} e^{-\alpha f \eta} - \frac{C_R(0,t)}{C_R^*} e^{(1-\alpha) f \eta} \right] \tag{2.8}$$

Here $C^*_{O/R}$ is the surface concentration (coverage) of O/R at the equilibrium potential. At small η the current is dominated by the electrode kinetics and is described by the exponential terms. At large η, however, the current levels off ("limiting current") and is

dominated by mass transport rather than interfacial kinetics. Mass transport is described by $C_{O/R}(0,t)/C^*_{O/R}$. In the absence of mass transport limitations the so-called Butler-Volmer equation is obtained:

$$j = j_0[e^{-\alpha f\eta} - e^{(1-\alpha)f\eta}] \tag{2.9}$$

The Butler-Volmer equation is a good approximation as long as j is smaller than 10 % of the limiting current in either the cathodic, or anodic branch [40]. For sufficiently large η either the cathodic, or anodic branch can be neglected (depending on the sign of the bias, for demonstration purposes we chose a cathodic bias) and equation 2.9 becomes

$$j = j_0 e^{-\alpha f\eta} \tag{2.10}$$

or in logarithmic form

$$\eta = \frac{RT}{\alpha F} ln\, j_0 - \frac{RT}{\alpha F} ln\, j \tag{2.11}$$

which is equivalent to Tafel's expression in equation 2.5. For a one step, one electron process we identify the Tafel parameters as:

$$a = \frac{2.3RT}{\alpha F} log\, j_0 \text{ and } b = -\frac{2.3RT}{\alpha F} \tag{2.12}$$

The Tafel plot for this process is depicted in Figure 2.6:

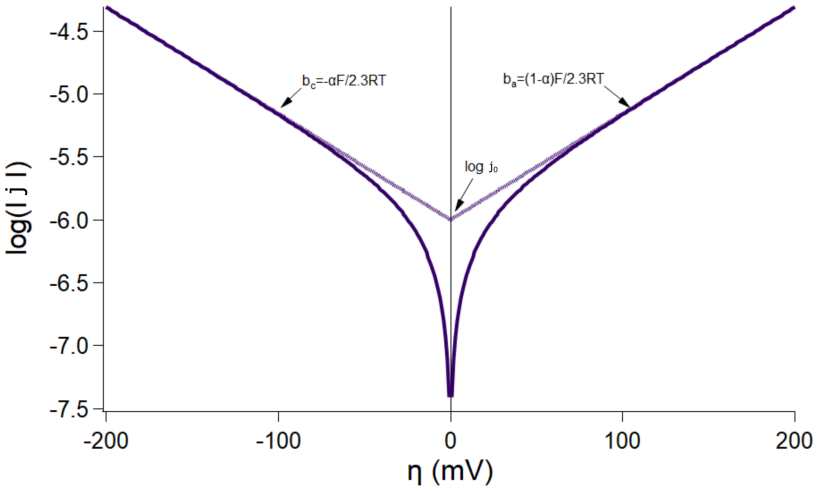

Figure 2.6: Tafel plot for a one step, one electron electrode reation. The dotted lines were calculated according to equation 2.10, neglecting the backward reaction; the solid lines were calculated according to the full Butler-Volmer equation 2.9. The intercept of the dotted lines with the y-axis yields the exchange current. Indices a/c denote "anodic/cathodic". The current was calculated with α=0.5, T=298 K and $j_0 = 10^{-6}$A/cm^2.

One obvious limitation for the determination of reaction mechanisms following the Tafel analysis is that it is only indirect, the movements and transformations of surface species are only inferred and not directly observed. Two assumptions that are made when determining reaction mechanisms by comparing measured and calculated Tafel slopes are further problematic: i) Coverages are assumed to be either 0 or 1, which is typically not justified, Tafel slopes are often observed to be coverage dependent [47]; ii) the transfer coefficient α is assumed to be constant, but should be a function of bias, because the potential energy landscape (and therefore the transition state) changes with bias [40].

As alluded to above, the most convincing way to determine the mechanism of a surface reaction is to observe the surface species directly under reactive conditions, e.g., by spectroscopy. For this purpose, as will be detailed in section 2.3, it is particularly desirable to watch the occuring processes on their natural timescale and not time averaged. One main objective of this work is to develop an experimental approach that allows direct observation of reaction intermediates during electrochemical reactions on their natural timescale. This will be done exemplarily for the HER by monitoring its reaction intermediate with vibrationally resonant sum-frequency generation (SFG) spectroscopy after triggering the reaction on the natural fs timescale of electron transfer by ultrashort optical pulses.

2.1.2 Cleaning, Electrode Preparation and Experimental Details

Cleanliness of glassware and electrodes along with purity of reactants is of utmost importance in interfacial electrochemistry, especially when dealing with relatively low surface area single crystal electrodes. Single crystals have a surface atom density on the order of 10^{15} atoms/cm^2 and accordingly, for a 1 cm^2 big single crystal electrode immersed in 10 ml electrolyte, an impurity concentration of $1.7^{-7 mol/l}$ is sufficient to block every surface site and entirely obfuscate the electrode's true behavior.

All electrochemical measurements were performed with a Biologic SP 200 electrochemical working station in a three electrode configuration.

Pt(hkl) Single Crystal Electrode Measurements

All Pt measurements were conducted in homebuilt glass cells that are illustrated in appendix section A. Two different types of cells were used, one for optical experiments employing an IR beam (these cells have an IR transmissive CaF_2 window) and all glass cells for measurements that only use visible light. Prior to measurement, the glassware was cleaned by immersion in an alkaline $KMnO_4$ solution for 24 h, subsequent immersion in Piranha etch (composed of 0.1 M H_2O_2 and 1 M H_2SO_4) for 2 h, followed by thorough rinsing with Milli-Q water. Subsequently, the glassware was immersed in Milli-Q water and placed insided a supersonic bath for at least 5 min; this was repeated for 3 times with the water replaced by fresh Milli-Q after each wash. Better results are obtained by repeatedly boiling in Milli-Q water, but this procedure is more time consuming and can only be done with the glassware (CaF_2 windows crack during boiling). Because the overall cleanliness of the cell is limited by a few "bottleneck pieces" that can not be cleaned as well as the

glassware (O-rings, sealings, Teflon wrap and the CaF_2 window), only the treatment in the supersonic bath is used (for all pieces). The IR transmissive CaF_2 window (Global Optics, UK) and O-rings that come into contact with electrolyte were first cleaned by immersion in acetone p.A. (AppliChem) and placed inside a supersonic bath for 5 min. In a second and third wash, acetone was replaced first by isopropanol and then ethanol (both p.A. AppliChem). Subsequently, window and O-rings were treated according to the two last steps of the glassware cleaning (rinsing, supersonic bath and rinsing with Milli-Q water). Solutions were prepared from Suprapur sulfuric acid, p.A. perchloric acid (both Merck) and Milli-Q water. The Pt(hkl) single crystal working electrodes (provided either by MaTeck, or the "crystal lab" of the Fritz-Haber-Institue; 5 mm diameter, 3 mm thick) were flame annealed in a butane air flame (1 x 15 min plus 4 x 1 min), cooled in a water saturated N_2 atmosphere, and quenched in and covered with a droplet of Milli-Q water (after all 5 annealing steps) that was deaerated for 45 min before use. Quenching water and electrolyte were deaerated with pure N_2 that was evaporated off of liquid N_2. All parts of the electrode except the oriented and polished surface were wrapped in Teflon tape after flame annealing and thoroughly rinsed with Milli-Q water before the working electrode was transferred to the cell. A homebuilt RHE - a Pt wire in deaerated and H_2 saturated electrolyte - was used as reference electrode [48].

Au Electrodes for Second Harmonic Imaging

A homebuilt Teflon cell was used for the microscopy experiments under potential control. The cell was cleaned by immersion in Piranha solution overnight and repeated supersonication in Milli-Q water before the experiment. The cleaning procedure for the glassware was the same as above. The Na_2HPO_4 solution was prepared from Fluka Analytical sodium phosphate dibasic ($\geq$ 99.999 %) and Milli-Q water, while the NaH_2PO_4 solution was prepared from Sigma-Aldrich sodium phosphate monobasic monohydrate ($\geq$ 99.0 %). The polycrystalline gold foils were purchased from Sigma-Aldrich (0.025 mm thickness, 99.99 % trace metal basis) and annealed at 500 °C for 2 h (with linear heating and cooling ramps) to achieve a grain size distribution characteristic of many practically relevant catalysts and suitable for our microscope (10 - 50 µm, see appendix section B). The nanocrystalline gold thin film sample (tens of nm big grains, see appendix section B) was obtained by physical vapour deposition of 200 nm of gold on an optically flat glass substrate with a 3 nm layer of Cr for increased adhesion. Before use both electrodes were cleaned using the following procedure: copiously rinsed in acetone, copiously rinsed with Milli-Q water, exposed to ozone for five minutes in a UV ozonator, copiously rinsed with Milli-Q water, copiously rinsed with electrolyte and annealed electrochemically until the CV was stable (generally 20-30 cycles of cyclic voltammetry). After this procedure no organic contamination is apparent in the CV. The counter electrode was a Pt mesh and cleaned identically to the Teflon cell. A self-made RHE was employed as reference [48].

2.1.3 Cyclic Voltammetry of Pt(111)

The cyclic voltammetry of any given electrode/electrolyte combination is a function of all aspects of its interfacial electrochemistry and is therefore not only sensitive to the nature of the electrode (chemical composition and surface structure), but also to the composition of the electrolyte (pH and ions). The two most popular electrolytes in physical electrochemistry are H_2SO_4 and $HClO_4$.

H_2SO_4 is the most studied strongly interacting electrolyte: the sulfuric acid derived anions (bisulfate and sulfate) adsorb specifically to Pt(111) [49] (and also to Au, the noblest electrode material [50], and therefore probably also to all other electrode materials). This adsorption is associated with a corresponding current (discussed below and in section 6) and a modification of the electrode. This implies that working with sulfuric acid, depending on the applied potential, may obscur the properties of the bare electrode and that, depending on the applied potential, the surface needs to be considered sulfate capped. Accordingly, specifically adsorbed ions can influence reaction rates and mechanisms [34, 35, 36, 37]. However, especially *because* sulfuric acid derived anions strongly adsorb to the electrode, sulfuric acid solutions have extensively been used to study the adsorption of anions to electrodes and to investigate adsorbate - adsorbate interactions. In this thesis I address some of the remaining urgent questions about the adsorption of sulfuric acid derived anions on Pt(111): i) is sulfate, or bisulfate adsorbed to the surface in 0.5 H_2SO_4 (due to this uncertainty the term (bi)sulfate was coined; see section 6); ii) how can we quantitatively describe the shift in the centre frequency of (bi)sulfate vibrations as a function of applied bias (i.e., how does a microscopic model for the electrochemical vibrational Stark shift look like)? The significance of this work is more general and goes beyond the system H_2SO_4/Pt(111). Determining the protonation state of adsorbates and understanding their spectral observables is also important for other adsorbates and many electrochemical reactions.

$HClO_4$ is the most popular acidic electrolyte because perchlorate anions only interact very weakly with the electrode [51]. There are no current features associated with perchlorate adsorption in CVs recorded in perchloric acid solution and therefore the surface is (in the absence of other adsorbates) considered to be bare. This is a major advantage over specifically adsorbing electrolytes for the assessment of what is a pure electrode property. $HClO_4$ has been used as electrolyte for the spectroscopic investigation of Pt-H in this work to exclude any influence from anion adsorption on the measurements.

The cyclic voltammetry of Pt(111) in contact with 0.5 H_2SO_4 and 0.1 M $HClO_4$, recorded at a scanning speed of 50 mV/s in a hanging meniscus geometry, is shown in Figure 2.7. Going in a positive direction from 0 V vs. RHE on, the CV is identical in both electrolytes up until 0.3 V[2]. The sharp spike towards negative current densities close to 0 V vs. RHE stems from water reduction in the HER (the size of this spike depends on how far negative the potential is scanned). Moving in a positive direction, the plateau from 0.05 to 0.3 V is assigned to the adsorption of so-called underpotentially deposited hydrogen (H_{UPD}) on (111) terraces [49]. The small current bump close to 0.15 V vs. RHE results

[2]Parts of this and the following paragraphs are copied from my own publication [52]

from H_{UPD} desorption from and OH adsorption to (110) like defects (OH desorption and H_{UPD} adsorption in the reverse scan); (100) like defects would result in a similar pair of current peaks around 0.3 V vs. RHE [24]. The H_{UPD} - H_{UPD} interaction is repulsive (the coverage vs. potential curve can be described by a Frumkin isotherm) and H_{UPD} on Pt(111) is considered to be located in the fcc threefold hollow sites with a coverage of around 0.66 at 0 V vs. RHE [24]. In the UPD region no anions are adsorbed on the (111) terraces and the CV in both electrolytes is identical.

Going further positive in perchloric acid solution results in the oxidation of H_{UPD}, which is accomplished by 0.4 V vs. RHE. From around 0.4 to 0.6 V vs. RHE only water is adsorbed to the surface and the CV shows the charging behavior of an ideal capacitor (pure EDL charging). The "butterfly" feature with a broad shoulder from 0.6 to 0.75 V vs. RHE and a sharp spike just before 0.8 V vs. RHE is due to the reversible adsorption of OH [24].

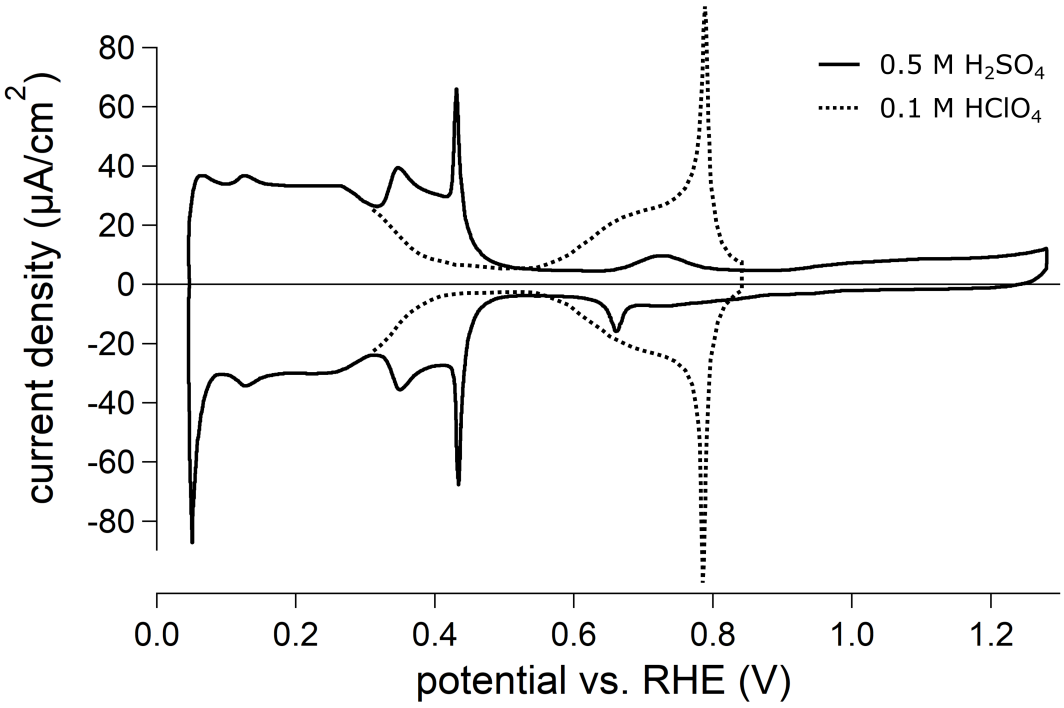

Figure 2.7: Cyclic voltammetry of a Pt(111) electrode in 0.5 M H_2SO_4 (solid line) and 0.1 M $HClO_4$ (dashed line, data taken from reference [53]) recorded at 50 mV/s in a hanging meniscus geometry.

In sulfuric acid solution, the two current features in the region between 0.3 - 0.45 V (a broad and a sharp peak) are also called "butterfly" feature and are thought to be the result of (bi)sulfate adsorption that sets in immediatly after H_{UPD} gets oxidized [49]. At even more positive potentials around 0.75 V vs. RHE, a small positive current feature is apparent that is also associated with adsorbed (bi)sulfate (it is still debated whether OH

adsorption is involved in this peak, though). A detailed discussion of the (bi)sulfate related current features of the Pt(111) CV in 0.5 H_2SO_4 will be given in section 6.

An analogous introdution to the cyclic voltammetry of Gold will be given when we talk about gold electrochemistry in chapter 5.

2.2 The Reaction Mechanism of the Hydrogen Evolution Reaction (HER) on Pt

We will first start with a general introduction to the HER on metal electrodes to introduce some important concepts, before focussing on Pt. The current mechanistic picture of the HER (the hydrogen oxidation reaction, i.e. the HOR, is the reverse reaction) on a metal M in acid consists of three steps [54]:

$$H^+ + e^-_M + M \rightleftharpoons M - H_{ads} \quad \text{Volmer reaction} \tag{2.13}$$

$$2\,M - H_{ads} \rightleftharpoons H_2 + 2\,M \quad \text{Tafel reaction} \tag{2.14}$$

$$H^+ + e^-_M + M - H_{ads} \rightleftharpoons H_2 + M \quad \text{Heyrovsky reaction} \tag{2.15}$$

The reductive adsorption of a proton, the Volmer reaction 2.13, produces the reactive species M-H, which is consumed to form H_2 in one of two ways: by chemical recombination (no electron transfer from the electrode to the adsorbate, or liquid side is involved) with another M-H in the Tafel reaction 2.14, or by electrochemical reaction (involving electron transfer from the electrode to the adsorbate, or liquid side) of M-H with a proton from solution and an electron from the electrode in the Heyrovsky reaction 2.15. In alkaline solutions the proton source is water.

The HER has a strong dependence of catalytic activity on electrode material [55]. This is typically explained by the dependence of reaction rate on the M-H bond strength that varies with M [55]. The M-H bond strength is termed "descriptor" of the reaction because trends in bond strength correlate with trends in catalytic activity [56]. For a reaction with a single descriptor that follows Sabatier's principle (a paradigm commonly employed in gas phase catalysis that predicts an activity maximum for a reaction with a single intermediate if the intermediate's bonding strength to the catalyst is neither too strong nor too weak), a "volcano"-like catalytic activity vs. M-H bond strength curve is expected [57, 58] and observed [55, 59] in acidic solution.

A critical evaluation of volcano plots for hydrogen electrocatalysis (HER and HOR) shows that even for a reaction that satisfies the assumptions underlying Sabatier's principle (only one intermediate), and if the M-H bond strength is the only factor determining catalytic activity, the shape of the catalytic activity of M vs. M-H bond strength curve is still influenced by the relative reaction rates of equations 2.13 - 2.15 for a given mechanism (that is: a combination of 2.13 with either 2.14, or 2.15). This implies that a volcano shaped activity vs. M-H bond strength curve with its apex at the ideal bond strength only results for a specific combination of rate constants for the forward and backward reactions

of 2.13 - 2.15 [60]. However, there is growing evidence that the M-H bond strength is not the only factor determining the catalytic activity and that the details of the electronic structure of the catalyst, its interaction with H, and solvation also matter [61]. It is further improbable that the assumptions underlying Sabatier's principle are valid for the HER.

Most of the work in hydrogen electrocatalysis is done with Pt catalysts owing to its unique combination of high activity and stability [24] and we will therefore continue to discuss the HER on Pt. The intermediate of the HER on Pt is called overpotentially (anything negative of 0 V vs. RHE, the reversible potential of the HER/HOR, is considered "overpotential") deposited hydrogen, H_{OPD} [62, 63], and is considered to be monocoordinated H atop a Pt atom [64]. Electrochemical evidence for the existance of H_{OPD} is based on potential-relaxation [65, 66], potential-step coulometry [67] and AC impedance spectroscopy measurements [68]. The great majority of prior electrochemical work has lead to the conclusion that H_{UPD} and H_{OPD} are different species that coexist on the electrode surface during the HER (but H_{OPD} only exists during the HER and not anywhere in the UPD region) [69, 70, 30, 31, 24]. A strong argument for this case is that the HER may still run on Pt(111) when all H_{UPD} adsorption sites have been blocked by S^{2-}, completely surpressing the H_{UPD} signature in the CV. While H_{UPD} is typically argued to be a spectator in the HER [69, 70, 30, 31], recent work on the HOR has made a strong case that it actually might be the reactive intermediate, or at least closely related to it [71, 72]. The exact relationship of H_{UPD} and H_{OPD} remains as one of the most important unresolved questions in HER/HOR research on metals forming H_{UPD} layers. It should be noted that the HER on Pt shows a strong dependence on crystal face orientation in acid and base, in both the catalytic activity increases in the order Pt(111) < Pt(100) < Pt(110) [30, 31].

That the M-H bond strength is not sufficient as sole descriptor for HER activity becomes evident when we compare activities in acidic and alkaline solutions. The HER reaction rate on Pt slows by 2-3 orders of magnitude going from acidic to alkaline media, but, as demonstrated by Markovic and coworkers, can be sped up again by introducing oxophylic surface species, most notably $Ni(OH)_2$, that are thought to facilitate the water dissociation step [73, 74, 75].

The strong apparent influence of water splitting on the HER rate in base has been rationalized by interfacial solvent reorganisation. The groups of Feliu and Koper concluded, based on measurements of the charge transfer resistance and laser-induced temperature-jump measurements during H adsorption and evolution on Pt(111) over a wide pH range, that the energy required to rearrange interfacial water molecules in order to transport H^+/H_2O to, or H_2O/OH^- away from the electrode surface is a function of interfacial field strength and therefore sensitive to the point of zero free charge (pzfc). Because the pzfc shifts anodically with increasing pH, it increases the interfacial field strength and energy barrier for interfacial solvent reorientation and consequentially also the activation energy for the HER. In this picture, the function of oxophilic additives like transition metal dihydroxides is to shift the pzfc cathodically, closer to the reversible potential of the HER [76, 77]. In a recent theoretical study, Rossmeisl and coworkers devised a framework in which pH dependent HER rate changes are rationalized by the activation barrier for proton adsorption, which is a function of entropy loss as the solvated proton is transferred from

bulk solution to the electrode surface and this entropy loss increases going towards more alkaline conditions [78]. A comprehensive overview of the HER in base is given by recent review articles [79, 80, 81], the HER in acid is reviewed by references [63, 82, 83, 84, 85, 24].

More generally descriptors are tools to aid our understanding of the reaction, but even if the right descriptors are identified, many relevant details of the reaction may remain not understood. For Pt in acidic solution the Pt-H bond strength appears to be a good descriptor for the reaction [55, 59], but our mechanistic understanding based on Equations 2.13 - 2.15 still can not explain several well established experimental facts, like the strong dependence of reaction rate on surface structure, or electrolyte composition (for identical surface structure and pH, the ions in solution may influence rate and mechanism), or clarify the relative importance of Tafel vs. Heyrovsky step with change in electrolyte or surface structure [31, 34, 86, 87].

The discussion above clarifies that there is still signficant uncertainty over the mechanism of the HER even for the best understood system (Pt(111) in acidic electrolyte). Our understanding of the reaction's mechanism would undoubtedly profit from directly observing the reaction's intermediate(s) (or the structure of the interfacial solvent, or other interfacial species that are related to the reaction), e.g., by spectroscopy. As will be discussed in detail in section 4.1, the task of gaining such insight has been approached by various vibrational spectroscopies. While the employed spectroscopies varied (and so did the results to some extent), from the point of view of the electrochemistry the approach was always identical. The researchers recorded spectra as a function of a stepwise decreasing potential (spectra acquisition at a fixed potential), saw vibrational bands growing in intensity close to the reversible potential of the HER at 0 V vs. RHE and concluded that these bands represent the reaction intermediate H_{OPD}. The perhaps most convincing study of this type was conducted by Kunimatsu et al. [88] who used a line shape model to extract H_{OPD} populations from their spectroscopic observable as a function of potential and could reasonably well explain the measured Tafel slope. The limits of this approach are significant: The intermediate of the rate determining step can not be distinguished from side products of parasitic reactions, or any interfacial species whose population scales similarly with potential as the intermediate (like a particular solvent arrangement, or potential dependent arrangement of H_{UPD} entities nearby that are needed for the intermediate to react). The time averaged nature of the probing scheme (apply a certain potential for a macroscopic period of time sufficient to record a spectrum) applied to a reaction under steady-state conditions further precludes insight into the temporal evolution of the involved interfacial species. This implies that applying a time averaged probing scheme to investigate a system under steady-state conditions can not distinguish between parallel and consecutive reaction mechanisms: a steady-state concentration of the involved species would be apparent in both cases. Figure 2.8 shows a graphical representation of this situation. The upper panel of the figure represents the evolution of interfacial species (reactant, intermediate and produt/side product) under steady-state conditions; in this scenario the reaction starts at the intercept of the axes and reaches steady-state by the time the probing starts (red box). The lower panel presents a schematic representation of a possible solution to this problem. The reaction gets triggered by a perturbation that is significantly shorter

than the time scale of the reaction. This perturbation provides a temporally short pulse of reactants that evolve in time according to the kinetics of the reaction. Performed with an appropriate probing scheme, this approach allows for distinguishing, e.g., parallel from consecutive reactions by monitoring the system's relaxation to the initial condition before the perturbation. The details of how I plan to trigger the HER on Pt are presented in the following section.

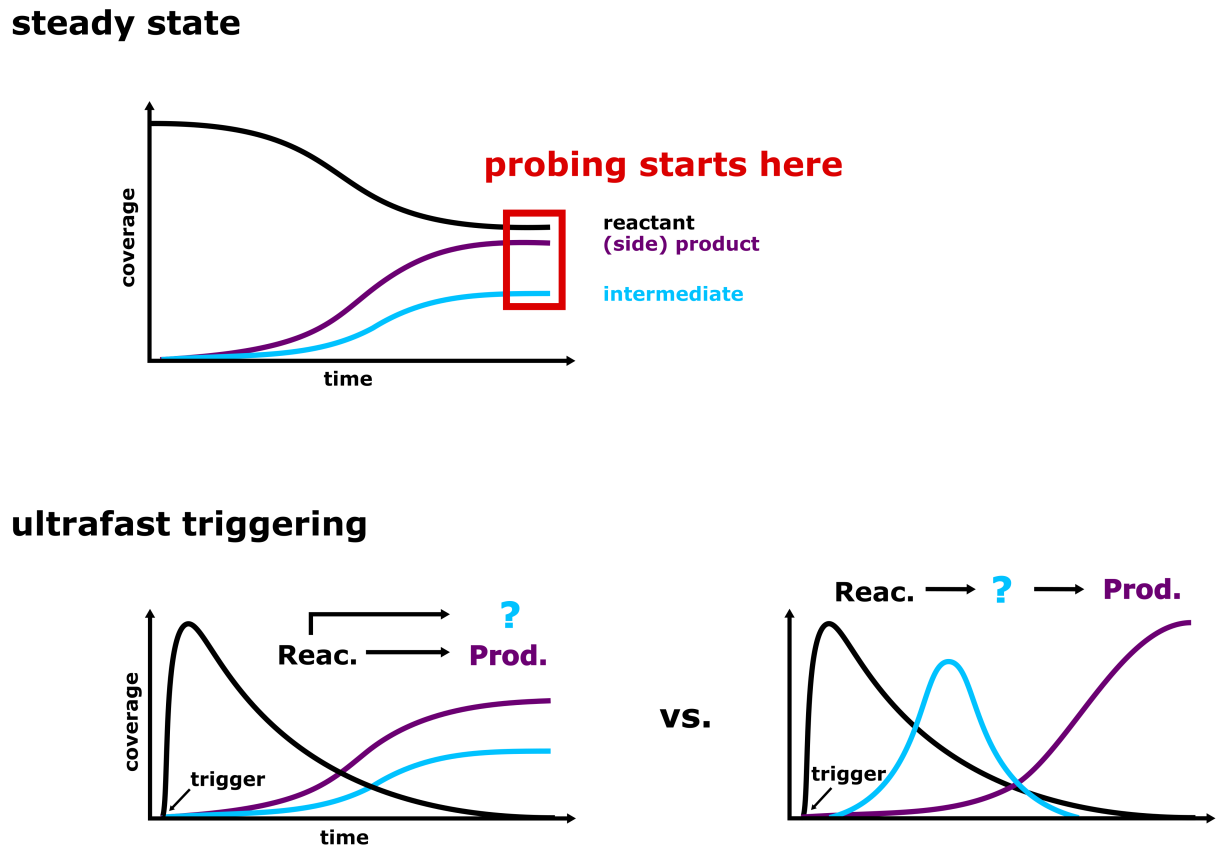

Figure 2.8: Top: cartoon representation of the coverage of surface species during a sample reaction under steady-state conditions, the reaction starts at the intercept of the axes and evolves towards its equilibrium. Bottom: the sample reaction gets triggered by a perturbation faster than the timescale of the reaction. The time evolution of interfacial species in the triggered scenario then allows for distinguishing parallel from consecutive reactions.

2.3 Triggering the HER on a Femtosecond Timescale

I wish to perform a perturbation experiment in which the HER is triggered by providing a temporally short pulse of reactants and to learn about the reaction mechanism by watching the temporal evolution of an interfacial response. As mentioned earlier, this can be a spectroscopic observable of the intermediate, or other involved species. Alternatively, because for many electrocatalytic reactions of interest electrons and holes are reactants/products/intermediates, probes of them, e.g. current, are also reasonable observables. Because I wish to use the results of this perturbation approach to gain insight into the mechanism of the HER under potentials relevant to (thermally equilibrated) electrocatalysis, this pulse of reactants should be sufficiently short that it does not perturb double layer structure (i.e., lead to ion diffusion within the double layer) and on the natural, femtosecond timescale of electron transfer[3]. Such rapid perturbations are not possible using classical electrochemical methods: the response time of an electrochemical cell is >5 ns for the smallest ultramicroelectrodes and hundreds of microseconds for millimeter-sized, single crystals [90].

Much prior work has shown that chemical reactions can be triggered on metal surfaces on ultrafast timescales using femtosecond laser pulses [91]. The concept is illustrated in Figure 2.9: an ultrashort laser pulse excites electrons above the Fermi energy (E_F) into a nonthermal distribution of energies. Over the ensuing few hundred femtoseconds these hot electrons thermalize to a Fermi-Dirac distribution that, after several picoseconds, equilibrates with the phonon system [92]. From a chemical perspective this transient change in electron energy is equivalent to an ultrafast perturbation of electron chemical potential. These higher chemical potential electrons may, e.g., fill Pt-H antibonding states, and induce chemistry that does not occur in their absence.

The possibility of using hot electrons to drive chemistry at extended electrochemical interfaces has been well established in prior studies: Diesing and coworkers have demonstrated that a steady-state supply of hot electrons (created employing an electrode that is a metal/insulator/metal junction) catalyzes the HER [93] and Krivenko et al. have shown that subpicosecond laser pulses on Hg or Ag electrodes can drive electrochemistry [94]. In more recent theoretical work, employing a simplified model of electrode electronic structure and reactant, Schmickler and coworkers have found that the effect of hot electrons is to lower the reaction barrier of (both adiabatic and nonadiabatic) electrocatalytic reactions [95].

In this thesis I utilize near-IR femtosecond irradiation to trigger the HER on an ultrafast timescale on Pt electrodes and monitor the interfacial response by two different approaches. In the first I collect cyclic voltammograms in the presence and absence of femtosecond pulsed laser irradiation and extract the photocurrent as observable.

[3]Parts of this and the following paragraphs are copied from my own publication reference [89]

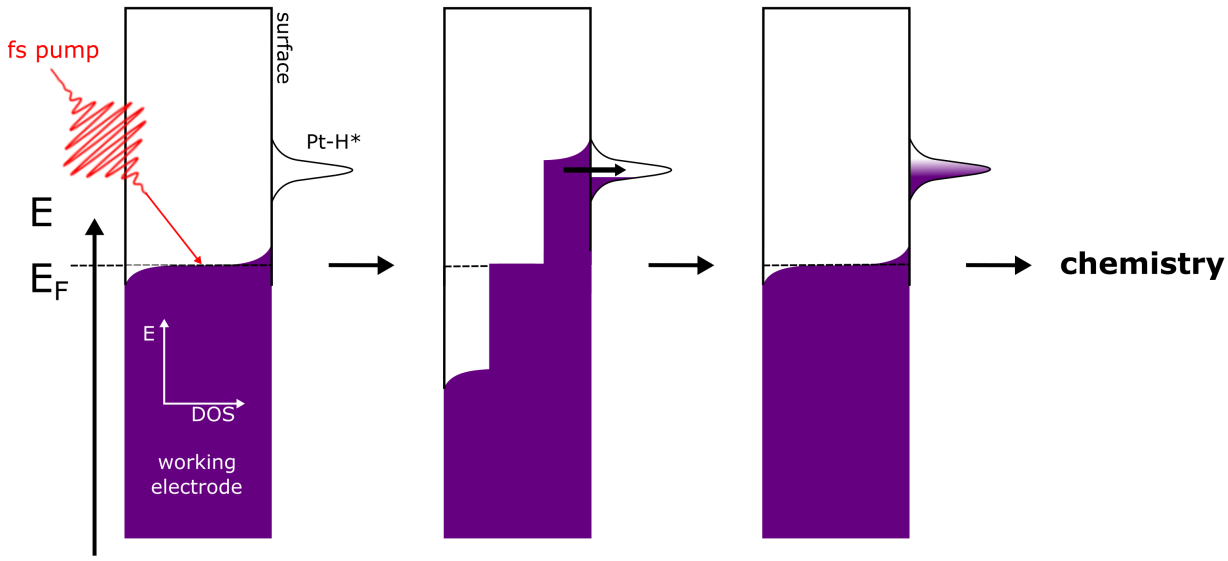

Figure 2.9: Left: schematic representation of the density of states (DOS) of the working electrode in purple at a fixed potential that is set by the potentiostat before arrival of the laser pulse. Middle: after excitation, but before electron thermalization; Right: after electron thermalization. In this scheme the excitation leads to population of a Pt-H anti-bonding state via tunneling of hot electrons to the adsorbate.

This approach is the subject of section 4.2, where I demonstrate that the HER can be triggered close to its reversible potential at 0 V vs. RHE with ultrashort near-IR pulses via excitation of hot electrons. I further show that charge transfer is driven from the electrode to Pt-H in the UPD region (but here the laser irradiation does not induce water splitting) and that charge transfer is only possible when the interfacial electrolyte is oriented in a manner that facilitates it.

The second probe I use to characterize the interfacial response after perturbation is vibrationally resonant SFG of Pt-H, where I scan the time delay between perturbation and SFG probe and therefore obtain insight into the temporal evolution of the interface with femtosecond resolution. One prerequisite for these time resolved studies is that Pt-H can be monitored by SFG. In section 4.1 it is demonstrated that H adsorbed on Pt can be monitored as a function of surface structure, applied potential and electrolyte composition. In section 4.3 I present and discuss the perturbation experiment with time resolved vibrationally resonant SFG probing. There it is demonstrated that an ultrashort 800 nm perturbation induces H adsorption and Pt-H dynamics on subpicosecond timescales both of which are dependent on the applied potential. Lastly, I present evidence that H_{OPD} evolves from H_{UPD} by a change in the interphase close to 0 V vs. RHE that results in an increased mobility for adsorbed H on subpicosecond timescales.

Chapter 3

Optical Methods – Background and Application

3.1 Monitoring Surface Adsorbates – Sum Frequency Generation (SFG) Spectroscopy

SFG is a second-order nonlinear optical process that is interface specific for centrosymmetric media (bulk liquids and gases behave centrosymmetric), which means for our purposes that only the electrode surface contributes to the optical signal and not the bulk of electrode, or electrolyte. Consequently, no bulk signal has to be accounted for and no reference spectra (a source of major uncertainty in linear spectroscopies of electrochemical interfaces that often introduces artifacts) are needed to extract the interfacial response. Put another way, SFG has an exceptionally high surface signal to noise ratio which enables the investigation of atomically smooth surfaces like single crystals. This sets SFG apart from many other spectroscopies (that carry the term "surface enhanced" in their description, like in surface enhanced raman spectroscopy (SERS), or surface enhanced infrared reflection absorption spectroscopy (SEIRAS)) that have a worse surface signal to noise ratio and rely on the plasmonic enhancement of the signal, that is achieved by microscopic roughening of the surface prior to measurement, to reach detectable signal strengths. Another advantage of SFG over linear IR spectroscopies is that the IR laser only has to travel through the absorbing electrolyte once, and not twice. This is important if a surface vibration is close in frequency to a bulk electrolyte mode that absorbs most of the IR power. Yet another positive aspect of SFG is that it is typically performed with ultrashort pulsed laser sources which enable a high time resolution in time resolved optical experiments.

These unique advantages over other commonly used vibrational spectroscopies for the investigation of electrode processes (that mostly are first-order optical techniques) motivated the use of vibrationally resonant SFG for the work presented in this thesis. SFG is a coherent second-order nonlinear optical process in which the output of two pulsed lasers, one in the mid-IR and one at visible frequencies, are overlapped in space and time at the interface of interest and the emitted sum frequency (SF) is monitored. The SF emission

is enhanced multifold if the mid-IR pulse is resonant with an adsorbate vibration, making SFG a spectroscopy.

Compared to linear vibrational spectroscopies, SFG also has some drawbacks. The experimental and financial effort necessary to record meaningful SFG spectra is substantially higher, to date SFG is still mostly performed by dedicated groups with specialized laser labs. As a second-order nonlinear optical probe, the SF contains more information than the linear optical response, but is often more complicated to understand.

3.1.1 Physical Background

Here an introduction to linear and nonlinear optics, necessary to understand the SFG process and how tunable broadband-IR light (that is for SFG) is generated, is given. *Non*linear implies that the response of the medium that interacts with the light changes in a nonlinear fashion when the electric field strength of the incident light is varied linearly. Nonlinear optical responses are typically observed when the driving field strenghts become very high (comparable to the electric field acting on electrons surrounding the nuclei), which is most often found in short laser pulses [96].

The interaction of light with matter relevant for our purposes can be described by the electric field component acting on dipoles. A dipole μ can be described by:

$$\mu = \mu^0 + \alpha E \tag{3.1}$$

where μ^0 is the permanent dipole and α is the polarizability that describes how easily a dipole can be induced by the driving field E in a given direction of the molecule. While this description is valid for isolated molecules in the gas phase, for condensed matter (where we probe ensemble averages of strongly interacting entities) typically the dipole moment per unit volume, the polarization P, is considered:

$$P = P^0 + \varepsilon_0 \chi^{(1)} E \tag{3.2}$$

where P^0 is the static polarization and the second term describes the light induced polarization with ε_0 as the vacuum permittivity constant and $\chi^{(1)}$ as dimensionless linear susceptibility. $\chi^{(1)}$ serves the same purpose as α in equation 3.1. $\chi^{(1)}$ is proportional to the molecular polarizability average over all moleculues and molecular orientations in the probed volume and the number of molecules per unit volume N, i.e., $\chi^{(1)} = N\langle\alpha\rangle/\varepsilon_0'$ (ε_0' denotes the permittivity multiplied by the probed volume). It is clear from this description that the susceptibility is a macroscopic property (in fact, and as detailed later, the second-order component of the susceptibility is what we aim to extract from the samples in the SFG measurement) and is related to the straightforwardly measurable refractive index n by $n = \sqrt{1 + \chi^{(1)}}$. The refractive index is a complex quantity, its real part determines the phase velocity of light in a certain medium (i.e., how fast it travels) and its imaginary part, the extinction coefficient, describes the attenuation of the light by absorption of the medium.

If the driving fields become strong the linear description of the polarization by equation 3.2 is no longer sufficient and higher order terms have to be taken into account [97]:

$$P = P^0 + \varepsilon_0\chi^{(1)}E + \varepsilon_0\chi^{(2)}E^2 + \varepsilon_0\chi^{(3)}E^3 + ... \tag{3.3}$$

where $\chi^{(n)}$ are nonlinear susceptibilities of n^{th}-order (n+1 rank tensors) that have units of $(m/V)^{n-1}$ (m denotes meters, V volts). $\chi^{(n)}$ becomes substantially smaller with increasing n. The $\chi^{(n)}$ give rise to so-called n^{th}-order optical processes.

Even-order nonlinear optical processes (like SFG) are interface specific (bulk forbidden) for centrosymmetric media, as can be demonstrated by performing an inversion operation. Centrosymmetric media possess inversion symmetry and therefore the electrostatic potential inside the material must be symmetric under the $x \rightarrow -x$ operation. This can be demonstrated by considering the second-order induced polarization and inverting the sign of the incomings fields:

$$P^{(2)} = \varepsilon_0\chi^{(2)}E_1E_2 \tag{3.4}$$

Where $E_{1/2}$ can also be identical, i.e., a second-order polarization can also be induced by a single beam, or by two overlapping beams with otherwise identical characteristics. While the polarization must change its sign when the sign of the incoming fields are reversed, $\chi^{(2)}$ remains unchanged because it is a property of the material (which is centrosymmetric) and we are only inverting the sign of the fields. We therefore obtain

$$-P^{(2)} = \varepsilon_0\chi^{(2)}(-E_1)(-E_2) \tag{3.5}$$

or

$$-P^{(2)} = P^{(2)} \tag{3.6}$$

which is only true if $\chi^{(2)} = 0$. This implies that even-order nonlinear optical processes are only allowed in non-centrosymmetric media and for centrosymmetric media only where the symmetry is broken: at the surface.

One important property of the induced oscillating polarization is that it acts as a source of radiation itself. We will illustrate this at the example of second-order processes, because they are at the heart of SFG and the way in which we generate broadband-IR pulses for our experiments. If we illluminate a material with two laser beams whose electric field components can be described by $E_1cos(\omega_1 t)$ and $E_2cos(\omega_2 t)$, then the induced second-order polarization is:

$$P^{(2)} = \varepsilon_0\chi^{(2)}(E_1cos(\omega_1 t) + E_2cos(\omega_2 t))^2 \tag{3.7}$$

Which can be expanded to:

$$\begin{aligned} P^{(2)} = {}& {}^1\!/_2\varepsilon_0\chi^{(2)}(E_1^2(1 + cos(2\omega_1 t) + E_1^2(1 + cos(2\omega_2 t)) \\ & +\varepsilon_0\chi^{(2)}E_1E_2(cos((\omega_1 + \omega_2)t) + cos((\omega_1 - \omega_2)t)) \end{aligned} \tag{3.8}$$

This illustrates that the induced second-order polarization emits light at frequencies $2\omega_1$, $2\omega_2$ (second harmonic generation, SHG, of both fundamental beams), $\omega_1 + \omega_2$ (sum frequency generation, SFG) and $\omega_1 - \omega_2$ (difference frequency generation, DFG, which we use for broadband-IR generation), respectively. SHG can be regarded as a special case of SFG where both photons have the same energy. A graphical comparison of SFG and DFG is given in Figure 3.1:

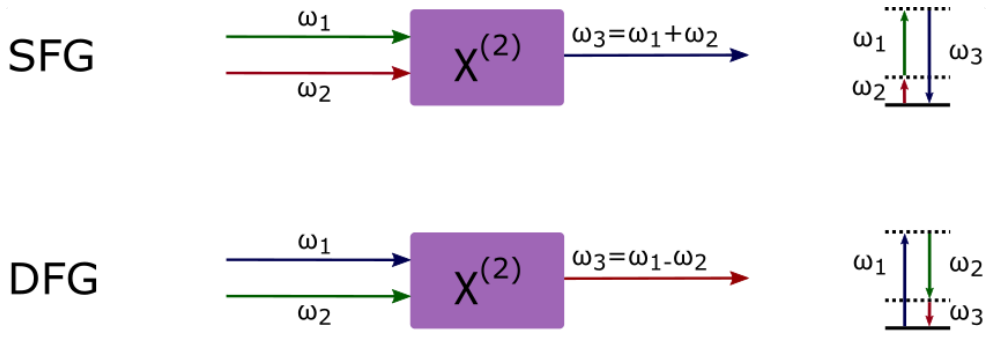

Figure 3.1: Schematic representation of the SFG (top) and DFG (bottom) processes. On the left the three-wave mixing inside a medium with a second-order nonlinear susceptibility $\chi^{(2)}$ is illustrated. On the right the according energy level scheme is presented. While the bottom solid lines represent the ground states, the dashed lines can either be actual, or virtual energy levels.

In the DFG process, one ω_3 photon is created by annihilation of one ω_1 photon and stimulated emission of a ω_2 photon. A similar process in which one incident photon with frequency ω_1 is split into two photons with energies ω_2 and ω_3 is called optical parametric[1] generation (OPG) and is used to generate optical pulses of tunable wavelength. Because usually the output beams of a OPG process are weak, they are amplified in a second stage called optical parametric amplification (OPA) in which one output beam from the OPG process (e.g. ω_2) is shone into a nonlinear optical crystal together with a strong pump beam (here denoted with ω_1). In the OPA process one ω_1 photon is consumed and two photons with frequencies ω_2 and ω_3 are created (the OPA process can be considered as a seeded DFG process). In this work, OPG, OPA and DFG are used to generate the broadband-mid-IR pulses to use in the SFG experiments.

The SFG process at the interface of two media (1 and 2) is shown in Figure 3.2. The SF (ω_3) is depicted in blue, the visible (ω_1) and IR (ω_2) pulses in green and red, respectively. The arabic numeral indices are replaced by abbreviations of the respective beams for the following discussion.
Energy conservation is satisfied during the SFG process by:

$$\omega_{3/SFG} = \omega_{1/VIS} + \omega_{2/IR} \tag{3.9}$$

[1] In a "parametric" process the initial and final quantum mechanical states are identical.

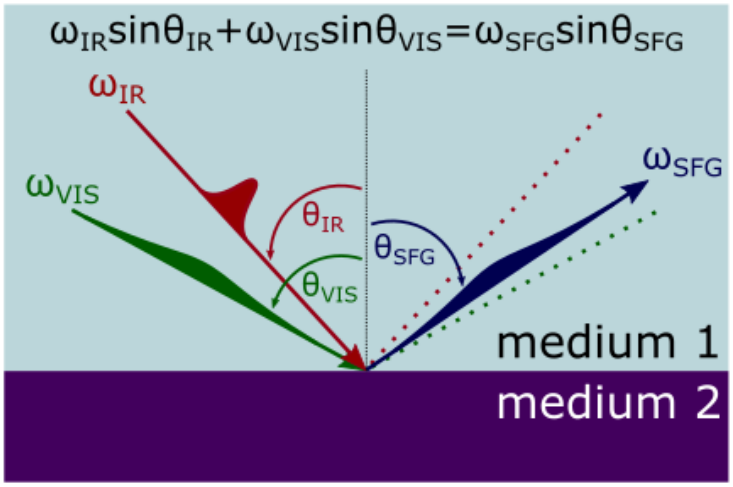

Figure 3.2: Schematic of the SFG process at an interface highlighting its coherent nature. The IR/VIS(SFG) pulse is meant to be short/long in time.

As shown in Figure 3.2, SFG is a coherent process. This coherence is described by momentum conservation:

$$\overline{p}_{SFG} = \overline{p}_{VIS} + \overline{p}_{IR} \tag{3.10}$$

Here the bar signifies that the momentum component parallel to the interface is considered. Rewriting equation 3.10 in terms of the wave vector k=$2\pi/\lambda$ using $p = \hbar k$ (where $\hbar$ is Planck's constant divided by 2π) yields:

$$k_{SFG} sin\theta_{SFG} = k_{VIS} sin\theta_{VIS} + k_{IR} sin\theta_{IR} \tag{3.11}$$

where the angels $\theta_{SFG/VIS/IR}$ are measured with respect to the surface normal. Writing out the momentum conservation condition in this way clarifies that the emission angle of the SFG is determined by the incident angles of visible and IR light and their frequencies. A more convenient version of equation 3.11 is obtained by expressing the momentum as frequency:

$$\omega_{SFG} sin\theta_{SFG} = \omega_{VIS} sin\theta_{VIS} + \omega_{IR} sin\theta_{IR} \tag{3.12}$$

This relationship is also depicted in Figure 3.2.

3.1.2 The Sum Frequency Signal

The intensity of the emitted SF signal I_{SFG} in photons per second can be described by [98]:

$$I_{SFG}(\omega_{SFG}) \propto \left| \sum_{i} \sum_{j,k} L_{ii}(\omega_{SFG}) \chi^{(2)}_{ijk} L_{jj}(\omega_{VIS}) L_{kk}(\omega_{IR}) \right|^2 I_{VIS} I_{IR} \tag{3.13}$$

Where i,j and k are the coordinates in the interface-fixed reference frame (and correspond to x,y and z in the laboratory reference frame). The L factors are the Fresnel coefficients that relate the input macroscopic electric fields to the fields at the interface and are a function of frequency ω, polarization and angle of incidence of the light and the refractive indices of bulk media 1 and 2 in Figure 3.2. $I_{VIS/IR}$ is the intensity of the VIS/IR beam, respectively.

The second-order susceptibility $\chi^{(2)}_{ijk}$ can be resonant (frequency dependent, R), or non-resonant (frequency independent, NR) and is more conveniently written as an effective quantity $\chi^{(2)}_{eff}$:

$$\chi^{(2)}_{eff} = \chi^{(2)}_{NR} + \chi^{(2)}_{R} \tag{3.14}$$

$\chi^{(2)}_{R}$ becomes non-zero if the IR beam is resonant with an interfacial vibration and is therefore dependent on adsorbate coverage, i.e. the number of oscillators in the probe spot. It is further a function of the angular average of the molecular hyperpolarizability (second-order polarizability of a molecule) $\langle\beta\rangle$ [96, 99]:

$$\chi^{(2)}_{R} = \frac{N}{\varepsilon_0}\langle\beta\rangle \tag{3.15}$$

Every mode q that is excited by the IR beam contributes to the total hyperpolarizability according to [100, 101]:

$$\beta_{lmn,q} = \frac{\langle g \mid \alpha_{lm} \mid q\rangle\langle q \mid \mu_n \mid g\rangle}{\omega_{IR} - \omega_q + i\Gamma_q} \tag{3.16}$$

Where l,m and n describe the molecular coordinate system and α_{lm} and μ_n denote the Raman and dipole vibrational transition moments, respectively. g and q denote the ground state and first vibrationally excited state. Γ_q is the damping constant of the q-th mode. The numerator of equation 3.16 is a product of the Raman and dipole vibrational transitions, which makes clear that only modes that are both Raman *and* IR active are SFG active. This implies that molecules with inversion symmetry are not SFG active, as they are either Raman, or IR active, but never both.

3.1.3 Data Analysis - Fitting the Sum Frequency Signal

The transition moments α_{lm} and μ_n are typically unknown and are merged into fitting constants for the practical analysis of the SFG data. A popular line shape model for the SFG signal is the homogeneous Lorentzian [102, 103, 104, 105, 106, 98]:

$$\chi^{(2)}_{eff} = \chi^{(2)}_{NR} + \sum_q \chi^{(2)}_{R} = \mid A_{NR} \mid e^{i\phi_{NR}} + \sum_q \frac{\mid A_q \mid e^{i\phi_q}}{\omega_{IR} - \omega_q + i\Gamma_q} \tag{3.17}$$

Where A_{NR} is the amplitude of the nonresonant background and ϕ_{NR} its phase. A_q, ϕ_q, ω_q and Γ_q are the amplitude, phase, centre frequency and damping constant (half width at

half maximum) of the q-th mode. In principle the resonant phase has to be 0 or π and the NR phase can have any value (and in the case of metal electrodes be potential dependent). However, if the resonant response is not fully resonant (e.g. has contributions from charge transfer from the metal) and if the measurement probes many tensor components of $\chi^{(2)}$ (without quantitative correction for Fresnel factors) one may end up with effective fractional phases. Therefore with ϕ_q only the relative phase between nonresonant background and the q-th resonance is considered in the following. Merging the Fresnel factors into the effective second-order susceptibility and inserting Equation 3.17 into Equation 3.13, one is left with the following expression that can be used to fit the SFG data:

$$I_{SFG} \propto \mid \mid A_{NR} \mid + \sum_q \frac{A_q e^{i\phi_q}}{\omega_{IR} - \omega_q + i\Gamma_q} \mid^2 I_{VIS} I_{IR} \tag{3.18}$$

3.1.4 Experimental Setup

The experimental setup that has been used for the SFG measurements in this work is sketched in Figure 3.3:

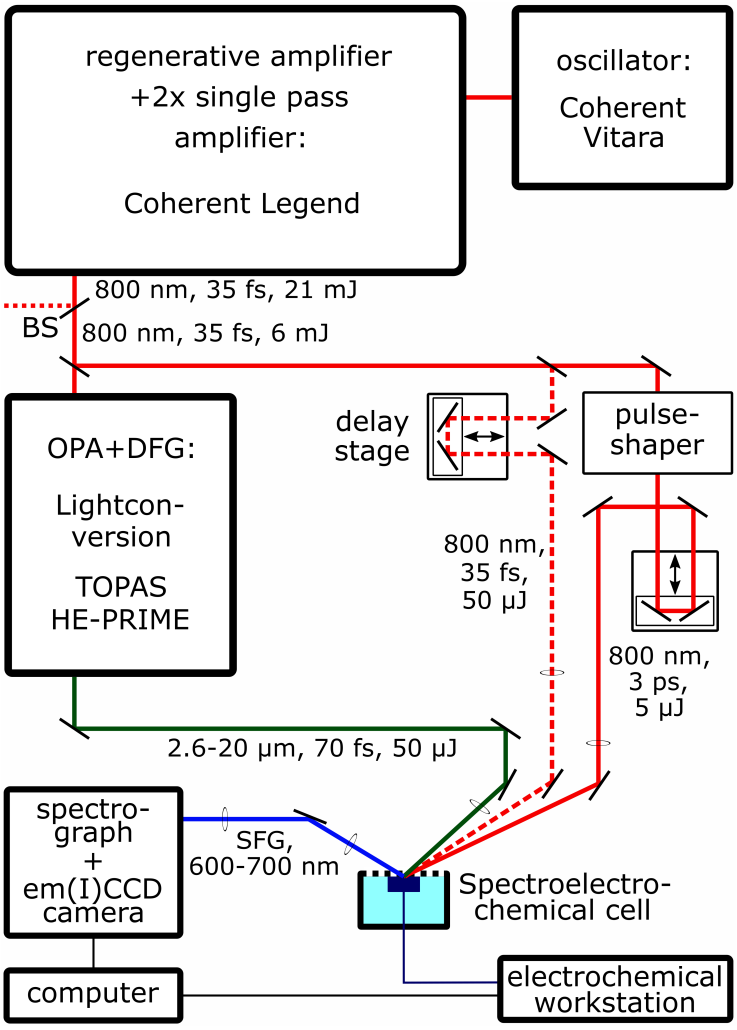

Figure 3.3: Schematic of the optical setup. The used devices are stated along with the respective manufacturer. BS stand for beam splitter, OPA and DFG for optical parametric amplifier and difference frequency generator, respectively. em(I)CCD stand for electron multiplying (intensified) charge-coupled device.

The light that is eventually used for the optical experiment is provided by the Coherent Vitara oscillator (800 nm, 80 MHz, <10 fs, >800 mW), amplified by chirped pulse amplification [107] in the Coherent Legend with additional cryo-cooled single pass amplifier (that is pumped by one pump laser more than in the commercial version) and after compression reaches a pulse energy of 21 mJ at 800 nm, 35 fs pulse duration and a repitition rate of 1 kHz. Of the total output, 6 mJ are split off with a beamsplitter for the SFG experiment.

5.7 mJ are used to generate the tunable broad-band IR light in the Lightconversion TOPAS HE-PRIME, while the remaining 300 mJ are used unaltered as a pump and to generate the temporally long upconversion VIS pulse in the pulse-shaper (a Fabry-Pérot etalon). The etalon produces spetrally narrow (0.735 nm full width at half maximum, FWHM), but temporally long pulses (>2 ps) with an energy of around 5 µJ.

The energies accessible for all incoming beams are well in excess of what is needed for the SFG experiment and are adjusted to the weak probing regime by combinations of $\lambda/2$ plates and polarizers, both for the respective frequency range. The pulse energies vary slightly depending on the investigated system and are stated in the description of the respective experiment. The focal lengths in the SFG experiments described in chapter 4 for the IR, VIS and pump beams were 300, 1000 and 1200 mm, respectively. The focal lengths in the SFG experiments described in chapter 6 for the IR and VIS beams were 100 and 500 mm, respectively.

After the sample, the SFG signal was dispersed in a spectrograph (SR303i, Andor Technology) and imaged with an emCCD camera (Andor Technology, experiments of chapter 4), or an emICCD camera (PI-MAX4, Princeton Instruments, experiments of chapter 6).

3.2 Monitoring Surface Heterogeneity – Second Harmonic Imaging

As mentioned above, SHG is a special case of SFG where both incoming beams have the same frequency and as spectroscopy, or microscopy, SHG is a popular tool for investigating charged interfaces [108, 109, 110] (of course, SHG is not limited to charged interfaces, the same selection rules as for SFG apply). In this work I employ Second Harmonic Microscopy (SHM) to investigate heterogeneity in the electrochemistry of poly- and nanocrystalline gold electrodes, see section 5.1.

At the electrified interface of silver and silicon surfaces, Lee et al. found that the SH intensity increases quadratically and the surface susceptibility varies linearly with applied potential under certain conditions [111]. The same behavior was later observed on mercury [112] and gold electrodes [113]. The observed behavior was rationalized by assuming that the nonlinear polarization at the electrified interface can be desribed as a sum of dipolar electric polarizations and a DC field-induced polarization contribution:

$$P(2\omega) = \chi^{(2)}(2\omega)E(\omega)E(\omega) + \chi^{(3)'}(2\omega)E(\omega)E(\omega)E_{DC} \tag{3.19}$$

$\chi^{(2)}$, the total second-order nonlinear susceptibility, of Au is dominated by the surface (over the bulk) term as gold is a centrosymmetric (fcc) material [114]. $\chi^{(3)'}$ is the effective total third-order nonlinear susceptibility, which has contributions from both gold surface (this term strongly dominates over the other contributions) and all oriented dipoles in solution[2]. $E(\omega)$ denotes the electric field of the fundamental and E_{DC} denotes the static electric field across the interface.

The SH intensity is written accordingly:

$$I(2\omega) \sim \mid \chi^{(2)} + \chi^{(3)'}\Phi_0 \mid^2 I(\omega)^2 \tag{3.20}$$

Here Φ_0 is the potential drop across the interface (from the metal surface to the bulk of the electrolyte) and $I(\omega)$ is the intensity of the fundamental. $\chi^{(2)}$ and $\chi^{(3)'}$ are assumed to be potential independent and writing the potential drop as

$$\Phi_0 = V - V_{PZC} \tag{3.21}$$

(where V is the applied potential and V_{PZC} is the potential of zero charge (PZC)) illustrates why this model is termed "parabolic" model: linearly varying the potential around the PZC leads to a parabolic inrease in SH intensity. It should be stressed that equations 3.20 and 3.21 are only valid in the absence of specifically adsorbing ions, or in a potential window where such ions do not adsorb specifically. Otherwise $\chi^{(2)}$ and $\chi^{(3)'}$ would be a function of potential (because the surface electronic structure changes with ion adsorption). This implies that the parabolic model is valid as long as tuning the electrode bias is analog

[2]The $\chi^{(3)}$ term is formally bulk active, but interface specific to the extent that it has one contribution that scales with the gradient in dielectric function and this gradient is at the interface.

to (de)charging a bare metal capacitor. Multiplying out equation 3.20 leaves us with an expression for a parabola:

$$I(2\omega) \sim (\chi^{(3)'}\chi^{(3)'*})\Phi_0^2 + (\chi^{(2)}\chi^{(3)'*} + \chi^{(2)*}\chi^{(3)'})\Phi_0 + (\chi^{(2)}\chi^{(2)*}) = Q\Phi_0^2 + L\Phi_0 + C \quad (3.22)$$

Q, L and C are the quadratic, linear and constant coefficient, respectively. The imaginary part of the third-order nonlinear susceptibility is estimated to be negligible at the fundamental's frequency following Miller's rule (see appendix section B). This allows us to simplify equation 3.22 to:

$$\frac{Q}{L} \sim \frac{Re(\chi^{(3)'})}{Re(\chi^{(2)})} \quad (3.23)$$

For $\chi^{(3)'} >> \chi^{(2)}$, the evolution of the SH signal as a function of potential is parabolic with a minimum at the PZC. On the contrary, for $\chi^{(3)'} << \chi^{(2)}$ the evolution of the SH signal as a function of potential is no longer parabolic. For $\chi^{(3)'} \approx \chi^{(2)}$ the signal evolution with potential is parabolic, but the minimum is shifted away from the PZC. Prior work by Guyot-Sionnest et al. has demonstrated that as long as the photon energy of the fundamental is too small to excite interband transitions (i.e. as long as the substrate reponse is free-electron like), $\chi^{(3)'}$ is likely dominant. However, if the fundamental has sufficient energy to excite interband transitions, $\chi^{(2)}$ becomes dominant [113]. While obtained on Ag and Au electrodes, the results of the work by Guyot-Sionnest et al. should be valid for metals (and probably semiconductors) in general.

Experimental

The optical setup and the electrochemical cell for SH imaging is shown in Figure 3.4.

The light source for the second harmonic microscope is a Pharos SP-1.5 (Light Conversion) laser, which delivers 180 fs pulses centred around 1030 nm at a maximum output power of 6 W and variable repetition rates between 1 kHz - 1 MHz[3]. For this work the laser system is operated at a repetition rate of 200 kHz. All mirrors on the optical path are of the protected silver type (Thorlabs, PF10-03-P01). The lenses (achromatic) and the other optical elements on the illumination path (1036 nm) are near-infrared antireflection coated (Thorlabs, B), while the optical elements on the detection path (518 nm) are antireflection coated for the visible region (Thorlabs, A). I use a spatial light modulator (Holoeye Pluto-NIR-015), which is a phase-only device coated for near-infrared wavelengths, to modify the illumination laser beam that later on passes through a water immersion microscope objective to illuminate the sample in a wide-field configuration. The illumination objective (Olympus, LUMPFLN 60XW) has 60-times magnification with a numerical aperture NA of 1.0 and a working distance of 2 mm. This objective illuminates the sample at 34° with respect to the surface normal in a one-beam reflection geometry. The laser is set to deliver

[3]This paragraph has been published in my own publication reference [33].

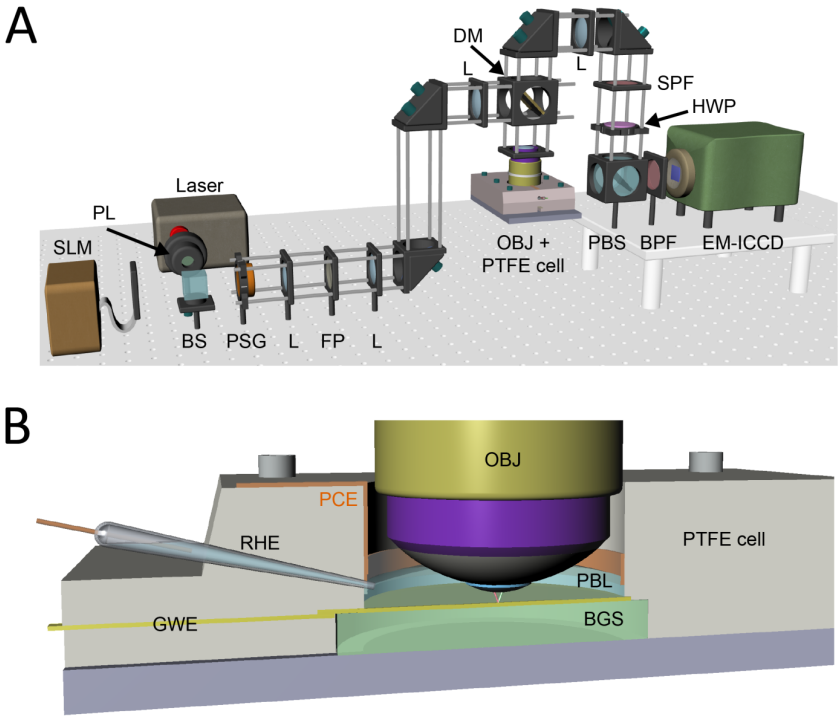

Figure 3.4: A) Second Harmonic Imaging setup in reflection mode: SLM – spatial light modulator, PL – polarizer, BS – beam splitter, PSG – polarization state generator, L – (achromatic) lense, FP – Fourier plane, DM – dichroic mirror, OBJ – microscope objective, SPF – short pass filter, HPW – half-wave plate, PBS – polarizing beam splitter, BPF – band-pass filter (for the second harmonic), EM-ICCD – electron multiplying intensified CCD (gated camera). B) Electrochemical cell for optical imaging: GWE – gold working electrode, RHE – reversible hydrogen electrode, PCE – platinum counter electrode, PBL – phosphate buffer liquid, BGS – borofloat® glass substrate.

a constant peak power density of 22.4 GW/cm^2 (4.3 mJ/cm^2 fluence) at the sample, on a field of view with a diameter of 75 µm full-width at half maximum. The position of the sample is manipulated by a XYZ translation stage (Asi Imaging, PZ-2000), where the XY-axes are controlled by actuators with 10 cm travel range, while the Z-axis is moved by a piezoelectric stage with 300 µm travel range. To extend this positioning system, the microscope objective is mounted on a Z-axis actuator stage (Asi Imaging, LS-200). Once the second harmonic photons are generated, they are collected by the same microscope objective used for illumination and further projected on a back-illuminated electron-multiplied and intensified CCD camera with 512x512 pixels (PI-MAX4: 512EM-HBf P46 GEN III).

Chapter 4

Triggering and Monitoring the HER on Pt on a Femtosecond Timescale

As detailed in section 2.3, in order to unravel the mechanism of the HER on Pt we want to observe the reaction on the natural femtosecond timescale of electron transfer after starting it with an ultrafast optical pulse.

As a first step towards this goal, in section 4.1 I monitor the reaction intermediate Pt-H_{OPD} and Pt-H_{UPD} with SFG and understand the relationship between interfacial structure and vibrational response on Pt(111) and Pt(110) and how it is affected by tuning the applied potential and adding alkali metal cations to the electrolyte.

The second step is to clarify wether we can start the HER on an ultrafast timescale with optical pulses. In section 4.2, I show that the HER can be driven with ultrashort optical pulses via excitation of hot electrons when the applied bias is close to the reversible HER potential. At more positive potentials, the light pulses initiate charge transfer that does not result in hydrogen evolution.

Both types of experiments are combined in section 4.3, where the time evolution of the Pt(111)-H SFG spectrum after excitation with an ultrashort optical pulse is recorded. The results demonstrate an ultrafast increase of atop (monocoordinated) Pt-H population after excitation that is dependent on the applied potential. They further show how the additional Pt-H population evolves on an ultrafast timescale allowing for mechanistic insights into the HER on its natural timescale for the first time.

The implications of each sort of data for understanding H adsorbed on Pt, the HER and its mechanism are described in each section. At the end of the chapter I describe how these different types of insights fit together and the additional insight considering them collectively offers.

4.1 Spectroscopically Resolving Adsorbed H on Pt(111) and Pt(110) Electrodes and the Influence of Alkali Metal Cations on Interfacial Solvation and the HER

4.1.1 Introduction to the Spectroscopy of Pt-H under Electrochemical Control

For our goal of watching the HER on its natural timescale, a structural probe would be particularly helpful (more helpful than merely measuring current). Such a probe could also help understanding the HER's dependence on interfacial solvent structure (discussed in detail in section 4.2), together with the established dependence on crystal face orientation for a given catalyst in acid and base [31, 75], as detailed in section 2.2. A direct structural probe for the HER reaction intermediate Pt-H_{OPD} (and interfacial solvent; see sections 2.1.3 and 2.2 for details on Pt-H and the HER) possibly is the most straightforward way to move beyond equations 2.13 - 2.15 towards a more realistic mechanism. Far from a novel concept, the spectroscopic in situ investigation of electrochemical Pt-H dates back to the 1970s [115], comparable results from various infrared spectroscopies are compared in Table 4.1 (if an author published multiple studies with identical results, only the first study is listed). The table lists the details of peaks that have been assigned to Pt-H vibrations for single and polycrystalline Pt electrodes: centre frequency, its (Stark) shift as a function of potential (over a rather narrow range of about 100 mV in case of the linear sectroscopies, the SFG study did not report shifting of the peaks with potential), full width at half maximum (FWHM) and the potential at which the peak(s) first appear(s) vs. RHE is listed along the employed spectroscopy.

While no entirely consistent picture emerges, the linear spectroscopies (SNIFTIRS, SERS and SEIRAS) clarify that on polycrystalline Pt only one apparent resonance exists. This resonance appears 100 - 120 mV positive of the reversible HER potential, is centered between 2080 and 2090 cm^{-1} and shows a blueshift with positively increasing potential (redshift with decreasing potential). Despite the 100 - 120 mV mismatch with respect to the reversible HER potential, it has been assigned to the intermediate of the reaction, because its intensity grows with decreasing potential, as discussed in section 2.2. The frequency around 2000 cm^{-1} clarifies that this is a singly bonded hydrogen atop a Pt atom [116]. However, the study by Ogasawara and coworkers on Pt single crystals demonstrates that Pt(100) and Pt(110) show discernable Pt-H resonances, of which at least the Pt(100)-H resonance can clearly be distinguished from the 2080 - 2090 cm^{-1} mode found on polycrystalline samples. Because polycrystalline Pt also shows (100) like facets and steps [117], this mode should also be observable on these polycrystalline samples, but has not been observed so far, perhaps because of an unfavorable signal to noise ratio in the respective measurements.

Table 4.1: Comprehensive overview of Pt-H vibrational spectroscopy. The studies are listed in order of appearance from top to bottom. The values for the Stark shift and FWHM were determined from the paper if not specified by the authors. In some cases values could not be specified due to the nature of the data, or because the authors did not publish the entire data set; this is noted as n.s. = not specified/specifiable. Acronyms in the methods column are short for: Subtractively Normalized Interfacial Fourier Transform IR Spectroscopy (SNIFTIRS), Sum Frequency Generation Spectroscopy (SFG), Surface Enhanced Raman Spectroscopy (SERS) and Surface Enhanced Infrared Absorption Spectroscopy (SEIRAS).

author	substrate	centre frequency (cm^{-1}) at ~0 V vs. RHE	Stark shift (cm^{-1}/V)	FWHM (cm^{-1})	onset potential vs. RHE (mV)	method
Nichols [64]	Pt_{poly}	2090	239	80	110	SNIFTIRS
	Pt(111)	2100	n.s.	160	90	SNIFTIRS
Ogasawara [118]	Pt(111)	-	-	-	-	SNIFTIRS
	Pt(100)	2020	74	30	250	SNIFTIRS
	Pt(110)	2082	n.s.	60	0	SNIFTIRS
Peremans [119]	Pt_{poly}	1770-2050 3+ peaks	-	n.s.	290	SFG
	Pt(111)	1770-2020 (3 peaks)	-	n.s.	290	SFG
	Pt(100)	1770-1970 (3 peaks)	-	n.s.	490	SFG
	Pt(110)	1765-2050 (4 peaks)	-	n.s.	290	SFG
Ren [120]	Pt_{poly}	2088	50	100	120	SERS
Kunimatsu [121]	Pt_{poly}	2079	131	75	100	SEIRAS

The Pt-H single crystal measurements, showing vibrational modes that were not observed on the polycrystalline samples, motivate revisiting this system, especially as a starting point for time resolved pump-probe studies that characterize Pt-H during electron transfer and subsequent (electro)chemical reactions [89]. To this end, I employ vibrationally resonant SFG. SFG, as discussed in section 3.1, is specifically well suited for this purpose, as it is interface specific and does not rely on reference spectrum substration (a step that often introduces spectral artefacts) to extract the desired interfacial information.

SFG has been used to investigate hydrogen sorption at Pt electrodes before by Peremans et al., see Table 4.1. Unlike the linear spectroscopy studies, their study showed multiple peaks that already emerged with the onset of underpotentially deposited hydrogen (see section 2.1.3 for details on Pt-H_{UPD}). Despite the higher surface specificity of SFG over the linear optical probes, the results of the SFG study do not seem to be as well received by the electrochemical community as the results from the linear spectroscopies. This may be due to the lack of isotope exchange measurements to confirm the chemical identity of the adsorbates (the appearance of atop adsorbed H in the UPD potential region is

not easy to explain) and the independence of the peak centre frequencies on the applied potential. The peak centre frequencies should change as a function of potential due to i) changes in adsorbate coverage and ensuing changes in adsorbate – adsorbate interaction and ii) changes in the interfacial field strength [52]. Isotope exchange measurements and shifting of peak centre frequencies are demonstrated in this work. In situ CVs in the spectroelectrochemical cell are also provided.

Here, I use vibrationally resonant SFG to monitor Pt-H on Pt(111) and Pt(110) as a function of potential in 0.5 M $HClO_4$ with and without Li^+ cations. The observed Pt-H peaks, that are surface structure and potential dependent, are assigned to surface sites by correlation with the in-situ CVs and prior temperature programmed desorption (TPD) studies of the same adsorbate systems (H/Pt(hkl)) in UHV. The chemical identiy of the adsorbates is confirmed as hydrogen in isotope exchange measurements. Evidence is presented that H_{OPD} evolves from H_{UPD}. Finally, the influence of adding Li^+ ions on the Pt(111)-H spectrum is demonstrated, suggesting the presence of solvated proton structures at the interface along with atop adsorbed Pt-H, and their sensitivity to the presence of cations. The relationship of these solvated proton structures with atop adsorbed Pt-H and Pt-H in hollow sites is discussed and a microscopic mechanism linking pH and cation dependent changes in HER activity to the transition from solvated protons to Pt-H, i.e., the Volmer reaction, is devised.

4.1.2 Static SFG Spectroscopy of the Pt(hkl)/Electrolyte Interface

In the left of panel a) of Figure 4.1, background corrected SFG spectra of Pt(110) (upper panel) and Pt(111) (middle panel) electrodes are shown as a function of potential in 0.5 M $HClO_4$ solution. The corresponding in situ CVs are shown on the right; minor impurities and other consequences of working in a spectroelectrochemical cell (wrapping the electrode in Teflon, pushing it against an IR transparent window) lead to small deviations from hanging meniscus CVs. The Pt(110) CV is dominated by the (1x2) reconstruction [122], but its sharp peak at 0.15 V vs. RHE, which is associated with H/OH sorption at the (110) step [123], is decreased in intensity and the CV shows minor (111) like defects towards higher potentials. The Pt(111) CV demonstrates a high surface quality also in the spetroelectrochemical cell, with the only exception that the H-adsorption starts at slightly too negative a potential when scanning cathodically (i.e. in the negative direction) [124]. For background correction of the VSF spectra, spectra at a higher potential were used, details can be found in the figure caption. The background correction[1] was performed in order to exclude a small (with respect to the signal size of Pt-H), potential independent, feature that likely stems from the CaF_2/H_2O interface.

[1]It should be stressed that this background subtraction is a cosmetic detail and not comparable to the background correction in SNIFTIRS that needs to be done in order to extract the interface signal.

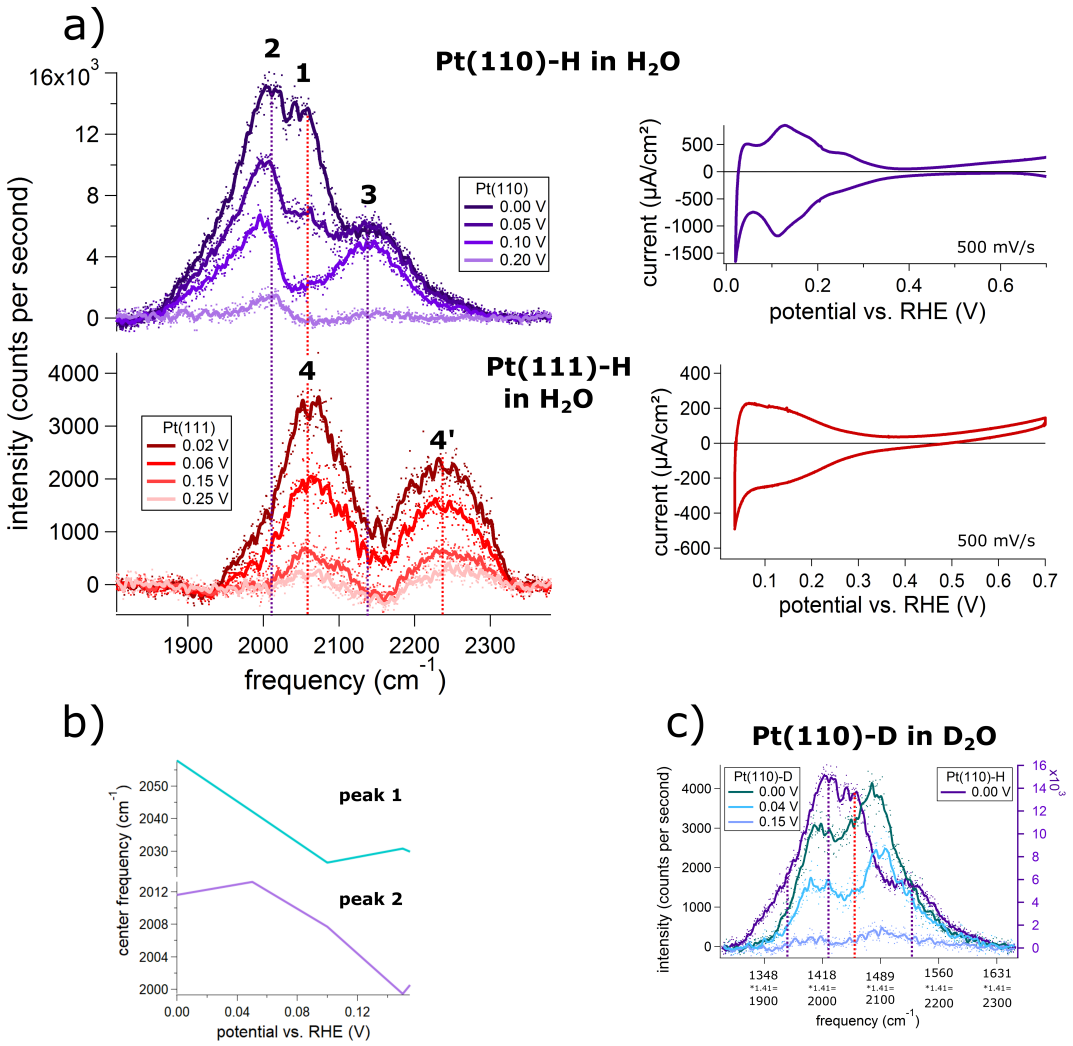

Figure 4.1: Background corrected SFG spectra of a) Pt(110)-H (the spectrum at 1.0 V vs. RHE was taken as reference for background subtraction) and Pt(111)-H (the spectrum at 0.5 V vs. RHE was taken as reference) in 0.5 M $HClO_4$ with dotted lines that indicate the main features of Pt-H on each crystal; b) Center frequency of Pt(110)-H peak **1** and **2** as a function of potential, extracted from a line shape analysis described in appendix section A; c) Pt(110)-D in 0.5 M $DClO_4$ (the spectrum at 1.0 V vs. RHE was taken as reference), the Pt-D spectrum was recorded from ca. 1300 to 1650 cm^{-1} and for comparison with Pt-H, the frequency axis is multiplied with 1.41 to account for the H/D exchange and shown below; a Pt(110)-H reference spectrum is shown in purple.

The SFG spectra of Pt(110) show three main features in the range 1900 - 2300 cm^{-1}, numbered **1-3** in order of appearance, emerging when going negative in potential. Coming

from the bilayer region (which extends from around 0.4 - 0.55 V vs. RHE), resonance **1** appears at 0.25 V vs. RHE as a dip around 2060 cm^{-1} (the appearance of this spectral feature is discussed in detail below and in appendix section A). At 0.2 V vs. RHE a second resonance, **2**, at around 2010 cm^{-1} starts to show. At 0.15 V (not shown) the remaining resonance **3** at 2140 cm^{-1} appears. By 0.1 V vs. RHE, **3** has almost reached its maximum intensity, which it reaches at 0.05 V, while **2** continues to grow linearly with decreasing potential. Resonance **1** only starts to appear as a positive peak at 0.1 V vs. RHE (it is a dip at higher potentials, see appendix section A) and continues to grow from then on. It is present and growing already at higher potentials (a sufficient intensity of this peak is necessary to obtain a satisfactory fit to the line shape) and is now discernable as a positive peak from pure inspection. Overall, the Pt-H resonances on Pt(110) show a very distinctive behavior as a function of potential. It is obvious from inspection that the peak positions shift as a function of bias, which is detailed in panel b): **2**, for example, shows a shift of 12 cm^{-1} from 0.1 to 0 V vs. RHE, which translates to 120 cm^{-1}/V - this value compares well with previously reported Stark shifts for Pt-H, see Table 4.1. Comparable values are also obtained for resonances **1** and **3**. The values plotted in b) were obtained from a line shape analysis. Details of the line shape analysis and a numerical evaluation of it showing that the results are not arbitrary solutions to an overdetermined system, but represent a minimum in phase space, can be found in appendix section A.

A tentative peak assignment for Pt(110)-H can be done based on the correlation of resonances **1-3** with current features apparent in the CV. Resonance **3** can be attributed to H on the ridge of the (110) steps that cause the peak in the CV just above 0.1 V, as its intensity does not increase after the CV peak ends around 0.05 V. Resonance **2** can be assigned to H on the (111) like microfacets of the Pt(110) surface (a (110)-(1x2) like surface can be regarded as a stepped (111) surface with 3 atom wide terraces, here denoted as microfacets, and (110) like steps) based on its early appearance and the linear growth throughout the entire potential range. Despite its appearance as a positive peak at 0.1 V vs. RHE as in the previous linear spectroscopy studies[2], the assignment of resonance **1** to the reaction intermediate of the HER is not straightforward (it is also not in the case of the earlier studies, there it is purely based on a correlation). I find that this species is underpotentially deposited H adsorbed to (111) like defects (the Pt(110) surface is slightly roughened and partially shows (111) like character, see section 2.1.3 for a detailed discussion of Pt cyclic voltammetry) that evolves into H_{OPD}, as will be elaborated in the discussion of Pt(111)-H below.

This assignment is in good agreement with TPD studies of hydrogen chemisorption on Pt(110)-(1x2) in UHV [125, 126, 127] . The TPD spectrum of H adsorbed on Pt(110)-(1x2) shows three distinct desorption peaks termed β_2, β_1 and α in order of decreasing desorption temperature/bonding strength to the surface. The site corresponding to β_2 is the first to become occupied with H with increasing H_2 dosage and corresponds to H adsorbed to the

[2]In SFG the sign of the peak has a different meaning than in the linear spectroscopies, in SFG it reflects the phase of the peak and gives insight into the orientation of the oscillator's transition dipole moment with respect to the interface.

ridge sites, corresponding to resonance **3** of the spectra reported here. When the ridge sites corresponding to β_2 are almost saturated with H, hydrogen adsorption on the (111) like microfacets, corresponding to the β_1 peak in the TPD studies and resonance **2** in the present work, begins. After the microfacets, the trough sites represented by the α peak get occupied at high H coverages, which possibly corresponds to resonance **1** that only becomes intense close to 0 V vs. RHE.

The occurence of resonances around 2000 cm^{-1}, a frequency region that is characteristic for atop adsorbed H species [116], for H on Pt above 0 V vs. RHE in the so-called underpotential region, is unexpected from an electrochemical perspective. Typically, underpotentially deposited H is assumed to be bi- or tricoordinated [24] and should therefore not have a vibrational signature in this frequency range [116]. However, the energetic differences for H adsorbed to hollow, bridge and atop sites of Pt (at least of Pt(111)) are sufficiently small to be overcome at room temperature by the higher energetic H adsorbates of the thermal distribution. For example, the activation barrier for fcc-hcp-fcc hopping of H on Pt(111) in UHV is only 70 meV [128]. A recent ab initio molecular dynamics study of the interconversion of hydrogen adsorbed to hollow sites and hydrated protons (and vice versa) on Pt(111), i.e., the Volmer reaction, demonstrated that adsorbed H first moves from hollow to bridge to atop site where it then becomes solvated and desorbs after about 3 ps [129]. After solvation, the solvated proton remains confined to the interface in an H-down configuration, a bonding interaction between the Pt atom and H remains that slows down the diffusion into the electrolyte bulk. The observation that the Volmer reaction proceeds via a atop adsorbed Pt-H species and the circumstance that it is a fast reaction in equilibrium rationalize the observation of vibrational resonances around 2000 cm^{-1} also for underpotentially deposited H: H_{UPD} exists in an equilibrium with atop adsorbed Pt-H. Experimental evidence for this is found when coadsorbing H_2 and water on Pt(110) in UHV. Neither H_2, nor water adsorption to Pt(110) alone produce resonances around 2000 cm^{-1}, but exposing the surface first to H_2 and then to water leads to three resonances at 2150, 2280 and 2415 cm^{-1} [130]. Furthermore, the experimental and the theoretical study both suggest that multiple hydrated proton structures exist at the interface.

The water structure at the interface critically depends on Pt atom surface structure [131]. The above discussion suggests that the Pt-H vibrations are either directly, or via the solvated proton, influenced by interfacial water (and therefore a function of its structure). This would rationalize why previous linear IR studies did not see a multiplicity of peaks, because these spectroscopies rely on surface roughening that results in an unordered surface atomic structure that is unable to support an ordered layer of interfacial water. Consequently, the influence of water on the vibrational modes of Pt-H is different in experiments on roughened Pt_{poly} and smooth Pt single crystals. This is a possible explanation why the Pt(100)-H mode observed by Ogasawara et al. [118] was not observed by the linear spectroscopy studies on Pt_{poly}.

The evolution of Pt(111)-H resonances with potential, shown in the lower half of panel a), is less complicated than on Pt(110) (as expected). At 0.25 V vs. RHE, two broad vibrational features centered at 2060 (resonance **4**) and 2230 cm^{-1} (resonance **4'**) begin to emerge and grow at the same rate over the measured potential range. Resonance **4'** likely

contains two broad overlapping resonances. The appearance of Pt(111)-H resonance **4** at 2060 cm^{-1} is consistent with the conclusion that resonance **1** on Pt(110) at 2060 cm^{-1} stems from a (111) like defect. Because of their distinct behavior as a function of potential, the peaks are not assumed to represent the exact same species and are, hence, given different names.

The appearance of more than one peak for H/Pt(111) appears reasonable in light of TPD results that show two H states (represented by peaks β_1, β_2) for a perfect (almost step free) Pt(111) surface, and a third H state represented by peak β_3 for an imperfect surface [132]. Additionally, solvated proton structures at a Pt(111) surface were also predicted to produce distinct vibrational resonances around 2000 cm^{-1} as a function of their water content [133].

That I actually see Pt-H resonances and not, for example, organic contaminants is clarified by two isotope exchange experiments. In panel c) of Figure 4.1, Pt(110)-D is recorded as a function of potential in D_2O around 1500 cm^{-1} with the Pt(110)-H spectrum (with its frequency axis divided by 1.41 to account for the change of the reduced mass) as reference. The number of resonances, centre frequencies and their potential dependence show good agreement; deviations in the vibrational line shape upon isotope exchange can be rationalized by the quantum nature of the H/Pt(111) system for which a classical description proved insufficient [128]. In D_2O no resonances are observerd arond 2000 cm^{-1}, adding further proof; the corresponding data can be seen in appendix section A.

The above discussion over why we see vibrational resonances of Pt-H in the underpotential region involves interfacial water that coordinates H as it gets oxidized to H^+ and holds it in place over the Pt atom on which H was initially adsorbed. If this picture is accurate, then a perturbation of the interfacial solvent structure should be reflected also in the Pt-H SFG spectra. Following this logic, 50 mM of $LiClO_4$ were added to the electrolyte in order to disrupt the structure of interfacial water. Li^+ ions were chosen for two reasons: i) Li^+ has the highest solvation enthalpy among the alkali metal ions, which suggests that it binds water the strongest and is best suited to disrupt the structure of interfacial water; ii) it has the highest solubility of all alkali metal perchlorates in water, e.g. $CsClO_4$, that was also considered because it is a strong chaotrope (disrupts water structure), is basically insoluble. The Pt(111)-H spectrum with and without 50 mM of $LiClO_4$ is compared at 0.02 V vs. RHE in Figure 4.2. Adding Li^+ does not affect resonance **4**, but leads to the complete disappearance of resonance **4'**. Two additional peaks, **2** and **5**, on the low frequency side appear. The position of peak **2** on this Pt(111) electrode coincides with the frequency of peak **2** on the Pt(110) crystal, suggesting that a spot on the Pt(111) surface was monitored that contained (110) type defects. (110) and (100) type of defects may exist on a (111) surface, see section 2.1.3, but only appear in the CV if they are abundant enough (i.e., constitute at least 5 % of the surface, which was not the case here, CV not shown). They may also be local (and not homogeneously distributed across the surface) if they stem from mechanical damage like pushing the electrode against the CaF_2 window[3].

[3]Even though single crystal Pt electrodes can routinely be prepared without defects, employing them in the spectroelectrochemical cell often leads to defects. This can be a consequence of pushing the electrode

Peak **5** possibly results from (100) like defects. An imperfect Pt(111) surface still shows the **4'** peak as demonstrated in Figure 4.4 (which shows the Pt(111)-H and Pt(110)-H of Figure 4.1 for reference together with a defective Pt(111)-H spectrum in black and the Pt(111)-H spectrum of the $LiClO_4$ containing solution in turquoise), ruling out that **4'** disappears with the appearance of (some) surface defects.

The apparent indifference of resonance **4** to the solvation environment suggests that this is a pure Pt-H peak of the (111) facet, implying that the 2080 cm^{-1} mode observed in previous studies is a UPD feature that belongs to (111) like facets of polycrystalline electrodes. The clear dependence of resonance **4'** on the solvation environment is consistent with the earlier assignment that this peak belongs to solvated proton structures at the interface that are influenced by cations in vicinity to the surface. The almost complete vanishing of peak **4'** furthermore suggests that the influence of alkali metal cations is not limited to changing the interfacial potential profile, but also leads to a distinctively different interfacial solvent structure [134].

The coadsorption of alkali metal cations and H (together with OH) to surface steps

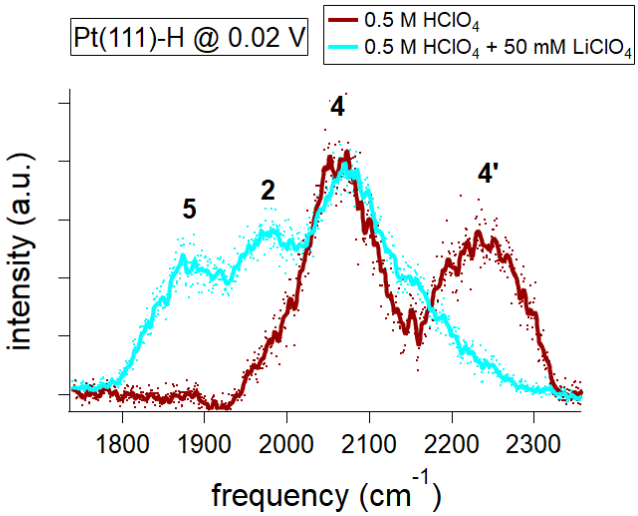

Figure 4.2: Background corrected SFG spectra of Pt(111)-H at 0.02 V vs. RHE in 0.5 M $HClO_4$ (red) and 0.5 M $HClO_4$ + 50 mM $LiClO_4$ (turquoise). The spectrum at 0.5 V vs. RHE was used for background correction of the red curve, while the respective spectrum at 0.6 V vs. RHE was used for the turquoise curve.

((110) and (100) like) has attracted significant attention lately and was argued to be

against the IR transparent window, or of breaking and reestablishing potential control, which is required for pushing the electrode against the window when the electrolyte gap is too big. If the electrolyte gap is sufficiently small for the optical measurement (so that only a fraction of the IR light is absorbed) can only be tested optically and under potential control with the current cell design, necessitating its breaking when the gap is too big. Breaking the potential control can be avoided with a dedicated cell design, but the potentially occuring damage from pressing the single crystal against the window is intrinsic to these measurements (even though it can be minimized with a better cell design.)

responsible for the non-Nernstian shift of the steps' CV peaks with changes in pH [123, 135, 136]. The peak related to H/OH sorption on the (100) like steps of Pt(533) shifts positive in potential when going from Li^+ to Cs^+ at pH values >1, but does not at pH = 1 [136]. The CV feature of hydrogen sorption on the (111) facet, however, is not affected by the nature of the cation, regardless of pH, which is thought to be due to the absence of coadsorbed OH. The results of this section agree that alkali metal cations influence on atop adsorbed Pt(111)-H is minimal. Even though the structure of the solvated interfacial proton can not be inferred from the presented data alone, it is obvious that its vibrational response changes dramatically in the presence/absence of Li^+ ions, which likely is a consequence of a changing solvation environment. Prior theoretical work [129] and the solvation structure of protons in bulk water [137] suggest that the solvated interfacial proton structures in peak **4'** possibly are Zundel-, or Eigen-like structures (maybe containing more water molecules) in an H-down geometry that are in equilibrium with atop adsorbed Pt-H (**4**) at potentials of underpotential hydrogen sorption.

The speed of, e.g., the Volmer reaction depends on how efficiently solvated protons at the interface can be converted into Pt-H. This acknowledges that the Volmer reaction is not an elementary step, but is composed of transfer of the solvated proton to the interface (from the bulk), desolvation of H^+ and cavity formation, and electron transfer. The efficiency of this sequence of events will depend on the activation barrier for breaking apart the solvated proton complex and forming Pt-H. This activation barrier is determined by the energy penalty that has to be paid in order to rearrange solvent molecules on the way from the reactant state to the transition state. It can be speculated that this energy penatly will be minimal if the transition dipole moments of reactant and product are both parallel to the reaction coordinate (which seems to be given [129]) and their resonance frequencies similar. This situation is depicted in Figure 4.3.

The observed vibrational resonances likely are collective modes that include mixing of solvent librations and stretching vibrations and, in this scenario, solvent rearrangement during Pt-H formation/oxidation will be efficient because the solvent of both reactant and product behave similarly. This concept can be used to explain why proton transfer in aqueous solution is almost barrierless [138].

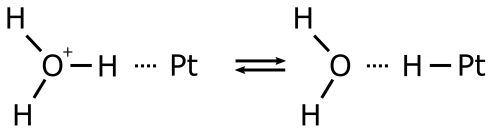

Figure 4.3: Scheme of Pt-H formation from a solvated proton in which the transition dipole moments of educt and product are parallel with the reaction coordinate.

Accordingly, if the vibrational frequencies of educt and product lie close together, the activation barrier is small and the interconversion from solvated proton to atop adsorbed Pt-H fast. It should be noted that the activation barrier can only be small enough for a barrierless reaction, if reactant and product have a similar energy (sit at a similar height on the potential energy landscape). This condition seems to be met for the situation depicted

in Figure 4.3 according to a theoretical study that explicitly models the oxidation of H adsorbed on Pt(111) in the presence of water [129]. If we assume that i) resonance **4'** represents stretching vibrations of the solvated interfacial protons with a transition dipole moment normal to the surface (this follows from the metal surface selection rule), which is supported by DFT calculations of (111) metal bound solvated proton structures [133], and ii) that the transition dipole moment of Pt-H is also normal to the surface (metal surface selection rule) and its resonance frequency is similar to the stretching vibration of the solvated interfacial proton, then solvent rearrangement during proton reduction will be favorable and the activation barrier small.

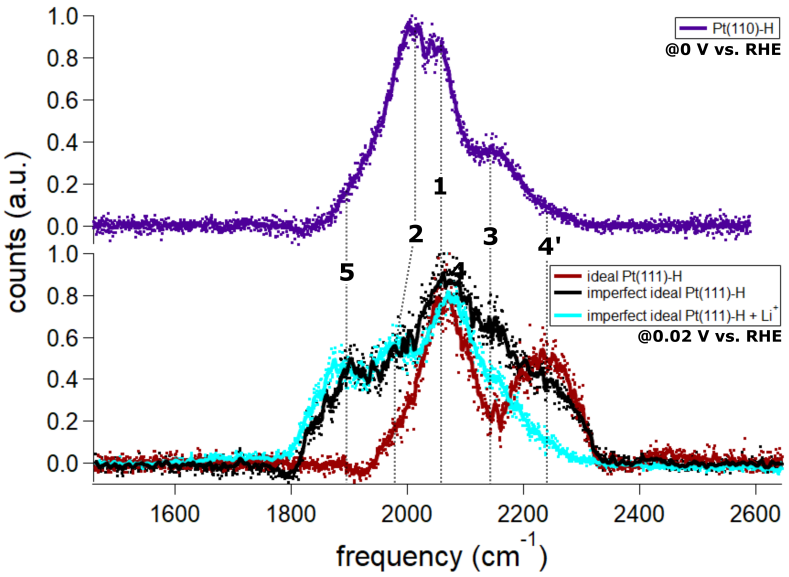

Figure 4.4: Normalized SFG spectra of Pt(110)-H at 0.0 V vs. RHE (top) and of Pt(111)-H at 0.02 V vs. RHE (bottom), both in 0.5 M $HClO_4$. In the bottom panel, defect free Pt(111)-H (red) is compared with defective Pt(111)-H (black) and Pt(111)-H recorded in 0.5 M $HClO_4$ + 50 mM $LiClO_4$ (turquoise).

Even though adding Li^+ to the electrolyte substantially alters the details of interfacial solvent structure, overlap of the vibrations of solvated protons (the shoulder that is left of **4'**) and Pt-H (**4**) is still given.

This argument potentially is of major importance in understanding the microscopic details of the pH and cation dependent [86] activity changes of the HER: changes in interfacial solvent structure, field strength and nature of the proton donor influence how favorable solvent rearrangement is during the reduction of the proton donor to Pt-H and will consequently alter the efficiency of Pt-H generation and therefore the overall reaction.

Having demonstrated that we can monitor H adsorbed to single crystalline Pt electrodes and understand the spectral response as a function of surface structure and potential, I will now investigate whether the HER can be initiated with ultrashort optical pulses.

4.2 Triggering Charge Transfer and the HER on Pt Electrodes on Femtosecond Timescales with Ultrashort Light Pulses

Monitoring adsorbates under steady-state conditions is insufficient if we want to gain insight into the HER's mechanism. That is because the intermediate of the rate determining step (whose chemistry we are interested in) may coexist with other adsorbates from, e.g., parallel reactions, or other steps in a sequential mechanism in a ratio we do not know beforehand. Extracting insight into a reaction mechanism in this scenario, however, would require this knowledge. This problem can be circumvented by performing a perturbation experiment, in which we provide a temporally short pulse of reactants and monitor the time evolution of the relevant surface species back to steady-state. As motivated in Section 2.3, ultrashort optical pulses may be used for this purpose that are not resonant with a Pt-H vibration and do not have sufficient energy to create solvated electrons: I intend to drive the HER with hot electrons.

I investigate if electrochemistry can be driven this way by collecting CVs from a Pt microelectrode and several Pt single crystals with and without 800 nm (1.56 eV), 55 fs illumination in acidic electrolyte. The illumination increases the HER rate close to the reversible HER potential on every electrode in a fashion consistent with hot electron driven chemistry, as evidenced by control experiments with illumination with varying fluence, pulse duration and wavelength. At more positive potentials in the UPD region, the illumination is demonstrated to induce partial charge transfer along the Pt-H bond. This partial charge transfer happens on a sub-picosecond timescale and is sensitive to both electrode surface and interfacial electrolyte structure. In contrast to conventional measurements of charge transfer resistance, the charge transfer dynamics observed here are sufficiently fast to not be influenced by the slower dynamics of ion diffusion, solvent reorganisation, or proton desolvation. These observations therefore only reflect the elementary electron transfer step from the Pt electrode to the adsorbate. The data further suggests that a necessary prerequisite for electron transfer is the right interfacial solvent structure and that this solvent structure is a function of applied bias.

The results discussed in this section have been published in the journal ChemElectroChem by Zwaschka and coworkers [89].

Results and Discussion

In the lower panel of Figure 4.5, I show CVs of a Pt microelectrode in a thin film spectroelectrochemical cell with (red curve) and without (black curve) pulsed 800 nm (1.56 eV), 55 fs, 1 KHz repitition rate, laser irradiation. After a short induction period, the laser-induced changes to the CV are stable over many cycles and fully reversible, as demonstrated in appendix section A. The CV shows clear current peaks at around 0.1 and 0.3 V vs. RHE that are characteristic for the electrosorption of H_{UPD} to (110) and (100) sites of Pt. The CV peaks appear to be not perfectly symmetric around zero current due to a minor oxygen

impurity and the resulting contribution of the oxygen reduction reaction (ORR, the reverse reaction of the OER, see appendix section A for details) to the current, making it slightly more negative (the charge contained in the cathodic and anodic peak is still identical) [139].

The laser irradiation affects the CV as follows. As predicted for a hot electron driven reaction [95], the HER current close to 0 V vs. RHE is increased and its onset is shifted to more positive potentials; both effects increase with increasing laser fluence, see inset in the bottom left corner. At more positive potentials in the UPD region, between 0.35 and 0 V, the illumination decreases the H_{UPD} related current in both the anodic and cathodic scan[4] to a varying extent as a function of potential, as emphasized in the I_{illum}/I_{dark} ratio in the top panel. The laser-induced changes to the H_{UPD} current are largest at potentials where the current is maximum in the absence of irradiation, namely at the peaks. This holds for all fluences, see inset on the right of the centre. The size of the laser-induced currents strongly varies on the mV scale of the UPD region, which is surprising because the photon energy, 1.56 eV, clearly exceeds the thermodynamic stability window of water, 1.23 eV, and a laser-induced current due to water splitting could be expected independent of minor changes to the working electrode bias. While changes in bias on a mV scale are comparatively insignificant from the perspective of the electronic structure of Pt [140, 141], they can dramatically alter the structure of the interfacial electrolyte [142, 143]: the amplitude of laser-induced currents in the H_{UPD} region apparently depends on the structure of the interfacial electrolyte.

The data clearly demonstrates that a laser-induced current is measured, however, exactly how the illumination produces the current and its relationship to hot electrons is unclear at this point. I see five ways in which the irradiation could possibly induce a current: (i) heating of the interfacial region that results in chemistry; (ii) charge transfer from the metal to the adsorbate by direct optical excitation; (iii) photochemistry in solution; (iv) hot electron driven chemistry; (v) changes in interfacial polarization, either by a laser-induced rearrangement of interfacial structure, or by charge transfer along the Pt-H bond [144].

Each of these possible mechanisms depends differently on Pt surface structure and the properties of the laser illumination. The influence of varying laser fluence on the laser-induced current is shown in the insets of Figure 4.5 and in Figure 4.6 a) and its dependence on pulse duration and photon energy is explored in Figure 4.6 b). The effect of Pt surface structure on the laser-induced current is evaluated by collecting CVs of various Pt single crystals with and without 800 nm, 55 fs, irradiation, see Figure 4.7 and appendix section A for data and below for detailed discussion. In order to compare the laser-induced current under different conditions (illumination details, different single crystal orientation), I

[4]The current around the (110) H_{UPD} feature at 0.1 V is decreased in the anodic scan, but apparently increased in the cathodic scan: the laser-induced current has the same sign in both scanning directions. This is neither observed on the (100) H_{UPD} feature of this electrode, nor on single crystal CVs. This is consistent only with a scenario in which the illumination results in an increased ORR current that obscures the pure laser-induced decrease of the (110) H_{UPD} adsorption current. I discuss this issue in more detail in appendix section A.

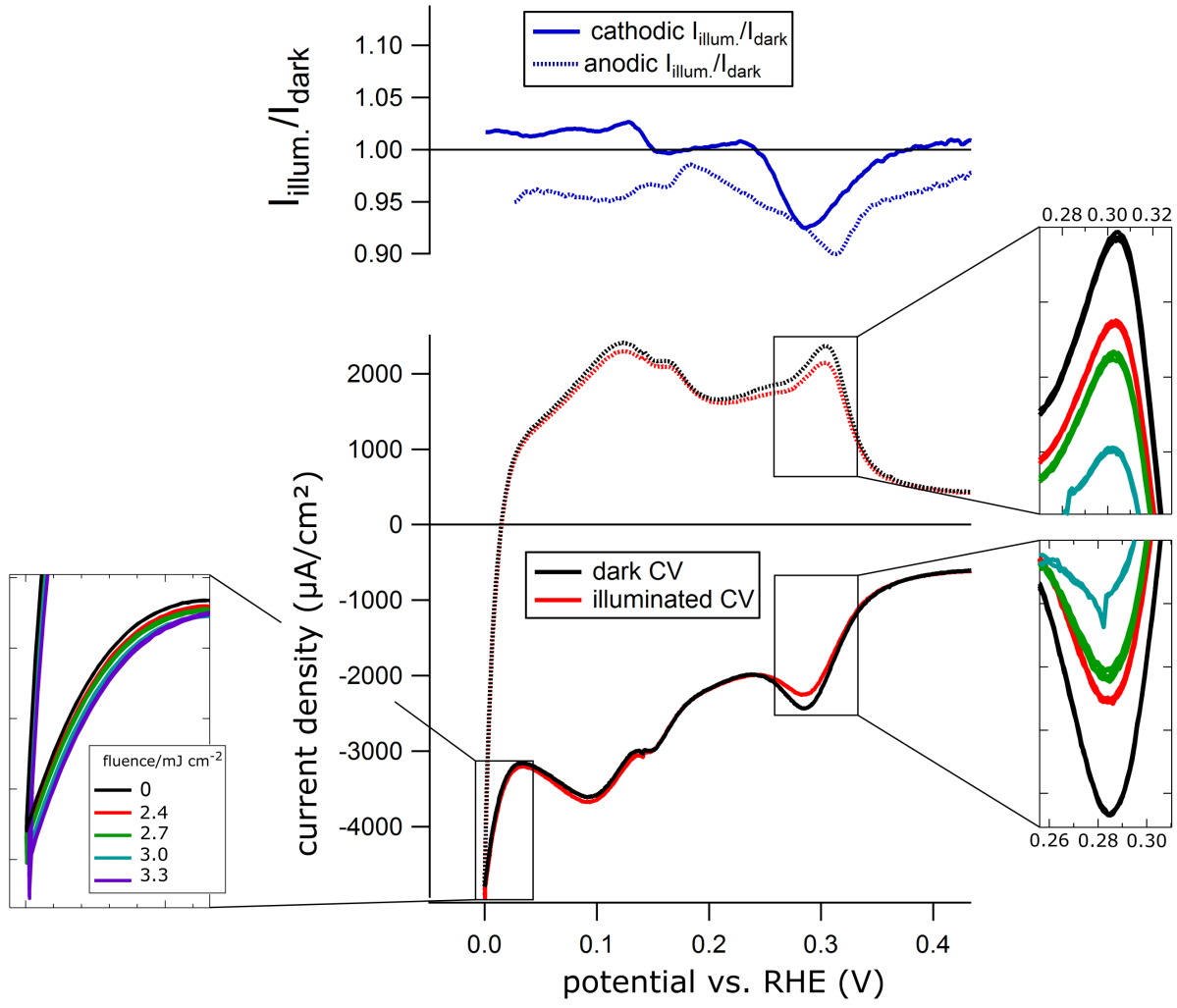

Figure 4.5: Lower panel: cyclic voltammetry (500 mV/s scan rate, in 0.05 M H_2SO_4) of a Pt microelectrode with (red) and without (black) 800 nm, 55 fs illumination at 1 kHz repitition rate and a fluence of 2.4 µJ/(cm^2*pulse) in a spectroelectrochemical cell with an electrolyte thickness of $\sim$ 5 µm. The excerpts show magnifications of the HER region (left) and (100) H_{UPD} sorption site (right) with varying laser fluence (legend in HER excerpt). Top panel: ratio of illuminated over not illuminated CV traces, the solid (dotted) line represents the cathodic (anodic) scan.

extract two metrics: one measure each for how strongly the irradiation affects the HER and H_{UPD} sorption. For this purpose, I take the currents with (I_{illum}) and without illumination (I_{dark}) and calculate $[(I_{illum}-I_{dark})/I_{dark}]*100$ at 0 V vs. RHE for the HER and at more positive values for H_{UPD}. As the potential at which H_{UPD} features appear in the CV is dependent on surface structure, I compare this metric at different potentials on different surfaces. The results of this analysis are qualitatively insensitive to the details of this choice of metric and to the presence of defects on the single crystal surfaces, as elaborated in appendix section A.

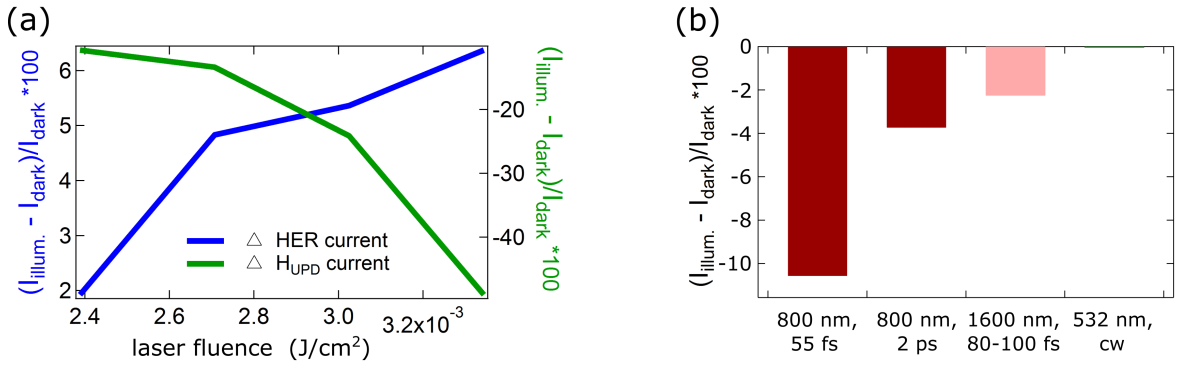

Figure 4.6: a) Change of the laser-induced currents expressed as $[(I_{illum}-I_{dark})/I_{dark}]*100$ as a function of a linearly varying laser fluence at 0 V vs. RHE for the HER (blue trace) and at 0.3 V vs. RHE for H_{UPD} in the anodic scan (green trace). b) $[(I_{illum}-I_{dark})/I_{dark}]*100$ extracted for H_{UPD} at 0.3 V in the anodic scan in four different experiments in which either pulse duration, or wavelength of the irradiation was varied at a constant laser fluence of 2.4 µJ/(cm^2*pulse). Details of the electrochemistry are identical to those in Figure 4.5.

If heating was the origin of the laser-induced currents I observe – either because of heat induced chemical reactions, or due to increased H_2 interfacial diffusivity – the laser-induced current should (a) be insensitive to pulse duration at a fixed pulse energy, (b) assuming simple Arrhenius kinetics for the HER (with a temperature independent prefactor), increase exponentially with linearly increasing pulse energy (that results in a linear temperature increase) and (c) not be sensitive to changes in surface structure. The observed laser-induced current strongly depends on pulse duration (Figure 4.6 b), changes nonexponentially (not in accord with Arrhenius kinetics) with linearly increasing laser fluence (Figure 4.6 a) and shows a substantial dependence on surface structure (Figure 4.7 and top panel of Figure 4.5). Consequently, I conclude that the results cannot be explained by heating. If one photon direct optical excitation from metal to adsorbate was the origin of the laser-induced current, I would expect the measured current to be independent of pulse duration. As demonstrated in Figure 4.6 b), this is clearly not the case. Solution phase photochemistry as origin of the measured laser-induced currents is ruled out by the strong dependence of the signal on surface structure (Figure 4.7 and top panel of Figure

4.5).

In light of this discussion the increase in HER current at 0 V vs. RHE and the shifting of the HER onset potential towards more positive values under illumination is attributed to the presence of hot electrons.

The origin of the laser-induced current in the H_{UPD} region is more challenging to understand. As demonstrated clearly in the right inset of Figure 4.5 for the microelectrode and in appendix section A for the single crystal electrodes, the laser-induced current changes sign with scanning direction: the irradiation decreases the current in the H_{UPD} region of the microelectrode (increases in the case of the single crystal electrodes, see below), relative to a CV without illumination, in *both* cathodic *and* anodic scans. If this symmetric decrease in current was a consequence of laser-induced redox chemistry (e.g., changes in Pt-H population), it would imply that the irradiation leads to oxidation of Pt-H in the cathodic scan and to reduction of protons and the formation of Pt-H in the anodic scan in equal amounts. As to my knowledge there is no physical mechanism that could accomplish both, I ascribe the laser-induced changes of the H_{UPD} current to a redistribution of charge *without* changes to the Pt-H population. To develop a qualitative understanding of such effects we need to review what happens when a charged species adsorbs to a metal electrode (like the formation of H_{UPD}) and introduce the concept of electrosorption valency (ESV).

The ESV is a concept to distinguish the *adsorption* of ions from electron, or ion *transfer* reactions (Faradaic processes) where the involved charges are always integer. In the case of electron transfer, the measured charge is a multiple of the elementary charge and for ion transfer, a multiple of the ion's valency. However, when an ion adsorbs to an electrode, the measured charge generally is *not* a multiple of the elementary charge, because a part of the charge will be stored in the chemical bond between adsorbate and electrode. How much of the positive/negative charge stored in the bond is transferred to the electrode is ill defined, because it requires a model to decide which portion of the charge contained in the bond belongs to the adsorbate, and which belongs to the electrode (which is a somehwat arbitrary decision). Even though a charge associated with the adsorption process can be measured, measuring the charge that results solely from ion discharge is not possible for two reasons: In most cases discharge is fractional (see above) and during discharging interfacial dipoles (adsorbate and electrolyte/solvent) will rearrange to compensate/screen, resulting in a capacitive current. Fractional discharge implies it is not possible to discriminate whether a small charge originates from the full discharge of only a few adsorbates, or from the fractional discharge of a larger amount of adsorbates. Because the ion discharge on adsorption (id) can not be separated from interfacial dipole rearrangement (dr) both terms are combined in the ESV. Even though defining the ESV in a model-free, thermodyncamically exact manner is critically debated [145, 146], for purposes of this work I only discuss changes to ion discharge and dipole rearrangement as a consequence of laser irradiation on a qualitative level. Under this premise we write the laser-induced ESV (l) [144] as:

$$l = \frac{1}{F}\left(\frac{\delta\mu_{(Pt-)H}}{\delta E}\right)_{\Gamma_{(Pt-)H}} = id + dr \tag{4.1}$$

$$id = zg - \lambda(1-g)$$

$$dr = \frac{m_{(Pt-)H/W/Elec}}{ed'}$$

where F is Faraday's constant, $\mu_{(\mathrm{Pt\text{-}})\mathrm{H}}$ the chemical potential of adsorbed H, $\Gamma_{(Pt\text{-})H}$ the surface excess of adsorbed H, z the valence of the adsorbing ion and E the bias. The so-called "thickness ratio" is defined as $g = \frac{\mathrm{E_{ad}} - \mathrm{E_{el}}}{\mathrm{E_M} - \mathrm{E_{el}}}$, where $\mathrm{E_M}$ is the potential at the metal surface, $\mathrm{E_{ad}}$ the potential at the position of the adsorbate and $\mathrm{E_{el}}$ the potential in bulk electrolyte. For complete discharge of adsorbates, e.g., in the formation of UPD layers, g is typically taken to be 1, implying that the distance between the metal surface and the inner Helmholtz plane is small relative to the distance between inner and outer Helmholtz plane [147] (see section 2.1 for a discussion of these terms in context of the electric double layer EDL). The partial charge transfer coefficient λ is negative one for a fully discharging monovalent cation. $m_{(Pt\text{-})H/W/Elec}$ represents the sum of the projection of Pt-H, water, and electrolyte dipoles onto the the surface normal and d' is the thickness of the double layer divided by the interfacial dielectric constant. e is the elementary charge. Equation 4.2 is derived, and the parameters discussed in detail, in a recent review by Schmickler and coworkers [144].

The energy of the excitation (1.56 eV) easily suffices to excite electrons from Pt into Pt-H antibonding states [140]. Such an excitation is expected to decrease g by increasing the metal electron potential $\mathrm{E_M}$, but not, or only to a much smaller extent, affecting $\mathrm{E_{ad}}$ (because it is situated farther from the metal surface that actually absorbs the excitation). $|\lambda|$ is also expected to decrease with laser excitation, as the population of antibonding Pt-H states reduces net charge transfer to Pt. The irradiation is therefore expected to decrease the *id* term. If the extent of ion discharge is affected by the irradiation, then likely the structure of either the adsorbate, electrolyte, or solvent will also be affected. Without independent information on interfacial structure it is reasonable to assume that the *dr* contribution to the laser-induced current can either be positive or negative. Figure 4.5 clearly demonstrates that the laser irradiation *decreases* the $\mathrm{H_{UPD}}$ related current on the Pt microelectrode. This decrease is consistent with hot electrons (generated by the laser excitation) inducing partial charge transfer along the Pt-H bond and rearrangement of interfacial structure that either leads to a decrease in *dr*, or an increase in *dr* that is smaller than the decrease in *id*.

In summary the results from the microelectrode clearly suggest that 800 nm, 55 fs laser illumination drive the HER on Pt close to its reversible potential (the potential at which HER and HOR are equally fast) at 0 V vs. RHE and induces charge transfer in the UPD region and that the size of the laser-induced currents are a function of the applied bias. The bias dependence of the laser-induced current was explained with rearrangement of in-

terfacial solvent and electrolyte as a function of potential (that has been observed by others in the absence of additional laser illumination [142, 143]); however, the structure of said solvent and electrolyte is also a function of the surface atom structure of the Pt electrode [131]. As previously mentioned, the microelectrode (more precisely a polycrystalline Pt electrode) has H_{UPD} features in the CV akin to those of Pt(110) and Pt(100).

However, disentangling the signal due to dipole reorientation (*dr*) after laser illumination simultaneously on multiple Pt grains with different surface crystallographic orientations is challenging. This task becomes even more difficult through the existance of a distribution of grain sizes (the structure of the interfacial solvent probably is a function of grain size). I approached this problem by conducting the same type of experiment on Pt single crystals.

The results are displayed in Figure 4.7, where $[(I_{illum}\text{-}I_{dark})/I_{dark}]*100$ is plotted for the HER on the employed single crystals and the microelectrode in the top panel and for the UPD region in the bottom panel. It is apparent, that the illumination increases the HER current on all surfaces. Identical to the results of the microelectrode, laser-induced changes to H_{UPD} currents change sign with the scan direction on the single crystals (additional data can be found in appendix section A). Accordingly, I conclude that the laser-induced currents in the UPD region of the single crystals do not result from changes in Pt-H population, but are a consequence of charge transfer along the Pt-H bond, or rearrangement of interfacial dipoles (analogous to the interpretation of the microelectrode results). However, in contrast to the laser-induced currents in the UPD region of the microelectrode, the irradiation acts to *increase* the H_{UPD} related currents on the single crystal electrodes in both scan directions.

As mentioned above, we expect changes in *id* with laser illumination to be only negative. This suggests that the laser-induced H_{UPD} currents on the single crystals are dominated by the *dr* term of Equation 4.2: changes in the structure of adsorbate Pt-H, or interfacial solvent and electrolyte overcompensate changes in charge density along the Pt-H bond. Prior work, both experimental [76] and theoretical [131], clarify that extended, long-lived (with respect to the life time of H-bonds in bulk water, which live for around 3 ps before being broken and reformed [6]) hydrogen bonded water structures may develop at the interface to Pt single crystals. The water's structure was found to depend on the structure of the single crystal's surface and that defects disrupt this structure. As a result these structures do not form at more disordered surfaces like polycrystalline Pt that has been roughened by electrochemical cycling. Perturbing the structure of ordered interfacial water is expected to require more energy than for more disordered interfacial water. It is further expected to occur on a picosecond or longer timescale, because it involves the concerted breaking and reformation of many hydrogen bonds. It is worth noting that while the microelectrode has Pt(110) and Pt(100) like H_{UPD} features in the CV, the effect of laser irradiation on these is opposite in sign compared to the effect on H_{UPD} on the respective single crystals. This contrast may be a consequence of the solvent structures on the single crystals being bigger than the sizes of the grains with (110) and (100) like surface termination on the microelectrode. As mentioned in footnote 3, the used single crystals are not entirely defect free. However, the opposite sign in the laser-induced H_{UPD} currents as compared to

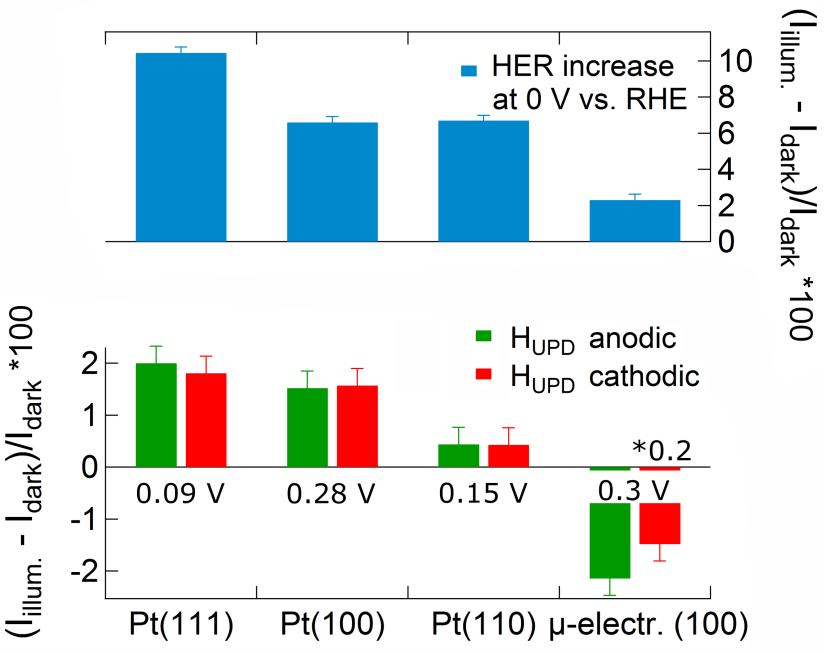

Figure 4.7: $[(I_{illum}\text{-}I_{dark})/I_{dark}]*100$ extracted for the HER at 0 V vs. RHE (top panel) and for H_{UPD} in both scanning directions (bottom panel) on four different Pt surfaces. For the single crystal measurements, 0.5 M H_2SO_4 was used as electrolyte and the laser fluence was 1.8 µJ/(cm^2*pulse). For the microelectrode, 0.05 M H_2SO_4 was used as electrolyte and the laser fluence was 2.4 µJ/(cm^2*pulse) (800 nm, 55 fs, radiation at 1 kHz repitition rate was used in both cases). The error bars represent uncertainty from replicated measurements.

the microelectrode suggests that defect densities must be significantly lower than on the microelectrode and are evidently low enough to not perturb the crystal face dependent electrolyte structure.

For H_{UPD} the $[(I_{illum}\text{-}I_{dark})/I_{dark}]*100$ metric can be understood as a measure for the ease of charge transfer on femtosecond timescales. This ease of charge transfer is a function of Pt surface structure (lower panel of Figure 4.7) and interfacial electrolyte structure (it varies with bias on a mV scale, upper panel of Figure 4.5). A related quantity that is routinely measured with standard potentiostats is the so-called electrochemical charge transfer resistance (ECTR). In contrast to the here defined measure for the ease of charge transfer on fs timescales, the ECTR integrates over solvent and electrolyte restructuring dynamics much slower than the picosecond dynamics to which our observable is sensitive. Despite these differences, similar trends are observed for ECTR and laser-induced changes to H_{UPD} current. The dependence of the ECTR on bias for H_{UPD} adsorption to (110) sites on Pt_{poly} was recently reported by Durst and corworkers [148]. Those authors found, in agreement with the measurements presented here, that the ECTR is minimal, i.e., charge transfer is most favorable, when the H_{UPD} current reaches its maximum at the (110) CV peak. This coincidence with the results from the laser-induced H_{UPD} currents

in this work suggests that the ease of charge transfer across the Pt/electrolyte interface is a function of both Pt surface and interfacial electrolyte structure, but independent of slower electrolyte reorganization dynamics. This implies a certain "prearranged" double layer structure (similar to the requirement for solvent structure allowing charge transfer in Marcus' theory [149]) that allows for charge transfer is required not only for time-averaged measurements, but also for ultrafast charge transfer induced by femtosecond irradiation.

This is seemingly in accord with the explanation for the observation of a vibrational response around 2000 cm^{-1} at potentials of H underpotential deposition on Pt single crystals in section 4.1. This is a frequency range characteristic for singly coordinated H atop Pt, but H_{UPD} is generally considered to be located in multicoordinated hollow sites in the surface and therefore not to produce a vibrational signature around 2000 cm^{-1}. I argued that H_{UPD} in these hollow sites exists in an equilibrium with singly coordinated H atop Pt (that produces the 2000 cm^{-1} vibrational signature) and solvated interfacial protons, because H_{UPD} formation and oxidation are *fast and reversible* (forward and backward reaction are in equilibrium, i.e., equally fast) processes. Following the discussion in this section, it is reasonable to assume that the structure of the solvated interfacial proton that is in equilibrium with atop adsorbed Pt-H and H_{UPD} in multicoordinated surface sites coincides with the interfacial electrolyte structure that allows for charge transfer on subpicosecond timescales.

The results presented in this section further suggest that partial charge transfer along the Pt-H bond depends on both the structure of the Pt surface and interfacial electrolyte and that the ease of charge transfer (the contribution of the *id* term in the UPD region) increases Pt(111) < Pt(100) < Pt(110) < microelectrode (it is most strongly overcompensated by the *dr* term on Pt(111)). This order coincides with HER activity as a function of surface structure in acidic media, which is Pt(111) < Pt(100) < Pt(110) < Pt clusters [31, 150]. Taken together these results and the prior work suggest that once interfacial solvent and reactants are in the optimal configuration for the reaction (which is set by the bias), the HER rate is limited by the elementary step of electron transfer across the interface in acidic electrolyte.

4.3 Optical Excitation Induced Pt-H Femtochemistry Monitored by SFG

We have clarified that we can monitor a type of Pt-H that is a candidate for HER intermediate as a function of bias and surface structure with vibrationally resonant SFG in section 4.1 and that we can drive charge transfer and the HER on ultrafast timescales in section 4.2.

Here I try to overcome the drawbacks of static spectroscopy for the determination of a reaction's mechanism, at the example of the HER, by triggering it on a femtosecond timescale with an ultrashort optical pulse and monitoring the temporal evolution of adsorbed H with vibrationally resonant SFG, effectively combining the approaches of sections 4.2 and 4.1 in a pump-probe experiment employing 800 nm, 35 fs, irradiation as a pump and monitoring the Pt-H vibration around 2000 cm^{-1} with SFG. The goal here is to learn how the individual Pt-H species behave as the HER is triggered. This promises insight into whether the conventional view of the HER, that only Pt-H_{OPD} is relevant for the reaction, is correct and holds out the prospect to learn about the reaction mechanism in perhaps the most direct way achievable today.

From the results of the previous two sections we might expect perturbing the Pt-H vibration of section 4.1 by pumping the interface with 800 nm femtosecond irradiation results in an ultrafast response that is bias and surface structure dependent. Following the results of the previous section, insight into how the response of Pt-H to the optical pump differs in the UPD region (0 - 0.35 V vs. RHE on Pt(111)) close to the HER at 0 V vs. RHE, where the pump drives the HER following the results of section 4.2, and far away from the HER but still in the UPD region (where we expect a different behavior), is expected. Because H adsorbed to different surface sites can be monitored simultaneously, we also might expect to gain insight into the function of different adsorption sites during the HER.

I chose Pt(111)-H for pump-probe investigation because it offered the prospect of understanding the full mechanism from the reduction of solvated protons (resonance **4'** in the language of section 4.1) to Pt-H via transformation of Pt-H species on the surface to bond breaking and H_2 formation.

Results and Discussion

I performed pump-probe experiments on a Pt(111) electrode at 0.025, 0.1, 0.2, 0.5 and 0.8 V vs. RHE[5] by scanning the delay of the 800 nm pump with respect to the SFG probe from -1000 to +8000 fs in varying time steps (finer time resolution around time zero, see appendix section A). In Figure 4.8, I summarize the results by plotting the ratio of SFG

[5]The potentials were chosen according to the results of section 4.2: one potential at which the HER is running at a low rate (0.025 V), one close to the HER onset (0.1 V), one inside the UPD region, but far away from the HER (0.2 V), one just outside the UPD region (0.5 V) and one far away from the UPD region (0.8 V).

intensity with and without pump, I_{pu}/I_{unpu}, of the entire measured frequency window for every time point. The vertical bar at 2300 fs in the 0.025 V vs. RHE curve represents the standard deviation for the measurement at 0.025 V[6]. The data has been corrected for a small contribution of scattered light to the signal at time delays 3 - 8 ps (that is potential independent and not a consequence of heating), see appendix section A.

I first note that the I_{pu}/I_{unpu} ratio, and its dependence on delay, is strongly potential dependent and shows subpicosecond dynamics, as expected from the discussion in section 4.2. It also should be noted that the position of time zero is only precise within ±200 fs[7]. For all potentials, the ratio is always positive over the recorded time frame and seems to have three different contributions for potentials in the UPD region (from 0 - 0.35 V vs. RHE on Pt(111), see section 2.1.3) and two components for potentials outside of the UPD region. In all cases the ratio sharply increases after time zero and reaches a maximum after 100 fs (0 in the case of 0.8 V vs. RHE). The ratio goes through a local minimum at 200 fs (100 for 0.8 V) and rises again to a second (local) maximum at 300 fs (200 for 0.8 V), after which the ratio declines either back towards one for potentials outside the UPD region (0.5 and 0.8 V), or towards a constant positive value for potentials inside the UPD region. This positive constant value in the UPD region at longer pump-probe delays is a function of potential: the lower the applied potential, the higher the value (even though the increase seems to converge to a common value for 0.025 and 0.1 V vs. RHE). Furthermore, the rate at which the ratio declines towards the positive constant offset is significantly slower close to the HER (0.025 and 0.1 V vs. RHE), where the ratio becomes constant only after about 2000 fs. In contrast, the ratio at 0.2 V becomes constant after only about 700 fs. Outside the UPD region, the ratio relaxes back to one faster at 0.8 V than at 0.5 V.

It is obvious from Figure 4.8 that we are perturbing the SFG response of the interface with the pump and that this perturbation is potential dependent. Because I am interested in learning about Pt-H chemistry, especially during charge transfer and the HER on ultrafast timescales, I would like to extract from the I_{pu}/I_{unpu} ratio the resonant contribution of Pt-H. From prior measurements it is clear that ultrashort 800 nm pulses first induce electronic excitations that affect the nonresonant contributions to the ratio [151]. These optical excitations result in a higher temperature of electrons ("hot electrons", see sections 2.3 and 4.2) in the metal surface. The hot electrons are expected to populate antibonding adsorbate states [152, 91] which results in changes to the resonant contributions to the ratio. Unfortunately, the relative sizes of the changes to resonant and nonresonant contributions are not a priori clear.

[6]Spectra were recorded for 1 s at every pump-probe delay and 60 pump-probe scans were recorded in total. The relative standard deviation was calculated by integrating the 60 spectra of a given pump-probe delay over the entire frequency range (resulting in one value for every of the 60 spectra) and dividing their standard deviation by the mean of the 60 values.

[7]The deviation of ±200 fs is the difference between time zero as determined at a gold mirror/CaF_2 interface and the start of pump-induced changes to the Pt-H SFG signal. It is important to note that this possibly, small, deviation is *identical* for all pump probe-traces, because the position of the sample was never changed, only the applied potential.

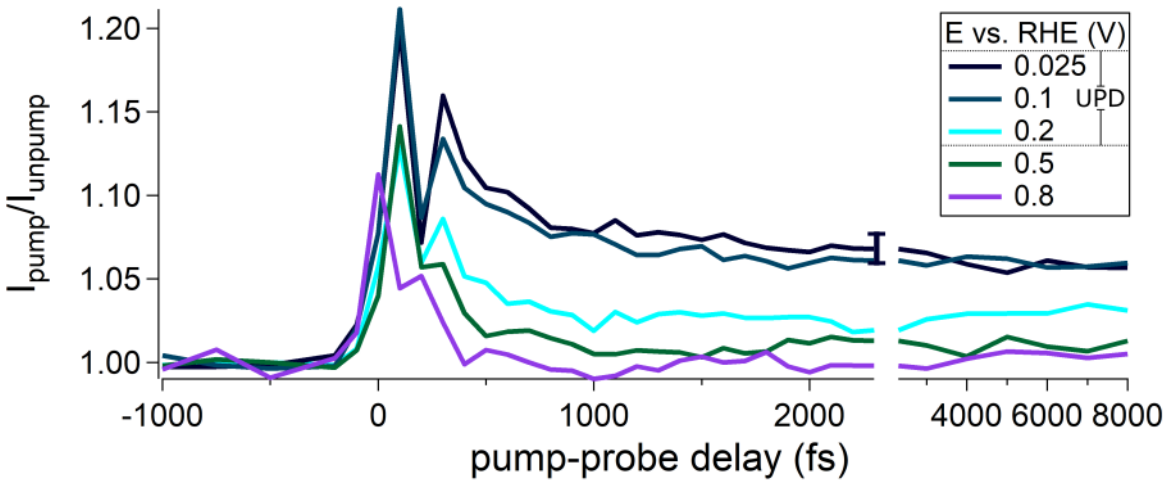

Figure 4.8: Results from pump-probe experiments at a Pt(111)/electrolyte interface at various constant potentials (see legend). The entire measured frequency window was integrated and plotted as a function of pump-probe delay. The time resolution is finer around time zero and coarser at delays >3000 fs. Spectra were recorded with 2 μJ pulse energy for upconversion and IR pulses and 9 μJ pulse energy for the 800 nm, 35 fs pump; the repitition rate was 1 kHz and the electrolyte 0.5 M $HClO_4$.

I therefore consider how every component of the ratio may be affected by the ultrashort 800 nm pump and derive the intensity ratio from equation 4.2:

$$\frac{E_{SFG,pumped}}{E_{SFG,unpumped}} \sim \frac{\chi^{(2)}_{eff}(\Delta t) \cdot E_{upc} \cdot E_{IR}}{\chi^{(2)}_{eff} \cdot E_{upc} \cdot E_{IR}} \tag{4.2}$$

This is a general description for the emitted SFG field E with and without the pump where (Δt) describes a dependence on pump-probe delay. $\chi^{(2)}_{eff}$ is:

$$\chi^{(2)}_{eff} = \sum_{i,j,k} [\vec{\varepsilon}(\omega_{SFG}) \cdot \vec{e_i} \cdot L_{ii}(\omega_{SFG})] \cdot \chi^{(2)}_{ijk} \times [\vec{\varepsilon}(\omega_{upc}) \cdot \vec{e_j} \cdot L_{jj}(\omega_{upc})][\vec{\varepsilon}(\omega_{IR}) \cdot \vec{e_k} \cdot L_{kk}(\omega_{IR})]$$

Where different tensor components are indexed i, j, k; L represents the Fresnel coefficients, $\vec{e_i}$ the unit vector in the ith direction and $\vec{\varepsilon}$ the normalized electric field vector. From reference pump-probe measurements of a Au/CaF_2 interface with identical details of the optical measurement I know that the temporal shape of upconversion and IR pulse do not produce any of the results reported here (see appendix section A). Fresnel coefficients (bulk properties) are not affected by the pump, allowing me to futher simplify the expression. The latter simplification is based on prior work that suggests pumping a Pt electrode with ultrashort 780 nm light only decreases the reflectivity transiently by a factor of 10^{-4} to 10^{-5}

[153]. Writing $\chi^{(2)}_{eff} = \chi^{(2)}_{NR} + \chi^{(2)}_{R}$ and taking the square of the simplified expression leaves us with the ratio of the SFG intensities (that are measured in this homodyne detected experiment):

$$\frac{I_{pumped}}{I_{unpumped}} \sim \frac{(\chi^{(2)}_{NR}(\Delta t) + \chi^{(2)}_{R}(\Delta t))^2}{(\chi^{(2)}_{NR} + \chi^{(2)}_{R})^2} \tag{4.3}$$

The pump-induced changes to the resonant and nonresonant nonlinear susceptibilities can be rewritten as unperturbed, $\chi^{(2)}$, plus perturbed, $\Delta\chi^{(2)}$, quantities:

$$\frac{I_{pumped}}{I_{unpumped}} \sim \frac{(\chi^{(2)}_{NR} + \Delta\chi^{(2)}_{NR} + \chi^{(2)}_{R} + \Delta\chi^{(2)}_{R})^2}{(\chi^{(2)}_{NR} + \chi^{(2)}_{R})^2} \tag{4.4}$$

Changes to $\chi^{(2)}_{NR}$ are a consequence of perturbing the electronic structure of the Pt surface by exciting hot electrons which typically relax within a few hundred fs if no long lived states are excited [92], and are therefore expected to be much shorter lived than the changes to $\chi^{(2)}_{R}$. The above mentioned transient reflectivity measurements on a Pt_{poly} electrode demonstrate that the reflectivity is decreased for tens of picoseconds, i.e. also after relaxation of the hot electrons and thermalization with phonons [153]. The authors argue that the increased phonon temperature is the reason for the longer lasting decrease in reflectivity. Here, however, a much bigger (tens of % vs. fractions of a % in the transient reflectivity study) and positive transient signal (in contrast to the decrease in reflectivity) is observed. I take this to suggest that the transient signal observed here is not dominated by changes to the nonresonant contribution, at least at longer delay times. Hot electron-induced changes to the inner Helmholtz layer like, e.g., partial charge transfer to adsorbates, or induction of librations, possibly affect $\chi^{(2)}_{NR}$ on a few hundred fs timescales as well. Following this discussion, I assign the positive offset of the I_{pu}/I_{unpu} ratio for potentials in the UPD region after 1 ps to changes in $\chi^{(2)}_{R}$: an increase in Pt-H population. This assumption is only physically reasonable, if Pt-H oxidation is fast enough to ensure return to the unperturbed steady-state Pt-H population before the next laser pulse arrives (because pumped and unpumped signal are identical at negative delays). This requirement would be met if the additional laser-induced H coverage could be oxidized within one ms (the repitition rate of the laser is 1 kHz). It is furthermore reasonable to assume that the additional coverage is a fraction of a monolayer. The exchange current density (see section 2.1 for detailed discussion of this quantity) of the HOR is $\sim$ 27 mA/cm^2 [71]; this is the overall speed of the reaction, including not only Pt-H oxidation, but also H_2 dissociative adsorption. The dissociation of H_2 is typically considered to be significantly slower than Pt-H discharge [71] and therefore my estimate for the speed of Pt-H oxidation from the HOR exchange current density is an underestimate. 27 mA/cm^2 roughly translates to 0.43 monolayers/ms (assuming one monolayer equals 10^{15} Pt-H and one electron per Pt-H; the monolayer coverage of H on Pt(111) at 0 V vs. RHE is approximately 0.66 [24]), implying that Pt-H oxidation is fast enough to explain the results as increase in Pt-H population.

For the changes to the ratio around time zero the relative contributions from $\chi^{(2)}_{NR}$

and $\chi_R^{(2)}$ are not obvious a priori. Assuming that $\chi_R^{(2)}/\chi_{NR}^{(2)} = 10$ (which seems to be a conservative estimate given the results of section 4.1), we can use Equation 4.4 to estimate how large the contribution of $\Delta\chi_{NR}^{(2)}$ would have to be in order to explain the observed I_{pu}/I_{unpu} ratio. If we assume that $\Delta\chi_R^{(2)} = 0$, then $\Delta\chi_{NR}^{(2)}$ would have to be 54 % of $\chi_{NR}^{(2)}$ to achieve even a moderate intensity ratio of 1.1. However, the results of the earlier mentioned transient reflectivity measurements on a Pt electrode and the earlier mentioned pump-probe reference measurements of a Au/CaF_2 interface suggest that $\Delta\chi_{NR}^{(2)}$ is much smaller and more likely on the order of only a few % (as detailed in section A of the appendix). On the contrary, if we assume $\Delta\chi_{NR}^{(2)} = 0$, then a change in $\chi_R^{(2)}$ of only 5.4 % is sufficient to explain an intensity ratio of 1.1.

In a scenario in which both $\chi_R^{(2)}$ and $\chi_{NR}^{(2)}$ are modulated by 5.4 % via the pump (for comparability with the last calculation), a ratio of 1.102 results and the contributions of terms containing $\Delta\chi_{NR}^{(2)}$ only sum up to ~ 0.9 % of the total pumped signal. This highlights that a moderate modulation of $\chi_{NR}^{(2)}$ only minimally affects the intensity ratio and also that the modulation of the signal via $\Delta\chi_{NR}^{(2)}$ cross terms is not significant.

I therefore assume that the I_{pu}/I_{unpu} ratio is dominated by changes to $\chi_R^{(2)}$ by an increased Pt-H population. That the pump is driving ultrafast H adsorption is supported by the first ultrafast feature at +100 fs, a sharp increase in the ratio, that is apparent also at potentials where no H is adsorbed to the surface (0.5 and 0.8 V vs. RHE, i.e. outside the UPD region) where, consequenetly, no $\chi_R^{(2)}$ and cross terms exist before the pump. H adsorption occurs on a timescale faster than the life time of hydrogen bonds in bulk water, < 3 ps (and presumably slower at the interface) [6]. This requires that the precursor for Pt-H formation, a hydrated proton at the interface (resonance **4'** following section 4.1), is in position to decompose and form Pt-H when the pump pulse arrives. This requirement is in accord with the microscopic models *independently* (from the discussion in this section) devised in sections 4.1 and 4.2: laser-induced charge transfer from the metal electrode to the solvated proton on an ulrafast timescale is only possible if the interfacial solvent structure accomodates it, i.e., "already is in position". Only then Pt-H can be formed by the perturbation on an ultrafast timescale. As mentioned earlier, the structure of the solvation environment at the interface is potential dependent [142, 143], which was used to explain the sensitivity of the laser-induced charge transfer on applied bias that was observed in section 4.2. The dependence on applied potential of the interfacial solvent structure is also a possible explanation for the bias dependence of the I_{pu}/I_{unpu} ratio in this section. The microscopic model for charge transfer at the Pt/electrolyte interface on ultrafast timescales, whether the probe for the ultrafast observable is photocurrent like in section 4.2, or a vibrational spectral response like in this section, is furthermore in accord with the *independently* devised microscopic model that was used to explain the observation of an atop Pt-H vibration in the UPD region from section 4.1. There I argued that at potentials of underpotential H deposition an equilibrium exists between H_{UPD} in threefold hollow sites, monocoordinated Pt-H atop Pt atoms and hydrated protons immediatly above these Pt atoms. As mentioned in section 4.1, this scenario is only plausible if the activation energy

for the interconversion of the equilibrium species is close to the energy provided by room temperature. This requirement seems to be met for H adsorbed on Pt(111) [128, 129]. It is important to note that the energy provided by room temperature alone is sufficient for this interconversion, the additional energy input by the laser is not needed. Figure 4.9 shows a schematic representation of this hypothesis.

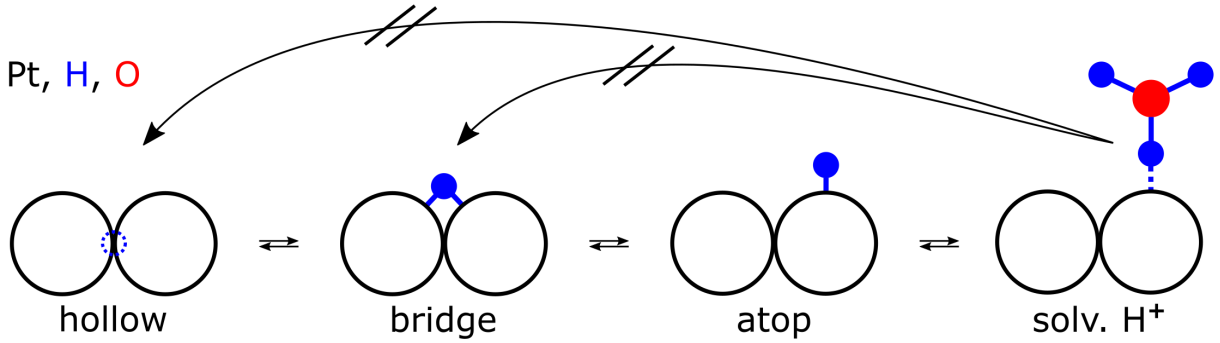

Figure 4.9: Cartoon representation of H adsorbed on Pt: the formation and oxidation of Pt-H are in equilibrium, consequently a steady-state population of bridge and atop bonded Pt-H exsists also in the UPD region.

Taking into account the results of section 4.1, 4.2 and this section, I devise a qualitative microscopic model that explains the fate of Pt-H in acidic solution when it is illuminated with intense femtosecond near-IR radiation. The pump creates a population of hot electrons that populate the antibonding O-H orbital of the solvated proton at the interface, break this bond and lead to the formation of atop bonded Pt-H. This sequence of events shifts the equilibrium reactions sketched in Figure 4.9 towards the left side, resulting in a transiently higher Pt-H coverage. The additional Pt-H ultimately gets oxidized and the Pt-H population returns back to its equilibrium value dictated by the applied potential on timescales $<<$ 1 ms.

Within this conceptual model, in Figure 4.8 the rising edge of the approximately 500 fs long peak around time zero (that in shape is similar for all potentials, but the magnitude strongly varies) can be understood as a rapid increase in the population of atop Pt-H through laser-induced charge transfer to the solvated proton at the interface, population of its antibonding O-H orbital, O-H bond cleavage and formation of a Pt-H bond. However, during charge transfer the arrangement of the involved species also allows the backward reaction from Pt-H to the solvated proton. Part of the newly formed Pt-H reacts back again as the Pt-H population overshoots (more Pt-H is formed than can be stabilized) due to the perturbation, which explains the rapid decrease after 100 fs. The ratio then immediatly increases again to a second, local maximum around 300 fs. This back and forth bouncing of the ratio can possibly be understood as the first steps in the approach back towards steady-state conditions after a strong perturbation. The atop Pt-H entities

that are not converted back to the solvated proton equilibrate with bridge and hollow site bonded Pt-H resulting in the slower decline of the I_{pu}/I_{unpu} ratio after 500 fs. The lasting (for the investigated timescale) increase in the ratio then is a consequence of an overall higher amount of atop adsorbed Pt-H (and higher amount of the other Pt-H species, respectively). This also explains why the ratio goes back to one after about one ps outside of the UPD region, because bridge and hollow site bonded H (i.e. H_{UPD}) are not stable in this potential window. Conversion of hydrated protons directly to bridge, or hollow site bonded H_{UPD} is unlikely because Pauli repulsion prohibits the hydrated proton from coming close enough to both sites [129].

In the dicussion of the data displayed in figure 4.8, I have discussed resonant changes by integrating over all frequencies, thereby losing information on site specific Pt-H dynamics. Additional information is gained by plotting the frequency resolved spectral response as a function of pump-probe delay in Figure 4.10.

Upon inspection of the top panel of Figure 4.10 it should be noted that we are dealing with a defect rich spot on the Pt(111) surface that, in agreement with Figure 4.4, shows resonances **2**, **4** and **5** and an additional peak around 1800 cm^{-1} (possibly a consequence of defects that are not clearly (110), or (100) like), but unfortunately almost no **4'** resonance (possibly because of a minor Ca^{2+} impurity due to dissolution of the CaF_2 window). While the quantitative line shape analysis of multiple overlapping peaks in an unpumped spectrum is challenging, but possible (see section 4.1 and appendix section A), the same task becomes substantially more complicated when pumped. Under these conditions in principle every line shape parameter can be pump-dependent, significantly increasing the parameter space for the fitting problem. In the following discussion I will assume that pump-induced changes to resonant, or nonresonant phase[8] are negligible and that pump-induced intensity changes in the spectrum are a consequence of a changing resonant amplitude. Furthermore, the pump induces changes rather to frequency windows that are dominated by multiple resonances than to single resonances (as detailed below) and I thus extract qualitative information from discussion of these frequency windows. Frequency window I) stretches from 1795 - 1960 cm^{-1} and is dominated by resonances **2** and **5**; II) stretches from 1960 - 2015 cm^{-1} and is dominated by resonances **2** + **4**; III) stretches from 2015 - 2300 cm^{-1} and is dominated by resonances **4** + **4'**.

At both potentials, the I_{pu}/I_{unpu} ratio immediatly after time zero is increased evenly from 1800 - 2100 cm^{-1}, while from around 1780 towards lower wavenumbers a small decrease in the intensity ratio is apparent. This decrease occurs in a frequency range where only little IR intensity is available and thus no SFG photons are produced in the absence of the pump. Because it is potential independent, and possibly a pump-induced signal from the CaF_2/electrolyte interface, we will not discuss it further.

[8]The nonresonant amplitude is small relative to the resonant amplitude, therefore changes the nonresonant phase are not important.

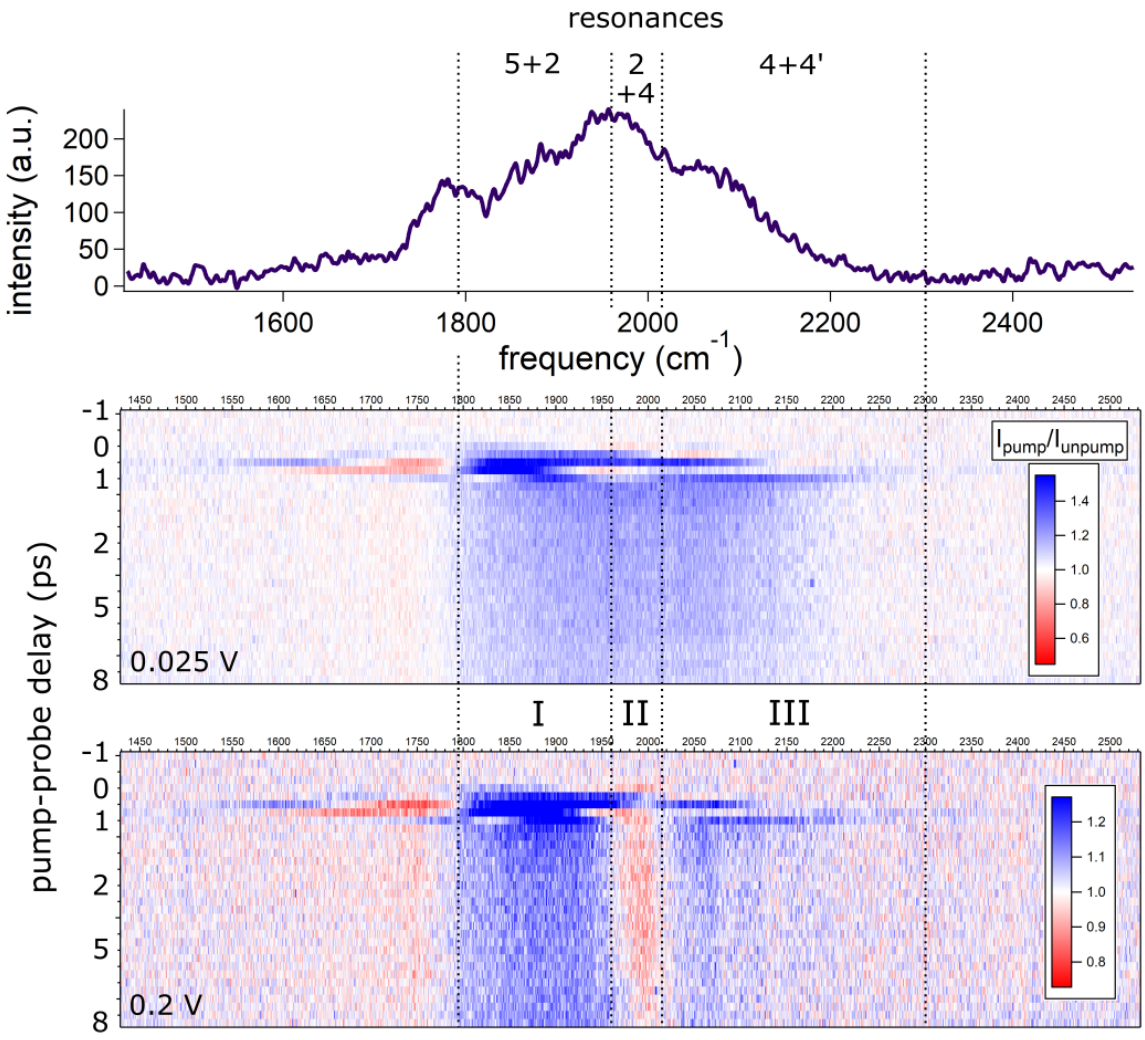

Figure 4.10: Top panel: background corrected SFG spectrum at 0.025 V vs. RHE without pump. Middle and bottom panel: I_{pu}/I_{unpu} ratio vs. frequency as a function of pump-probe delay at a Pt(111)/electrolyte interface at 0.025 (middle) and 0.2 V vs. RHE (bottom). The time resolution is finer around time zero and coarser at delays > 3000 fs. Spectra were recorded with 2 μJ pulse energy for upconversion and IR pulses and 9 μJ pulse energy for the 800 nm, 35 fs pump; the repitition rate was 1 kHz and the electrolyte 0.5 M $HClO_4$.

The increase in the ratio around time zero is better visible in Figure 4.11 a). From the apparent independence of the I_{pu}/I_{unpu} increase on frequency at +100 fs, I conclude that the first pump induced changes to the spectrum can either be described by a scenario in which an ultrafast change in $\chi^{(2)}_{NR}$ modulates $\chi^{(2)}_{R}$ via the cross terms, or by ultrafast laser-induced H adsorption. As detailed below equation 4.4, cross terms including $\Delta\chi^{(2)}_{NR}$ basically do not contribute to the intensity ratio for moderate pump-induced changes to

$\chi^{(2)}_{NR}$. Also this first ultrafast feature at +100 fs is apparent at potentials where no H is adsorbed to the surface (0.5 and 0.8 V vs. RHE) and it is therefore concluded that the pump is driving ultrafast H adsorption. In the early stages of adsorption (and potentially with an excess of energy), H possibly is highly mobile and not localized, which explains that an increase in population leads to an increase in spectral intensity that is not site specific and spectrally broad. It should be noted that the pump-induced signal increase discussed here does not have the same shape as the unpumped spectrum, adding further proof that the pump-induced signal is not $\chi^{(2)}_{NR}$ driven. However, only 100 fs later at +200 fs the increase in the ratio sharply localizes at 1860 cm^{-1}. At the other frequencies the ratio is back to 1 at this point, presumably due to the fast back reaction of newly formed Pt-H to the solvated interfacial proton. This sharp drop in the ratio at the other frequencies is explained in the discussion following Figure 4.8 as follows: the geometry of the interfacial solvent that allows ultrafast charge transfer and the laser-induced formation of Pt-H also, necessarily, allows the back reaction. Because the pump leads to a higher Pt-H coverage than can be stabilized by the applied potential (and the interfacial structure and electric field it dictates), part of the laser-induced Pt-H immediatly reacts back to the solvated proton (assuming that Pt-H depletion via H_2 formation is too slow for the observed subpicosecond dynamics). A site-specific behavior towards additional Pt-H population could be expected from the adsorption isotherms of H on different Pt single crystal electrodes: different surface structures have distinct adsorption isotherms and therefore their ability to stabilize additional H at a certain potential is different [24]. The sharply localized increased intensity at +200 fs increase then apparently diffuses to resonance **5** around 1900 cm^{-1} and resonance **4** around 2100 cm^{-1} at +300 fs. So far the pump-induced changes to the spectrum were qualitatively identical for both potentials (however, the magnitude of I_{pu}/I_{unpu} differs). At more positive delays differences between the two potentials become apparent. At 0.025 V vs. RHE, the intensity ratio is increased seemingly evenly in all three frequency windows, but not for 0.2 V. Here the intensity ratio is slightly decreased in frequency window II. In the other frequency windows (I and III) the qualitative behavior is identical (only the magnitude differs compared to 0.025 V). This is highlighted in Figure 4.12, where I show the frequency integrated pump-probe traces of regions I to III.

The full pump-probe dataset including the other potentials, plotted analogously to Figure 4.10, can be found in the appendix section A.

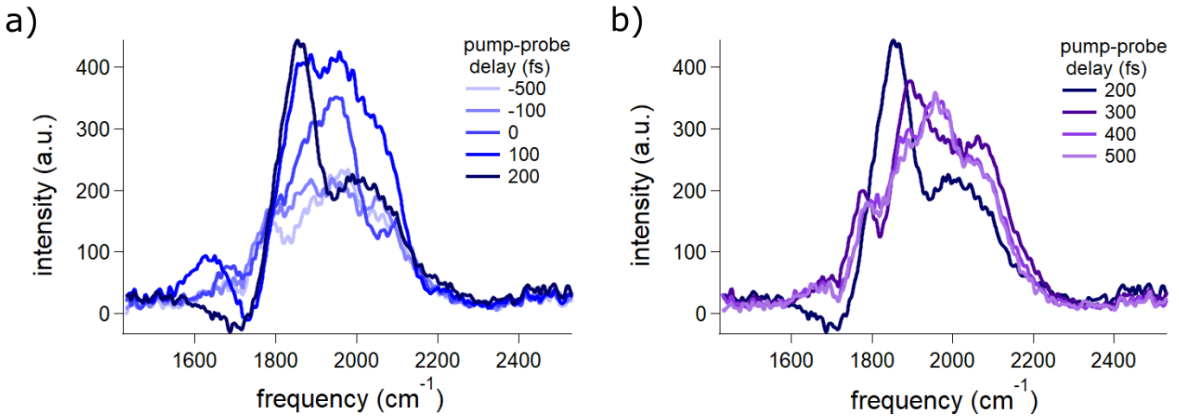

Figure 4.11: a) Background corrected SFG spectrum at 0.025 V vs. RHE as a function of pump-probe delay from -500 to +200 fs. b) Pump-probe delays +200 to + 500. Spectra were recorded with 2 μJ pulse energy for upconversion and IR pulses and 9 μJ pulse energy for the 800 nm, 35 fs pump; the repitition rate was 1 kHz and the electrolyte 0.5 M $HClO_4$.

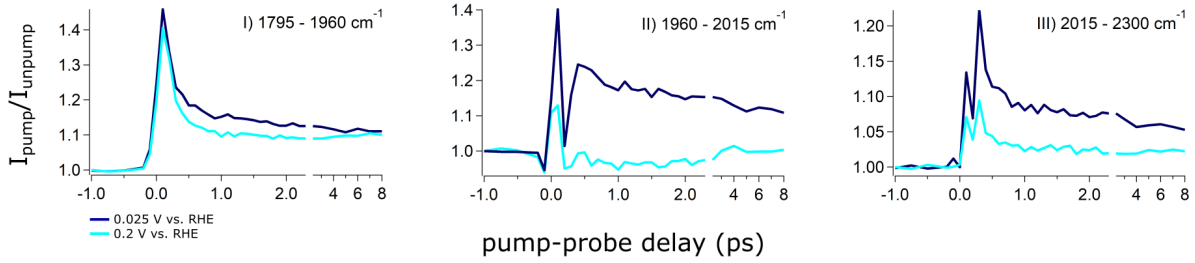

Figure 4.12: Frequency integrated pump-probe traces of regions I-III of Figure 4.10 at 0.025 (dark blue curve) and 0.2 V vs. RHE (turquoise curve). Experimental details are described in the caption of Figure 4.10.

Inspecting the data displayed in Figure 4.10 and 4.12, with the microscopic model of Figure 4.9, explaining the fate of Pt-H after pumping with ultrashort near-IR pulses in mind, offers direct insight into the HER and the nature of H_{UPD} and H_{OPD} on Pt(111). The I_{pu}/I_{unpu} ratios at 0.025 and 0.2 V vs. RHE behave qualitatively similar in frequency windows I and III (only the absolute value is higher for 0.025 V vs. RHE). This implies that the mechanism by which the pump affects Pt-H is similar on the surface sites that produce the vibrational responses of these frequency windows and that tuning the potential affects the amplitude of the effect, but not its shape (or sign). This kind of behavior is expected for H_{UPD} on Pt(111), where with decreasing potential only the coverage of otherwise identical H adsorbates increases (see section 2.2 for more information on H_{UPD} on Pt(111)).

The Pt-H entities that produce the vibrational response of frequency window II, however, show an entirely different behavior after perturbation by the pump at 0.025 V than at 0.2 V vs. RHE. At 0.2 V the ratio increases around time zero, but almost immediatly returns back to, or even below, one akin to the behavior observed for 0.5 and 0.8 V vs. RHE in Figure 4.8. It appears that at this potential additional hydrogen due to the pump can not be stabilized at the surface sites that produce the vibrational response of frequency window II. A possible explanation for this behavior is a lack of mobility on subpicosecond timescales of H adsorbed to this surface site: additional atop Pt-H is formed by charge transfer to the solvated proton, but can not be converted to bridge, or hollow site bonded H and is therefore immediately converted back. If at all, the respective Pt-H subpopulation is decreased which would be in accord with the initial idea of how hot electrons would initiate the HER: hot electrons occupy antibonding Pt-H orbitals which leads to Pt-H bond cleavage and recombinative H_2 formation (see section 2.3). On the contrary, at 0.025 V vs. RHE the intensity ratio shows a lasting increase after its initial sharp rise and decline around time zero. Following the above logic, interconversion of atop Pt-H to bridge and hollow site bonded H is also possible in frequency window II if the potential is reduced to 0.025 V vs. RHE. Such a discontinuous behavior towards the reversible HER potential, no lasting increase of the ratio at 0.2 V, but at 0.025 V vs. RHE, would be expected for H_{OPD}. According to the classical electrochemical notation H_{OPD} is the intermediate of the HER and only appears close to 0 V vs. RHE, the reversible HER potential, see section 2.2 for more background information. In the microscopic model picture of Figure 4.9, atop Pt-H exists already at UPD potentials at the surface sites that produce the vibrational response of frequency window II (and other sites as well), but only becomes "HER active" close to 0 V vs. RHE due to an increase in H mobility at these surface sites on subpicosecond timescales as a consequence of the potential decrease.

That I am observing pump-induced dynamics of H_{OPD} in frequency window II at 0.025 V is further corroborated by the partial overlap of frequency window II and the modes to which H_{OPD} has been assigned in previous spectroscopic experiments, see Table 4.1. In section 4.2 I found that the pump only drives the HER at potentials close to 0 V vs. RHE, adding further evidence that the Pt-H entity that produces the vibrational response of frequency region II is related to the reaction and possibly H_{OPD}. In hindsight, the conclusion that H mobility on ultrashort timescales is a prerequisite for the HER possibly is a part of why the HER could not be triggered with the ultrashort 800 nm pump in the UPD region at potentials farther away from the HER in section 4.2. Earlier, this was explained exclusively as a consequence of the (potential dependent) interfacial solvent structure not allowing charge transfer that results in the HER, unless the potential is already close to the reaction's onset potential. The results of this section highlight that the structure of the interface still dictates HER reactivity even after charge transfer: if the intermediate that has been formed through charge transfer can not move to its reaction partner, it is discharged again and the reaction can not commence. One possible way in which the applied bias could affect the mobility of adsorbates on the surface is by lowering the activation barrier for site-hopping processes (like fcc => bridge => fcc) by changing the adsorption energy of the adsorbate in the respective sites.

The vibrational response of frequency window II already exists at 0.2 V vs. RHE in the absence of the perturbation. This implies that if the corresponding Pt-H entity actually is H_{OPD}, it must evolve from H_{UPD} (that produces a vibrational response in frequency window II) when going from 0.2 V on negative by a change of the interphase that leads to a higher mobility of adsorbed H on ultrafast timescales.

As noted also by Osawa et. al (however, based on intuition and not on an experimental observable like in this thesis), a high mobility of adsorbed H appears to be a prerequisite for H_2 formation following the Tafel mechanism (equation 2.14, combination of two identical Pt-H species to H_2 and bare Pt), because the distance of two atop H entities adsorbed on two neighboring Pt atoms far exceeds the bond length of molecular H_2 (0.279 vs 0.074 nm) [88].

4.4 Implications for the Understanding of the HER and H Adsorbed to Pt Electrodes

Here I summarize the key conclusions of the previous sections to highlight the implications of the observations reported in this thesis for understanding of the HER, H adsorbed to Pt electrodes (H_{UPD} and H_{OPD}) and charge transfer at the Pt/electrolyte interface in general. The new insights will be sketched in a thought experiment in which we consider a Pt(111)/electrolyte interface and, starting from a potential in the bilayer region (no adsorbates except for water), apply a negative potential ramp. The Pt(111) CV is discussed in detail in section 2.1.3.

Starting at a potential of 0.5 V vs. RHE, the surface is only covered by water. Going negative in potential, H_{UPD} adsorption starts at around 0.35 V vs. RHE. This potential coincides with the PZC of Pt(111) in acidic solution (0.3 - 0.35 V vs. RHE [154, 155]), from which on cathodically protons may be expected at the interface (because it is negatively charge below the PZC). According to the argumentation of reference [129] and section 4.1 of this thesis, Pt-H formation occurs by reduction of a solvated interfacial proton that has one H pointed at the top of a Pt atom. The now atop adsorbed H then diffuses to a fcc three-fold hollow site via a bridge site, which is consistent with recent theoretical work [129]. The hollow site-bonded H is typically considered as H_{UPD}. Until now, the general electrochemical notion of H_{UPD} not only on Pt(111), but also on other crystal faces (possibly with other adsorption sites for H_{UPD} [24]), is that it is statically sitting in its adsorption site. Sections 4.1 and 4.3 of this thesis and reference [129], however, make a strong case that H_{UPD} exists in an equilibrium with the solvated interfacial proton immediatly above a Pt atom via bridge and atop bonded Pt-H. Following the thermodynamic description of equilibrium processes, it is assumed that H_{UPD} formation and H_{UPD} oxidation (both processes occur via atop Pt-H) are ongoing processes with identical rates even when H_{UPD} coverage is constant.

According to section 4.2, the necessary charge transfer for H_{UPD} formation/oxidation requires a specific structure of the interfacial solvent and may not occur in its absence. The structure of the interfacial solvent is a function of potential [142, 143] (and section 4.2), which has direct implications for charge transfer. On Pt surfaces other than Pt(111) that have UPD peaks (and not a plateau), the interfacial solvent structure at the apex of a UPD peak is optimal for the charge transfer that results in the formation of the respective H_{UPD} species and the charge transfer resistance is minimal. This hypothesis is supported by the study of charge transfer at the Pt/electrolyte interface on ultrafast timescales (initiated by fs optical pulses) in section 4.2 of this thesis and time-averaged measurements of the charge transfer resistance of a Pt_{poly} electrode as a function of potential [148].

In section 4.3 it was concluded that the mobility of H on Pt on a subpicosecond timescale has major implications for the HER. Pt-H entities that produce a vibrational response in the frequency window 1960 - 2015 cm^{-1} can not diffuse from the atop adsorption site to bridge and hollow site bonded Pt-H on subpicosecond timescales when the potential is not close to the reversible HER potential at 0 V vs. RHE (but still inside the UPD region, e.g.,

at 0.2 V). At all other adsorption sites, H is mobile on these timescales at any potential inside the UPD region. However, close to the HER onset potential H also becomes mobile in the respective adsorption sites. The respective Pt-H entities are assigned to H_{OPD}, the HER reaction intermediate, which is supported by prior spectroscopic studies (that have assigned a mode to H_{OPD} that partially overlaps in frequency with the Pt-H entities reported in this thesis) and section 4.2 of this work. To the best of my knowledge, this work is the first to report spectroscopic evidence for the interrelation of H_{UPD} and H_{OPD}: a subpopulation of H_{UPD} that produces a vibrational signature from 1960 - 2015 cm^{-1} turns into H_{OPD} close to the onset potential of the HER by a change in the interphase that enables mobility of H adsorbed to these surface sites on subpicosecond timescales.

The dependence of H mobility on interfacial structure is possibly related to the strong dependence of HER activity on electrolyte composition (pH [148, 76] and cations in alkaline solution [86]). Understanding the interrelation of electrolyte composition, interface structure, adsorbate mobility and catalytic activity would accelerate our journey towards HER catalysts that i) match Pt's activity and stability in acid at a fraction of its cost, ii) perform as well in alkaline as in acidic electrolyte. One possible way to probe the potential dependence of H diffusion on an electrode would be to simultaneously monitor H adsorbed to two different sites, e.g. fcc three-fold hollow and atop sites, while selectively exciting only one of them, e.g. by vibrationally resonant excitation. The potential dependence of population transfer from one site to the other should be a direct function of H mobility.

Finally, the use of ultrashort optical pulses enabled for the first time experimental insight into the kinetics of a true elementary step of the HER (as opposed to the rate of the Volmer/Tafel/ Heyrovsky reactions, which are not elementary steps, but sequences thereof). Charge transfer on Pt electrodes was concluded to be rate limiting for the HER in acidic electrolyte once the interfacial solvent and reactants are in the optimal configuration (that is set by the external bias) for the reaction.

Chapter 5

Operando Insights into the Oxygen Evolution Reaction (OER): Activity is Highly Local on Au_{poly}; on Pt Higher Oxidation States are Inactive

The previous chapter dealt with the HER and as noted in the introduction, understanding thereof is important for creating new generations of catalysts. These are either based on non-noble metals and can compete with Pt's combination of activity and stability at a fraction of its cost, or (for Pt based catalysts) have the same activity at lower loadings [23]. Comprehending the HER is further important for understanding the substantial decrease in activity when going from acidic to alkaline conditions [72]. Despite the decrease in HER activity, the use of an alkaline electrolyte is desirable: the oxidative half cell reaction of water splitting, the OER, is slow and strongly performance limiting under acidic conditions [156] and only noble metals are active *and* stable under these conditions [25] (and still require high loadings [157]). At high pH cost effective non-noble metal catalysts reach similar activities for the OER [158, 25, 159] (and ORR [160]) as noble metal catalysts in acidic solution [157]. Clearly, understanding why the oxygen chemistry is catalyzed poorly is fundamental to building better catalysts and more efficient devices on our way towards a carbon neutral society[1].

The OER is kinetically limitated: the high overpotential necessary to drive it is a result of a high activation barrier. In principle, choice of an appropriate electrocatalyst should be able to lower the overpotential. However, the rational design of an efficient OER catalyst is hampered by our incomplete understanding of the reaction mechanism. This lack of understanding is presumably exacerbated by the OER's complexity: it requires the transfer of 4 electrons and involves an unknown number of corresponding intermediates on surface sites whose structure and oxidation state is not known.

The ability to monitor the surface structure of an OER catalyst is important, as cata-

[1]Parts of the following paragraphs are copied from my own publication reference [33].

lyst surface atomic structure can often be correlated with activity [10]: certain atomic-scale structural motifs outperform others by many orders of magnitude (e.g. steps vs. terraces). Quantifying such structure/reactivity correlations is powerful, it makes it possible to infer the identity of catalytically *active sites* [161]. It is perhaps unsurprising that the identity of the active site depends on reaction, catalyst, and catalyst surface structure: *predicting* the active site of a particular catalyst for a particular reaction has proven extremely challenging. Part of the difficulty is that any such prediction requires knowledge of the mechanism of the reaction of interest, which may also be a function of the same parameters.

Most studies that have shown clear correlations between surface atomic structure and catalytic activity, whether in gas phase or electrocatalysis, have done so on single crystals [162, 163, 164]. Because surface structure and bonding can be well characterized on such substrates they are useful systems to demonstrate differences in activity of terraces and steps for different crystal faces (e.g. (111) vs. (100) terraces and/or steps). Such comparisons can be done indirectly by comparing the activity of stepped and unstepped surfaces in an (electro)catalytic experiment [162, 163, 164], or directly by operando imaging of the activity of steps and adjacent terraces [165]. While the reactivity of single crystals is not generally of practical interest, some more complex catalysts, e.g. shape-selected supported nanoparticle systems, have reactivities that can be rationalized as a linear combination of the reactivity of the crystal faces of which their surface is composed [166].

Unfortunately, virtually all candidate electrocatalytic materials have complexity that cannot be straightforwardly understood as a linear combination of features apparent in idealied model systems: e.g. for the great majority of catalysts relevant in industrial contexts, both surface structure and catalytic activity have been shown to be heterogeneous on length scales from nm to mm [167]. This structural heterogeneity is thought to influence reactivity in at least five ways: i) grain boundaries (or other microscopic defects) stabilise reactive atomic defects or high step densities that can not exist on extended surfaces [13]; ii) differences in local conductivity [168]; iii) differences in local pH [169]; iv) heterogeneity in transport (e.g. local turbulent flow or nonuniform diffusion) and v) a resulting spatial heterogeneity in the extent to which the catalyst restructures under reactive conditions [167]. It therefore seems clear that optimising catalyst performance requires *operando imaging of reactivity* on the nm-mm spatial scales of structural heterogeneity. I meet this challenge by imaging the OER activity and structural heterogeneity of polycrystalline Au electrodes on the 200 nm - 100 µm length-scales of particular relevance for this material.

Understanding the OER on noble metals in general, and on Pt and Au in particular, is important both for possible applications and as a useful model system in OER electrocatalysis. Despite decades of study, neither for the OER, nor for the electrooxidation of Au (which begins at potentials cathodic of and continues through potentials relevant to the OER) does a universally agreed on picture exist. The following discussion of what happens when a positive bias is applied to a gold electrode is illustrated by a CV of a polycrystalline gold electrode and a linear sweep voltammogram of the same electrode in 1 M $HClO_4$ in Figure 5.1, which has been plotted with data from reference [156].

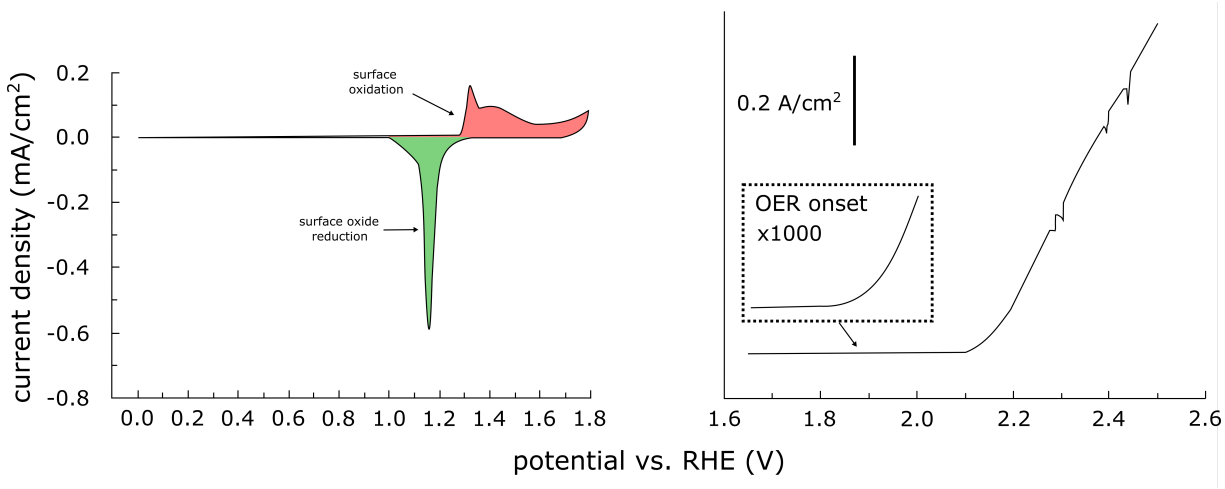

Figure 5.1: The left shows a CV of Au_{poly} in 1 M $HClO_4$ recorded at 50 mV/s; the current features associated with surface oxidation/reduction are colored red/green. On the right a linear sweep voltammogram recorded at 1 mV/s can be seen; The inset shows a magnified (current density *1000) excerpt of the potential region around 1.8 V vs. RHE. Note that the y-axes are scaled differently, the current densities during the OER (on the right) far exceed the respective current densities during cyclic voltammetry (left). The data has been taken from reference [156].

It is generally accepted that at sufficiently low potentials the Au surface is covered with anions [170, 171] and that, as the potential is scanned increasingly positively, the first step of surface oxidation includes the reversible replacement of anions with either O or OH through water discharge (or OH^- adsorption in base) [172, 173, 170, 171, 156] that produces the positive current peak(s) after 1.3 V vs. RHE in the CV. While less work exists on the subsequent stages of oxidation, increasing the potential is thought to lead, after completion of the oxygen species monolayer, to site exchange of the oxygen containing species with gold atoms [174] and the formation of a quasi three-dimensional hydroxy-oxide film [170, 171, 175] in which the oxidation state of gold is +3 [176]. Koper and coworkers have found that further increasing the potential does not change gold's oxidation state, but rather dehydrates the film towards Au_2O_3 [156]. The existence of Au_2O_3 was reported from 1.5 V vs. RHE upwards [177]. However, the dehydration of the oxide film towards Au_2O_3 cannot be complete, as pure gold oxide is not stable thermodynamically under oxygen evolution conditions [178]. Regardless of their detailed structure the first three layers of oxide are typically termed α-oxide and thought to be compact [177], while the following layers, termed β-oxide, have been found to be disordered [177, 176]. For the actual OER, Koper and coworkers presented evidence from online electrochemical mass spectrometry that the first molecular oxygen is evolved as α-oxide (thought to be formed from the the first three layers of Au as one goes from bulk H_2O to bulk Au) is transformed to β-oxide by a disproportionation of gold hydroxy oxide at 2 V vs. RHE in 1 M $HClO_4$

[156] (right panel of Figure 5.1). Burke and coworkers also found 2 V vs. RHE to be the onset potential for the OER on Au in basic electrolyte [179]. At even more positive potentials, other mechanisms for the OER may be active where, for example, one oxygen atom of an O_2 molecule comes from the surface oxide and the other from the electrolyte [180, 181, 182]. While the onset potential of the OER on the RHE scale appears to be relatively insensitive to electrolyte pH, much work has clarified that OER activity is not: most OER catalysts are more active in alkaline media (IrO_x is a notable exception) [25].

The surface electrooxidation of Pt and the OER on Pt resemble the situation on Au and will be discussed in section 5.2, where I investigate the influence of Pt's oxidation state in the oxide film on OER activity and conclude that higher oxidation states of Pt (+IV/+VI) are not OER active.

5.1 Second Harmonic Imaging of Au Surface Electrochemistry *Operando*: Heterogeneity in Charging, Oxidation and the OER

This body of prior work clarifies that, if we are to understand the spatial heterogeneity of the OER on Au we also need to understand the spatial heterogeneity of Au surface oxidation: we require an imaging technique sensitive to both processes that can be employed operando. This requirement is nontrivial for at least two reasons: (i) much prior work has clarified that oxidation (and subsequent reduction) lifts atomic order even for initially well defined Au single crystals [172] and (ii) it implies that methods that use electrons as probes (e.g. STM) or use the optical response of the metal to enhance a photon-based observable (e.g. SEIRAS or SERS) are not applicable.

Here I apply **S**econd **H**armonic generation **M**icroscopy (SHM) to image two different Au electrodes, a polycrystalline one with a grain size distribution on the order of 10 - 50 µm, and a nanocrystalline electrode that is composed of tens of nm big clusters, under reactive conditions as Au is charged and oxidized and as oxygen bubbles are produced. SHM is a nonlinear optical technique that is surface specific by its symmetry selection rules: only the surface dielectric function is probed (see chapter 3 for details on the SFG process). This surface specificity allows investigation of surface processes and a precise alignment of the focal plane of the microscope with the Au/electrolyte interface not possible in linear optical approaches [183]. A sketch of the experimental setup together with the electrochemical cell for optical imaging is shown in section 3.2. Scanning electron micrographs of the investigated samples can be found in the appendix section B.

The work on surface electrooxidation and the OER on Au electrodes is shortly summarized in the following. In section 5.1.1 the SH response of the two different types of Au electrodes is recorded as a function of potential. I perform cyclic voltammetry from 0 - 1.7 V vs. RHE where gold is first metallic and later oxidized. These experiments are performed to obtain insight into the spatial heterogeneity of gold electrooxidation and in an effort to potentially correlate this heterogeneity in gold surface oxidation with hetero-

geneity in OER activity. The heterogeneity of OER activity on gold is the subject of section 5.1.2. On the polycrystalline sample, the SH response as a function of potential shows heterogeneity on the lengthscale of the grain size distribution (as determined by scanning electron microscopy) while the SH response of the nanocrystalline sample (the clusters' size is well below the imaging resolution) is homogeneous across the entire field of view (FOV). The SH signal is analyzed over a particular potential range according to the so-called "parabolic model" that has been described in detail in section 3.2. In short, this model describes the intensity of the SH emitted from a charged interface by a dipolar electric and a DC field-induced contribution:

$$I(2\omega) \sim \mid \chi^{(2)} + \chi^{(3)'} \Phi_0 \mid^2 I(\omega)^2 \tag{5.1}$$

Φ_0 is the potential drop across the interface (explained in detail in section 2.1; $\Phi_0 = V - V_{PZC}$, V_{PZC} is the PZC, which was taken as 0.4 V vs. RHE, see discussion below), $I(\omega)$ is the intensity of the fundamental beam. Equation 5.1 can be expanded to an expression that is parabolic in Φ_0:

$$I(2\omega) \sim Q\Phi_0^2 + L\Phi_0 + C \tag{5.2}$$

With Q, L and C as quadratic, linear and constant coefficient, respectively. Q and L can be positive, or negative. The relative size of Q and L give insight into the dominant contribution to the SH signal, as will be recapped in detail at the appropriate position below.

On the polycrystalline sample, the SH signal increases quadratically with potential in the majority of areas prior to surface oxidation. In these areas the main contribution to the SH signal comes from electronic polarization contributions of the metal/electrolyte interface. In other regions I observe a quadratic *decrease* of SH intensity with increasing potential. These regions show the strongest changes in SH signal from one CV cycle to the next and I argue that these areas are particularly prone to potential-induced surface reconstruction, which is further corroborated by a correlation coefficient analysis, a statistics based image analysis. The negative quadratic dependence of SH signal intensity on applied potential and the stronger propensity towards potential-induced surface reconstruction are discussed in terms of metastable surface states and anion adsorption at potentials lower than the PZC of the average surface due to local PZCs.

I then move on to more anodic potentials and investigate the OER on both types of electrodes in section 5.1.2. I find the OER activity to be highly local and to occur in two distinct types of active areas. The first is observed at potentials anodic (i.e. positive) of the OER onset and is stable with respect to surface atom reconstruction during repeated potential cycling. This first type is consistent with a defect that is oxidized and penetrates through the surface into the bulk (potential cycling of Au electrodes leads to surface reconstruction of the first 2-3 Au layers [172]). The second type of active area is active at potentials below the OER onset potential and is likely a highly active, metastable surface atom motif (not stable with respect to surface atom reconstruction). The first type of active area identified in section 5.1.2 lies on the border of regions with positive and negative

Q value in the parabolic model analysis of section 5.1.1. Such a position appears to be a necessary, but not sufficient (not all such borders show a high activity for the OER) criterium for a high OER activity. The wide-field imaging of two distinct types of OER active sites on spatially heterogeneous Au offers an essential tool for both fundamental and applied studies: e.g. the systematic dependence of active site distribution on electrolyte and the possibility of engineering novel Au samples that stabilize few atom layer thin, highly active sites for application in electrolyzers.

5.1.1 Mapping Heterogeneity in Au Surface Electrooxidation and Potential-Induced Surface Reconstruction *Operando*

The results reported in this section have recently been submitted to The Journal of Physical Chemistry C [184].

I imaged the surface of the nanocrystalline gold sample in PPP polarization combination (the electric field component of all in- and outgoing beams lies in the plane that is defined by the respective beams) in 0.5 M NaH_2PO_4 (pH = 2.8) while performing cyclic voltammetry in Figure 5.2. A phosphate buffer was chosen to ensure pH stability during measurements and because phosphoric acid derived anions show a rather low propensity to adsorb specifically [185].

In panel A) a SH image shows the surface at 1.2 V vs. RHE during the forward scan. The range of the color scale comes from an analogous SH image of the polycrystalline sample that shows a much larger spread in SH intensities and therefore enables a more direct comparison between the two samples. No specific spatial features (like confined areas with higher, or lower SH intensities than other areas) are apparent and the SH signal is homogeneous across the FOV with only small fluctuations. This is highlighted by a line-scan following the black line in panel A), plotted as SH counts vs. line pixels in panel B). According to panel B), the SH counts across the FOV range from $7.0 \cdot 10^3$ to $9.7 \cdot 10^3$ and have a standard deviation of $0.5 \cdot 10^3$. In panel C) I show the CV in black (with arrow heads indicating the scanning direction) and the simultaneously recorded SH intensity averaged over the entire FOV in red (green) for the forward (reverse) scan. I will refer to SH intensity vs. applied potential curves as 'SH-V' curves in the following discussion.

The CV shows the expected behavior of a gold electrode, see reference [170] and the introduction to this section above; the CV can be roughly partitioned into three potential segments with distinctive chemistries in the forward scan: In the first region from 0 - 0.4 V vs. RHE, no reactions and little to no anion adsorption occurs, the electrode is only increasingly polarized and this region is accordingly called the polarization, or double layer charging region (PR). Because of the electrode surface charging, the double layer structure reorients accordingly to screen this charge. In the second region from 0.4 - 1.1 V vs. RHE the electrode is further polarized and anions adsorb and depending on the exposed surface structure, the surface may reconstruct [175, 50, 172, 173]. This potential region is chosen to contain anion adsorption, but not surface oxidation, it ends before the first peak associated with surface oxidation at around 1.2 V vs. RHE.

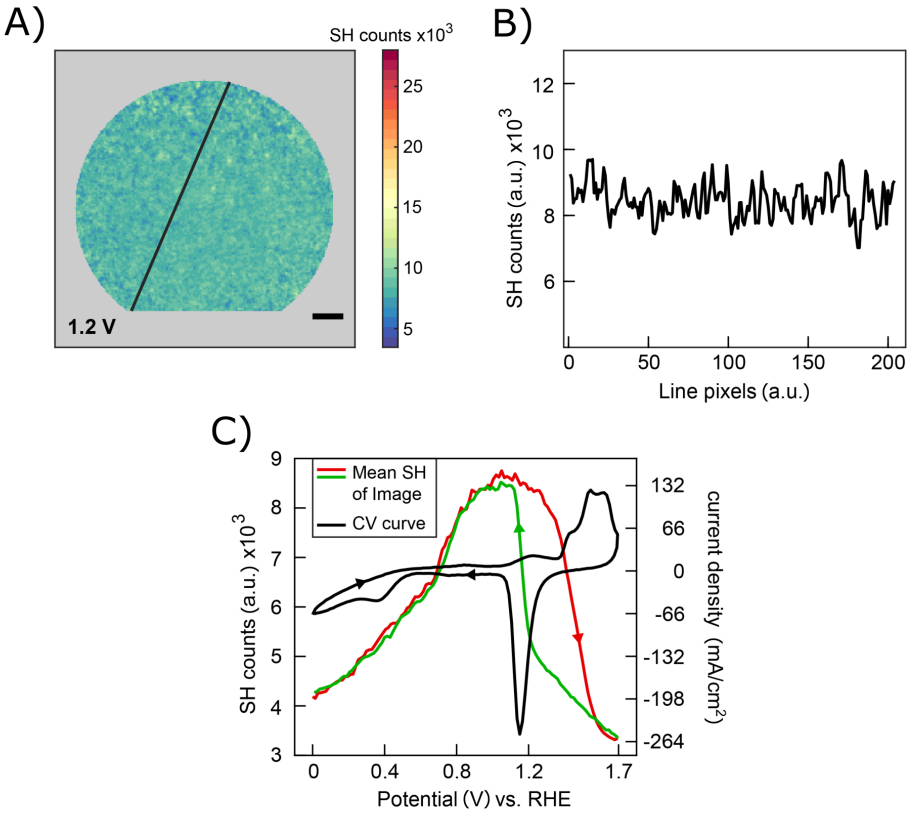

Figure 5.2: Panel A) shows a SH image of the nanocrystalline electrode at 1.2 V vs. RHE that was recorded during the forward scan (60 mV/s, 0.5 M NaH_2PO_4) with an acquisition time of 0.25 s in the PPP polarization combination. The scale bar measures 10 µm and the black line indicates the position of a line scan that is displayed in panel B). Panel C) shows the CV in black, together with the averaged SH intensities of the entire FOV during the forward (red curve) and reverse (green curve) scan.

In the third potential interval from 1.1 - 1.7 V vs. RHE the surface is oxidized. This potential window will be referred to as oxide generation region (OG). Surface oxidation is thought to start at undercoordinated surface sites, steps and defects. The oxidation of such species is apparent in the small positive current peak around 1.2 V vs. RHE. The series of positive current peaks after 1.35 V vs. RHE correspond to the oxidation of the first full layer of Au atoms including the terraces. The oxidation (regardless, if step, or terrace) happens by a replacement of adsorbed anions by either O or OH. By 1.7 V vs. RHE the oxidation of the first layer of Au atoms is complete, deeper layers only get oxidized at higher potentials by site exchange of O/OH with metal ions [170, 171, 175, 172, 173]. The reverse scan only shows two current features: an intense negative current peak at 1.1 V vs. RHE that results from reduction of the surface oxide and a smaller negative current peak

at 0.4 V vs. RHE that is due to an impurity[2]. The slight bend towards negative current densities from 0 - 0.5 V vs. RHE stems from the reduction of oxygen in the solution in the ORR that produces a cathodic current.

The integrated SH intensity increases rapidly in the forward scan from 0 - 0.9 V vs. RHE, continues to increase from 0.9 - 1.1 V vs. RHE at a strongly reduced rate, slightly decreases from 1.1 - 1.2 V vs. RHE and then sharply falls off towards more anodic potentials. In the reverse scan, the SH signal is significantly smaller at potentials 1.7 - 1.2 V vs. RHE (as long as the surface is covered by oxide) and is only back to its maximum value at 1.1 V vs. RHE as soon as the entire oxide is reduced and the surface is metallic again (which is known from the CV), thus displaying a pronounced hystersis behavior. It is noteworthy that the SH-V behavior from 0 - 0.9 V vs. RHE is identical in both scanning directions and that the SH-V curve is parabolic. The above described SH-V behavior, which is an average of the entire FOV of the nanocrytalline electrode, is in good agreement with previous SHG studies on gold electrodes [113, 186] and correlates well with the CV: from 0 - 1.1 V vs. RHE the surface is increasingly polarized and the SH intensity increases with increasing (positive) charge density. At 1.1 V vs. RHE undercoordinated minority sites of the surface get oxidized and the increase in SH intensity comes to a halt. Subsequently the surface gets oxidized and the SH intensity decreases suddenly.

Analogous SH images of the polycrystalline Au electrode during cyclic voltammetry (60 mV/s, 0.5 M NaH_2PO_4) recorded (PPP polarization combination, 0.25 s acquisition time; three CV cycles were recorded in total) at 0.2, 1.2 and 1.51 V vs. RHE in the forward scan are shown in panel A) - C) of Figure 5.3. The range of the color scale is identical to the one used in Figure 5.2 A). Pronounced spatial heterogeneity in the SH intensity is apparent: tens of µm big areas with varying SH intensities can be distinguished. Ex-situ scanning electron microscopy micrographs show structural heterogeneity on similar length scales (see appendix section B), implying that I observe the metal's grain structure in the SH micrographs. The line scan below panel B) (the position is indicated by the black line in the panel) shows that SH intensities in this FOV range from $4.4 \cdot 10^3$ to $5 \cdot 10^4$ with an average of $8.4 \cdot 10^3$ and a standard deviation of $7.6 \cdot 10^3$. The averaged SH-V curve of the entire FOV is shown as black curve in CV cycle 2 of panel D) and is qualitatively similar to the averaged SH-V curve of the nanocrystalline electrode, only the plateau of maximum SH intensity is reached already by 0.8 V vs. RHE. Despite the similar behavior of the electrode average, locally the signal intensity and the shape of the SH-V curve vary dramatically on the polycrystalline electrode. Averaging obscures this variation. I visualize the locally varying SH-V behavior by plotting the SH-V curves of three pixels 1 - 3 (blue, red and green rectangles in panels A) - C)), each belonging to an area that has a distinctive SH-V behavior, for three consecutive CV cycles CV 1 - 3. Pixel 1 and 3 belong to neighboring areas with distinctive SH intensities and SH-V curves (the area of pixel 1 has a higher SH intensity), and pixel 2 lies on the border of these areas. The PR region is

[2]At the potential at which this potential impurity shows up in the reverse scan, 0.4 V vs. RHE, no changes to the SH-V curve occur that could be attributed to the impurity. Pt from the counter electrode might have plated on the fringe of the gold working electrode. This would explain why the CV, but not the optical data shows the impurity.

colored yellow, the OG region orange. In the PR, the SH intensity of P1 strongly increases with increasing bias, however, the SH intensity of P3 *decreases*. The signal intensity of P2 slightly increases. Contrarily, in the OG region all three pixels show a similar trend: SH signal intensity decreases. It perhaps is interesting to note that the SH-V curve of the entire forward scan of pixel 2 appears to be an intermediate of the curves of pixels 1 and 3 (note that pixel 2 lies on the border of the areas that are represented by pixels 1 and 3).

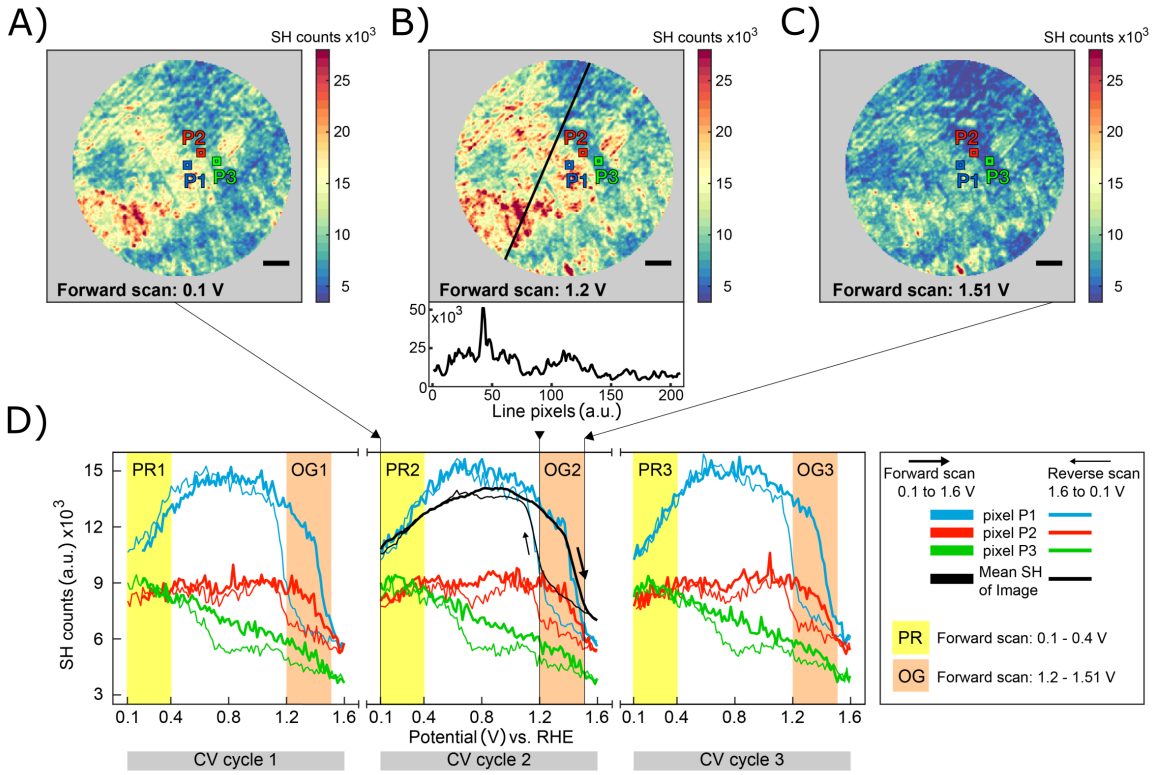

Figure 5.3: A), B) and C) show SH images of the polycrystalline Au sample at 0.1, 1.2 and 1.51 V vs. RHE during the forward scan of the CV (60 mV/s, 0.5 M NaH_2PO_4) and were recorded in the PPP polarization combination with an acquisition time of 0.25 s. The range of the color scale is identical to the one used in Figure 5.2 A). The black line in B) indicates the position of a line scan that is shown as intensity vs. line pixel below the panel. The scale bare measures 10 µm. In D) The SH-V behavior of three single pixels P1 - P3, that are marked in panels A) - C), is shown in three consecutive CV cycles 1 - 3. The black curve in the subpanel of CV cycle 2 corresponds to the average SH intensity of the entire FOV. The polarization region (PR, 0.1 - 0.4 V vs. RHE) is marked in yellow, the oxide growth region (OG, 1.2 - 1.51 V vs. RHE) is marked in orange.

For comparison, SH-V curves of three different pixels on the nanocrystalline sample can be found in appendix section B. There the SH intensity increases quadratically with linearly

increasing bias in the PR of all three pixels, implying that no local variations exist on the nanocrystalline sample.

Prior work clarifies that the efficacy of SH generation strongly depends on exposed surface crystallographic orientation (e.g., (111) facets have a SH-V behavior different from (110) facets) and the azimuthal orientation (with respect to the plane of incidence) of a given facet [187, 188]. This possibly is the origin of the difference in magnitude between, for example, the SH-V curve of pixel 1 and 3, but unlikely to explain why pixel 3 shows a decline in SH intensity inside the PR. This behavior will be discussed in detail below. It is noteworthy, that the SH-V behavior of pixels 1 - 3 is qualitatively similar in the OG region: the specifics of the surface that are known to influence SH generation in the PR, like surface crystallographic orientation, microscopic roughness and grain boundaries, do not dominate SH generation in the OG region.

The discussion above clarifies that disentangling all contributions to the SH signal is a formidable task even on well defined single crystals. Consequently, understanding the signal in detail on the polycrystalline sample, where the surface crystallographic orientation of the imaged metal grains is not known, is exceptionally challenging. Yet we can still extract useful information by fitting the SH-V curve of each pixel with the parabolic model described in section 3.2 (and recapped in the introduction to this section above) and by correlating changes to the SH images to CV features (like surface oxidation and reduction). I plot the results of fitting the SH-V curve of every pixel with equation 3.22 in Figure 5.4. It is perhaps useful to recall some aspects of the parabolic model: the parabolic model predicts that the SH intensity increases quadratically when tuning the potential around the PZC for $\chi^{(3)'} >> \chi^{(2)}$ as a consequence of increasing surface charge density and therefore the charge gradient at the interface. For a given PZC, the position of the parabola's minimum can shift if $\chi^{(2)}$ gets stronger relative to $\chi^{(3)'}$. We generally expect that $\chi^{(3)'} >> \chi^{(2)}$ holds, because the photon energy of the fundamental (1030 nm) in the experiment is not sufficient to excite interband transitions in gold [113]. However, as shown in Figure 5.4 D) and explained in detail below, for certain areas the $\chi^{(2)}$ contribution is relevant and the minimum of the parabola is shifted negative from the PZC.

Fitting of the SH-V curves provides us a with a quadratic (Q), linear (L) and constant (C) coefficient (with respect to applied potential) for every pixel in the PR (only here the premise of no specific ion adsorption is met). For this analysis the knowledge of the PZC is a prerequisite, which, for a given electrolyte, is dependent on the exposed surface structure. The electrode was prepared according to a procedure by Mariano et al. [13] that results in a surface exhibiting (111) and (110), but almost no (100) facets. For (111) and (110) Au single crystals a large spread in PZC values was reported [189, 190] and I have used an average value of 0.4 V vs. RHE for the analysis. The values reported in panels A), B), C) and D) of Figure 5.4 were calculated from the second CV cycle and therefore carry the index "2" (Q_2, L_2). The quadratic coefficient is plotted in A), the linear coefficient in B). While both maps look similar at first glance, large scale features with similar intensities (either bright, or dark) are more homogeneous in B) and display larger variations in A) (and the absolute values differ). In C) areas with $Q > 0$ are plotted in yellow and areas with $Q \leq 0$ are plotted in blue. $Q > 0$ areas account for 59.7 % of the total surface, while

$Q \leq 0$ areas account for 40.3 %. Areas with a negative Q value can be found in larger patches, as well as in smaller areas and spots. A negative Q value indicates that the SH intensity decreases quadratically with positively increasing potential, which implies that the increase in (positive) charge density due to the increasing potential is counteracted, possibly by anion adsorption[3]. This anion adsorption would screen the surface charge and lead to a reduction in SH emission. The physical origin of this decrease, however, is not entirely clear. It could, in principle, result from a charge inversion with increasingly positive potential due to the increasing adsorption of anions (without anion adsorption the surface would be charged increasingly positively). The degree to which anion adsorption actually leads to a negative charge on the surface is not trivial to answer, because the anions are partially discharged (charge flows along the external circuit to the counter electrode and can be measured) and part of the anions charge is stored in the bond that is formed with the electrode surface. This question of fractional discharge is discussed in detail in section 4.2. Anion adsorption at potentials cathodic of the PZC seems counterintuitive at first, but this could be the result of local PZCs [155] that are substantially lower than the average PZC I have chosen for the analysis. Anion adsorption can furthermore drive, or influence electrochemical processes in the PR below the PZC like surface reconstruction [50, 172, 173], or oxidation of metastable surface states. Such processes would also influence SH emission because of its sensitivity to surface structure. In this scenario the premiss of no specific anion adsorption is not met in $Q \leq 0$ areas and the parabolic model can not be applied there. For comparison, on the nanocrystalline sample almost no $Q \leq 0$ spots can be found, see appendix section B.

For the $Q > 0$ areas, the parabolic model is applicable and by plotting $Q/|L|$ in Figure 5.4 D), we gain insight into the spatial disctribution of $\chi^{(3)'}/\chi^{(2)}$. The absolute value of L is chosen for convenience so that no distinction between + and - L regions has to be made. In principle the L coefficient is related to the local PZC and consequently to ion sorption, but is influenced also by other factors such as local surface plasmon (LSP) excitation. Disentangling it's contributions is particularly complicated at $\pm$Q boundaries: there additional measurements, e.g., of the dependence of SH generation of the azimuthal orientation of the electrode at various potentials, may be necessary for a thorough understanding. I expect $Q/|L|$ to be in the range of 0 - 10 from measurements of $\chi^{(2)}$ and $\chi^{(3)}$ of Au[4] and find values ranging from 0 - 4. Values above 1 (79.35 % of the $Q > 0$ areas) are colored in yellow to red and values below 1 (20.65 % of the $Q > 0$ areas) are colored in blue. Pixels with $\chi^{(2)} > \chi^{(3)'}$ ($Q/|L| < 1$) tend to accumulate at the border of areas with distinctive SH-V behavior and particularly where areas with a negative Q value border areas with a positive Q value ($\pm$Q boundary): 20.65 % of the total pixels (in $Q > 0$ areas) have a Q/L ratio below one, 14.21 % of the total pixels in $Q > 0$ areas have a Q/L ratio below one and are

[3] A negative Q value can not be related to the relative sign of $\chi^{(2)}$ and $\chi^{(3)}$, because $Q = \chi^{(3)'}\chi^{(3)'*}$, meaning that it must reflect potential dependent sample chemistry. This is different for $L = \chi^{(2)}\chi^{(3)'*} + \chi^{(2)*}\chi^{(3)'}$, whose sign could be a material property.

[4] $\chi^{(2)}$ of Au at 1064 nm was reported to be around $2 \cdot 10^{-19}$ m/V [114] and for $\chi^{(3)}$ $2 - 7 \cdot 10^{-19}$ m/V was reported [191]. While $\chi^{(3)}$ is not the same as $\chi^{(3)'}$, they are typically considered to be of the same order of magnitude for a metal [113].

located at a ±Q boundary and 6.44 % lie elsewhere. On the contrary, areas with a Q/L ratio above one are more homogeneously distributed across the surface: 79.35 % of the total pixels in Q > 0 areas have a Q/L ratio above one, 40.68 % have a Q/L ratio above one and are located at a ±Q boundary and 38.67 % lie elsewhere.

In Q > 0 areas with a Q/L ratio above one ($\chi^{(3)\prime} > \chi^{(2)}$, 79.35 % of the respective pixels) the modulation of the SH emission as the potential is tuned is likely dominated by the increase in surface charge density. In Q > 0 areas with a Q/L ratio below one ($\chi^{(2)} > \chi^{(3)\prime}$, 20.65 % of the respective pixels) the surface term dominates and the SH emission is likely substantially intensified by excitation of a LSP (making the SHG process partially resonant) [113]. LSP excitation is generally not possible on a perfectly flat gold surface in a simple one-beam reflection experiment, but can be enabled through the presence of three-dimensional irregularities at the surface [192, 193]. The extension of these irregularities normal to the surface is no longer than a few µm (every part of the image is in focus) and likely below the resolution of the microscope. It is therefore likely that the areas with the highest $\chi^{(2)}$ contribution (Q/L below one) coincide with various defects like grain boundaries, scratches , or other areas with increased surface roughness. This is further corroborated by the propensity of pixels with a Q/L ratio below one to accumulate at grain boundaries (see above).

While the assumptions underlying the parabolic model are not met in Q < 0 areas (likely due to the adsorption of anions, see above argumentation), we can still obtain insight into local changes in between potential cycles. For this purpose I plot $Q_3/L_3 - Q_2/L_2$ (not differentiating between Q > 0 and Q < 0 areas) in Figure 5.4 E). A larger difference, positive or negative, indicates larger changes to the SH-V behavior in between cycles 2 and 3. Most of the changes from cycle to cycle occur at ±Q boundaries where also the largest differences between cycles are found. This means that the SH-V curves of pixels close to ±Q boundaries are more likely to change from cycle to cycle than others and change more strongly. I define a difference of larger than ±2 as threshold criterium for substantial changes to the surface and find that 40 % of the entire surface undergo such changes from cycle to cycle which coincides with the percentage of the surface covered with Q < 0 areas (40.3 %). Of the 40 % of total pixels that show a difference larger than ±2, 27 % are located at ±Q boundaries and 13 % are located somewhere else, highlighting that these boundaries are particularly prone to changes from one cycle to the next. Q > 0 areas appear to be more stable with respect to changes during potential cycling.

The $Q_3/L_3 - Q_2/L_2$ difference indicates changes to the surface structure by surface reconstruction as a consequence of oxidation and reduction. The coincidence of regions that show pronounced surface reconstruction from cycle to cycle with Q < 0 areas (for which I argued that anion adsorption is responsible for the decrease in SH intensity with increasing potential in the PR) suggests that anion adsorption may be responsible for, or at least increases, said inclination towards stronger surface reconstruction during potential cycling. Anion adsorption induced surface reconstruction has previously been observed by SHG on gold electrodes [187, 188, 194].

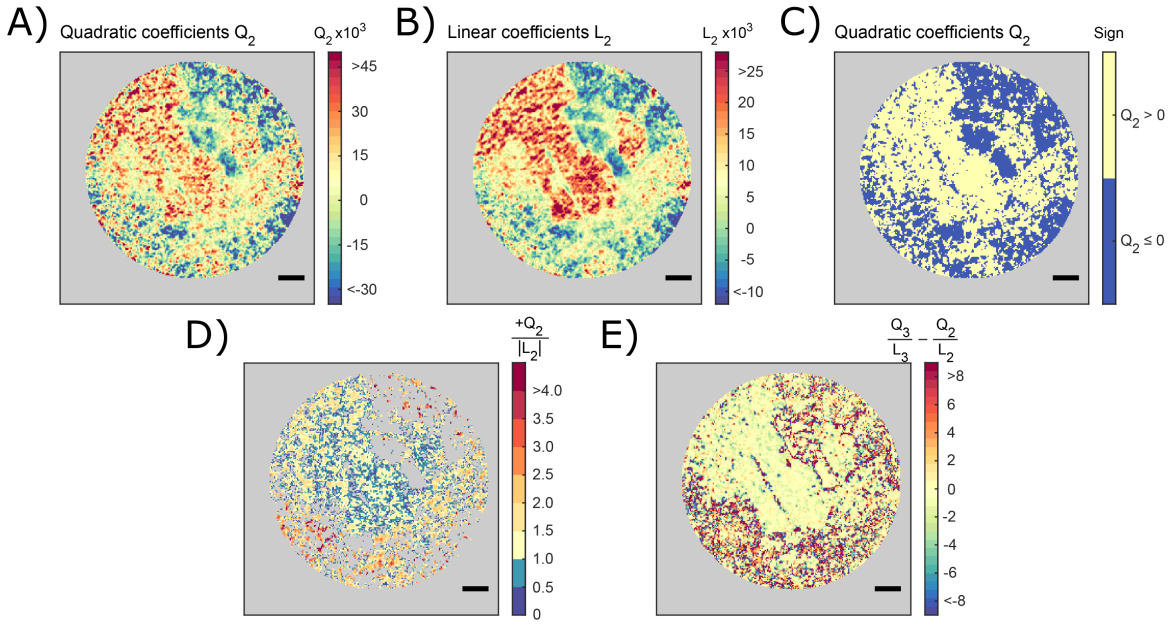

Figure 5.4: Fitting the SH-V curve (details of the measurement are described in the caption of Figure 5.3) at every pixel with the parabolic model and a PZC of 0.4 V vs. RHE. The index "2/3" denotes that the quantity was extracted from fitting of the second/third CV cycle in a series of three consecutive cycles. A) and B) show maps of the quadratic (Q) and linear (L) coefficients. C) shows a map of areas with Q $>$ 0 in yellow and areas with Q $<$ 0 in blue. D) shows a map of Q over the absolute of L for Q $>$ 0 areas. E) Q/L difference map of the third and second CV cycle. The scale bar measures 10 µm.

The previous discussion focussed on the parabolic model analyis, a physics based model that is only applicable in the PR where no specific ion adsorption occurs. Application of this model highlights potential dependent spatial correlations. Here I introduce a statistical way of accessing the same quantity at all other potentials (including regions where anion adsorption and other electrochemical processes occur) and in order to corroborate the conclusions from above. For this purpose I compare the SH-V curve of each individual pixel (*pix*) with the average SH-V curve of the entire FOV (*FOV*) by calculating their correlation coefficient:

$$Corrcoeff(pix, FOV) = \frac{cov(pix, FOV)}{\sigma_{pix}\sigma_{FOV}} \tag{5.3}$$

Here *cov(pix, FOV)* is the covariance of *pix* and *FOV* and σ_i denotes the standard deviation of *i*. The correlation coefficient is calculated for an arbitrary potential window and is a measure for the correlation of pix and FOV as a function of potential. It ranges from -1 to +1, where +1 indicates an ideal positive correlation between pix and FOV: a positive increase in pix is correlated with a positive increase in FOV. -1 signifies that pix

and FOV are anticorrelated: a positive increase in pix is correlated with a decrease in FOV. 0 signifies no correlation.

I take the SH-V curves (single pixel *pix* and average over the entire FOV *FOV*) from the three cyclic voltammetry cycles depicted in Figure 5.3 and plot the correlation coefficient for the full potential range (0.1 - 1.6 V vs. RHE) in Figure 5.5 A). Red signifies a strong positive correlation, blue anticorrelation. Strong correlation in the red areas implies SH-V curves similar to the FOV average (because these areas are the biggest and emit the strongest SH signal). The red areas coincide with the yellow Q $>$ 0 areas in Figure 5.4 C). On the contrary, in the blue areas the SH-V behavior is anticorrelated with the FOV average and those areas match well with the blue Q $<$ 0 areas in Figure 5.4 C).

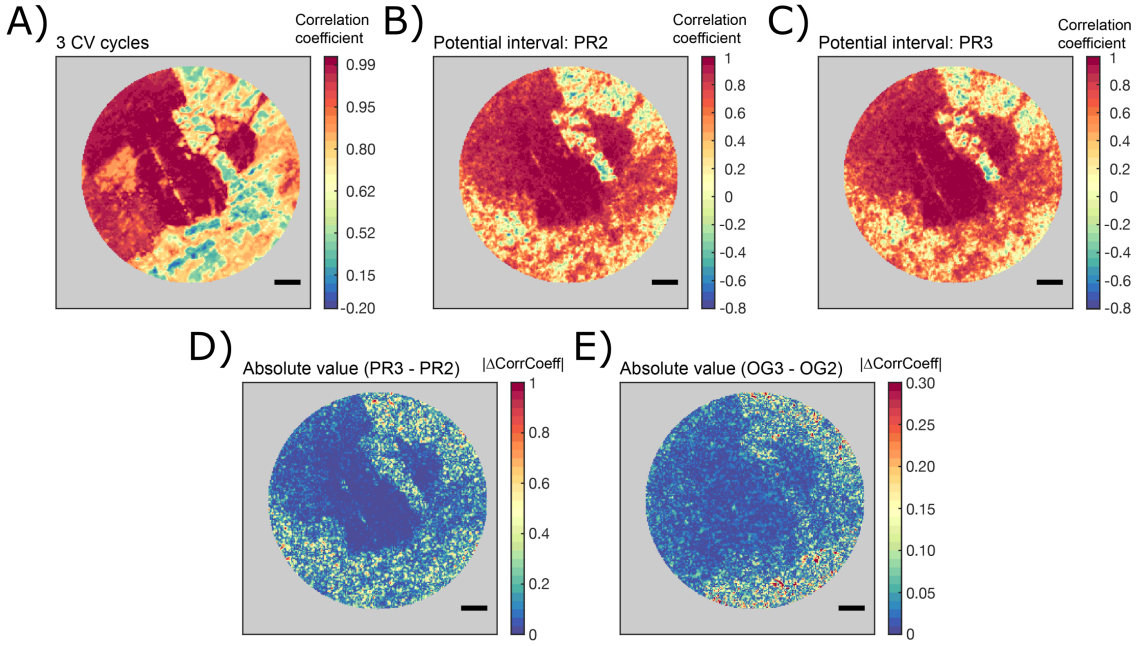

Figure 5.5: Results of the correlation coefficient analysis. A) shows a map of the correlation coefficient of the SH-V curve of every pixel with the FOV average for the three cyclic voltammetry cycles shown in Figure 5.3 (details of the optical measurement can be found in the corresponding figure caption). B) and C) map the correlation coefficient calculated from the PR regions of cycle 2 and 3, while in D) their difference is plotted. E) shows an analogous difference map, but calculated from the OG regions in cycle 2 and 3. The scale bar measures 10 µm.

I additionally performed the correlation coefficient analysis on the PR (0.1 - 0.4 V vs. RHE, little/no anion adsorption) and OG (1.2 - 1.51 V vs. RHE, oxidation of the first Au layer) potential regions to try to gain deeper insight into why, in the parabolic model analysis, areas at ±Q boundaries are more susceptible to surface reconstruction during potential cycling. Correlation coefficients were calculated in the second and third CV

cycle for both potential windows, the results for the PR in the second and third cycle are plotted in panel B) and C). The difference of the correlation coefficients in the third and second cycle, $\mid \Delta CorrCoeff \mid$, is plotted in panel D) and E) for the PR and OG region, respectively[5]. This metric allows for direct location of areas in which the SH-V behavior has changed from cycle to cycle (or remained the same). A large value of $\mid \Delta CorrCoeff \mid$ (PR3 - PR2) implies that the SH-V behavior in the PR has changed strongly from cycle two to cycle three, however, it does *not* imply that the changes to the surface structure that are responsible for the different SH-V behavior actually happened in the PR. The same is true for $\mid \Delta CorrCoeff \mid$ (OG3 - OG2).

Both the absolute values of $\mid \Delta CorrCoeff \mid$ and its spatial distribution differs in the PR vs. the OG region. The absolute value in the PR ranges from 0 to 1, while in the OG region it only ranges from 0 to 0.3. Clear large scale features with values close to 0, areas that do not change from cycle to cycle, resembling the Q > 0 areas in the parabolic model analysis (and presumably the grain structure of the surface), are apparent both in the PR and OG region. Similar large scale features with higher values, indicating changes from cycle to cycle, resembling the Q < 0 areas, are also apparent in both potential regions. However, these features are more clearly separable in the PR (higher contrast between areas with a $\mid \Delta CorrCoeff \mid$ close to 0 and those that have a higher $\mid \Delta CorrCoeff \mid$) and additionally appear as more homogeneous (the spread of $\mid \Delta CorrCoeff \mid$ values inside the respective areas is smaller). It is noteworthy that the spots with the highest $\mid \Delta CorrCoeff \mid$ values in both potential windows do not form extended areas and are rather isolated. More generally, areas with a $\mid \Delta CorrCoeff \mid$ value close to zero are more homogeneous in both potential windows than such with a higher value.

The absolute magnitudes of $\mid \Delta CorrCoeff \mid$ in the PR and OG region can not be directly compared, because the SH signal has different contributions in both regions. This is apparent from the discussion of Figure 5.3, where pixels 1 and 3 show opposite SH-V behaviors in the PR, but a similar behavior in the OG region. Put another way, the same changes to the surface structure could result in different $\mid \Delta CorrCoeff \mid$ values in the PR and OG region, because not all contributions to the SH are affected equally by this hypothetical change to the surface. However, we can discuss the *spatial extent* of $\mid \Delta CorrCoeff \mid$ in both potential regions. It is worth noting at this point that the surface was electrochemically annealed (repeated potential cycling between oxidizing and reducing potentials, 0.1 - 1.6 V vs. RHE, at 500 mV/s) before all measurements and should therefore be clean and free of nonequilibrated high surface energy sites (unless they are continuously produced by a bulk structural motif). For this purpose, I define a threshold for what is a substantial change from cycle to cycle by multiplying the error of $\mid \Delta CorrCoeff \mid$ (0.04 for the PR and 0.02 for the OG region, see appendix section B) by 2.5[6]. I find that 39.7

[5]Because I want to make meaningful statements about the difference of correlation coefficients in two successive potential cycles, I need to ensure that the reference curve (so far the FOV SH-V mean was used, but this may vary from cycle to cycle) does not change in between cycles. I therefore use a simple y = x line to calculate the correlation coefficients in both cycles.

[6]This value is chosen to be at least twice as large as the highest local fluctuations of the error. It is somewhat arbitrary and the size of the areas that are defined to experience a significant change would be

% of all pixels experience a change in $\mid \Delta CorrCoeff \mid > 0.1$ in the PR and that 22.7 % of all pixels experience a change in $\mid \Delta CorrCoeff \mid > 0.05$ in the OG region. Apparently, a larger fraction of the surface undergoes substantial changes in structure during one CV cycle, when the surface is at first metallic (when the cycle starts with PR2) and then gets oxidized and reduced again. A smaller fraction of the surface undergoes substantial changes in surface structure when the surface is at first oxidized (when the cycle starts with OG2) and then gets reduced and oxidized again. A different result in surface structure for the pathways reduced => oxidized => reduced (PR3 - PR2) vs. oxidized => reduced => oxidized (OG3 - OG2) appears resonable in light of prior studies using in situ STM and SHG that have demonstrated that oxidation and reduction affect surface structure differently [186, 172, 173].

For the nanocrystalline electrode, no significant surface reconstruction is apparent from the results of the correlation coefficient analysis, as expected from the results of the parabolic model analysis. $\mid \Delta CorrCoeff \mid$ values are close to zero in both potential windows and no spatial features are apparent, see appendix section B. I imagine two possible scenarios that explain the observation of no apparent surface reconstruction on the nanocrystalline sample: i) The surface reconstructs substantially on every grain and the SH-V behavior of every grain is altered, but the averaged SH-V behavior remains the same because the changes are averaged over the approximately 40 grains per pixel; ii) The nanocrystalline gold sample is more stable with respect to potential-induced surface reconstruction. The first option appears unlikely because the grains' shapes appear to be random (see appendix section B). For a random shape distribution (and with only about 40 grains/pixel) it would be surprising if the changes to the SH-V behavior of one grain due to potential-induced surface reconstruction would be entirely counteracted by another's. We are therefore left with a scenario in which the apparent stability with respect to potential-induced surface reconstruction of the nanocrystalline sample *actually is* due to higher stability. One possible explanation for this increased stability is the size of the grains that constitute the electrode: the 50 nm diameter particles can not support large scale defects like grain boundaries that show the largest changes in surface structure during potential cycling on the polycrystalline electrode, as demonstrated by Figure 5.4 E) and discussed below.

Comparing the correlation coefficient analysis in the PR with the results from the parabolic model analysis (Figure 5.4), it seems clear that areas with a high $\mid \Delta CorrCoeff \mid$ value (substantial changes in surface structure during potential cycling) coincide with areas that show a negative quadratic coefficient (the SH intensity decreases quadratically with linearly increasing potential in the PR) in Figure 5.4 C). 39.7 % of all pixels experience a change in $\mid \Delta CorrCoeff \mid > 0.1$ between PR2 and PR3, which coincides well with the fraction of the surface for which the quadratic coefficient is negative (40.3 %). The areas displaying the highest $\mid \Delta CorrCoeff \mid$ (PR3-PR2) value also match well with the areas that show the largest $Q_3/L_3 - Q_2/L_2$ difference in Figure 5.4 E). I take this to support the previous result that $Q < 0$ areas are particularly prone to surface reconstruction during

smaller if a higher value was chosen.

potential cycling due to electrochemical reactivity likely involving anion adsorption.

In the next subsection I will investigate spatial heterogeneity in OER activity on the same poly- and nanocrystalline Au electrodes (at different locations, however) at more anodic potentials. From the results and discussion of this subsection we might expect that activity is localized at areas with a negative quadratic coefficient, either at the boundaries to areas with a positive quadratic coefficient (±Q boundaries), or at the isolated spots with the highest $\mid \Delta CorrCoeff \mid$ values.

5.1.2 Imaging the OER Activity on Gold Electrodes *Operando*: It is Highly Local

The results and discussion of this section have been published in reference [33] by Zwaschka et al.

For the investigation of the OER on Au, I examined a polycrystalline gold foil working electrode in 0.5 M Na_2HPO_4 (to ensure stable conditions throughout the optical measurements), pH = 9, and collected SH micrographs while conducting linear sweep voltammetry from 1.8 - 2.2 V vs. RHE. The range of the sweep was chosen to start well before oxygen evolution commences (at 2.0 V vs. RHE [156]) and to end at a potential where oxygen evolution is fast enough to produce macroscopic O_2 bubbles (as showcased in Figure 5.6) whose growth rate allows real-time imaging of bubble growth and detachment (given the 0.25 seconds necessary to acquire an image at sufficient signal/noise). The potential sweep is displayed from 1.9 V on in the lower panel of Figure 5.7 in red. In the SH micrographs, structural heterogeneity with a length scale of 10 – 50 µm is apparent if the potential is kept below the oxidation threshold, and as in section 5.1.1 above, I attribute this to the metal's grain structure, as supported by scanning electron micrographs (see appendix section B).

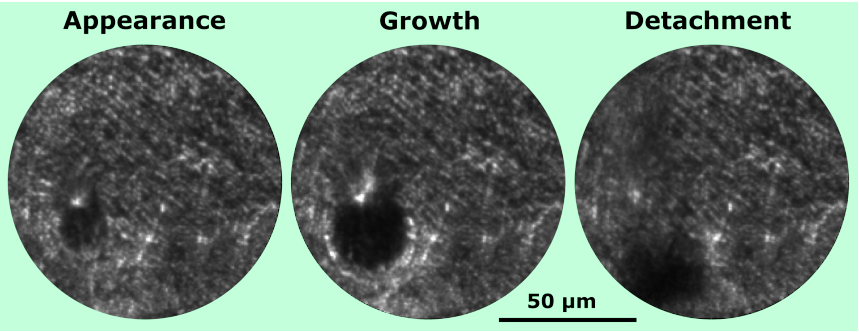

Figure 5.6: Life-cycle of an oxygen bubble imaged by SHM in ppp polarization combination: (left to right) appearance, growth and detachment as observed. White (black) indicates higher (lower) SH intensity.

At potentials above oxidation, the different domains can no longer be distinguished clearly and SHM images appear almost featureless, as shown for 1.8 V in the top panel of

Figure 5.7. However, as the potential is scanned increasingly positively bubbles appear, grow and detach from the electrode. On the top left of Figure 5.7, the entire field of view is displayed as a grayscale image with red dots indicating sites of O_2 bubble formation above 2.0 V vs. RHE. The half width at half maximum spatial resolution of the microscope is 188 nm [169]. I approximate the site of bubble formation, i.e. determine where to plot the red dots, by examining the first frame in which a spherical bubble could be clearly discerned from the background and taking the centre of the circle as the bubble nucleation site (red dot). The average bubble radius at this point was about 3 µm (a detailed discussion of the nucleation radius of a bubble can be found in appendix section B). As is apparent from Figure 5.7, the vast majority of bubbles appear within a highly confined *active area* encircled in purple.

As is evident from the figure, in a single potential sweep at some spots only a single bubble appeared, while in others multiple appeared either in direct succession or with a pause in between. In addition, with increasing potential, oxygen bubbles start to appear at more spots. Inspection of the data in Figure 5.7 clarifies that the first bubble I observe is 0.07 V higher in potential than the onset of the OER at 2 V vs. RHE. This offset can be rationalized if the low current densities close to the onset potential indicate an O_2 formation rate insufficient to locally supersaturate the electrolyte with O_2 (which is a prerequisite for bubble nucleation).

While the series of SH micrographs shows that bubble appearance is strongly localized, they do not demonstrate whether activity is localised: whether the current flow necessary to explain bubble production is a significant portion of the measured current flow through the whole electrode. To make this comparison I estimate the number of O_2 molecules necessary to explain the observed bubbles by measuring the diameter of each bubble in the frame that it detaches from the surface, assuming the bubble is formed of 1 atm of O_2 and using the ideal gas law. I then compare this estimated bubble related current to the current expected to flow through the FOV based on measurement of the whole electrode. If the current necessary to produce the observed O_2 bubbles is large with respect to that expected based on measured current over the whole electrode and the size of the FOV it suggests that O_2 generation that does not result in bubble formation and Au oxidation do not contribute significantly to measured electrode current. For the results shown in Figure 5.7 this condition is clearly met: under these conditions for the series of micrographs shown in the main panel, inset A and inset B, the current required to generate the bubbles is 188, 195 and 134 % of the current expected to flow through an area the size of the FOV, respectively. Clearly, under the conditions of this linear sweep voltammetry, current flow is dominated by electrochemical oxygen evolution resulting in bubble formation.

The local, high, density of sites at which oxygen bubbles appear can be rationalized either as the result of transport or of chemistry: I observe *either* an active area for bubble nucleation from a neighbouring electrolyte supersaturated in O_2 *or* an active area for O_2 generation. As shown in detail in appendix section B, the high time resolution of the experiment allows me to finely resolve bubble growth rate and to show that its time dependence is incompatible with a diffusion limited scenario (growth rate does not scale with bubble surface area). The fact that bubble growth rate is independent of bubble

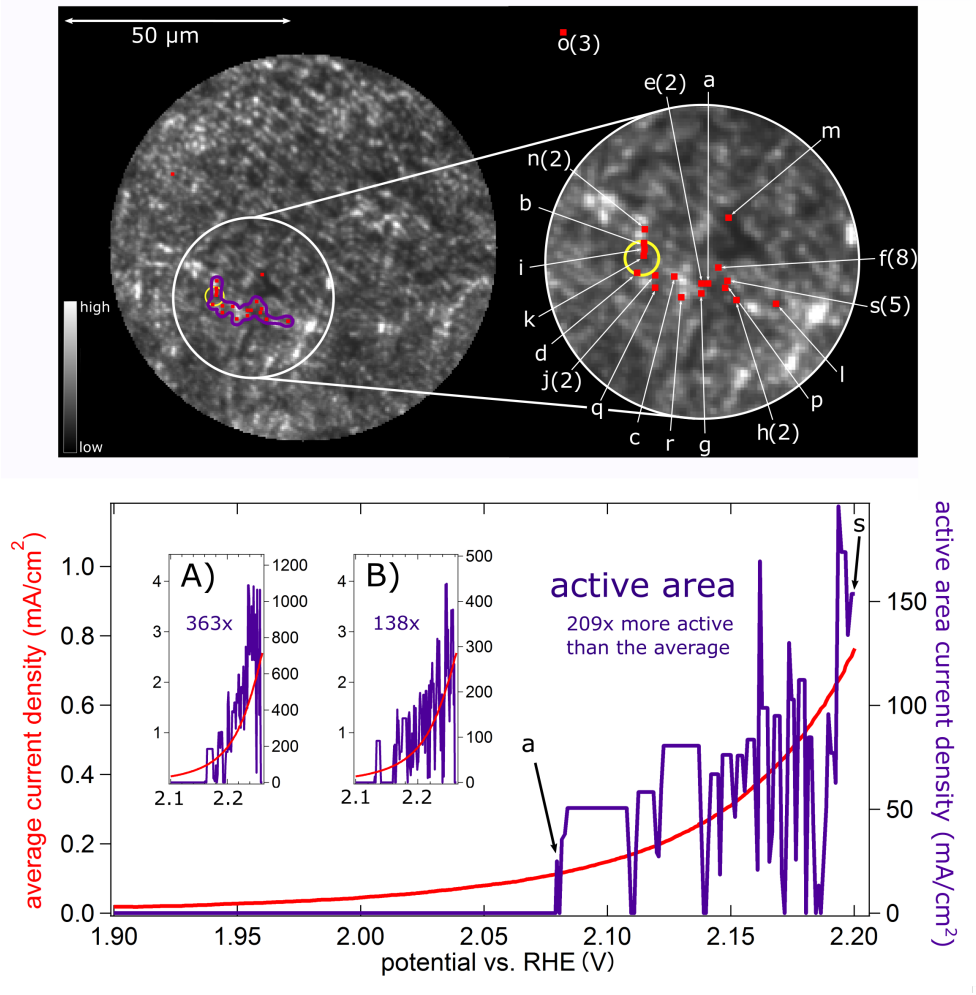

Figure 5.7: Top left panel: circular FOV of the electrode at 1.8 V vs. RHE in our SH microscope. As shown in the scale bar, white (black) indicates high (low) SH intensity. Red dots indicate sites at which O_2 bubbles nucleated during the linear potential sweep shown in the bottom panel. On the top right a magnified excerpt is shown that contains nearly all nucleation sites/red dots. The letters assigned to the dots designate the order in which bubbles appeared from the respective spots during the potential sweep. The number in brackets denotes the amount of O_2 bubbles that emerged from each site. The yellow circle denotes the area from which the first O_2 bubbles emerged when repeating the experiment after potential cycling. The bottom panel shows the current density of the average electrode (in red) and the active area (in purple, calculated as discussed in the text) as a function of potential during a linear sweep from 1.9 to 2.2 V vs. RHE with a sweep rate of 1 mV/s. 'a/s' denotes the first/last bubble, as in the top right panel. Insets A) and B) show comparable current density vs. potential plots for two more spots on the same surface that were the sole active areas in different FOVs during repeated experiments. The electrolyte was 0.5 M Na_2HPO_4.

surface area suggests that, for bubbles of radius 3 µm and larger, the O_2 responsible for bubble growth is produced *locally*: the observed active areas on the µm length scale are active with respect to O_2 generation.

Much prior work suggests that the bubbles observed nucleate at length scales much smaller than those accessible in the microscope. For example, White and coworkers have extensively studied electrochemically generated *nanobubbles* of H_2, N_2 and O_2, on Pt nanoelectrodes, and microelectrodes in confinement [195, 196, 197, 198]. These studies suggest that, on the *nano*electrodes, bubble nucleation occurs with a critical size as small as 4-5 nm [199] and is driven by a strong supersaturation of the electrolyte close to the electrode with the respective gas (up to 300 times larger than the saturation concentration under standard conditions [200]) rather than local differences in activity. Work by others suggests that the necessary degree of supersaturation is extremely sensitive to details of the surface. For larger Pt microelectrodes reported supersaturation values for nucleation ranged from 1.5 to 24× standard saturation concentration [201, 202]. For other surfaces the formation of surface nanobubbles without supersaturation of the electrolyte with gas has been reported [203, 204].

Clearly the 4-5 nm length scale of bubble nucleation is not observable in the SH microscope and thus it is difficult to draw conclusions about the nucleation and growth mechanism on these length scales. However, these results are consistent with a scenario in which the nucleation of O_2 bubbles occurs inside of nanopores in the surface that enable local supersaturation of the electrolyte with O_2 even at minute current densities (e.g. 0.11 mA/cm^2 during the observation of bubble A in Figure 5.7), or one in which on the macroscopic electrode a much lower supersaturation is required due to heterogeneous nucleation at structural motifs that are active sites with respect to bubble nucleation and are larger than the electrodes used by White et al., e.g., grain boundaries. Regardless of the mechanism of bubble nucleation, however, as soon as bubbles are large enough to be observed in the microscope, I find bubble growth to be driven not by mass transport from solution via diffusion, but by local electrochemical O_2 evolution.

To quantify the reactivity of these *active areas* with respect to the OER a current density is required. For this purpose, I calculate the current necessary to explain the observed bubble formation as described above and obtain a current density by dividing it by the geometric surface area of the active area, 69.9 $µm^2$ in the case of the data shown in the main panel of Figure 5.7 (see appendix section B for a detailed description of the calculation of the surface area and the sensitivity of the results to the method I employed). The resulting current density is plotted in the lower graph as a purple curve starting with **a** around 2.07 V vs. RHE and is denoted "active area current density". Its increase with potential correlates well with the potential dependent behaviour of the average electrode (red curve), but its current density is significantly higher. Integrating the current density from the active area over the course of the experiment (from **a** - **s**) and comparing it to the integrated current density of the entire electrode (during the same period), I find that the active area's charge density is 209× higher than the electrode average. The similarity of the change in current density with potential of the active area and measured electrochemical current density is shown for two more spots in different positions of the electrode, monitored

individually by SHM in repeated experiments, as insets. The integrated current densities of the active areas corresponding to the two insets are 363 (A) and 138 (B) times higher than the electrode average[7]. Assuming that the FOVs I measure are representative of the electrode as a whole, the active areas in Figure 5.7 are 138 to 363 times more active than the electrode average and the measured current results from 0.28-0.72 % of the area of the electrode.

While the molecular level structure of an active site is substrate and reaction dependent for both electro- and gas phase catalysis, the estimate for the fractional coverage of the surface with active areas compares well with active site coverages from gas phase catalysis studies, but is considerably lower than ex-situ estimates of active site coverages in electrocatalytic systems. Studies of gas phase catalysis, e.g. the catalytic dissociation of NO [205] and N_2 [206] on well defined single crystals and propene metathesis on less well defined metal oxides [207], find active site coverages of 1-2 %. The similarity of these estimates to the 0.28-0.72% active area in this experiment is consistent with the conclusion that I observe active sites for O_2 generation. In contrast, previous estimates for the fraction of active sites on Au electrocatalysts for hydrogen evolution, determined from the spontaneous deposition of Ag, Pd and Pt at active sites to poison the surface, find 5 [208, 209] to 7 [210] % of the surface to be active. In part these differences in active site coverage may be the result of the means of characterization: while in the electrocatalysis studies active site coverage was determined by ex-situ methods, both in this and the metathesis study active site coverages were determined operando. Prior work, much of it on gas-phase catalytic chemistry, has emphasised the importance of active site characterisation operando because active sites evolve [211, 212] or even only appear [167] under reaction conditions. As described above, prior work characterizing active site abundances in electrocatalysis is largely either indirect, i.e. inferred from current voltage measurements of well-defined single crystal surfaces, or ex-situ, i.e. measured by mass spectrometry of adsorbed metal offline. The SH imaging of active sites overcomes both of these shortcomings.

Correlation coefficient analysis from 1.5 - 1.9 V vs. RHE reveals that the active areas mostly lie on the border of regions that perform like the average FOV in this potential window and areas that perform different from this average, see appendix section B (in the previous section I showed that these areas are particularly prone to potential-induced surface reconstruction, see Figures 5.5 and 5.3). This appears to be a necessary, but not sufficient condition to explain the outstanding activity of the active areas: such borders exist across the entire FOV, yet active areas only appear on a small fraction of these borders.

Having observed an active area for electrochemical oxygen production and O_2 bubble formation I next investigated this area's stability. As has been demonstrated by prior authors in a variety of electrochemical STM studies, cycling the bias across an Au electrode between 0 and 1.7 V vs. RHE, i.e. repeatedly oxidizing and reducing the surface, results in surface reconstruction [172]. While the extent of reconstruction is a function of scan rate and time spent at oxidizing potentials, current features that persist after such cycling are

[7]The area that was used to calculate the charge density was 72.8 µm^2 for A and 38.7 µm^2 for B.

presumably related to structural motifs that are insensitive to surface reconstruction. Put another way, if the activity of the active area was the result of a specific arrangement of surface atoms only, one might expect that that the active area for bubble generation would shift with every oxidation/reduction cycle. Repeating the experiment after restructuring the electrode surface yields bubble growth from the same active area: the yellow ring shown in the upper panel of Figure 5.7. Given that O_2 bubble formation only starts close to 2.1 V vs. RHE, the data are thus consistent with a scenario in which highly active sites for the OER on this intermediate complexity Au electrode are the result of an oxidized structural defect penetrating into the bulk.

The polycrystalline Au foil makes validation of this conclusion challenging: it is not accessible from the SH micrographs how deeply this structural feature might penetrate and, as discussed above, I expect the structural character of the active area is likely to change under ex-situ conditions (where, for example, one might imagine investigating the depth dependent electrode structure by focussed ion beam milling and subsequent scanning/transmission electron microscopy). Instead, I approach this problem from the sample side. That is, I also examined a gold electrode obtained by physical vapour deposition of gold on an optically smooth glass surface. This electrode is mirror smooth and comprised of about 50 nm big clusters (see appendix section B for an scanning electron micrograph of the as-prepared sample). After positioning the microscope FOV over a surface defect I ramped the bias from 0 - 2.3 V vs. RHE with a scanning speed of 60 mV/s and then held it at 2.3 V for two minutes. The FOV including the defect is shown in the top left, a view of the forming bubble on the upper right, and the measured current (inferred from the microscope FOV and the area of the working electrode) and integrated SH intensity both on and off the defect on the lower half of Figure 5.8.

The measured current clarifies that scanning the bias from 0 - 2.3 V vs. RHE produces the expected oxidation current feature at 1.5 V: from an electrochemical point of view the surface is clearly oxidized when it reaches 2.3 V. The upper half of the lower panel of Figure 5.8 shows the average SH intensity per pixel for areas on and away from the "defect". Two characteristics of these curves are evident from inspection: (a) both increase up to the oxidation current peak and decrease rapidly thereafter and (b) the SH intensity on the defect appears to be offset positively from that in the surroundings. Both observations are consistent with previous literature and the results and discussion of the previous section 5.1.1: for a wide variety of Au electrodes and electrolytes SH intensity has been observed to increase with increasing potential up to oxidation and decrease thereafter [113, 186], while, at a given potential, SH intensity on Au has been found to be a function of surface structure and even azimuthal angle for a given surface structure [213]. It is worth emphasising that, because SHG intensity is a sensitive probe of surface dielectric function, the qualitatively identical change in SHG intensity with potential on and off the defect during the linear sweep strongly suggests the defect is composed of Au and not a contaminant.

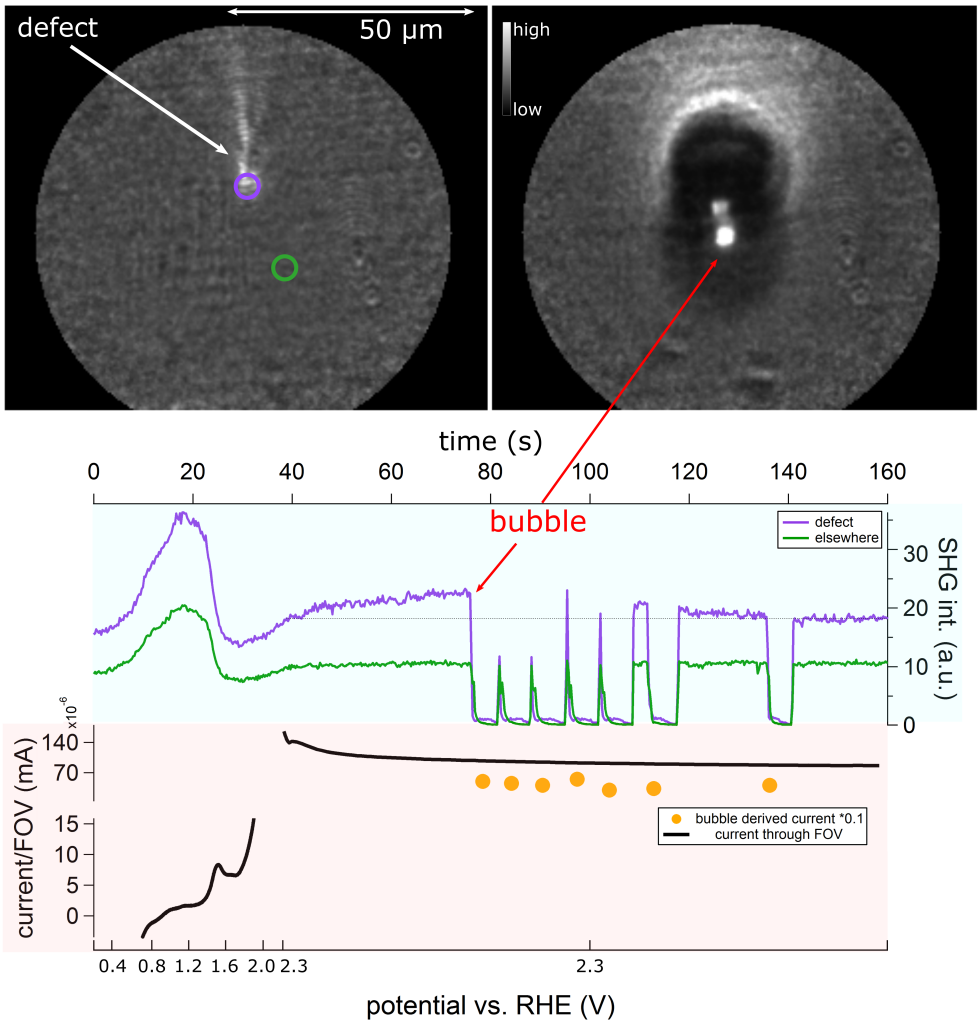

Figure 5.8: The top left panel shows the circular FOV of a physical vapor deposited gold electrode at 2.3 V vs. RHE, including a defect, as observed within the SH microscope. The same view is shown on the right including an oxygen bubble forming from the defect. As shown on the scale bar, white (black) indicates high (low) SH intensity. The lower half of the bottom panel shows the current passed through the FOV (calculated from the size of the FOV vs. the geometric area of the electrode) during the linear potential sweep up to 2.3 V and the potentiostatic experiment at 2.3 V in black together with the current that is passed in order to form bubbles after 75 s in gold (dots). The upper half of the lower panel shows the SH intensity on and away from the defect. The scanning speed of the linear sweep was 60 mV/s and 0.5 M Na_2HPO_4 was used as electrolyte.

As shown in Figure 5.8, after the bias reaches 2.3 V vs. RHE the sample was kept under potentiostatic conditions. Under these conditions the measured current was constant, the integrated I_{SH} off the defect was also constant and that on the defect slowly increased. While understanding this potential-induced change in local SH contrast is challenging,

the different behaviour is most easily rationalised if under these electrochemical conditions local structure near the defect continues to evolve while that away from the defect is stable. Thirty six seconds after the potential has been fixed at 2.3 V vs. RHE, bubbles start to emerge at the defect. As these bubbles grow, detach and diffuse out of the field of view the local SH signal decreases due to scattering and then recovers as the bubble moves out of site. The frame in which the first bubble detaches is shown in the top right of Figure 5.8. The first five bubbles emerge from the defect in rapid succession with no waiting period in between. Between bubbles five and six there is a waiting period of $\approx$ 5 s. Between bubbles six and seven this waiting period grows to almost 20 s. The SH intensity on the defect during the waiting periods and after bubble seven is decreased with respect to its value before the first bubble. The current passed in order to create the bubbles is shown as golden dots in the lower panel with the current passed through the FOV as reference in black. As expected for these potentiostatic conditions, the current is approximately constant. In contrast to the polycrystalline Au electrode shown in Figure 5.7 here the bubble estimated current exceeds the expected current for an area the size of the FOV (based on the measured current from the whole electrode) by 10$\times$ (bubble derived current is scaled by 0.1$\times$ to fit on the same plot). This result can be rationalized by noting that these defects are relatively uncommon on the PVD sample, i.e. the great majority of FOVs I observed did not have them, and thus the FOV showing the data in Figure 5.8 is not representative of the electrode as a whole.

The increase in waiting time and the decrease of the signal intensity on the defect after the fifth bubble is consistent with a scenario in which the structure of the active area evolves and its reactivity decreases under OER conditions. The former conclusion is consistent with the results of much prior work (although only through indirect means at solid/liquid interfaces): catalyst active sites are dynamic under reaction conditions [211, 212, 214]. I rationalize the apparent decrease in reactivity by noting that the OER on Au is known to occur on an increasingly oxidized surface and the thermodynamic driving force for O_2 generation by disproportionation of the metal oxide lattice is larger than that of the splitting of water itself [178]. Together with the prior observation that metal corrosion accompanies the OER [215], the data displayed in Figure 5.8 are thus consistent with a scenario in which the OER at 2.3 V consumes catalytically active, partially oxidized, Au cations more quickly than they are created.

I also observed a second type of dynamic active area behaviour qualitatively different from that shown in Figure 5.7 on the polycrystalline Au electrodes. This type of active area differs from that described previously in two ways: (i) they are sites at which oxygen bubbles appear at potentials lower than 2 V vs. RHE and (ii) they disappear after potential cycling (presumably they are not stable with respect to potential-induced surface reconstruction). A representative series of experiments is shown in the left panel of Figure 5.9. Here repeated CVs were collected, using the polycrystalline electrode of Figure 5.7 but monitoring a different spot with SHM, between a lower limit of 0 V vs. RHE and an upper limit that started at 1.6 V and increased to 2.05 V in steps of 0.15 V. In experiment 1), for example, an O_2 bubble was produced in the penultimate cycle at 1.9 V and in the last cycle at 2.05 V. The potentials at which bubbles were produced are marked in the respective

voltammogram by stars that have a separate colour for each experiment. In experiment 2, a bubble was only produced at 2.05 V. Experiment 3 and following cyclic voltammetry experiments did not yield bubble growth at all. On the right of Figure 5.9, the production of a bubble in experiment 1 is shown together with stars in red and turquoise that indicate the location of bubble appearance/nucleation. This behaviour is unexpected, prior empirical work [156], and my findings discussed above, suggest that O_2 should be generated on polycrystalline Au only anodic of 2 V vs. RHE. The observation of O_2 bubble formation under conditions in which the electrode as a whole is clearly *not* active with respect to the OER is most easily understood if the areas indicated are highly active with respect to electrochemical O_2 production. That is, the observation of bubbles forming on these sorts of *dynamic* active areas is extremely unlikely to be the result of just bubble nucleation from a supersaturated solution.

In chronoamperometric experiments analogous to the experiments shown in Figure 5.8, but at a potential of 1.9 V vs. RHE (i.e. also before the expected onset of the OER), formation of a single bubble per experiment was observed in two successive experiments, but not subsequently. The bubbles formed in the chronoamperometric and cyclic voltammetry experiments originated from spots that lie outside the active area of Figure 5.7. Corresponding SH count vs. time curves, that show the signature of bubble formation during chronoamperometry and cyclic voltammetry, can be found in appendix section B.

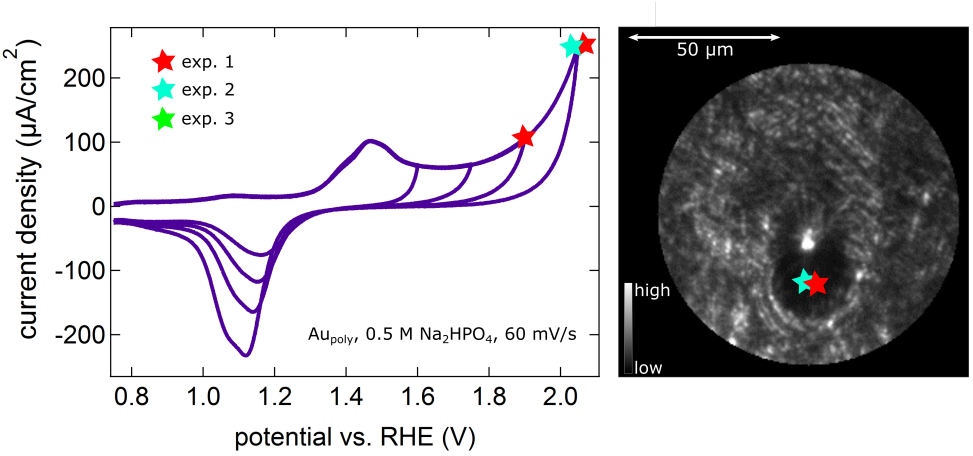

Figure 5.9: Left panel: cyclic voltammograms collected in three separate experiments on the polycrystalline Au electrode also used in Figure 5.7. In each experiment four CVs are collected in order: 0 - 1.6, 0 - 1.75, 0 - 1.9 and 0 - 2.05 V vs. RHE. For all CVs the scan rate was 60 mV/s and 0.5 M Na_2HPO_4, pH = 9, was used as electrolyte. The right panel shows the formation of a bubble during the experiment. The SH micrograph shown was collected during experiment 1 at 1.9 V vs. RHE. The nucleation sites during experiment one and two are shown as coloured stars. The FOV was different from the three fields of view summed up in Figure 5.7.

Given the body of prior work discussed earlier, and the results shown in Figure 5.7 and 5.8, Au oxidation is clearly a prerequisite to O_2 evolution. The metasable active sites

shown in Figure 5.9 are consistent with a scenario in which high energy, high reactivity sites exist on the polycrystalline Au that are oxidized, and begin to emit O_2, at potentials cathodic of O_2 evolution observed by both me and others on more homogenous surfaces [156]. Because these sites appear to be largely removed on voltammetric cycling, such defects are likely surface bound. Oxygen evolution from such transient surface sites, 200 mv before the regular onset of the OER, has previously been observed, indirectly, by Burke et al. [216].

Despite being the noblest of metals and relatively inert with respect to chemisorption, Au electrodes show surprising activity in a variety of oxidation and reduction reactions [179]. Burke and coworkers hypothesized that this activity could be explained by he presence of surface bound undercoordinated metal species (adatoms, clusters) that are oxidized at potentials substantially below that of the bulk metal. The result of this premonolayer oxidation, a minority species called "incipient hydrous oxide", is argued to be the catalytically active entity of Au, and noble metal electrodes in general, for a wide variety of different reactions [217]. In order to correlate the presence of the incipient hydrous oxide with catalytic activity, electrode pretreatment protocols to increase the abundance of this minority species (until they were no longer a minority species) were invented that allowed these authors to observe anodic features in the bilayer region of the *first* CV scan which were assigned to the formation of the incipient hydrous oxide (which is structurally distinct from α- and β-oxide) [218, 219]. Surfaces with stronger anodic features in the bilayer region showed an increased catalytic activity. Taken together these experiments suggested what Burke and coworkers termed an "Incipient Hydrous Oxide/Adatom Mediator" (IHO/AM) model of noble metal electrocatalysis. Such a pretreatment also significantly enhanced the oxygen gas evolution from transient sites at around 1.8 V vs. RHE [216], linking the IHO/AM model also to fully oxidized surfaces and the OER. This correlation can be rationalized by asserting either the incipient hydrous oxide persists at higher potentials on an oxidized surface, or the surface structure that produces the adatom (that is oxidized to form the incipient hydrous oxide) becomes catalytically active when oxidized or produces a catalytically active oxide at higher potentials.

As noted above, the approach of Burke and coworkers to characterize this "incipient hydrous oxide" was indirect: the electrode structure was perturbed sufficiently such that a minority species becomes a majority and the presence of this species is apparent in electrochemical observables. This approach greatly complicates insight into what the high energy sites actually are, or which underlying structure produces them. The imaging approach presented here circumvents this problem by virtue of its local character: I characterize the transient reactivity of surface species with extremely low coverage. In the case of the first produced bubble in experiment 1 of Figure 5.9, the current at 1.9 V vs. RHE is on the same level as for the monolayer oxidation and no oxygen evolution would be expected, yet local oxygen production can be detected. The production of a bubble under conditions in which no clearly assignable OER current is apparent from voltammetry is consistent with the presence of such transient strongly catalytically active sites on this electrode.

5.2 Switching Oxidation States of Pt *Operando* with near-IR Femtosecond Radiation: High Valent Oxides do not Catalyze the OER

The last section was concerned with spatial confinement of OER activity and its local characterization with SHM. The two distinct types of active sites that were observed are likely structurally *and* electronically different from the remainder of the surface. The electronic structure is a direct function of the atomic structure (and composition), which in turn is influenced by the valence of the metal cation in the oxide. The valence of the metal ion was found to play a major role in OER activity [220]. In this section, I aim to manipulate the oxidation state of a Pt electrode operando with pulsed, ultrashort near-IR radiation to investigate the effect it has on OER activity. The reported results are consistent with a scenario in which higher oxidation states of Pt (+IV/+VI) are not OER active.

The oxygen aqueous electrochemistry of Pt plays a critical role in both PEM fuel cells and electrolyzers. As for gold (discussed above in sections 5.1.1 and 5.1.2), the oxidation of Pt is known to be a prerequisite for the OER [156] but the mechanistic link between these processes is unclear. A detailed understanding of Pt oxidation, the resulting oxide and their link to the OER at more anodic potentials would accelerate our journey towards a sustainable energy economy.

Despite decades of study, no general consensus exists on the nature of the oxide and its formation mechanism. This is possibly because it is a surface structure sensitive process [221, 222] that at the same time changes the structure of the surface [223, 224, 225]. As perhaps expected for a surface structure sensitive process, the oxidation (onset potential, likely also rate and extent) of Pt clusters is a function of their size [226, 227]. Additionally, the pH and electrolyte composition (anions *and* cations) also strongly affects surface oxidation [228, 34, 229, 230, 51].

Several conceptual pathways for Pt oxidation have been proposed that assume different growth mechanisms and morphologies of the two and three dimensional oxide [231, 232, 233, 234, 235, 236]; the seemingly best received mechanism, originally proposed by Bockris and coworkers [231], is the place exchange [224] and consists of the following steps with increasingly anodic potentials: i) water discharge and the formation of a monolayer of surface platinum oxygen species; ii) site exchange of the oxygen species and Pt atoms to form a three dimensional oxide (possibly after a transformation of surface hydroxide to oxide); iii) growth of the three dimensional oxide and possibly change of oxidation state.

The most widely employed method to learn about Pt surface oxidation, reduction and how these processes are affected by electrolyte composition and surface structure is cyclic voltammetry. Figure 5.10 shows a typical CV of a Pt microelectrode with a radius of 50 micrometer in a spectroelectrochemical cell and highlights the most important surface processes. Going positive in potential from 0.5 V vs. RHE, surface oxide formation starts slightly before 0.8 V and continues until the potential is reversed and the surface oxide is reduced. The oxide formation is an electrochemically irreversible process (this is slightly

different from the conventional chemical definition of "irreversible", see section 2.1 for an explanation), which is reflected in the potential difference of the reduction peak (ca. 0.8 V vs. RHE) in the reverse scan and surface oxidation.

In step i) of the Bockris et. al model, water discharge is considered to result in the formation of a PtOH adlayer and the desorption of previously adsorbed anions. It starts as early as 0.1 V vs. RHE on Pt(110) [123] (and consequently on polycrystalline Pt), but only at ca. 0.6 V vs. RHE on Pt(111) [237]. This steps dependence on surface structure manifests itself for Pt clusters in a particle diameter dependent onset potential [227]. Contrary to the belief that the first step of water discharge results in a hydroxy adlayer, for polycrystalline Pt the direct formation of PtO was suggested on the basis of quartz crystal balance measurements mostly by Jerkiewicz and coworkers [238, 239, 240, 241].

In step ii) the surface hydroxide undergoes a place exchange with Pt atoms and forms a three dimensional (hydr)oxide. This process starts around 1.05 V at typical scan rates [242] in the absence of dissolved molecular oxygen, but was found to start at considerably less anodic potentials in its presence [243]. On Pt(111), this process is fully reversible as long as less than 15 % of the top most Pt atoms participate. If more surface atoms participate the process becomes irreversible and a metal structure different from (111) is recovered after reduction [244]. It has both been suggested that the place exchange happens before and after the OH is transformed to O. For polycrystalline Pt, Bockris and coworkers proposed that the place exchange precedes the deprotonation of the hydroxide to the oxide [231], whereas the opposite has also been suggested [242]. Recent theoretical studies provide insight into the mechanism of this place exchange on Pt(111): with increasing oxygen coverage the metal surface starts to buckle and at a critical coverage Pt atoms are extracted. This extraction is facilitated by increasing solvation of the Pt atoms as they move out of the surface. After a Pt atom has been pulled out of the surface, oxygen can move into the subsurface and oxidation into the bulk commences [245, 246]. Based on shell-isolated nanoparticle-enhanced Raman spectroscopy (SHINERS) of Pt(111) during electrooxidation, Koper et. al proposed that the surface hydroxide is transformed into a mixed two dimensional (su)peroxo Pt surface oxide around 1 V vs. RHE, before the formation of three dimensional oxide starts at 1.3 V [222]. At this state the metal cations of the oxide are typically assumed to have oxidation state +II.

In step iii) the three dimensional oxide grows with time and increasing potential [247, 240] and, at least partially, platinum ions oxidize from the +2 to the +4 state [248, 240, 249, 250, 222, 236, 251]. The nature of the growing three dimensional oxide is different from the initial oxide monolayer, possibly hydrous α-PtO_2 [238, 222]. Based on ellipsometric measurements during Pt oxide growth [248], purely electrochemical studies [252, 253], SHINERS [222] and operando near ambient pressure X-ray photoelectron spectroscopy (NAP-XPS) studies [249, 236, 251], it is concluded that the growing three dimensional oxide does not replace the initial oxide monolayer, but rather forms on top of it, possibly as porous [251], or inhomogeneous film [236] in which at least a fraction of Pt ions have oxidation state +4, instead of +2.

Increasing the potential further anodically results in oxygen evolution on Pt at around

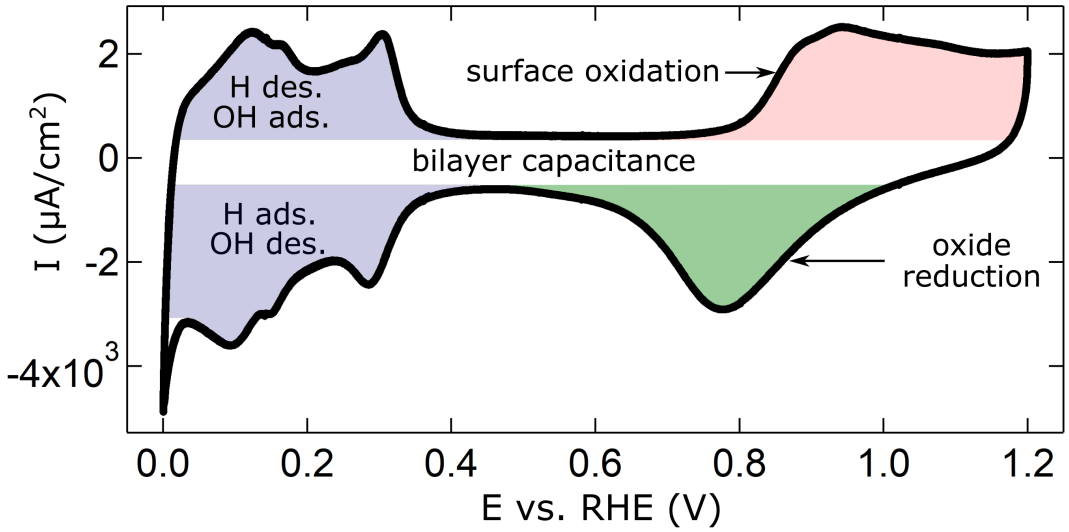

Figure 5.10: Cyclic voltammetry of a Pt microelectrode with 100 micrometer diameter in 0.05 M H_2SO_4, recorded at 500 mV/s in a spectroelectrochemical cell. Trace amounts of oxygen in this cell are responsible for the bilayer capacitance and the H/OH sorption not being symmetric around 0 current.

1.6 V vs. RHE. Following the above discussion, the OER proceeds on a Pt oxide film that is slowly growing. This growing oxide film slows down the OER at constant potential by an increased mass transport resistance because O_2 is generated below the oxide [251]. The three dimensional oxide film has to be porous enough to enable mass transport for water, O_2 and protons, or to be inhomogeneous and not cover the entire surface. The mechanism, thermodynamics and kinetics of the OER on Pt have been described in detail elsewhere [254, 255, 256, 257, 258].

The oxidation state of the metal cation has been shown to be intrinsically linked to OER activity and catalyst (in)stability, where at least for Ru and Ir (and generalizing from the result of these two), a higher OER activity and decreased stability was observed on oxide films containing a larger fraction of oxidation states higher than +2 [220]. For Pt specifically, it was initially suggested that the consecutive oxidation of Pt to PtO to PtO_2 finally arrives at the instable PtO_3, which then decomposes to PtO_2 and O_2 [259]. Conway and Liu found a change in OER Tafel slope from 117 to 57 mV/decade at 1.85 V vs. RHE in acidic solution and suggested this increase in reaction rate to be due to the appearance of a higher oxidation state of Pt ions, e.g. Pt^{4+}, that functions as redox mediator with Pt^{2+} [256]. However, more recent operando NAP-XPS studies evidenced that the active

Pt species is not ionic, but rather metallic based on the evolution of the abundance of the different oxidation states of Pt before and during the OER [249, 251]. For the OER on Pt_{poly} in base, Favaro et al. found that the OER activity is directly correlated with the abundance of a metallic surface hydroxyl Pt-OH_{ads}. While switching off the OER lead to the immediate disappearing of the Pt-OH_{ads} population, the Pt^{2+} and Pt^{4+} populations remained basically constant [251]. So far, the question which Pt oxidation state is active for the OER remains open. To this end, it would be desirable to conduct an experiment in which the Pt oxidation state is manipulated while the OER is going on and to compare the impact of different oxidation states on the OER activity.

In this section, I use intense femtosecond near-IR radiation to oxidize Pt beyond the oxidation state that is achieved under thermal conditions during cyclic voltammetry with a potential range including the onset of the OER.

The irradiation of the Pt working electrode in the anodic scan produces an additional, intense oxidation peak centered at 1.4 V vs. RHE whose corresponding reduction peak is shifted cathodically to ca. 0.5 V. I argue that this oxidation peak represents the formation of a stable Pt oxidation state higher than +II, likely +IV, as further corroborated by ex situ XPS measurements. Potentiostatic experiments under illumination further hint at the periodic formation and depletion of another unstable Pt oxide, possibly PtO_3 (i.e. Pt=+VI). The presence of the higher valent Pt oxides formed during illumination decreases the OER current density at low overpotentials. It therefore seems reasonable to conclude that these higher Pt oxidation states do not catalyze the OER and only act as barrier for mass transport.

Results and Discussion

In figure 5.11 the effect of femtosecond near-IR radiation on the anodic half of the CV of a Pt microelectrode is shown, experimental details can be found in the figure caption.

Panel a) shows the CV without illumination in black ("dark") and the red curve depicts the CV while the Pt electrode is illuminated throughout the entire potential range ("illum."). The red curve starts to deviate from the black one at around 0.95 V vs. RHE and shows an intense, well pronounced peak at around 1.4 V. At the onset of the OER, between 1.6 and 1.7 V [260], the current under illumination is still appreciably higher than without illumination, but at 1.8 V both currents are virtually identical. During the reverse scan the current under illumination is still considerably more anodic than without and the maximum of this additional anodic current again seems to be around 1.4 V vs. RHE.

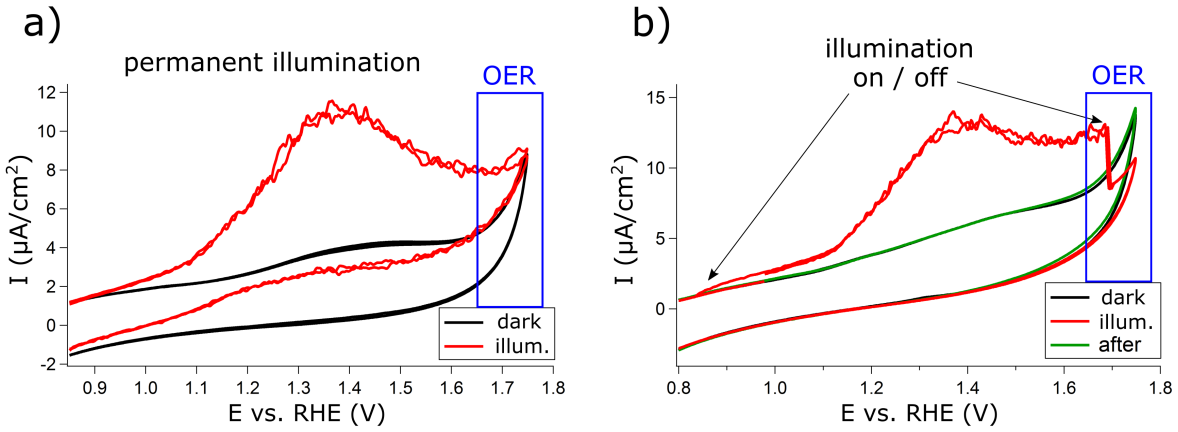

Figure 5.11: Anodic half of the CV of a Pt microelectrode with 100 micrometer diameter in 0.5 M $HClO_4$ at 50 mV/s in a spectroelectrochemical cell. Panel a) shows the CV without illumination as a black curve ("dark") and the CV during illumination with 55 fs, 800 nm light at a repetition rate of 1 kHz and a fluence of 3 mJ/cm^2 in red ("illum."). For this experiment, the electrode was illuminated for the entire course of the CV. Panel b) shows the CV before illumination as a black curve, during illumination (identical experimental details as in panel a)) from 0.85 to 1.7 V vs. RHE in the anodic sweep as a red curve, and after switching off the illumination entirely as a green curve. The blue rectangles highlight the potential window of oxygen evolution.

The oxide reduction peaks in the reverse scan (shown in appendix section B) contain the additional charge contained in the illumination induced oxidation peak at 1.4 V vs. RHE and are shifted cathodically with respect to the oxide reduction peak without illumination to about 0.5 V.

Details about the nature of the surface species formed in the additional oxidation peak at 1.4 V during illumination can be inferred from the position and shape of the peak and knowledge about Pt oxides from prior studies, vide supra. Its appearance as a single well pronounced peak hints at the predominant formation of a single oxidation state. Based on the discussion in the introduction, this oxidation state is likely +IV, as the regular oxide without illumination is mostly composed of Pt(+II). This assumption is corroborated by the thermodynamics of Pt oxide formation: PtO_2 is thermodynamically stable anodically (i.e. positively) of 1.05 V vs. RHE [259] in 0.5 M $HClO_4$, but its formation is kinetically hindered [242]. Further support for the formation of an oxide with a higher oxidation state comes from the shifting of the oxide reduction peak towards more cathodic potentals (This typically indicates a higher oxidation state, and/or a thicker oxide, see appendix section B). In the simplest scenario, the irradiation provides the activation energy necessary for PtO_2 formation. This is corroborated by ex situ XPS measurements of a polycrystalline Pt electrode (5 mm diameter) after a similar electrochemical treatment under illumination that produces the anodic oxidation peak. The results demonstrate a higher degree of Pt oxidation with illumination than without, see appendix section B for data and details.

Potentiostatic experiments in the same potential range under illumination, see Figure 5.12, show periodic oscillations in the current vs. time traces. The oscillation's amplitude, but not its period, is a function of potential. At higher potentials, close to the OER, additional features appear, see appendix section B. The current oscillations sit on top of a current background that is highest at the beginning of the illumination and then decays with time. The oscillation's amplitude also decreases with time.

Additionally formed PtO_2 under illumination possibly is responsible for the current background that is decaying with time in the current vs. time traces. The oscillations, however, indicate the periodic formation and depletion of an unstable, likely oxide, species. The independence of the oscillation period on potential further suggests that the same species is formed at the investigated potentials. A possible candidate species is PtO_3, which is not stable thermodynamically below around 2 V vs. RHE under these conditions [242] and which has not been observed under steady state OER conditions by operando NAP-XPS [249, 236, 251], unlike PtO_2. The periodic oscillations in current associated with the creation and depletion of what possibly is PtO_3 likely explain the high level of noise in the red curve from 1 V on anodically in the CV.

The additional oxide due to laser illumination only appears at fairly anodic potentials at which the surface would already be covered in oxide in the absence of the illumination. This is perhaps unexpected, because the photons have sufficient energy, 1.55 eV, to generate holes capable of splitting water and forming an oxide at basically any investigated potential. However, holes are very short lived in metals and have lifetimes of only a few fs [261]. The observation that neither oxide formation, nor OER are induced by the laser illumination at potentials below 1 V vs. RHE (when the surface is metallic) suggests that the excited holes decay before being able to participate in chemistry. However, the lifetime of holes in semiconductors is substantially longer and can reach up to tens of µs [262]; PtO_2 is a semiconductor with a bandgap ranging from 1.2 to 1.9 eV depending on modification and preparation [263, 264, 265], while PtO likely is metallic [266]. The additional oxide that is formed during illumination likely originates from electrochemically grown oxide that is transformed by the illumination. One scenario that is consistent with the experimental data and prior studies (on the lifetime of photoexcited quasiparticles and bandgaps of the involved oxides) is that the illumination provides the necessary activation energy for the PtO to PtO_2 transformation.

From Figure 5.11, conclusions on the impact of certain Pt oxidation states on OER activity can be made under the assumption that the laser irradiation leads to a strongly increased coverage of stable PtO_2 and possibly a certain, fluctuating, coverage of PtO_3, i.e., higher valent Pt oxidation states, and the observation that the OER current at 1.8 V vs. RHE under illumination (red) is identical to the OER current on the electrode without illumination (black).

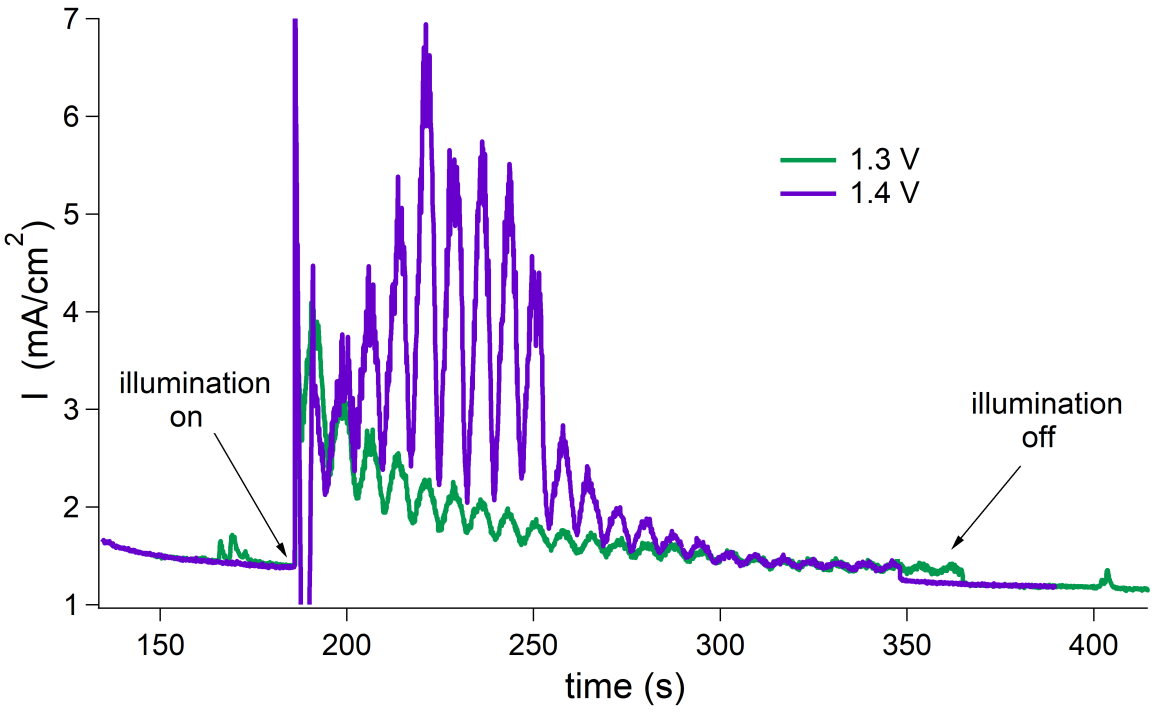

Figure 5.12: Potentiostatic experiments of a Pt microelectrode with 100 micrometer diameter in 0.5 M $HClO_4$ in a spectroelectrochemical cell before, during and after illumination with 55 fs, 800 nm light at a repitition rate of 1 kHz.

This suggests that the higher valent Pt oxidation states that are produced by the illumination are not active in the OER. It is, moreover, sensible to assume that the higher valent Pt oxides are detrimental to OER activity by exacerbated mass transport: the laser irradiation per se should increase OER activity [89] through its heat impact, and/or the presence of holes, yet the current at 1.8 V under laser illumination is identical to the current without.

If the presence of the higher valent oxides is in fact detrimental to OER activity was investigated in a similar cyclic voltammetry experiment, but shutting off the illumination before the OER commences: the electrode was only illuminated in the anodic scan from ca. 0.85 to 1.7 V vs. RHE. The results are displayed in panel b) of Figure 5.11, the black curve shows CV scans before the illumination started ("dark"), the red curves shows CV curves during selective illumination from 0.85 to 1.7 V vs. RHE ("illum.") in the anodic scan and the green curve corresponds to CV scans after the illumination has been turned off entirely. As in the experiment depicted in panel a), illumination leads to the additional oxidation feature at 1.4 V in the anodic scan, but opposed to the experiment in panel a), this feature is not present in the reverse scan, as the illumination is turned off at 1.7 V. After turning off the illumination at 1.7 V, the illum. current is considerably smaller than the dark one during the OER from 1.7 to 1.8 V (blue rectangle). From about 1.7

V on in the reverse scan, dark and illum. curve match until the start of oxide reduction (the corresponding reverse scans can be found in appendix section B). This is reflected in the oxide reduction peaks: the oxide reduction peak corresponding to the illum. curve of panel b) contains less charge and is less strongly shifted negative in potential than the illum. curve of panel a), because no additional illumination-induced oxide is formed during the reverse scan. The green curve after illumination is almost identical to the dark curve before illumination, only the green OER current is slightly enhanced. This suggests that the light induced oxide formation does not significantly roughen the electrode surface.

The decreased OER current of the illum. curve (with respect to the dark one) after turning off the illumination at 1.7 V vs. RHE suggests that the higher valent oxides formed during the illumination do not contribute to the OER and only act as a barrier for mass transport. As for the oxide that is grown under thermal conditions in the absence of illumination, the additional oxide that is grown in the presence of the illumination has to be porous. This can be concluded from the observation that a current is flowing even after the illumination has started and caused the growth of the additional oxide. If the oxide was not porous, neither further oxide formation, or oxygen evolution would be possible, because water (a reactant in both cases) would not be able to reach the conducting/metallic phase. This supports the hypothesis from above that the current of illum. and dark curve in panel a) are only identical at 1.8 V vs. RHE because of laser-induced oxide formation and laser induced increase in OER current and that higher Pt oxidation states do not catalyze the OER. This reasoning is in line with the above mentioned more recent operando NAP-XPS studies of the OER on Pt that conclude that the active species is metallic [249, 251].

Future experiments may focus on the manipulation of oxidation states of metal electrodes independent of external bias also in a way that reduces the oxidation state. This could be achieved by tuning the photon energy, e.g., towards X-rays and using the photoelectrons to reduce the electrochemically formed oxide layer. Alternatively, an electron beam could be used in an experimental setup akin to transmission electron microscopy cells that utilize ultrathin electron transparent windows and ultrathin eletrolyte layers. Such an approach would be suited to confirm the conclusions of this section by increasing the abundance of lower valent Pt oxidation states while running the OER.

Chapter 6

Identifying the Chemical Nature and Modelling the SFG Response of H_2SO_4 Derived Anions on Pt(111)

The previous chapters were concerned with the two half-cell reactions of water electrolysis, the HER (chapter 4) and the OER (chapter 5). In the case of the HER on Pt, we were interested in the structure and potential dependent behavior of the reaction intermediate Pt-H_{OPD} (and other Pt-H adsorbates) both under steady-state conditions and after perturbation by an ultrashort optical pulse (that excites hot electrons, which, depending on the applied potential, drive the HER close to 0 V vs. RHE, or drive charge transfer at higher potentials). In the case of the OER, we were interested in its activity's spatial heterogeneity on Au electrodes and heterogeneity in their electrochemistry at lower potentials. For Pt as a OER catalyst, the activity of differently valent Pt oxidation states was investigated. In the discussion about Au and Pt surface oxidation and reconstruction the influence of adsorbed anions was mentioned: the stronger the anions adsorb to the surface, the higher the potential necessary to replace them by O/OH and oxidize the surface. Nevertheless, if one were to write an expression for the oxidation of the surface, then the anions would not show up, even if they strongly influence the overall process. For this reason anions are often referred to as "spectator" species.

However, much prior work has demonstrated that the efficiency of water electrolysis, and other important electrocatalytic reactions such as fuel cell chemistry and CO_2 reduction, depend on the composition of the supporting electrolyte [34, 35, 36, 37]. The effect of anions on reaction efficiency is a consequence of the potential dependent interaction of electrode, solvent and ions. However, the molecular level details of this interaction have proven challenging to unravel and even for well studied systems very basic questions regarding the link between electrode, electrolyte and activity remain [267, 268, 269, 143].

The adsorption of sulfuric acid derived anions on Pt(111) is one such popular system. This system has been extensively studied with a wide variety of experimental and theoretical approaches over the past decades [35, 267, 124, 270, 271, 272, 273, 274, 275, 276, 277, 52]. While many aspects of the electrode-electrolyte interaction have been elucidated, perhaps

the most fundamental aspect, the chemical identity of the adsorbing anions, has remained controversial. As mentioned in section 2.1.3, the uncertainty over whether sulfate, or bisulfate is adsorbed lead to the usage of the term "(bi)sulfate".

In principle vibrational spectroscopy should be able to discern the two species; the vibrational response in bulk liquid is clearly different for sulfate and bisulfate [278]. Consequently, much prior work has addressed this issue with various forms of vibrational spectroelectrochemistry [270, 279, 280, 281, 275]. The experimental observable is similar in all studies, a narrow resonance around 1250 cm^{-1} that blueshifts with increasing potential. This frequency is higher than the resonances of both species in bulk solution which has led to controversial peak assignments including HSO_4^-, SO_4^{2-} and SO_4^{2-}+H_3O^+ ion pairs. This uncertainty about the chemical speciation at the interface has also complicated the analysis of the potential dependent spectral response: the shift of the centre frequency of the observed resonance is not linear over the investigated potential range, but was interpreted to be piece-wise linear [275]. Without a microscopic model that would explain a linear shift in centre frequency with linearly varying external bias, such an approach is not justified (while intuitively appealing, linear correlations are also not self-explanatory). A change in slope was then interpreted as a change in surface speciation (by, e.g., deprotonation of bisulfate, or desorption of a specific co-adsorbate), or surface structure (by, e.g., reconstruction of an adsorbate layer). This a general problem in spectroelectrochemistry and not specific to (bi)sulfate adsorbed on Pt electrodes; consequently, a general approach to how the shift in centre frequency of a vibrational mode can be modelled quantitatively would profit the entire community.

One of the most direct ways of determining the surface speciation would be an isotope exchange experiment: vibrational modes of HSO_4^- would be sensitive to an exchange of H with D, while the modes of SO_4^{2-} would remain unaffected. Unfortunately, the strong absorption of the D_2O bending mode at 1200 cm^{-1} makes data interpretation highly challenging (the vibrational mode of interest is situated at around 1250 cm^{-1}) for linear spectroscopies that rely on the subtraction of a reference spectrum to extract the interfacial spectrum due to introduction of artefacts to the spectrum [279, 281].

Here, I exploit the interface specificity of SFG (subtraction of a reference spectrum is not needed to extract the interfacial response) to quantify the spectral response of sulfuric acid derived anions adsorbing to Pt(111) in 0.5 M H_2SO_4/H_2O and D_2SO_4/D_2O solutions from 1100 - 1400 cm^{-1} as a function of applied potential. In section 6.1 I show that the bias dependent spectral response is identical for both electrolyte solutions, confirming the identity of the adsorbate as SO_4^{2-}. This result is supported by density functional theory (DFT) on a meta-GGA (Generalized Gradient Approximation) level performed by collaborators: normal mode frequencies of bisulfate adsorbed to a Pt cluster are sensitive to isotope nature and different from sulfate's vibrational modes. I thus offer the most direct experimental evidence so far that sulfate is the dominant adsorbate species at the Pt(111) surface in 0.5 M H_2SO_4.

If sulfate is the sole adsorbate, then the nonlinear shift of its vibrational mode's centre frequency with applied potential is not trivial to explain. This is particularly true because sulfate's coverage is constant over the investigated potential range (see below for a detailed

discussion). In section 6.2 I address the potential dependence of the vibrational response of sulfate by devising a microscopic model that explicitly accounts for dipole-dipole interaction. There I show that a linear change in molecular polarizability (that results from a linear change in applied potential) causes a nonlinear change in centre frequency and intensity. This model offers a physical explanation for the shift of centre frequency as a function of applied bias without the need to invoke piece-wise linear segments and, consequently, changes in surface speciation, or structure.

At first, we recall what is known about the adsorption of sulfate to Pt(111) and how this is reflected in the CV. The CV of Pt(111) (0.5 M H_2SO_4 in H_2O, 50 mV/s) in hanging meniscus geometry is shown in Figure 6.1 A).

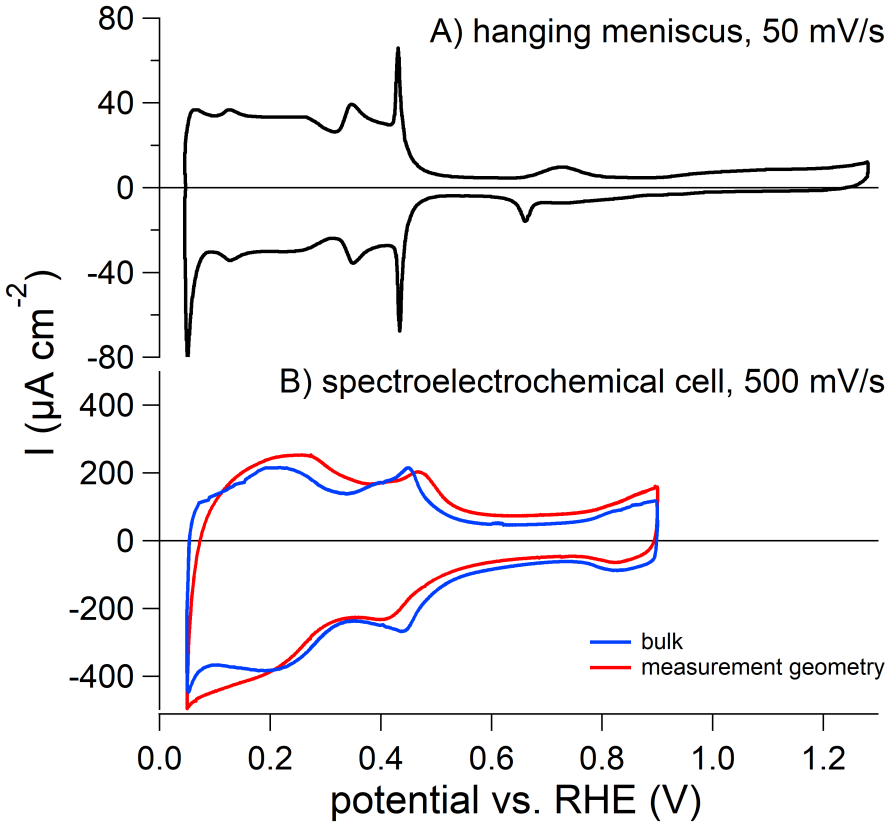

Figure 6.1: Cyclic voltammetry of a Pt(111) electrode in 0.5 M H_2SO_4. A) in hanging meniscus geometry, recorded at a scanning speed of 50 mV/s. B) in the spectroelectrochemical cell, recorded at 500 mV/s. The blue CV was recorded in bulk electrolyte within the spectroelectrochemical cell, the red line with an electrolyte film thickness of about 1 µm between the working electrode and the CaF_2 window.

As discussed in detail in section 2.1.3, the sharp spike towards negative current densities at around 0.05 V vs. RHE is due to water electrolysis in the HER and the broad current plateau from around 0.05 - 0.3 V vs. RHE is due to H_{UPD} adsorption. Continuing to more

positive potentials the butterfly feature (∼0.35 - 0.45 V vs. RHE) arises from (bi)sulfate (we will use this term for the literature survey to stress that the chemical identity of the adsorbate used to be a controversial question) adsorption[1]. The broad feature in the lower potential portion of the butterfly is thought to result from formation of an unordered layer of (bi)sulfate that adsorbs in a bidentate fashion and the large current spike at 0.45 V vs. RHE from a disorder - order phase transition [29]. At potentials positive of the spike STM studies have shown that the (bi)sulfate adlayer has a ($\sqrt{3}$ x $\sqrt{7}$)R19.1° structure and a coverage of 0.2 ML (3x10^{14} ions/cm^2) [282, 272, 273]. The low coverage has lead to the conclusion that a co-adsorbate must also be present over this potential range. The identity of this co-adsorbate is unknown but is typically argued to be either water or perhaps adsorbed OH [283]. Going to still more positive potentials, a small positive current is apparent at around 0.7 V vs. RHE. The assignment of this feature has been strongly debated. It has been argued to be the result of the conversion of bisulfate to sulfate [284], a second order to disorder transition of the adsorbed anions [29], OH co-adsorption and/or the possible desorption of (bi)sulfate anions [285, 276]. It is important to note here that the anion coverage is essentially constant from the butterfly feature until the onset of surface oxidation (the charge involved in the small peaks is almost negligible compared to the butterfly feature). Panel B) of Figure 6.1 shows CVs collected from a Pt(111) working electrode within the spectroelectrochemical cell with the electrode retracted (this is labelled bulk) and in measurement position. The CVs clearly show similar current features to that in the meniscus geometry[2]. It is finally worth noting that the small current feature around 0.7 V that is observed in the hanging meniscus geometry is absent in the electrochemical cell used for the optics measurements. We will return to this point when discussing the optical response.

6.1 Isotope Exchange SFG Measurements Clarify the Chemical State of the Anions: they are SO_4^{2-}

The content of this section has been published in reference [286].

I monitor the Pt(111)/electrolyte interface at IR frequencies between 1100–1400 cm^{-1} as the potential is cycled between 0.05 and 0.9 V vs. RHE in Figure 6.1. At the potential of the sharp current spike of the butterfly feature, 0.42 V vs. RHE, a peak appears around 1220 cm^{-1}. This peak increases in intensity, narrows in frequency and shifts towards higher wavenumbers with increasing potential. All spectral changes are reversible: spectra in the forward and reverse scan are identical at identical potentials. This potential dependent vibrational response has previously been observed both by SNIFTIRS and SFG [281, 275].

The above mentioned controversy in assigning this vibrational response to a specific interfacial species arises, at least in part, from the fact that adsorption of the anion to the

[1] The remainder of the paragraph has been published in reference [52].

[2] I take the asymmetry in current features between the cathodic and anodic scans to be due to leakage of small amounts of O_2 into the cell which leads to a negativ current via the ORR, see section 2.

electrode surface will to some extent break its symmetry and alter its electronic structure by the presence of interfacial fields, or charge transfer/bonding and consequently also its vibrational response [52, 287, 281, 288, 289]. This is probably the reason why the interfacial (bi)sulfate's vibrational response is blueshifted with respect to the bulk sulfate and bisulfate vibrational modes. The difficulty in assigning the vibrational mode can be avoided by performing an isotope exchange experiment: the vibrational response of an adsorbate is shifted upon deuteration, if the vibrating adsorbate entity that evokes the monitored vibrational response contains hydrogen.

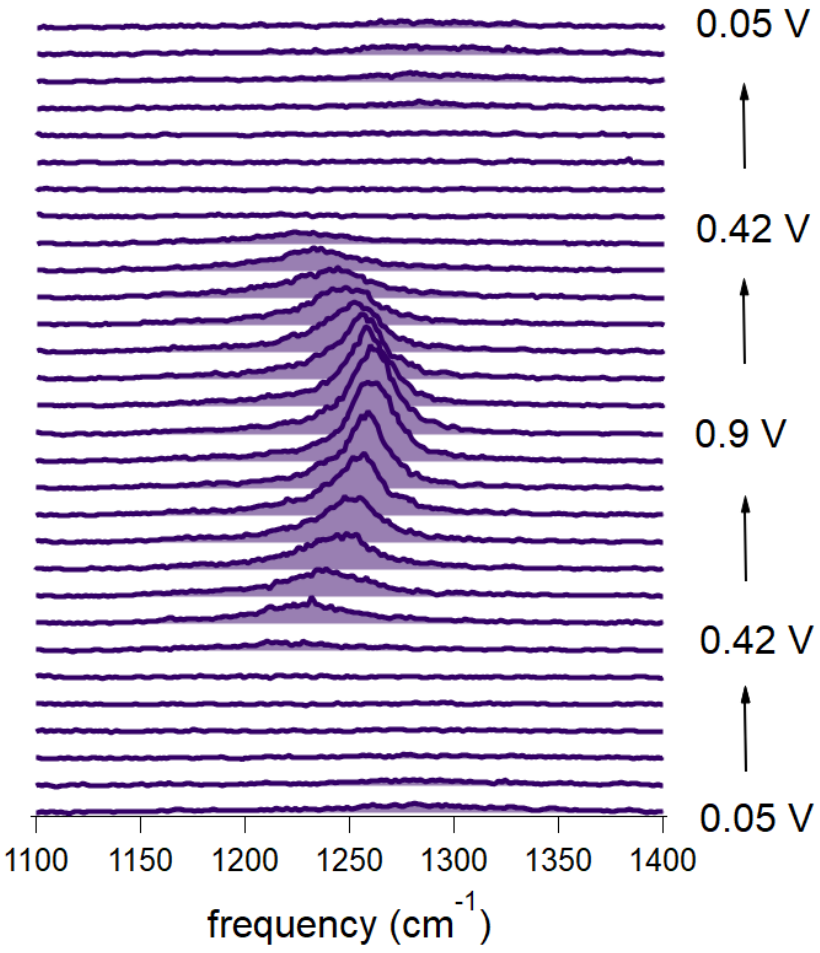

Figure 6.2: Pt(111)/(H)$SO_4^{(2)-}$ SFG spectra as a function of potential in 0.5 M H_2SO_4 (in H_2O).

I therefore repeat the experiment described in Figure 6.2 in 0.5 M D_2SO_4 in D_2O and plot the results in Figure 6.3 (the full dataset of the isotope exchange experiment can be found

in appendix section C).

The spectra recorded in deuterated solution are lower in intensity because of the strong IR absorption of the D_2O bend at 1200 cm^{-1} and are shown twice, once scaled to match the intensity of the spectra recorded in H_2O for comparison purposes[3]. The spectra recorded in deuterated and undeuterated solutions are quantitatively identical at all potentials (even though only two are shown here), clearly suggesting that for potentials above 0.42 V vs. RHE, sulfate is adsorbed on Pt(111) in 0.5 M H_2SO_4.

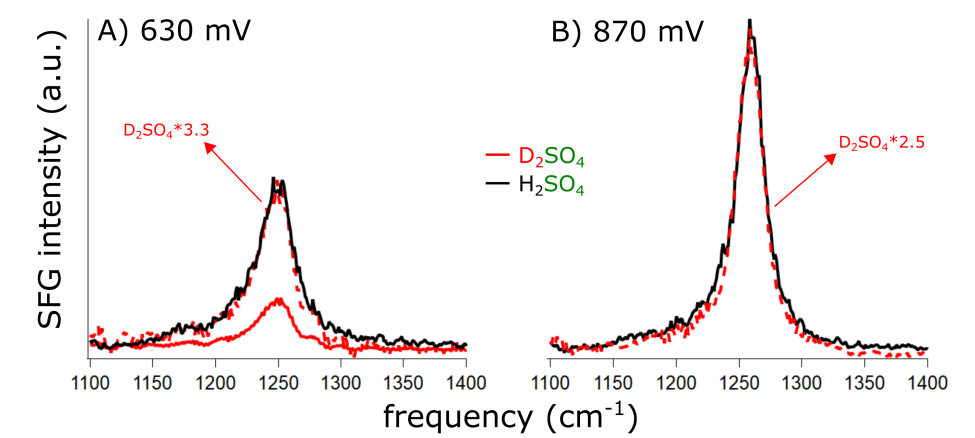

Figure 6.3: SFG spectra of a Pt(111) electrode in H_2SO_4 vs. D_2SO_4 at A) 630 and B) 870 mV vs. RHE. The spectra recorded in deuterated solution (red) are shown in original size (solid red line) and scaled to match the spectra in protonic solution (dashed red line).

This conclusion is in agreement with prior work: Based on the invariance of the 1250 cm^{-1} mode (monitored by SNIFTIRS) with pH from 1 - 5.6, Feliu, Lipkowski and coworkers suggested that SO_4^{2-} is the dominant adsorbate [281]. Thermodynamic analyses that probe the adsorbate's valence found it to be close to +2 at 0.45 V vs. RHE and to decrease with increasing potential [273, 276] (this, however, is only indirect evidene, as co-adsorption of, e.g., HSO_4^-+OH^- would give the same result as SO_4^{2-}). Recent electronic structure calculations on extended (periodic) Pt surfaces and a Pt cluster consisting of 54 atoms that exposes a (111) surface are also consistent with this conclusion [290, 287].

The isotope exchange measurements were complemented with DFT calculations[4] of bisulfate and sulfate adsorbed on a Pt(111) cluster consisting of 55 atoms in the absence of water (i.e., at a solid/vacuum interface). Even though strongly simplified, the calculation reproduces the most important structural aspects of this system previously reported by others: bisulfate adsorbs in a bidentate, sulfate in a tridentate geometry [291]. Harmonic normal modes for the given structures were calculated and it was found that both adsorbates have resonances around 1250 cm^{-1}, see Figure 6.4. The sulfate vibrational mode

[3]The fact that the scaling factor is a function of potential suggests that not only IR absorption by the electrolyte bulk is important, but also by interfacial water whose absorptivity is a function of bias.

[4]DFT calculations were performed by collaborators Igor Ying Zhang and Zhenhua Wang from Fudan University and Beijing Insitute of Technology, respectively, see reference [286].

corresponds to the stretch of the non-coordinated S-O bond, while the bisulfate vibration is a more intricate combination of OH bending and stretching of the non-coordinated S-O bond (see supporting information of reference [286] for an animation). In support of the conclusion that sulfate is adsorbed to Pt(111) from 0.42 to 0.9 V vs. RHE, the calculation clearly shows that, as expected, the bisulfate $\sim$ 1250 cm^{-1} vibrational mode substantially shifts upon deuteration.

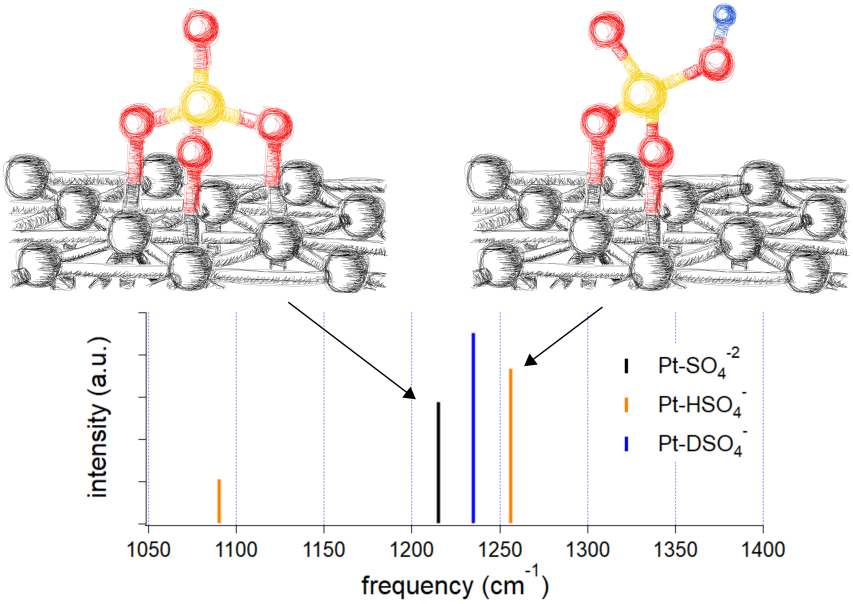

Figure 6.4: Adsorption geometries of SO_4^{2-} and HSO_4^- (top left and right; no discernable structural difference between HSO_4^- and DSO_4^- was found) and vibrational normal modes (bottom) around 1250 cm^{-1} for SO_4^{2-}, HSO_4^- and DSO_4^- adsorbed on Pt(111); adsorption geometries were determined by DFT.

It is somewhat surprising that sulfate is the dominant adsorbate on Pt(111) in 0.5 M sulfuric acid, as the bulk pH of the electrolyte is close to 0 and at this pH bisulfate is the only anion bulk species. This implies that the pK_a value of bisulfate is substantially lowered by the interface from 2 in bulk to < 0. The experimentally observed shifting of acid-base dissociation constants at metal interfaces has been explained for many relevant electrochemical reactions by the surface charge [292][5]: a positively charged surface (Pt(111) is positively charged at 0.42 V vs. RHE, its PZC is 0.3 - 0.35 V vs. RHE [155]) will favor the dissociation of bisulfate by stabilization of the doubly negatively charged sulfate anion and the expulsion of the positively charged proton from the interface.

If this shift in pK_a value at the interface actually is related to surface charge then it should be a function of the applied potential with respect to the PZC. In this scenario, one could expect that the deprotonation from bisulfate (bulk species) to sulfate is not

[5]The shifting of reaction equilibria, for example of acid-base chemistry, at interfaces due to surface charge can be quantitatively explained by Guoy-Chapman theory, see reference [293] and references therein.

concomitant with adsorption, but that bisulfate adsorbs and deprotonates at a higher potential (when the surface charge is sufficiently positive). This scenario is consistent with the observations made here and prior work. We only start to see the sulfate vibration with SFG from 0.42 V vs. RHE on, but the butterfly CV feature (that is associated with (bi)sulfate sorption) starts at considerably lower potentials around 0.35 V vs. RHE. This implies a transformation of the initial adsorbate to tridentate adsorbed sulfate with increasing potential. As mentioned above in section 6, while the broad feature in the lower potential portion of the butterfly is thought to result from formation of an unordered adsorbate layer[6] that adsorbs in a bidentate geometry, the sharp current spike is thought to be the consequence of a disorder - order phase transition after which the adsorbate (that has been indentified as sulfate here) binds to the surface in a tridentate geometry [29]. This idea is supported by recent electronic structure calculations [290, 287]. Bisulfate is predicted to be the dominant adsorbate from 0.35 - 0.41 V, at higher potentials from 0.41 - 0.48 bidentate adsorbed bisulfate and SO_4^{2-}+H_3O^+ ion pairs are predicted to coexist on the surface and above 0.48 V sulfate prevails.

The DFT calculations presented in this work suggest that I (and other investigators that have employed vibrational spectroscopy to probe this system) do not see bisulfate vibrations at potentials <0.42 V vs. RHE because the corresponding transition dipole moment is parallel to the surface and presumably small, see appendix section C. The tridentate adsorbed sulfate has a substantially larger transition dipole moment that is normal to the surface (making detection by vibrational spectroscopies possible) and its interaction with the surface is stronger than that of bisulfate.

The normal orientation of the (transition) dipole of sulfate's uncoordinated S-O bond with respect to the surface makes this bond susceptible to polarization through the interfacial electric field. This bond polarization that is induced by the interfacial electric field (which varies with applied potential) is also key in understanding why the sulfate vibrational mode, at constant sulfate coverage, substantially grows in intensity and blueshifts with increasing potential (and the electrochemical vibrational Stark shift in general), as will be discussed in the following section.

[6]Unordered in a sense that STM images do not show a clear "x by y" structure of the adsorbate layer at the corresponding potentials [29].

6.2 A Microscopic Model of the Electrochemical Vibrational Stark Effect of SO_4^{2-} on Pt(111): Understanding the SFG Response

The content of this section has been published in reference [52] by Zwaschka and coworkers.

As mentioned above, the uncoordinated S-O bond of sulfate can be polarized by the interfacial electric field (that is tuned with the applied bias). In this section I will explain the observed potential dependent changes in peak amplitude and centre frequency of the sulfate vibration by an increasing polarization of the bond with increasing interfacial electric field as the potential is tuned. To account for the effect that the interfacial field has on the sulfate bond, I make use of prior experimental and theoretical work that describes how the dipoles of small adsorbate molecules interact with their image dipoles, the dipoles of other adsorbates and their respective image dipoles (often referred to as "dipole - dipole coupling"). I further exploit the fact that the sulfate coverage is essentially constant after the butterfly feature in the CV to quantitatively explain the potential dependence of the spectroscopic observables.

The shifting of vibrational modes of adsorbates with applied macroscopic potential, also known as Vibrational Stark Effect (VSE), is an intricate phenomenon. Tuning of the potential not only changes the interfacial field, depending on the system under investigation, it may also change solvent structure at the interface, adsorbate coverage(s) and structure(s) (plural forms in the case of co-adsorption). Every one of these may nontrivially influence centre frequencies and intensities of vibrational resonances, yet in the great majority of studies a linear relationship between the frequency shift and the applied bias has been used to rationalize the data [294, 295, 275, 296, 289, 297]. While the microscopic basis of this linear relationship has not been well explored, it has typically been taken to suggest potential independent structures of the solvent, electrolyte and adsorbate in the potential region over which the center frequency linearly shifts. As a result, changes in slope with potential are typically justified as the result of interfacial chemical or structural change.

A similar observation to the electrochemical VSE has been made in the study of CO adsorption on metal single crystal surfaces in UHV: as CO's coverage increases the frequency of the CO stretching mode blueshifts and the work function of the surface decreases significantly [294]. The blueshift with increasing coverage has been quantitatively explained within classical electrodynamic theory by dipole-dipole coupling [298, 299, 294, 300, 301]. An important insight provided by this model is that over a substantial range in surface coverage the relationship between coverage and centre frequency will be nonlinear.

Viewed from the perspective of chemical bonding of the adsorbate, adsorption on a metal surface in UHV or on a metal working electrode seems similar. In both cases we are interested in understanding the vibrational response of a small molecule within a, small, volume in which local potential is changing significantly (see Figure 6.5). Because of this similarity it seems natural to ask whether insight into vibrational response, and local potential, gained from the study of small molecules adsorbed in UHV may also be

useful in understanding small molecules adsorbed on metal electrodes. Several pioneering studies [302, 303] have tried to answer this question using the "UHV double layer (or electrochemical) modeling" strategy. In this approach a double layer is mimicked by dosing water, and the adsorbate whose vibrational response one is interested in, onto a metal surface in UHV. Ions in the double layer and "tuning of the potential" is obtained by dosing alkali metal atoms onto the surface that discharge upon impact (the work function changes with alkali metal coverage, hence the "potential tuning"). The mentioned studies have proposed that, if changing the surface coverage (of the adsorbate whos vibrational response one is interested in) in UHV produces a change in frequency ($\Delta\omega$) and a change in work function ($\Delta\Phi$), within an electrochemical cell the change in bias (ΔV) that produces the same $\Delta\omega$ will be such that $\Delta\Phi/e = \Delta V$ [288]. Given this insight the different contributions to the potential drop within the double layer can be disentangled.

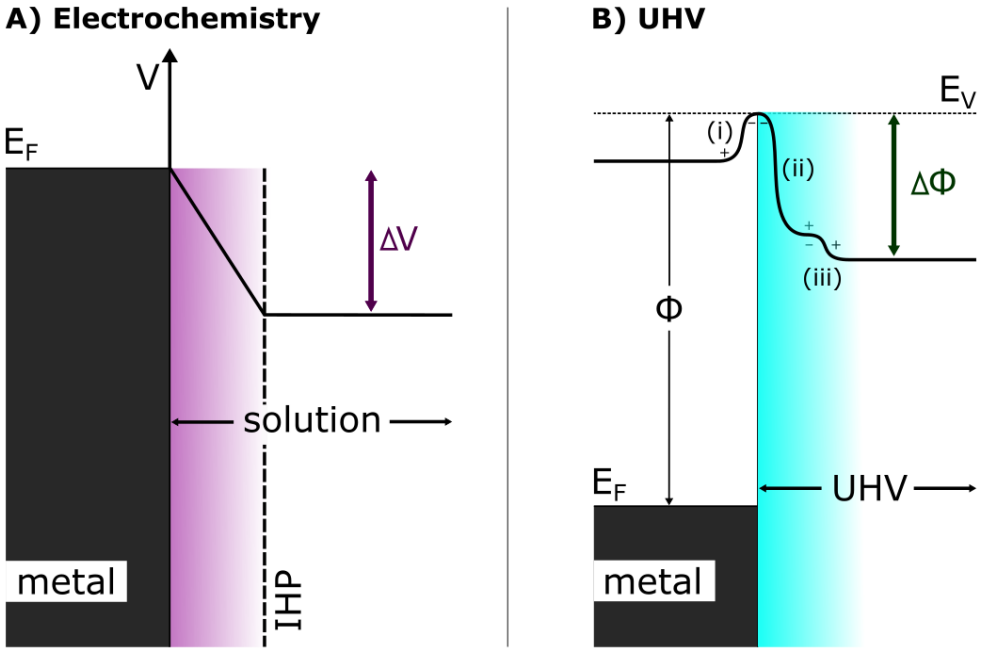

Figure 6.5: Schemes for A) the potential drop in the inner Helmholtz plane (IHP, a layer consisting of a monolayer of adsorbates, see section 2.1 for details) of an electrochemical bilayer and B) the work function change as a function of adsorbate coverage in UHV. The potential drop ΔV in the electrochemical system can be adjusted via the applied potential, which effectively shifts the Fermi level E_F. The work function of a surface in UHV is affected by different surface contributions, including (i) surface dipole; (ii) charge double layer (charges and their image charges); (iii) dipole contribution, of which (ii) and (iii) and consequently $\Delta\Phi$ can be modulated by the nature and coverage of the adsorbates. A linear correlation has been found between ΔV and $\Delta\Phi/e$ in a previous UHV electrochemical modeling experiment [288].

Inspired by this approach, here I extend the microscopic model developed to explain

the coverage dependent change in vibrational frequency of adsorbates on metal surfaces in UHV and ask whether the electrochemical VSE of sulfate adsorbed on Pt(111) can be explained by the bond polarization induced by the interfacial electric field. Sulfate adsorbed on Pt(111) has the particular advantage that there is a fairly large potential range in which previous work (see section 6) makes clear that sulfate coverage is potential independent: we can assess the influence of the applied bias on the VSE without the need to account for changes in coverage[7]. Because I perform these measurements with higher potential resolution than previous studies I am able to show that the relationship between the applied bias and center frequency is clearly nonlinear over chemically important changes in bias. I further show, by applying a model inspired by these previous UHV studies that this nonlinear dependence of the S-O stretch frequency on applied bias can be straightfowardly understood as a potential induced change in the local, interfacial field polarizing the sulfate adsorbate. Importantly, it is not necessary to invoke potential dependent chemical or structural changes to rationalize the evolution of the sulfate vibrational response with potential.

Modeling the SFG Line Shape in the Absence of Interfacial Fields

As detailed in section 3.1, in a homodyne detected experiment, the intensity of emitted SFG can be described by:

$$I_{SF} \propto \mid \chi^{(2)} \mid^2 I_{VIS} I_{IR} \tag{6.1}$$

The meaning of terms that have been introduced before will not be repeated here, see section 3.1. The macroscopic second order nonlinear polarizability can be related to the frequency dependent nonlinear response of a single molecule by the hyperpolarizability $\beta^{(2)}$ (N_S is the number of molecules in the probed spot):

$$\chi^{(2)} \propto N_S \beta^{(2)} \tag{6.2}$$

The hyperpolarizability is defined by the product of an oscillator's transition dipole moment and polarizability with respect to the normal coordinate Q:

$$\beta^{(2)} = \frac{\delta\alpha}{\delta Q}\frac{\delta\mu}{\delta Q} \tag{6.3}$$

It can be described as a coherent sum of a nonresonant and resonant interaction, where the frequency dependence is described by a Lorentzian around ω_{pzc}, the resonance frequency of the mode of interest (of sulfate) at the PZC:

$$\beta^{(2)} = \beta^{(2)}_{nr} e^{i\phi} + \frac{\beta^{(2)}_{r,pzc}}{1 - \omega_{IR}/\omega_{pzc} - i\Gamma_{pzc}/\omega_{pzc}} \tag{6.4}$$

here Γ is the dephasing time constant at the PZC.

[7] As mentioned earlier, the centre frequency may be influenced, in a nontrivial way, by interfacial solvent and adsorbate structure *and* adsorbate coverage.

Modeling the SFG Response with Interfacial Fields/Applied Bias

Using equations 6.1 - 6.4 one can construct a lineshape model where all spectral parameters are independent of applied bias. To describe the electrochemical VSE, however, we need a model that connects each of these parameters to the external field. As mentioned earlier, previous workers have shown that the change in frequency of the CO stretch vibration on a metal surface in UHV as a function of surface coverage can be written:

$$\chi^{(2)} \propto \frac{\theta \times \beta^{(2)}}{[1+\alpha_{IR}\theta U_0][1+\alpha_{VIS}\theta U_0][1+\alpha_{SF}\theta U_0]} \tag{6.5}$$

where θ is adsorbate coverage, α_i is the polarizability of the adsorbate at frequency i, U_0 is the "dipole sum factor" [301] and is defined as $U_0 \propto \sum_{j,k} \frac{1}{(r_j - r_k)^3} + ...$, and the $r_{j/k}$ denote the adsorption sites (position vector) of the adsorbates [299]. In equation 6.5 it is implicitly assumed that $\beta^{(2)}$, the molecular response, is independent of coverage: the local field induced by dipole-dipole interaction is too small to induce coverage dependent structural changes in CO that would change its second order response. This study of the adsorption of sulfate on the Pt(111) electrode differs from CO adsorption in UHV in two important ways: the vibrational response of the adsorbate changes as a function of applied bias but *coverage is constant* and the permanent dipole of sulfate is small relative to that of CO. The former implies we need an expression for the relationship developed in equation 6.5 where external bias appears explicitly and, as we show below, the latter implies that to reproduce our data the molecular response must also be a function of the applied field.

Given a perfect surface and independent insight into adsorbate structure, U_0 can be calculated, by summing over all adsorbate positions and accounting for the local electric field due to all other dipoles and image dipoles. For the electrochemistry problem we require a similar physical description: we would like to relate the applied external field to the local field sensed by the adsorbate. For small applied external fields we expect the effect of macroscopic bias on α_i, i.e. molecular polarizability at frequency i, to be linear [288]. This suggests that we might replace the θU_0 term in equation 6.5 with a local field parameter L:

$$L = L_{pzc} + L_{ext}(V - V_{pzc}) \tag{6.6}$$

in which L_{pzc} is the local field proportionality constant in the absence of net surface charge, V is the applied external bias, and V_{pzc} is the PZC. From a microscopic perspective the quantity $L_{ext}(V - V_{pzc})$ is the local field, normalized by the single molecule dipole moment in the monolayer as a function of the applied bias, sensed by an adsorbed sulfate. In what follows I refer to this quantity as the *local field* for convenience. I here follow prior work and take 0.3 V vs. RHE to be the PZC of Pt(111) in 0.5 M H_2SO_4 [154]. As a practical matter I make two simplifying assumptions in analyzing the data. First, I consider a sulfate mode that is only SFG active in the presence of an applied field (i.e., when $L_{pzc} << L_{ext}(V - V_{pzc})$). Second, because the sulfate coverage does not change over the potential range of interest of the model, the local field does not account for concentration

dependent effects. This still leaves the question of the effect of the applied bias on $\beta^{(2)}$. If polarizability changes linearly with the applied macroscopic field, i.e. $\alpha(E) \propto \alpha \cdot E$, the induced dipole will change quadratically $\mu(E) \propto \alpha(E) \cdot E$. Given equation 6.3 we thus expect that $\beta^{(2)}$ of the isolated sulfate should depend cubicly on applied macroscopic field. Because small deviations from linearity with respect to the influence of the external field on the applied potential will have large effects on $\beta^{(2)}$, in practice I will treat this as a fit parameter and test the cubic prediction from the data. Given these assumptions the version of equation 6.5 appropriate for description of the electrochemical VSE is (where $\Delta V = (V - V_{pzc})$):

$$\chi^{(2)} \propto \frac{\beta^{(2)}[L_{ext}\Delta V]^n}{[1 + \alpha_{IR}L_{ext}\Delta V][1 + \alpha_{VIS}L_{ext}\Delta V][1 + \alpha_{SF}L_{ext}\Delta V]} \tag{6.7}$$

Note that I have implicitly assumed, in writing equation 6.7, that the orientation of sulfate is potential independent over our range of interest (if it were not, per equation 6.2, we would expect that the potential dependent $\chi^{(2)}$ would be a function of sulfate orientation). I make this simplifying assumption because previous in situ-electrochemical STM measurements have shown that the adsorption geometry of sulfate in the potential region that is investigated here is independent of the externally applied potential [29, 282].

The molecular polarizability at the i^{th} frequency, α_i in equation 6.7, can be written as a sum of the electronic and vibrational contributions [301][8]:

$$\alpha_i = \alpha_e + \frac{\alpha_\nu}{1 - (\omega_{IR}/\omega_0^2)(\omega_{IR} + i\Gamma)} \tag{6.8}$$

in which the vibrational and electronic polarizabilities at the PZC are denoted as α_ν and α_e. Since both the SF and visible fields are far off an electronic transition and their frequencies much larger than those of the vibrational transition I approximate the molecular polarizability at these frequencies as $\alpha_{SF} \approx \alpha_{VIS} \approx \alpha_e = 1.775$ Å^{-3} [304][9].

Results and Discussion

To understand the potential induced spectral changes to the sulfate vibration in Figure 6.2 I first quantified the line shape changes using the model in equations 6.1 - 6.4 and different parameters to describe the resonance at each potential. This approach allows me to extract the center frequency, $\beta_r^{(2)}$ and Γ for the S-O stretching vibration at *each* potential. The extracted center frequencies, plotted as a function of applied bias in Figure 6.6, clearly illustrate that as potential is changed from 0.5 - 0.9 V vs. RHE the centre frequency of the S-O stretching vibration shifts from 1225 to 1260 cm^{-1}. As described above, a number of prior studies of this system have observed a similar potential dependence of the center frequency. Typically this observation has been rationalized by assuming that the change in

[8] In reference [301], there is a factor of 2 attached to the last term of the denominator. This factor is absent from the derivation in the original reference [299].

[9] The numerical value of α_e I adept here was taken from a DFT simulation of a solvated sulfate anion [304]. The results were found to be relatively insensitive to the precise value chosen.

frequency with applied bias is linear, or composed of multiple linear segments, and a slope extracted. The inset of Figure 6.6 suggests that at least two such line segments would be necessary to fit the presented data. If I choose to have one line segment from 0.5 - 0.7 and one from 0.7 - 0.9 V vs. RHE I find slopes of 118 ± 6 cm^{-1}/V and 56 ± 3 cm^{-1}/V respectively. A prior SFG study has found slopes of 75 cm^{-1}/V and 56 cm^{-1}/V over the same potential regions [275]. The low slope from 0.5 - 0.7 V vs. RHE in this prior study is particularly surprising because earlier IR studies of the same potential region found a slope of 120 cm^{-1}/V [295], essentially identical to the slope I find. I found in preliminary measurements that the slope of the change in center frequency with potential, for the potential region between 0.5 and 0.7 V vs. RHE was extremely sensitive to IR power.

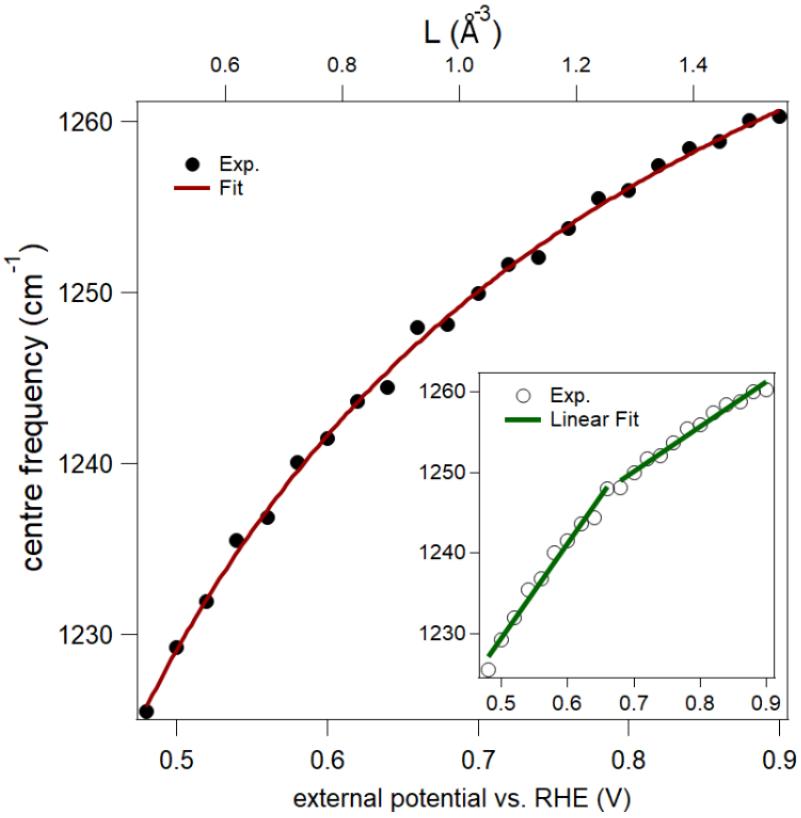

Figure 6.6: Peak center frequency as a function of applied external potential. The black dots represent the experimental data, while the red line shows the fit to equation 6.9. The inset shows that the experimental observations can be also fitted with two linear functions with slopes of 118 ± 6 cm^{-1}/ V and 56 ± 3 cm^{-1}/ V for the low and high potential region, respectively.

IR energies above 3.6 µJ per pulse lead to apparent slopes consistent with the earlier SFG studies (see appendix section C for one additional data set with an IR pulse energy of 4.2 µJ), presumably because irradiating the surface with high enough peak power leads to laser induced sulfate desorption and a new, dynamic sulfate coverage that now depends on

laser power. As has been demonstrated previously and discussed above, changes in surface coverage would be expected to change the slope of the VSE [298, 299, 301].

While the data thus appears to be qualitatively and quantitatively consistent with both prior IR and SFG studies, it is clear that simply fitting the extracted center frequencies (or line widths or intensities) with a line provides little insight into the mechanism by which the external field affects the spectral response nor is there any electrochemcial justification in spectroelectrochemical cells (see Figure 6.1 B)) for choosing to break this potential range into two segments at 0.7 V vs. RHE (i.e. there is no current peak in the CV that suggests a surface reaction at this potential). Combining equations 6.7 and 6.8 allows the derivation of an expression for the potential dependent peak center frequency (see appendix section C for detailed discussion of the derivation):

$$\omega_{\Delta V} = \omega_{pzc}\sqrt{1 + \frac{\alpha_\nu L_{ext}\Delta V}{1 + \alpha_e L_{ext}\Delta V}} \tag{6.9}$$

where the electronic polarizability α_e is set to be 1.775 Å^{-3} as mentioned in the theory section above. The three unknown parameters in equation 6.9 are the center frequency (ω_{pzc}) and vibrational polarizability (α_ν) at the PZC and the scaling factor L_{ext} between the local field and the externally applied potential.

As demonstrated in Figure 6.6 the VSE can be well reproduced by this model. I find, given the fit displayed in Figure 6.6 that $\alpha_\nu = 0.4$ Å^{-3}. While no independent insight into the vibrational polarizability of interfacial sulfate exists, our extracted value is similar to other strongly interacting adsorbates on metal surfaces: e.g. for CO on Pt(111) $\alpha_\nu = 0.52$ Å^{-3} [301]. While independent evaluation of L_{ext} is challenging, we can at least compare the product: $L_{ext}\Delta V$. This quantity varies from 0.52 to 1.55 Å^{-3} with a change in external bias of 0.5 - 0.9 V vs. RHE. This local field is of the same order of magnitude as that sensed by a single sulfate anion on Pt(111) in a recent DFT simulation [296]. Finally, from the fit I determine $\omega_{pzc} = 1168$ cm^{-1}. With these parameters in mind the physics of the problem become clear: a linear perturbation of molecular polarizability with changing bias leads to a change in center frequency with bias that is nonlinear, as predicted in equation 6.9. In this picture the slope of the change in frequency with external bias continually decreases due to the increasing polarization of interfacial sulfate[10].

It is worth pointing out that this kind of nonlinearity only becomes obvious when two conditions are met: (i), the net local field (L_{pzc} in equation 6.6) is small at the PZC; (ii), change of the potential is sufficiently large (the second terms in the denominator and the numerator of equation 6.9 are close to unity). As shown in appendix section C, a too large net local field at the PZC or a too small change of the local field as a function of the external bias will only cause an apparently linear change of the centre frequency with potential (see appendix section C for a numerical exploration of this effect). I thus expect that the extent to which a particular system has a nonlinear shift in centre frequency

[10]Note that a nonlinear relationship of polarizability to applied bias would only serve to amplify this trend: small changes in external bias would lead to even larger decreases in slope.

with applied bias will depend sensitively on local structural parameters (coverage, dipole moment, etc.). Presumably it is this relationship which explains why similar studies of other systems, particularly recent, high resolution work by Lian and coworkers and Dawlaty and coworkers, see only a linear dependence of centre frequency on applied field [294, 295, 275, 289, 297, 305, 306, 307, 308, 309].

The potential dependent peak amplitude of the data in Figure 6.2 is shown as black triangles in Figure 6.7, and the corresponding fit of the model to the data shown as a solid red line. The parameter n in the numerator of equation 6.7, which describes the dependence of the hyperpolarizability on the external bias, is determined from a global fit of both the peak centre frequency and the peak amplitude by linking the vibrational polarizability, α_ν, and the local field factor, L_{ext}, as described above. The n was determined to be 3.3, quite similar to that expected if the polarizability is linearly modulated by the applied field (3, as discussed earlier). It is clear from inspection that the presented model overestimates amplitudes from 0.8 - 0.9 V vs. RHE.

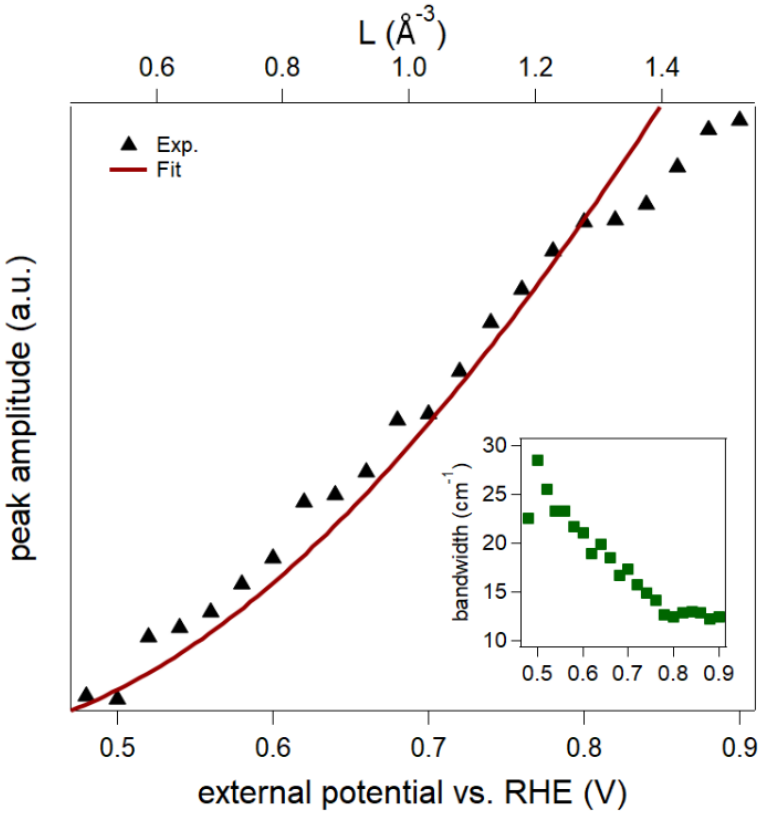

Figure 6.7: Normalized peak amplitude as a function of applied external potential. The black triangles represent the experimental data, while the solid red line shows the simulated peak amplitude as a function of local field factor according to equation 6.7. The inset displays the peak bandwidth as a function of the external electrode potential.

I cannot offer a definitive explanation for this discrepancy but note that the CVs in Figure 6.1 B) also show small oxidation (forward scan) and reduction (reverse scan) currents over this potential range. These currents are consistent with a change in surface structure, or chemical reaction, occurring over this potential range that is clearly not accounted for in the model.

In the model developed in the section 6.2 I, implicitly, treated the bandwidth as a potential-independent. However inspection of the data, and the bandwidth extracted from the data and plotted in the inset of Figure 6.7, clarifies that the bandwidth decreases monotonically with increasing potential from 0.5 - 0.8 V vs. RHE and that at potentials above 0.8 V vs. RHE it is potential independent. Also at 0.8 V vs. RHE the amplitude starts to deviate from the monotonic behavior it showed from 0.5 - 0.8 V vs. RHE. The observed change in bandwidth from 0.5 - 0.8 V vs. RHE can be rationalized within the framework of the so-called electronic friction theory, if we assume that the bandwidth is mostly determined by lifetime broadening, as is the case for CO adsorbed on Pt(111) and Cu(100) both in UHV and in electrochemical systems [310, 311]. Within this approach, the spectral bandwidth of an adsorbate vibration is proportional to rapid, thermal, charge density oscillations between the Fermi level of the metal surface and an antibonding orbital of the adsorbate during the vibrational period [310, 311]. Applying a positive potential to an electrode shifts its Fermi level downwards in energy thus causing the adsorbate antibonding orbital to be populated less frequently during the vibrational period, and, therefore, the linewidth to narrow. This linewidth narrowing has also been observed by others and attributed to a surface reconstruction, or chemical reactions [295, 275]. I show here that it is not necessary to invoke such effects to rationalize the potential dependent centre frequency and intensity of adsorbed sulfate and so strongly suggest any conclusions about potential dependent line widths should be revisited. Unfortunately, quantifying the potential dependent change in line width requires detailed insight into the electronic structure of the electrode/electrolyte interface beyond that accessible from time averaged vibrationally resonant SFG spectroscopy of the Pt(111)/electrolyte interface. One possible solution to this problem would be electronically resonant pump-probe SFG spectroscopy.

6.3 Perchlorate Adsorption to Pt(111) Monitored by SFG

The last two sections were concerned with the adsorption of sulfate on Pt(111) and its behavior as a function of potential. As noted in section 2.1.3 and explored immediatly above, sulfate adsorbs specifically (forms chemical bonds) to this surface; however, its electronic polarizability is small [38, 39]. On the contrary, perchlorate interacts only very weakly with the surface, but its electronic polarizability is high [38, 39]. To explore this opposite end on the reactivity and polarizability spectrum, we investigate here the potential dependent interaction of perchlorate anions with a Pt(111) electrode in 0.5 M $HClO_4$ solution.

Perchlorate anions are known to adsorb at hydrophobic interfaces of aqueous perchlorate solutions with, e.g., air [312]. On Pt single crystal electrodes perchlorate anions influence the surface oxidation, presumably by interacting/competing with OH [51]. Furthermore, on polycrystalline Pt adsorption of a species whose mass is consistent with $ClO_4^-{\cdot}2H_2O$ was observed during cyclic voltammetry in 0.1 M $HClO_4$ by a quartz microbalance measurement [313]. Further evidence for perchlorate adsorption on Pt(111) comes from IRRAS measurements of a Pt(111) electrode as a function of potential [314]. The authors have observed a resonance around 1234 cm^{-1} that appears around 0.52 V vs. RHE, blueshifts with increasing potential, reaches a maximum in intensity around 0.72 V vs. RHE, then decreases in intensity and finally disappears by 1.02 V vs. RHE. The observation of a perchlorate mode around 1234 cm^{-1} appears reasonable because perchlorate's triply degenerate stretching vibration (ν_3, C_{3v} symmetry) in bulk electrolyte is at 1102 cm^{-1} [315] and vibrational modes often blueshift when molecules are adsorbed to (positively charged) metal electrodes, see reference [314] and the discussion of sulfate and bisulfate modes earlier. Even though OH adsorbs from 0.6 V vs. RHE on, the decrease in intensity is argued to result from competitive OH adsorption (the authors assume that perchlorate adsorbs directly on the surface). Unfortunately, the resonance that the authors assign to perchlorate is partially overlapped by a more intense solution feature that presumably is a consequence of the referencing necessary to extract interfacial information from linear spectroscopies. An interface specific SHINERS study of Pt(111) surface oxidation in 0.1 M $HClO_4$ by Huang and coworkers assigned a 933 cm^{-1} resonance to adsorbed perchlorate, but did not see the 1234 cm^{-1} mode [222]. The 933 cm^{-1} mode appears with the onset of OH adsorption at around 0.6 V vs. RHE in this study and its intensity increases with increasing OH coverage as the potential is ramped up. The signal intensity diminishes as surface OH is converted during the further course of surface oxidation. Huang and coworkers conclude that perchlorate does not interact with the bare Pt(111) surface, but with the OH adlayer. This assumption is consistent "with the conventional wisdom that perchlorate is not specifically adsorbed" [222].

Here I monitor the 1234 cm^{-1} mode of perchlorate adsorbed to Pt(111) and compare it to the 1250 cm^{-1} mode of sulfate discussed in the last section. This comparison should give insight into how a vibrational mode is affected by chemical bonding plus interfacial electric

fields (in the case of sulfate) vs. only interfacial electric fields (in the case of perchlorate). Furthermore, additional knowledge about the poorly understood behavior of perchlorate at the Pt(111)/electrolyte interface is expected.

Results and Discussion

I monitor a Pt(111) electrode surface in the frequency region from 1100 - 1400 cm^{-1} by SFG while running cyclic voltammetry in 0.5 M $HClO_4$ in Figure 6.8. The figure shows SFG spectra after correction for the intensity distribution of the IR beam by dividing the raw data with the nonresonant background of a Au mirror. A resonant feature centered aroud 1240 cm^{-1} emerges at 0.56 V vs. RHE and grows in intensity with increasing potential, consistent with the above mentioned prior spectroscopic studies [314, 222]. This peak likely corresponds to a Cl-O stretching vibration akin to that of sulfate. The feature is fairly broad and presumably consists of two resonances already at 0.56 V vs. RHE with the lower frequency shoulder becoming increasingly apparent with increasing potential. The higher frequency peak is labelled "peak 1", the lower frequency peak "peak 2" in Figure 6.8. While peak 1 shifts towards higher frequencies with increasing potential, peak 2 shifts towards lower frequencies.

The centre frequencies of peak 1 and 2 have been extracted by a line shape analysis based on the theory presented in section 3.1 and are plotted as a function of potential in Figure 6.9. The centre frequencies of peak 1 and 2 bifurcate at 0.65 V vs. RHE: peak 1 shifts to higher frequencies, peak 2 towards lower frequencies.

The presence of two perchlorate peaks with distinctive potential dependent behavior hints at the existence of two distinct interfacial perchlorate subpopulations that presumably have a different solvation environment and/or interact differently with the surface. A further notable difference with the sulfate/Pt(111) data and the data recorded at the air/water interface [312] is that perchlorate apparently does not adsorb on the bare Pt(111) surface. This potentially is a consequence of hydrophobicity of the interface: for Pt(111), a hydrophobic first water adlayer was predicted (no H-bonds towards the bulk electrolyte) [131]. In agreement with the work by Huang and coworkers [222] the perchlorate vibration only becomes apparent at potentials at which OH adsorption starts. As suggested by the authors, this observation is consistent with a scenario in which ClO_4^- adsorbs due to an interaction with preadsorbed OH.

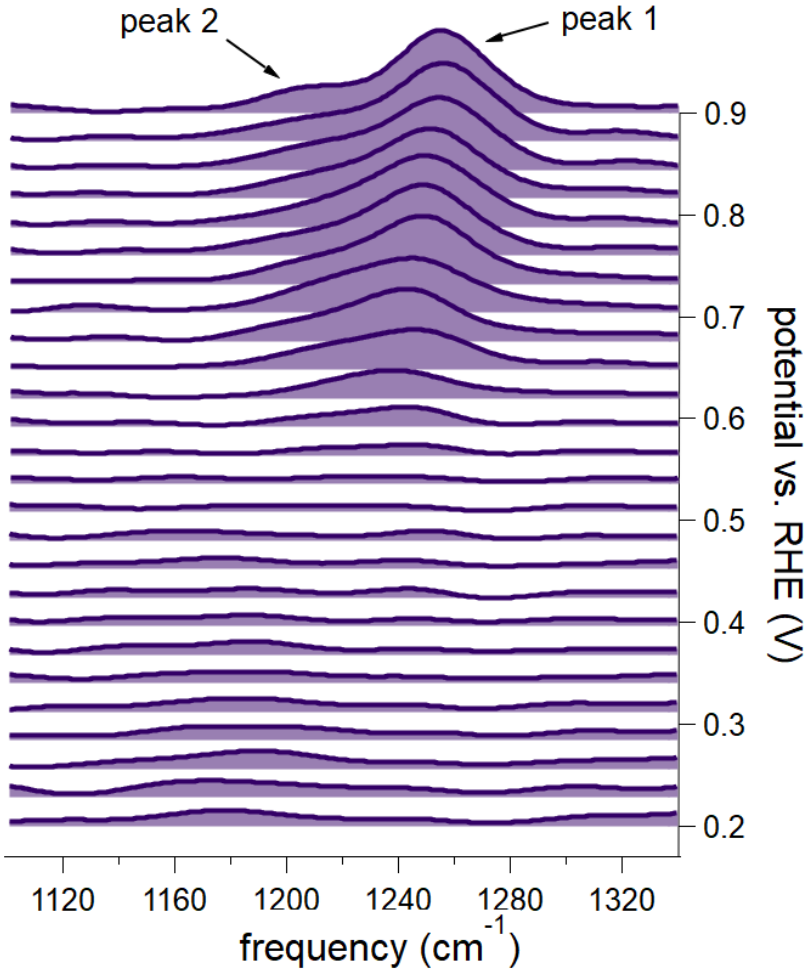

Figure 6.8: Potential dependent SFG spectra of a Pt(111) electrode in 0.5 M $HClO_4$. The spectra have been corrected for the frequency dependent intensity distribution of the IR beam by division with a spectrum of the nonresonant background of a Au mirror. Details of the optical measurement are identical to the sulfate/Pt(111) measurements.

Given the mentioned differences to the sulfate data, one similarity is worth pointing out: despite the different valencies (singly vs. doubly negatively charged), other molecular properties like polarizability and electronegativity and the differences in bonding (specifically vs. nonspecifically) the centre frequencies of perchlorate and sulfate vibrations are fairly similar. This proximity probably is a consequence of their identical structure (tetrahedral oxyanions) and the fact that they are isoelectronic: in infrared spectroscopy, the vibrational response of sulfate and perchlorate in bulk salt solutions is very similar, both show a fairly broad (ca. 100 cm^{-1}) resonance centered around 1100 cm^{-1} [278, 316].

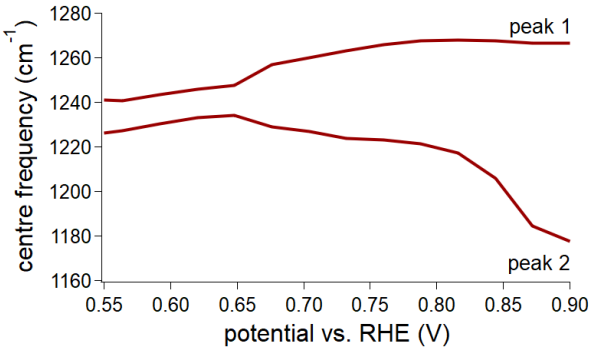

Figure 6.9: Potential dependence of the two peak centre frequencies of perchlorate adsorbed to Pt(111).

However, both the sulfate and the perchlorate vibrations are blueshifted by around 150 cm^{-1} at the Pt(111)/electrolyte interface. I assume that this is a consequence of increased anion polarization at the electrified interface due to the strong interfacial electric fields. The VSE of peak 1 is also qualitatively similar to the VSE of the sulfate mode in the previous section. This is, however, not true for peak 2. The centre frequency of peak 2 is redshifted with increasing potential. This implies that peak 2 either represents a different type of interfacial perchlorate (different bonding to the surface and/or different solvation environment), or a different vibrational mode of the same species that is affected differently by the interfacial field [287].

The stretching modes of sulfate and perchlorate adsorbed to Pt(111) in the presented SFG spectra are both blueshifted with respect to the modes in bulk electrolyte. If the blueshifting of stretching vibrations of tetrahedral polyoxoanion adsorbates at the Pt(111)/ electrolyte interface is truly general was further investigated in 0.5 M H_3PO_4 whose anions are also tetrahedral and isoelectronic to sulfate and perchlorate. The polarizability of phosphoric acid derived anions is intermediate between sulfate and perchlorate. Phosphoric acid is a triprotic acid and in 0.5 M H_3PO_4 (pH≈2) the fully protonated form H_3PO_4 is the dominant bulk species. Accordingly, acid-base chemistry at the interface is possible and following the results from the sulfate study in section 6.1, where I concluded that the pK_A value of bisulfate anions is substantially lowered at the Pt(111)/electrolyte interface, perhaps expected. This expectation is further strengthened because the pK_A values of bisulfate and phosphoric acid are essentially identical (≈2) [317]. Therefore, in contrast to the sulfate and perchlorate measurements, a discontinuous behavior of vibrational modes may be expected, e.g. due to abrupt deprotonation at a certain threshold potential.

The potential dependent SFG spectra show resonances in a similar frequency region around 1200 cm^- and a rich, potential dependent behavior that is not trivial to understand and likely the consequence of acid-base chemistry (as expected). The dataset can be seen in appendix section C.

The results of sulfate, perchlorate and phosphate experiments in this chapter imply that the vibrational response of these anions adsorbed to a Pt(111) electrode, oversimplified,

has two components: one that comes from the anion itself, and one from the interaction of the anion with the electrode and/or the interfacial electric field. Unfortunately, neither one can be extrapolated from bulk anion properties (as, for example, illustrated by the shift in pK_A value of bisulfate at the Pt(111)/electrolyte interface compared to bulk electrolyte) and (possibly new) structural in situ probes for the electrified interface are necessary to understand these components.

The former component, the individual behavior of anions at the electrified interface, proves to be nontrivial to understand. For example, the here reported behavior of sulfate and perchlorate vibrations as a function of potential do not allow by themselves to conclude which anion is strongly interacting with the surface and which is weakly interacting. If at all, this information is encoded in the absolute signal strength, a quantity that generally can not be compared for different measurements (because of differences in local surface quality, electrolyte layer thickness, laser beam characteristics, alignment of optics and sample, etc.). However, the sulfate signal was *substantially* larger than perchlorate's which, despite the mentioned difficulties, points towards a stronger interaction with the electrode.

As for the latter component, the work presented in this chapter shows that specific vibrations of tetrahedral polyoxoanions adsorbed to a Pt(111) electrode, i.e., the stretching vibration of the uncoordinated X-O moiety (where X is S, Cl, or P), are blueshifted presumably by additional X-O bond polarization through the strong interfacial electric field. Future work in this direction may use the extent of this blueshift (from the stretching vibration in bulk electrolyte) to quantify the electric field strength at a certain electrode/electrolyte interface. Such an "interfacial voltmeter" is desirable from a fundamental, this is maybe the closest one can get to measuring a Galvani potential (see section 2.1), and a more practical point of view, because it gives direct access to measuring one fundamental driving force of electrochemical reactions. This is, of course, a formidable challenge because the centre frequency of a vibrational resonance at an electrified interface is an intricate function of many parameters, but the work presented in this thesis may help in disentangling the individual components.

One particularly interesting open question this interfacial voltmeter may help answer is the actual makeup of the electric double layer, e.g. position and function (purely electrostatic, or specific interaction with the adsorbed anions) of cations.

This discussion, and this thesis in general, highlights the complexity of seemingly simple electrode processes (anion adsorption, the HER, etc.) and stresses the need for in situ and operando structural probes for the electrified interface and it seems that a combination of complementary tools and theory will be necessary for a complete understanding of these processes.

Chapter 7

Conclusion and Outlook

Electrocatalysis and Climate Change

In principle, electrocatalysis offers solutions to many energy and environmental problems that our civilization is facing, most notably man-made climate change. The perhaps most promising approach to mitigate the negative effects of fossil fuel combustion on our climate and to improve air quality is building an energy infrastructure based on hydrogen from water electrolysis where the required energy input for water splitting comes from renewable sources.

Several technological approaches to water electrolysis exist that operate under different conditions, most notably alkaline and polymer exchange membrane (PEM) electrolysis (as discussed in the introduction 1). Regardless of approach, the actual splitting of water molecules happens on the catalyst, for which Pt and Ir are used in PEM electrolyzers as cathodes and anodes, respectively. The usage of noble metals makes these devices costly and their economic success could be drastically enhanced by replacing Pt and Ir with cheaper alternatives. However, catalyst design is still stuck on a trial and error basis because the mechanisms of the catalytic reactions are only poorly understood. So far, even for the most studied systems (water splitting on Pt and Ir), many established experimental facts can not be explained by the current mechanistic understanding.

In part, this is the case because the electrochemical interface is complex: all aspects of the electrode and electrolyte can potentially influences reaction rates (see Figure 7.1). In particular for the former the precise details of the surface atomic structure (that in turn dictates the interfacial solvent structure) and the oxidation state of the atoms are crucial for electrocatalytic activity.

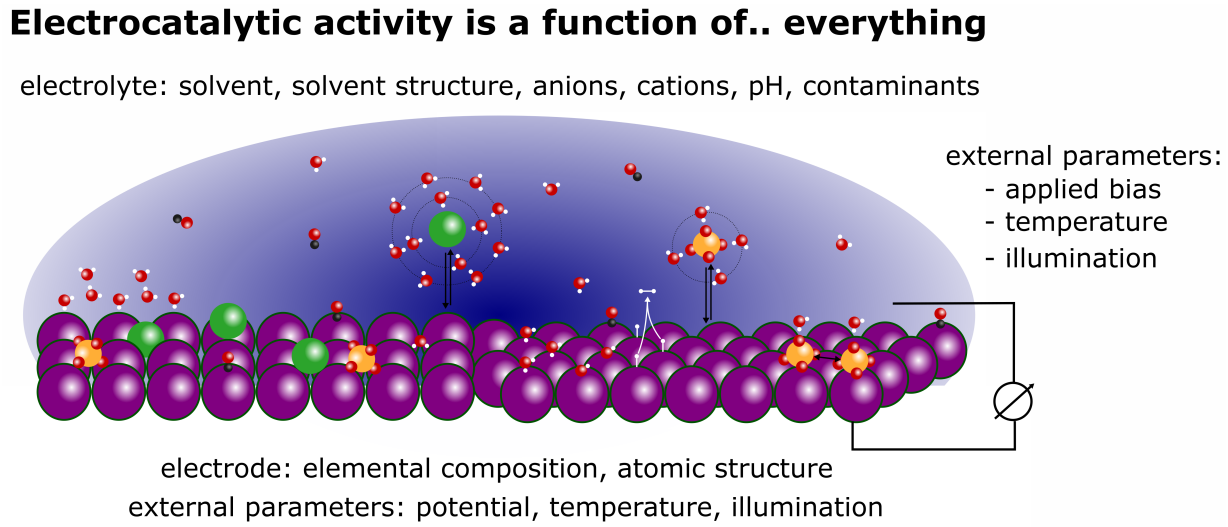

Figure 7.1: Influences to electrocatalytic activity.

In part, the reaction mechanism for water electrolysis is poorly understood because probing interfaces, and solid/liquid interfaces in particular, is challenging and because observing the reaction under steady-state conditions is insufficient for the determination of its mechanism. Monitoring the reaction under steady-state conditions is, for example, not suited to distinguish between adsorbates of the reaction of interest and of parallel reactions and spectator species. Similarly, the order of steps in a consecutive reaction mechanism can not be determined. The perhaps most promising approach to gain experimental insight into reaction mechanisms is by performing time resolved perturbation experiments. Unambiguous information on the reaction mechanism can be obtained by providing a temporally short pulse of reactants and monitoring how these reactants evolve on the natural timescale of the reaction (see section 2.2 for a detailed discussion of this issue).

As mentioned above, a reaction's mechanism and its rate crucially depend on surface structure on the Å scale [10]. For inhomogeneous surfaces (like polycrystalline metals [11]) this implies spatial heterogeneity in reactivity and reaction mechanism. Resolving this heterogeneity is desirable because virtually all industrially relevant catalysts have heterogeneity on the nm - mm lengthscale [167].

In this thesis I have investigated electrolytic water splitting on Pt and Au, materials that are important both in application and fundamental science. For the reductive half-cell reaction of water splitting, the hydrogen evolution reaction (HER), on Pt I have answered (or have tried to answer) open questions in chapter 4 that will improve our understanding of the HER reaction mechanism and help us progress towards better catalysts. The most important questions I adressed are: i) how does H adsorb to Pt prior to (at this point called "underpotentially deposited H", Pt-H_{UPD} [69, 70, 49, 30, 31, 24]) and during the HER (prior work came to the conclusion that during the HER a second type of H, "overpotentially deposited" H, Pt-H_{OPD}, emerges as the reaction intermediate [62, 63]) on various Pt single

crystle surfaces? ii) How are Pt-H_{UPD} and Pt-H_{OPD} related? Does Pt-H_{OPD} emerge from, or interact with Pt-H_{UPD}? iii) Can we get insight into the true elementary steps of the reaction on their natural fs timescale? Which step is rate-limiting for the HER in acidic electrolyte and is this a function of surface structure?

For the oxidative half-cell reaction of water splitting, the oxygen evolution reaction (OER), I have worked on the relationship of surface oxidation and OER activity on Au and Pt electrodes (surface oxidation is a necessary prerequisite for the OER on all metals [24, 156, 220]) and I have investigated spatial heterogeneity in OER activity on Au electrodes. In this thesis I have addressed the following questions in chapter 5: i) Can we spatially resolve surface oxidation and OER activity on Au electrodes? ii) Can we link trends in surface oxidation to trends in OER activity on Au electrodes? Which oxidation state is active (or more active) for the OER on a Pt electrode?

As alluded to in Figure 7.1, the composition of the electrolyte can dramatically influence electrocatalytic activity and is known to for water splitting [35, 34, 36, 37]. This is, at least in part, a consequence of anion - electrode interaction. Many open questions remain in the field of anion - electrode interaction, even for the most studied/used interfaces: Pt with sulfuric, or perchloric acid. In this thesis, I have addressed the following questions in chapter 6: i) What is the chemical identity of the adsorbate on Pt(111) in 0.5 M sulfuric acid, sulfate or bisulfate? ii) How does changing the interfacial electric field strength (by tuning the applied bias) affect spectroscopic observables? iii) Can we detect the adsorption of "weakly" (or nonspecifically) adsorbing anions (such as perchlorate) and what does "weakly" adsorbing even mean microscopically?

The Hydrogen Evolution Reaction and H Adsorption on Pt

The main goal for the HER was to gain mechanistic insight by triggering the reaction with an ultrashort optical pulse and monitoring it with vibrationally resonant sum frequency generation spectroscopy (SFG) on the natural fs timescale of charge transfer. I approached this endeavor in three steps: i) Monitoring the HER reaction intermediate Pt-H with SFG as a function of potential and surface structure on Pt(111) and Pt(110) without ultrashort light trigger; ii) Clarifying that ultrashort 800 nm light pulses, depending on the applied potential, can trigger charge transfer from the electrode to Pt-H, or the HER; iii) Investigating the temporal evolution of the Pt(111)/electrolyte interface during and after excitation with an ultrashort 800 nm pulse with SFG by scanning the time delay between fs trigger and SFG probe.

i) Monitoring H Adsorption on Pt(hkl) with SFG

Novel insight into the adsorption of H on Pt(110) and Pt(111), especially in the underpotential region, is gained. So far, H_{UPD} is considered to be located (immobile) in three-fold hollow sites on Pt(111) (and other multi-coordinated adsorption sites on different crystal

faces) [24]. However, in sections 4.1 and 4.3 of this thesis, supported by reference [129], I conclude that H_{UPD} in these three-fold hollow sites exists in an equilibrium with bridge and atop bonded Pt-H on all timescales and furthermore, that atop bonded Pt-H is in an equilibrium with a solvated interfacial proton state in which the proton sits immediatly above the Pt atom. This conclusion is in line with the thermodynamic description of chemical equilibria: the formation and oxidation of H_{UPD} (both processes occur via atop Pt-H [129]) are continuously ongoing, competing processes and their relative rates (that are tuned with the potential) determine whether the H_{UPD} population increases, decreases, or is constant.

The equilibrium of H adsorbed to different Pt surface sites and the solvated interfacial proton is illustrated in Figure 7.2:

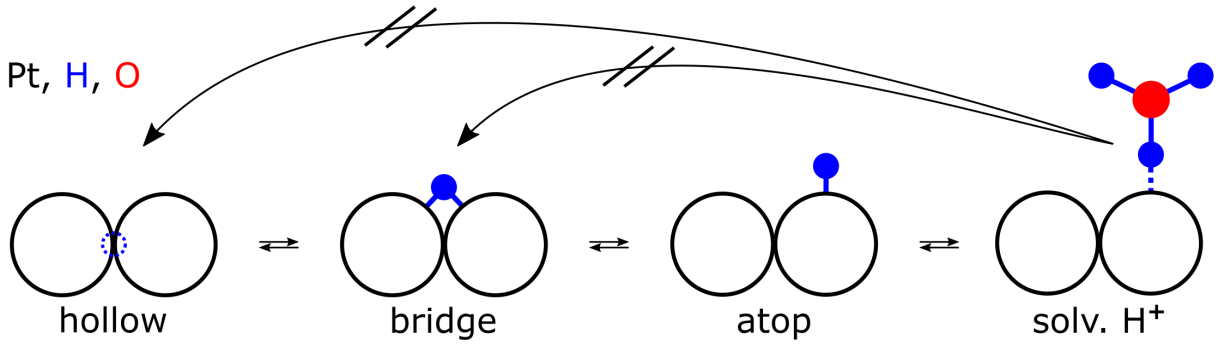

Figure 7.2: Cartoon representation of H adsorbed on Pt: the formation and oxidation of Pt-H are in equilibrium, consequently a steady-state population of bridge and atop bonded Pt-H exsists also in the UPD region.

ii) Initiating Charge Transfer and the HER with fs Optical Pulses

In section 4.2 I conclude that the charge transfer necessary for H_{UPD} formation/oxidation is only possible when the interfacial solvent has a specific structure that allows for it. The structure of the interfacial solvent is dependent on the applied bias [142, 143] (and section 4.2), which, together with the conclusion that charge transfer is only possible when the solvent accomodates it, implies that the likelihood of charge transfer at the interface continually changes with potential. This change is reflected in the potential dependence of the charge transfer resistance at the Pt/electrolyte interface. In the UPD region of polycrystalline Pt electrodes, the charge transfer resistance is minimal at potentials of current peaks (H_{UPD} formation/oxidation on structural motifs different from (111) terraces) in the cyclic voltammogram (CV). This has been observed both on ultrafast timescales (with charge transfer initiated by fs optical pulses, see section 4.2) and in time-averaged measurements [148]. Apparently, at these potentials the interfacial solvent structure is optimal for the respective charge transfer reactions.

Triggering charge transfer and the HER with ultrashort optical pulses enabled, to the best of my knowledge, for the first time experimental insight into the kinetics of a true elementary step of the HER. The notion of a "true elementary step" is used here as a distinction from the Volmer/Tafel/Heyrovsky reactions, which are not elementary steps, but sequences thereof. The charge transfer step of the HER was concluded to be rate limiting on Pt electrodes in acidic electrolyte once reactants and the interfacial solvent are in the optimal geometry (that is dictated by the external bias) for the reaction.

iii) Femtosecond Resolved Temporal Evolution of the Pt(111)/ Electrolyte Interface During and After Charge Transfer

In section 4.3 I concluded that mobility on a subpicosecond timescale of H adsorbed to Pt has major implications for the HER. While possible for all other Pt-H species, a particular Pt-H subpopulation (that is associated with a specific adsorption site) can not diffuse from the atop adsorption site to bridge and hollow site bonded Pt-H on subpicosecond timescales when the potential is not close to the reversible HER potential at 0 V vs. RHE (but still inside the UPD region, e.g., at 0.2 V). Close to the HER onset potential this Pt-H subpopulation also becomes mobile on subpicosecond timescales. Because of this abrubt change in behavior close to the reversible HER potential, this Pt-H subpopulation is assigned to the HER reaction intermediate, H_{OPD}. This assignment is supported by prior (not time-resolved) spectroscopic studies that have assigned a vibrational mode to H_{OPD} whose frequency partially overlaps with that of the Pt-H subpopulation discussed here, see Table 4.1 for references.

This work is, to the best of my knowledge, the first to report spectroscopic evidence for the interrelation of H_{UPD} and H_{OPD}. A Pt-H_{UPD} subpopulation turns into H_{OPD} close to the HER onset potential by a change in the interphase that enables mobility of this Pt-H subpopulation on subpicosecond timescales.

Future work in this field, the spectroscopic investigation of the HER and H adsorption on Pt, should repeat the experiments presented in this thesis in alkaline media. A comparison to the situation in acidic electrolyte, investigated here, will provide us with direct insight about why the HER activity on Pt decreases two orders of magnitude when going from acidic to alkaline conditions. Further information on the interrelation of H_{UPD} and H_{OPD} and in general, whether H adsorbates on Pt interact with one another could be obtained from 2D IR experiments, or pump-probe experiments with a resonant excitation around 2000 cm^{-1}. Finally, action spectroscopy of the HER on Pt is worth pursuing. In such an experiment the Pt electrode is illuminated with a high intensity, narrowband IR beam while the HER is running at a low rate. The IR frequency is tuned from 1700 - 2400 cm^{-1} while the current is recorded. When the IR excites the intermediate of the rate determining step, weakening its bond, the activation barrier is lowered and the rate enhanced (if bond cleavage is rate limiting). This approach could potentially eliminate the ambiguity that arises from peak assignment based on the correlation of, e.g., peak intensity with reaction rate (that is tuned via potential, temperature, or other external parameters).

For the first time, this would enable a direct correlation of a Pt-H mode with HER activity (that *all* spectroscopic studies of the HER are lacking so far).

The Oxygen Evolution Reaction

Catalyst improvement can also be approached from the materials side (as opposed to the reaction side via mechanistic studies). If we identify which materials and which structural features of these materials (like surface crystallographic orientation, or type of steps) are particular active for a reaction, then we can build a catalyst that ideally only consists of these most active features. This is desirable if the respective catalyst materials are expensive, as for example in current generation PEM electrolyzers, because this approach minimizes the required amount of catalyst. I have followed this approach for the OER on poly- and nanocrystalline gold electrodes in chapter 5. The investigation of the OER is complicated by the fact that the reaction only occurs on oxidized surfaces that are further oxidized during the course of the reaction. For this reason an imaging tool was used that is both sensitive to surface oxidation and oxygen evolution activity: second harmonic microscopy (SHM). As mentioned above, spatially resolving surface reactions also is a prerequisite for mechanistic studies on heterogeneous catalysts.

The oxidation state of catalyst atoms (which is inherently linked with structure) also greatly influences OER activity [220]. Within the scope of this thesis, I have tried to manipulate the oxidation state of a Pt microelectrode with intense, fs near-IR illumination while running the OER, hoping to gain insight into the impact of different Pt oxidation states on OER activity.

In chapter 5, I investigated i) the spatial heterogeneity in the electrooxidation and surface reconstruction during potential cycling on poly- and nanocrystalline gold electrodes and, on the same electrodes, ii), spatial heterogeneity in OER activity: are trends in surface oxidation linked to trends in OER activity?; iii) The impact of higher oxidation states of Pt on OER activity on a Pt microelectrode.

i) Spatial Heterogeneity in Au Electrooxidation and Surface Reconstruction

SHM in a wide-field configuration was used in situ to investigate poly- and nanocrystalline Au electrodes (with grain sizes on the order of tens of µm and nm, respectively) during cyclic voltammetry. I show that while the SH intensity averaged over the entire field of view (FOV) follows a similar trend with potential as previously reported [113, 186], it varies strongly on the (sub)micron level: spatial averaging obscures much of the ongoing surface physics and chemistry.

The parabolic model (PM[1]) was fitted to every pixel of the Au_{poly} data from 0 - 0.4

[1]The PM predicts a quadratic increase of SH intensity with increasing potential by assuming a DC field-induced contribution to the nonlinear polarization that contributes to SH emission and is a function of the applied bias. It was successfully applied by prior workers to describe the SH emission of an electrified

V vs. RHE, as no specific anion adsorption occurs in this potential range. As in prior spectroscopic (no spatial resolution) studies [113, 186], the SH intensity averaged over the entire FOV can be well described with the PM. However, the details of SH emission as a function of applied potential (the SH-V curve) are highly local and can strongly deviate from this behavior predicted by the PM. Around 60 % of the surface show a positive quadratic dependence of SH intensity on the applied potential ($Q > 0$ areas/grains) in line with the PM. The remaining 40 %, however, show a *negative* quadratic dependence of SH intensity on applied potential ($Q < 0$ areas/grains), a behavior that has not previously been reported. It is likely that the $\pm Q$ areas coincide with different grains of the metal surface (e.g., grains with (111) and (110) like surface atom structure). The SH emission from $Q > 0$ areas is substantially stronger than from $Q < 0$ areas and the (so far reported) spatial average is dominated by $Q > 0$ areas. The parabolic decrease with potential is tentatively explained by anion adsorption to rough and non-equilibrated surface domains at potentials lower than the average point of zero charge (PZC). The SH-V curves of boundaries of $Q > 0$ and $Q < 0$ areas, $\pm Q$ boundaries, change most strongly during repeated oxidation and reduction cycles and are concluded to be most susceptible to potential-induced surface reconstruction during potential cycling. On the nanocrystalline sample, no $Q < 0$ areas and no areas that are particularly prone to potential-induced surface reconstruction could be identified.

Correlation coefficient analysis, a statistics based image analysis, enabled further insight into $Q < 0$ areas where the PM is not valid and into potential regions where anion adsorption and surface oxidation occur. The correlation coefficient is calculated from the shape of the SH-V curve at every single pixel vs. the FOV's average SH-V curve for an arbitrary potential interval (without the limits on potential of the PM). A pixel wise comparison of the correlation coefficient in two successive potential cycles then gives insight into areas that undergo changes in surface structure during potential cycling. Areas that show a substantial change in correlation coefficient from one potential cycle to the next coincide well with $Q < 0$ areas. This analysis suggests that $Q < 0$ areas are less stable with respect to potential-induced surface reconstruction than $Q > 0$ areas. On the nanocrystalline electrode no such areas can be found and the entire FOV shows a homogeneous behavior (in the correlation coefficient analysis, as well as in the PM analysis). This implies that the extent of rough and non-equilibrated surface domains (that are particularly prone to surface reconstruction) is highly sensitive to details of the surface, such as grain size, boundaries and nature thereof. The correlation coefficient analysis further suggests that the extent of potential-induced surface reconstruction during potential cycling depends on whether you start with a reduced surface, oxidize and reduce it again, or start with an oxidized surface, reduce and oxidize it again.

SH imaging under potential control with following correlation coefficient analysis could be a valuable tool for determining particularly corrosion resistant surface structural motifs

interface as the potential is tuned [111, 113]. The PM is only valid in the absence of specific ion adsorption, because in this case the second- and third-order nonlinear susceptibilities would become a function of the applied bias and the PM assumes they are not. This also implies that the PM can not be used to describe SH emission during surface oxidation.

of a given material (e.g. for coatings).

ii) Spatial Heterogeneity in OER Activity

In section 5.1.2 I characterized the same heterogeneous polycrystalline Au foils with a grain size of tens of µm and nanocrystalline Au electrodes composed of tens of nm big clusters grown by physical vapour deposition with SHM while performing voltammetry and chronoamperometry at more anodic potentials to investigate the OER[2]. The use of SHM enabled us to directly identify and characterise active sites/areas for the OER operando at the interface of a partially oxidized, non-ideal electrode and a liquid phase. At potentials positive of the onset of the OER, we observed that the evolution of O_2 bubbles is restricted to small, tens of μm^2 (0.28-0.72 % of the total electrode surface area), but highly active areas on the polycrystalline foil. The current required for O_2 bubble formation quantitatively explains the current measured over the entire electrode over a range of moderately anodic potentials. The relative area covered by active sites is consistent with prior in-situ and operando work in gas phase catalysis, but considerably lower than the active site estimates for electrocatalysts from ex-situ studies. Because understanding the relationship of local oxidation and O_2 bubble formation on heterogeneous Au foils is challenging, I conducted similar experiments on the nanocrystalline gold sample at a potential high enough for a steady state OER current, but low enough to avoid widespread bubble formation on the smooth surface. In this bias window only at a single defect (that was stable with respect to repeated surface atom rearrangement during electrochemical cleaning) and after the formation of a sufficiently thick oxide layer, did bubbles appear. The results of both experiments suggest that this class of highly active areas/active sites for the OER on gold needs a structural defect penetrating to the bulk and a sufficiently thick layer, or specific type, of oxide to form. Finally, in a third type of experiment, the production of O_2 bubbles was observed on the polycrystalline foil at potentials below the onset of the OER in active areas that were unstable under potential cycling. Such metastable active sites are consistent with those suggested by Burke and coworkers previously as the catalytically active entity in the incipient hydrous oxide/adatom mediator (IHO/AM) model of electrocatalysis. This model explains the electrocatalytic activity of noble metals by the presence of undercoordinated metal atoms (a minority species) that oxidize significantly earlier than the remainder of the surface. These undercoordinated, oxidized metal atoms, the incipient hydrous oxide, then participate in the catalytic reaction [216, 217, 218, 219].

This work is, to my knowledge, the first to describe the spatial heterogeneity of an electrocatalytic reaction at the electrode/aqueous electrolyte interface under reaction conditions through wide field imaging of product formation. While the spatial resolution of the microscope precludes molecular level structural insight into the composition of the active sites and, presumably nm scale, bubble nucleation, these results clearly suggest that a combined program of higher resolution, near field, operando microscopy and systematic electrode modification holds out the hope of understanding the relationship of surface

[2]This paragraph was modified from my own publication [33].

structure and active site abundance and in doing so creating Au electrodes with dramatically enhanced reactivity. The particular issues I address in this study – separating the spatial heterogeneity of oxidation and the OER on Au – are obstacles in the optimization of essentially all practical OER catalysts. As a result, and because the operando SHM approach described here is not restricted to Au or electrooxidation/OER (another important application is the investigation of bubble formation and surface wetting behaviour of bubbles in water electrolyzers [318]), I expect this work to be of wide interest. Furthermore, the PM analysis offers the exciting prospect of mapping the PZC, a parameter directly determining the electrocatalytic behavior of a surface (or parts thereof, as the PZC is highly local), while simultaneously monitoring reactivity.

iii) Which Oxidation State of Pt is Active for the OER?

As discussed above, surface oxidation is a prerequisite for the OER and the oxidation of metal electrodes is continuously ongoing during the OER. This is particularly important, if the oxidation state of the metal ions in the oxide changes with time and/or potential and the OER activity of the metal is influenced by its oxidation state. For Pt, the most important catalyst material in fuel cells and electrolyzers, the influence of the metal's oxidation state on OER activity is subject to debate [249, 220]. In section 5.2 I present an approach to changing the oxidation state of Pt during the OER and assessing the influence of Pt's oxidation state on OER activity operando.

I performed cyclic voltammetry on a Pt microelectrode in acidic solution over a potential range including surface oxidation and the onset of the OER with and without femtosecond, near-IR illumination. The illumination leads to a strong oxidation peak at 1.4 V vs. RHE that was assigned to the formation of PtO_2, whose formation is kinetically hindered in the absence of light [242], despite being thermodynamically stable [259]. The reduction peak of the oxide formed under illumination in the reverse scan is accordingly enhanced and shifted cathodically to ca. 0.5 V vs. RHE. Potentiostatic experiments in the potential range of oxide formation and the OER display periodic current oscillations that were interpreted as the periodic formation and depletion of an additional, instable, Pt oxide that was assigned to PtO_3. Ex situ XPS measurements confirmed a stronger oxidation of Pt with illumination than without, implying that electrooxidation in the presence of the illumination leads to higher valent Pt oxides than electrooxidation in the dark.

When the electrode is illuminated during the entire potential range including the OER, the current density at the highest investigated potential, 1.8 V vs. RHE, is identical to the current density in the CV without illumination. This indicates that the purely electrochemical OER current is decreased by the presence of the higher valent Pt oxides, as the laser illumination induces an oxide formation current and increases the OER rate by heating and/or the presence of holes and still the current under illumination at 1.8 V vs. RHE just matches the current without illumination. That the higher valent Pt oxides do not catalyze the OER, but only act as a barrier for mass transport is demonstrated in a second, similar experiment in which the electrode is illuminated only in the anodic CV scan from ca. 0.85 to 1.7 V vs. RHE, but not during the OER from 1.7 to 1.8 V vs. RHE. This

experiment also shows the additional oxidation peak at 1.4 V vs. RHE during illumination, but a considerably reduced OER current from 1.7 to 1.8 V vs. RHE after switching off the illumination at 1.7 V vs. RHE. I therefore conclude that higher valent Pt oxides are not active during the OER and only act as a barrier for mass transport on Pt electrodes. These results suggest that the active species for the OER is either a metallic phase, or Pt(+II).

Future experiments may crosscheck the conclusion from above, that the OER active species is either a metallic phase, or Pt(+II), with a similar approach, trying to lower the Pt oxidation state during the OER by reducing the Pt oxide. This could be achieved by photoelectrons that are emitted after X-ray illumination, or by using an electron beam (in an experimental setup akin to transmission electron microscopy cells that utilize ultrathin electron transparent windows and electrolyte layers).

Sulfate and Perchlorate Adsorption on Pt(111)

As mentioned in the introduction to this chapter, the interaction of anions with the electrode strongly influences the activity of many electrocatalytic reactions including water electrolysis. At the microscopic level, however, little is known about this interaction. Even some of the most basic aspects, for example, which chemical state the anion adsorbate of a diprotic acid has, remain open for one of the most studied electrode electrolyte combinations, Pt/sulfuric acid [319, 270, 272, 273, 276]. This uncertainty is likely a consequence of the interaction of the electrode surface with the anion. This interaction influences the chemistry of the anion and its spectroscopic response. Therefore, predictions about the interfacial chemistry of the anion from bulk properties are not helpful and in situ probing is required.

In chapter 6, I i) determined the chemical identity of the anion adsorbate on Pt(111) in 0.5 M sulfuric acid by isotope exchange measurements and vibrationally resonant SFG as sulfate; ii) derived a microscopic model that quantitatively explains the SFG response of sulfate adsorbed on Pt(111) with varying bias; iii) investigated perchlorate (and phosphoric acid derived anion) adsorption on Pt(111) with SFG while tuning the applied bias.

i) Identifying the Chemical Identiy of the Anion Adsorbate on Pt(111) in 0.5 M H_2SO_4

In section 6.1 SFG spectra of a Pt(111) electrode were recorded in H_2SO_4/H_2O and D_2SO_4/D_2O while cycling the applied bias from 0.05 to 0.9 V vs. RHE. In the spectra a single resonance emerges at 0.42 V vs. RHE around 1225 cm^{-1} that increases in intensity and blueshifts with increasing potential. The spectra in protonic and deuteric solutions are quantitatively identical after correcting for the stronger IR absorption of the deuteric solution. I take this to answer the long-standing question, whether bisulfate (HSO_4^-), or sulfate (SO_4^{2-}) is adsorbed on Pt(111) in 0.5 M H_2SO_4: from 0.42 V vs. RHE on, sulfate is adsorbed. For bisulfate a shift in centre frequency would be expected upon isotope exchange due to the change in reduced mass. This is further corroborated by normal mode

calculations performed by collaborators. To the best of my knowledge, this study is the most direct evidence for sulfate as sulfuric acid derived anion adsorbate on Pt(111) at potentials > 0.42 V vs. RHE in 0.5 M H_2SO_4 to date.

That the sulfate vibrational resonance only appears at 0.42 V vs. RHE after the so-called "butterfly" feature and not already with its onset (which marks the beginning of anion adsorption) is explained by the initial adsorption of bisulfate in a bidentate adsorption geometry. The bidentate adsorbed bisulfate's transition dipole moment (for the vibration in the investigated frequency window) is parallel to the surface and hence no SFG resonance is observed. The bisulfate is deprotonated with increasing potential and after a disorder-order phase transition at 0.42 V vs. RHE, tridentate adsorbed sulfate is adsorbed to the surface and observed via its vibrational resonance.

That sulfate and not bisulfate, the bulk anion species, is adsorbed at potentials > 0.42 V vs. RHE in 0.5 M H_2SO_4 is explained by the electrode's surface charge. In a positive potential sweep, bisulfate adsorbs around 0.35 V vs. RHE, almost immediatly after the PZC. With increasing potential the surface is increasingly positively charged and the positive surface charge favors the doubly negatively charged sulfate over the single valent bisulfate and further shifts the acid base equilibrium towards sulfate by expelling H^+ from the interface.

ii) A Microscopic Model for the Spectroscopic Response of SO_4^{2-} Adsorbed to a Pt(111) Electrode

In section 6.2 the potential-dependent shift in sulfate centre frequency (the electrochemical vibrational Stark effect, VSE) and intensity is described with a microscopic model that explicitly accounts for the effects of dipole-dipole interaction[3]. This approach is inspired by many prior studies of the coverage dependent shift in adsorbate spectral response of small molecules adsorbed on metal surfaces in UHV [298, 310, 301] and prior conclusions that the local field 'sensed' by adsorbates on an electrode will vary linearly with applied bias [302, 288].

For purposes of understanding the electrochemical VSE, sulfate adsorbed on a Pt(111) electrode has the particular advantage that there is a relatively large potential range over which the CV makes clear that there is effectively no change in population but the adsorbate SFG line shape significantly evolves. One might thus expect to be able to use this range to understand the effect of applied, macroscopic bias, independent of any change in adsorbate coverage. Prior studies have examined this system, using SFG and linear IR spectroscopies, and fit the potential dependent spectral changes using an empirical form, typically a line. This relationship is generally not justified microscopically and changes in the slopes of the resulting spectral parameters with potential are usually inferred to indicate changes in surface structure or surface chemistry.

The work presented in this thesis clearly demonstrates that if linear changes in applied macroscopic bias are linearly related to changes in local field 'sensed' by individual

[3] ii) has been adapted from my own publication reference [52].

adsorbates, dipole-dipole interaction may cause them to be *nonlinearly* related to the adsorbates' spectral observables like peak centre frequencies and intensities. Thus changes in adsorbate centre frequency or intensity that are nonlinear with potential do not necessarily imply changes in interfacial structure or chemistry.

iii) Perchlorate Adsorption to a Pt(111) Electrode Monitored by SFG

In section 6.3 the (potential) adsorption of perchlorate on a Pt(111) electrode was investigated. Perchlorate behaves significantly different from sulfate, it is considered to not adsorb specifically [51] (to not form chemical bonds with the electrode surface) and, in contrast to sulfate, it is highly polarizable [38, 39]. SFG spectra recorded in 0.5 M $HClO_4$ reveal that perchlorate does indeed interact with the surface: a vibrational resonance that is assigned to a Cl-O stretch emerges at 0.56 V vs. RHE around 1240 cm^{-1}, grows in intensity and shifts towards higher frequencies with increasing potential. This peak has a smaller shoulder that also grows in intensity, but shifts towards lower frequencies with increasing potential.

The absence of perchlorate vibrational resonances from 0.35 - 0.56 V vs. RHE (in the double layer region, a potential range in which the surface is only covered by water) implies that perchlorate does not interact with the bare Pt(111) surface, presumably due to a hydrophobic first water adlayer [131]. In agreement with the work of Huang and coworkers [222], the perchlorate vibration only appears at a potential at which OH adsorption is apparent from the CV. This coincidence strongly suggests that the interaction of OH with (solvated) perchlorate is responsible for the appearance of perchlorate at the interface and the observed vibrational resonances. The presence of two vibrational resonances with a distinctive potential dependent behavior further implies the existence of two subpopulations of perchlorate at the interface that differ in solvation and/or how they interact with the surface. The substantial blueshift of the Cl-O stretching vibration at the Pt(111)/electrolyte interface compared to bulk electrolyte is explained by polarization of the molecule due to the strong interfacial electric fields.

This blueshift is also observed for phosporic acid derived anions (that are isoelectronic to perchlorate and sulfate and have the same structure) on Pt(111), which further reveal a complex potential dependent spectral behavior that likely is the consequence of acid-base chemistry.

Future work in this field may focus on the spectroscopic characterization of OH adsorbed on Pt(111) and the interaction adsorbed OH with anions in the inner Helmholtz plane, either by 2D-SFG spectroscopy, or pump-probe experiments employing a resonant pump.

The physics described in the microscopic model for the electrochemical VSE is applicable to adsorbates on all (photo)electrochemical interfaces. While systems in which both bias and interfacial population are changing will complicate interpretation, by collecting SFG spectra in multiple spectral windows and simultaneously collecting in situ CVs it should be possible to quantitatively account for changes in interfacial population or co-

adsorption and unambiguously extract the molecular-level structural insight within the spectral observable. This work further implies that spectroelectrochemical studies that have attributed chemical, or structural significance to changes in slopes of spectral parameters need to be revisited. Dipole-dipole interaction can induce such changes independent of any chemical or structural change.

Future Directions

The work presented in this thesis further stresses the importance of structural in situ and operando (for ongoing reactions) probes for the electrode/electrolyte interface: rich and complex adsorbate behaviors may arise at the electrified interface of otherwise well understood bulk species due to the interaction of adsorbate and electrode. The details of this interaction are a function of adsorbate and substrate composition and structure, interfacial fields, and electrolyte composition and structure at the interface. Interface specific structural probes like SFG, together with theoretical modeling, offer the prospect of understanding the interfacial electrochemistry that is fundamental to many processes that will decide over the success, or failure, of our societies transition towards clean and renewable energy.

For both investigated systems, Pt and Au electrodes, the tools used in this thesis are not the last word and can be improved. In the chapter concerning the OER (chapter 5), I pointed out that while SHM allows us to characterize the spatial extent and behavior of OER active sites, its spatial resolution and the lack of element specific information so far prohibits us from understanding exactly *why* these active sites are active. A combination of the wide-field SHM with a higher resolution near-field microscopy that also provides chemical information (like tip-enhanced Raman spectroscopy) would be suited to answer this question. Of course, such a tool would also enable us to investigate many more open questions about the OER, like the influence of surface topography on the nucleation behavior of nm sized bubbles. The dependence of ultrafast processes on surface structure could be investigated by pump-probe wide-field microscopy. Furthermore, more experimental approaches mixing optical stimuli and read outs with electrical stimuli and read outs are desirable. For example, the combination of potential step methods with spectroscopy promises to be useful for the operando investigation of reaction mechanisms similar to the optical perturbation, optical probe approach employed here. Using an optical stimulus with electrical read out of the current/reaction rate, akin to how I triggered and investigated charge transfer and the HER in section 4.2, could prove to be useful in determining the rate determining step of reactions. In such an action spectroscopy scheme, the electrode surface is illuminated with a high intensity, narrow band IR beam whose frequency is tuned over a range where adsorbate vibritional bands are expected. If the reaction is limited by the cleavage of a bond, then resonant excitation will weaken this bond and enhance the reaction rate/measured current.

Future directions specifically for the HER, OER and anion adsorption on electrodes were sketched above in the corresponding sections of this chapter.

Appendix A

Triggering and Monitoring the HER on a Femtosecond Timescale

Spectroscopically Resolving Adsorbed H on Pt(111) and Pt(110) Electrodes

Normalizing and Fitting the Pt-H SFG Spectra

Before fitting the spectra and extracting details from the line shape analysis, the IR intensity distribution has to be accounted for. For this purpose typically the nonresonant background off of a gold mirror is used in SFG spectroscopy, as it directly reflects the pulses IR intensity distribution. However, placing a window atop the mirror complicates the spectrum by inteference effects, the SFG signal off the metal surface interferes with itself after reflecting off the window and the metal surface again. As a consequence, the nonresonant SFG spectrum off a gold mirror in direct contact with an IR transparent window is sensitive to the tilt between mirror and window and therefore also to the rotation of the window (if mirror and window are not perfectly plane parallel, which unfortunately they never are). As a result, the nonresonant background off of gold + window can not be used to account for the intensity distribution of the IR pulse (the tilt between the Pt single crystals and the window can not be precisely controlled).

I approached this problem by approximating the intensity distribution of the IR pulse by a sum of Gaussian functions that spans the spectral range from which I collect the SFG signal. The resulting IR intensity distribution function that I used for signal normalization is labeled "IR envelope combined" in Figure A.1 (red curve). This choice of intensity distribution only affects the relative intensities of the resonances for a given potential, but not their center frequency. The same IR intensity envelope was used for all potentials. Consequently, the relative changes in the peak's parameters as a function of potential are not affected by details of the envelope and purely reflect how the resonances change with potential.

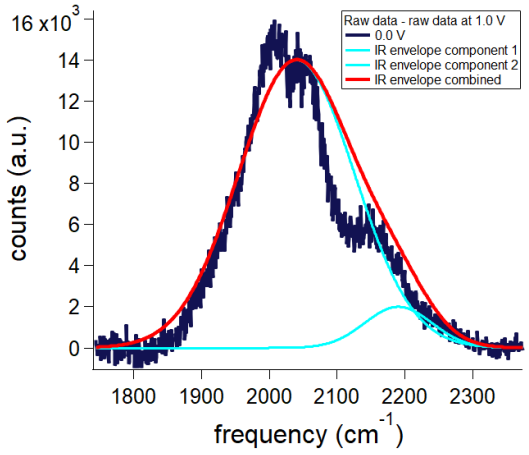

Figure A.1: Background corrected Pt(110)-H SFG spectrum at 0.0 V vs. RHE in 0.5 M $HClO_4$ (dark blue) and envelope of the IR intensity distribution in red together with its components in turquoise.

The normalized spectrum is shown in Figure A.2 (dark blue curve) together with a fit containing five resonances (resonances 1 - 5 from the main text). The single resonances are plotted without attached phase, which is why position and amplitude of resonance 5 appear unphysical.

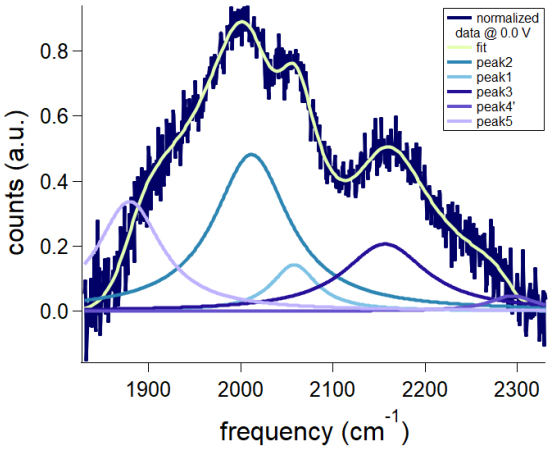

Figure A.2: Pt(110)-H SFG spectrum at 0.0 V vs. RHE in 0.5 M $HClO_4$ after background correction and normalization (dark blue) together with the fit and its components. The parameters used are listed in Table A.1.

The Pt(110)-H spectra at 0.00, 0.05, 0.1 and 0.15 V vs. RHE were fitted simultaneously in Igor Pro using the "Global Fit" function in which certain parameters can be "linked" meaning that the same value of one parameter (for example the phase) of one resonance will be used for all four spectra. For this purpose the Global Fit determines the value for

Table A.1: Parameters for the global fit of Pt(110)-H spectra at 0.00, 0.05, 0.1 and 0.15 V vs. RHE. NR denotes nonresonant.

parameter	0.00 V	0.05 V	0.1 V	0.15 V
NR amplitude	0.077	0.082	0.042	0.007
NR phase	1	1	1	1
amplitude peak 5	24.503	21.913	20.851	10.386
centre frequency 5	1879.639	1881.586	1882.987	1891.843
bandwidth 5	42.207	40.245	42.652	28.405
phase 5	-0.711	-0.711	-0.711	-0.711
amplitude peak 2	34.197	32.775	20.471	11.276
centre frequency 2	2011.670	2013.252	2007.731	1999.392
bandwidth 2	49.302	48.366	44.671	29.0492
phase 2	2.559	2.559	2.559	2.559
amplitude peak 1	11.284	5.088	2.627	5.952
centre frequency 1	2057.932	2042.148	2026.429	2030.712
bandwidth 1	29.849	23.11	15.858	29.341
phase 1	2.122	0.509	-1.433	-1.354
amplitude peak 3	24.768	31.327	31.692	19.034
centre frequency 3	2156.502	2151.332	2144.628	2144.905
bandwidth 3	54.515	59.512	53.956	42.307
phase 3	2.686	2.686	2.686	2.686
amplitude peak 4'	6.604	6.146	4.787	1.802
centre frequency 4'	2294.689	2294.689	2294.689	2294.689
bandwidth 4'	30.433	30.433	30.433	30.433
phase 4'	5.732	5.732	5.732	5.732

this parameter that results in the lowest chi square for all spectra. Here, the nonresonant phase and the phases of resonance 2,3,4 and 5 were linked.

Variation of Initial Guesses

The result of the fit potentially is subject to numerical ambiguity, as it requires four parameters (center frequency, peak area, bandwidth and phase) for every resonance and two for the nonresonant background of the SFG spectrum. This implies that an apparent shift in centre frequency of, e.g., resonance 1 (that is overlapping with two other resonances) could also be fitted by changes in the bandwidth, or phase.

Here I explain how I know that the results of the line shape analysis are not arbitrary solutions to an overdetermined system, but represent a minimum in phase space by systematically varying initial guesses.

The values of the fit parameters in Table A.1 are the results of a minimization in Igor Pro (Wavemetrics) using a Levenberg-Marquardt algorithm. The algorithm manipulates the parameters so that the goodness of fit of the fit function is minimal. I demonstrate that the parameters in Table A.1 represent a minimum in phase space by varying the parameters around the value shown in the table by a percentage (plus and minus) and using every permutation possible of the modified parameters as initial guesses for the same minimization process. If I modify the parameters by a certain percentage, as shown schematically in Table A.2 for 1 % and obtain the same goodness of fit parameter and the same parameter values for every possible permutation of the modified fit parameters, I conclude that the initial parameters constitute a minimum in phase space and that the fit is not just an arbitrary solution to an overdetermined system.

The initial guesses were varied in the following fashion (at the example of Table A.2: At first, all 18 parameters are multiplied by 0.99, which is also the first set of initial guesses for the minimization. For the second minimization, only parameter 18 is changed to P18*1.01, all other parameters remain at P*0.99. For the third and fourth minimization, P17 is changed to P17*1.01 and the minimization is conducted once with P18*0.99 and once with P18*1.01. Subsequently, P16 is changed to P16*1.01 and the minimization is performed after permutating P17 (plus and minus) and P18 (plus and minus). This continues up until P1 is changed to P1*1.01 (here again miminizations for all permutations plus and minus of the other parameters are conducted) and the final set of initial parameters is given by all parameters multiplied with 1.01.

I performed this variation of initial guesses from 1 to 5 % and recovered the same goodness of fit parameters and parameter values from 1 to 4 %, but at 5 % the fit did no longer converge, resulting in a a high goodness of fit parameter and physically meaningless parameter values. I therefore conclude that the parameters displayed in Table A.1 represent a minimum in phase space.

Table A.2: Schematic of the matrix that was used to create the initial guesses: the value of the respective fit parameter (from the minimization) is multiplied by either 0.99, or 1.01, representing a deflection of 1%.

Parameter	-	+
P1	P1*0.99	P1*1.01
P2	P2*0.99	P2*1.01
..		
P17	P17*0.99	P17*1.01
P18	P18*0.99	P18*1.01

Pt(111)-H spectrum in D_2O recorded around 2000 cm^{-1}

That I truly observe Pt-H vibrations around 2000 cm^{-1} is further corroborated by the lack of resonances, when D_2O is used as solvent. In D_2O, only the nonresonant background can be seen on Pt(111), but no distinct resonances 4, or 4'. As demonstrated in the main text, the resonances are shifted according to the change in reduced mass when going from H to D by a factor of 1.41 (to around 1450 cm^{-1}) and are accordingly not visible anymore in this frequency window.

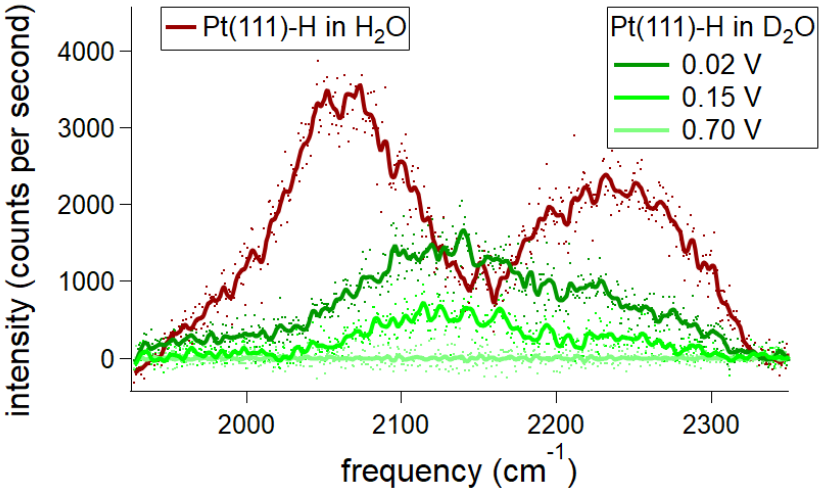

Figure A.3: Background corrected SFG spectra of Pt(111)-H in 0.5 M $HClO_4$ in D_2O (green) and of Pt(111)-H at 0.02 V vs. the reversible hydrogen electrode in H_2O (red).

Appearance and Phase Flip of Resonance 1

Resonance **1** appears as the first spectral feature as the potential is scanned towards increasingly negative potentials as a dip in the nonresonant background of Pt(110), see Figure A.4. Top right panel: fitting the spectra as a function of potential with a phase attached to each resonance yields a flip in phase from negative to positive for resonance **1** as the potential is lowered. The phases for all other peaks were constant during this analysis. Bottom right: fitting the spectra as a function of potential without phases attached to the resonances requires that resonance **1** has a negative peak area at higher and a positive peak area at lower potentials.

These results suggest that the species that produces the spectral response of resonance **1** undergoes a change in orientation with decreasing potential. This scenario is consistent with the adsorption of H in the sub-surface (empty sites beneath the first layer of atoms) of sites producing resonance **1** at higher potentials and the subsequent migration of these H entities to the surface at lower potentials.

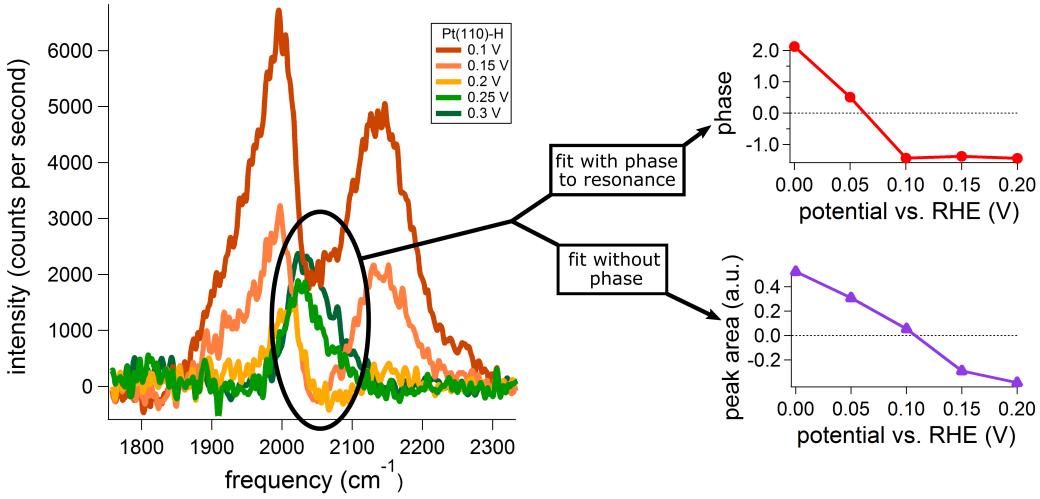

Figure A.4: Appearance and phase flip of resonance **1** on Pt(110). The data has been processed as described for the data displayed in Figure 4.1 of the main text. Potentials are quoted vs. the RHE.

Spectroelectrochemical Cell for SFG

A cartoon of the spectroelectrochemical cell that was used the SFG measurements of sections 4.1 and 4.3 is displayed in Figure A.5. The electrodes were pushed against the IR transmissive window to create an approximately 1 - 2 µm thin electrolyte film.

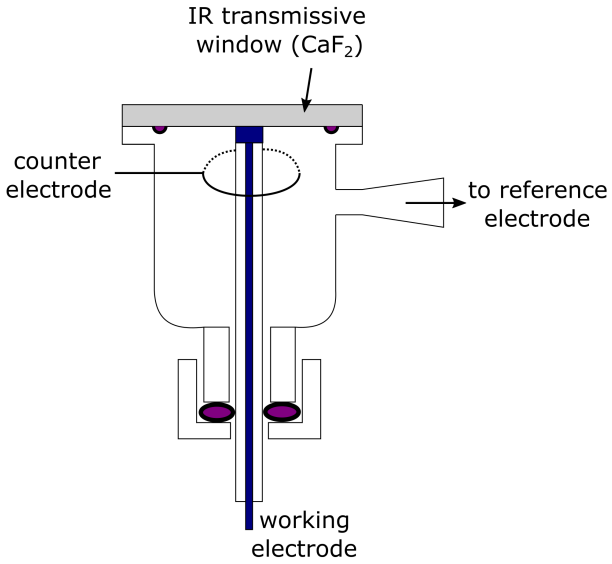

Figure A.5: Sketch of the cell that was used for SFG experiments under potential control.

Triggering Charge Transfer and the HER on Pt Electrodes on Femtosecond Timescales with Ultrashort Light Pulses

This section was modified from the supporting information of my own publication reference [89].

CV Evolution After Starting the Laser Illumination

In Figure A.6 multiple CV traces of the anodic H_{UPD} feature of a Pt(100) electrode are shown in the absence (black curve) and presence of 800 nm, 55 fs, laser irradiation with a fluence of 1.8 µJ/cm^2*pulse. After unblocking the kHz train of laser pulses the CV does not instantaneously stabilize, it rather gradually approaches a new dynamic steady state over the course of about 30 s after which the CV trace is stable for arbitrarily many cycles. If the illumination is switched off again, the CV returns back to its initial state (black curve, return not shown) over a course of about 30 s. This induction period likely is the consequence of mass transport in and out of the interphase region after steady state concentrations have been perturbed by the presence/absence of illumination.

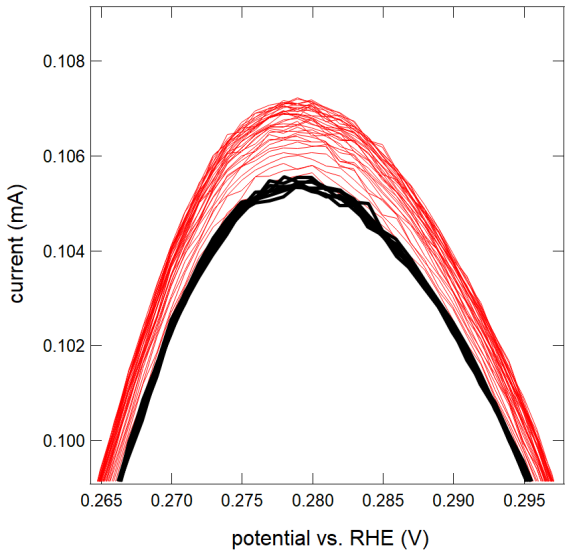

Figure A.6: Anodic H_{UPD} feature of a Pt(100) over multiple voltammetric cycles in the presence (red trace) and absence (black trace) of 800 nm, 55 fs, laser illumination with a fluence of 1.8 µJ/cm^2*pulse (1 kHz repitition rate). The black curve evolves into the red curve after switching on the illumination.

Influence of Dissolved O_2 on the Cyclic Voltammetry of the Pt Microelectrode

As mentioned in the main text, the cathodic and anodic section of the UPD region of the microelectrode are not perfectly symmetric around 0, this behavior is particularly apparent below 0.25 V vs. RHE (currents in the cathodic scan are slightly larger). This is likely a consequence of the oxygen reduction reaction (ORR) which, as much prior work has shown, is irreversible and starts at around 0.9 V vs. RHE. on Pt in acidic media. It adds a negative current to the CV that increases with increasingly negative potential in the absence of mass transport limitations [24]. For the microelectrode, I therefore expect a stronger contribution to the CV current from the ORR at the potential of H_{UPD} adsorption to the (110) site at around 0.15 V than at respective potential for H_{UPD} adsorption, 0.3 V vs. RHE.

Trace amounts of oxygen do not appear to influence the single crystal measurements, presumably because the reduced mass transport in the thin electrolyte film between electrode and window over the larger single crystal make reduction of oxygen more straightforward than for the microelectrode.

The ORR contributes a negative current to the CV signal and I would therefore expect the CV current to decrease in both cathodic and anodic scan if we enhanced the ORR by the illumination (or presence of hot electrons), which is clearly not the case for any single crystal electrode and the (100) H_{UPD} feature of the microelectrode; this condition only appears to hold for the (110) H_{UPD} feature of the microelectrode.

Justification for the Choice of Metric

The data in the main text clarifies that laser-induced changes to the current are substantial in the UPD region, but negligible in the double layer charging region. The laser-induced HER current at 0 V is relatively simple to understand, but this is not the case for the UPD region. As discussed in the main text, laser-induced redox chemistry would result in a current that has the same sign in cathodic and anodic CV scan, while laser-induced changes to the ESV change sign with scanning direction. For the microelectrode I observe a maximum of laser-induced current at the position of H_{UPD} features which changes sign with scanning direction, at least in the absence of other current contributions. For single crystals the UPD portion of the CV greatly depends on surface structure [24] and ESV contributions, as well as non-ESV contributions to the current arise under laser illumination. In the following, I discuss each single crystal surface and disentangle these different contributions.

Pt(111)

Pt(111) is the most investigated and best understood among Pt single crystal facets. In the cathoic scan H_{UPD} adsorption starts around 0.35 V vs. RHE, it is assumed to be located in fcc three fold hollow sites [69, 70] and that H_{UPD} - H_{UPD} interaction with increasing coverage

is repulsive and can be described by a Frumkin isotherm [320, 321, 322]. A current plateau results in both scanning directions (H_{UPD} sorption is reversible) and in the cathodic scan an additional, irreversible current arises close to 0 V vs. RHE due to the HER. The HER current is a negative spike in the cathodic scan and if the current is large enough it can also result in a positive current feature between 0 and ca. 75 mV in the anodic scan that is generally ascribed to the oxidation of the HER intermediate H_{OPD}. Figure A.7 displays the anodic scan of a Pt(111) electrode within the spectroelectrochemical cell. As mentioned in the main text, avoiding defect formation on single crystals in such cells is not always possible and (110) and (100) like defects are apparent at around 0.12 and 0.27 V. Defect free Pt(111) CVs can be seen in prior work [124, 323, 52].

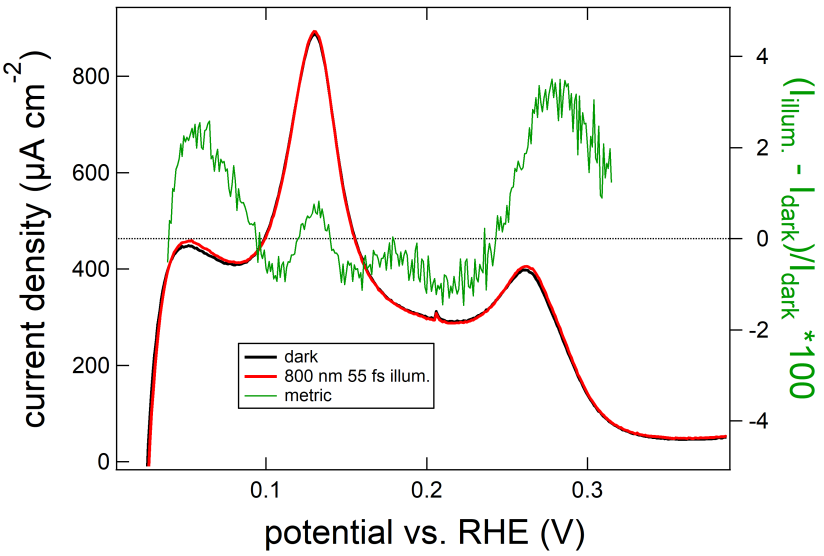

Figure A.7: Anodic H_{UPD} feature of a Pt(111) over multiple voltammetric cycles in the presence (red trace) and absence (black trace) of 800 nm, 55 fs, laser illumination with a fluence of 1.8 µJ/cm^2*pulse (1 kHz repitition rate). The scan rate was 500 mV/s, the electrolyte 0.5 M H_2SO_4. The green trace shows $[(I_{illum}-I_{dark})/I_{dark}]$*100 as a function of potential.

It is challenging to separate the laser-induced currents on the overlapping (111) and (110) features, and because our Pt(100) surface has a well defined (111) like current plateau (see below), the results in the manuscript were derived from this Pt(100) crystal. The results in the main text are qualitatively insensitive to this decision as demonstrated in Table A.3. The table shows that the trend of the laser-induced current to the different CV features of the Pt(111) CV in Figure A.7 is similar to the trend obtained from Pt(100) ((111) and (100) like feature) and Pt(110) that is reported in the main text. The values for the (110) and (100) feature obtained on the Pt(111) crystal are slightly larger than on the respective single crystals which possibly is due to a contribution to the laser-induced current from the underlying (111) H_{UPD} feature.

Table A.3: Laser-induced H_{UPD} current features on Pt(111), Pt(110) and Pt(100). $Pt(111)_{100}$ indicates the laser-induced Pt(111) current extracted from the (111) like current feature we observed in the CV collected with the Pt(100) crystal.

electrode suface/feature	$\left(\frac{I_{illum}-I_{dark}}{I_{dark}}\right) \times 100$
$Pt(111)_{(100)}$	2.0
$Pt(100)_{(100)}$	1.5
$Pt(110)_{(110)}$	0.4
$Pt(111)_{(111)}$	2.4
$Pt(100)_{(111)}$	2.1
$Pt(110)_{(111)}$	0.8

I conclude from the results of Table A.3 that the sign and size of laser-induced changes to the ESV that I observe are rather insensitive to the exact way in which I extract this signal. As mentioned in the main text, regardless of the exact defect densities on the Pt(111), Pt(110) and Pt(100) crystals, I emphasize that the laser-induced H_{UPD} signal on the single crystals is *qualitatively* different than that from the microelectrode. I imagine that the defect densities on the single crystals are not sufficient to disrupt the crystal-face specific structure of interfacial water, but that they are on the microelectrode.

Pt(100)

As prior work has shown, H_{UPD} sorption on Pt(100) often leads to current features in the CV near 0.27 and 0.37 vs. RHE [324]. This is most easily explained by H adsorption to two distinct surface sites. This is in contrast to mostly theoretical work that concludes that H_{UPD} adsorbs only at the two-fold coordinated bridge site on Pt(100) [24, 322]. The ratio of the two experimentally observed current features is highly sensitive to the atmosphere in which the crystal is cooled after flame annealing [323].

The Pt(100) CV in the spectroelectrochemical cell, see Figure A.8, shows a broad current feature around 0.28 V vs. RHE togehter with another extended feature around 0.1 V vs. RHE. I do not see the two higher potential features described earlier, which is possibly a consequence of the sample preparation, or minor contamination in this cell. The current feature observed in Figure A.8 close to 0.1 V is absent from all Pt(100) CVs in the literature but strongly resembles the current response on Pt(111) at these potentials. I have taken the laser-induced Pt(111) signal reported in the main text from this feature, because it is well separated from the (100) feature at 0.28 V vs. RHE. It is noteworthy, that the maximum in laser-induced current is at the potential at which the H_{UPD} CV feature has its current maximum in the absence of illumination, as shown in the main text for the microelectrode and that the laser-induced signal changes sign with scanning direction.

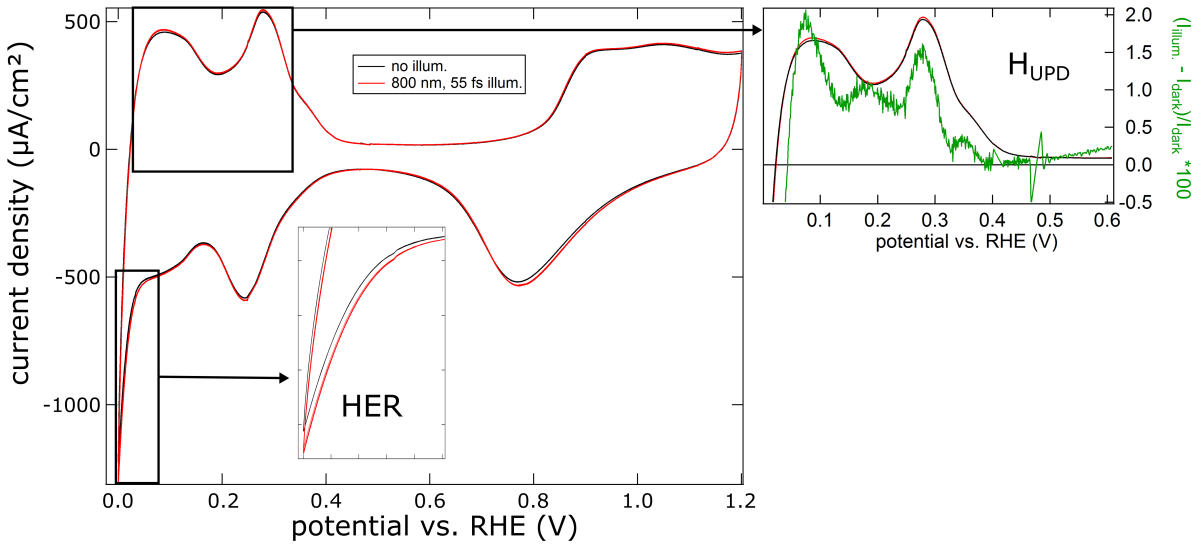

Figure A.8: CV of a Pt(100) electrode in the presence (red trace) and absence (black trace) of 800 nm, 55 fs, laser illumination with a fluence of 1.8 µJ/cm^2*pulse (1 kHz repitition rate). The scan rate was 500 mV/s, the electrolyte 0.5 M H_2SO_4. Insets show the HER region around 0 V vs. RHE and the anodic section of the UPD region , here the green trace shows $[(I_{illum}\text{-}I_{dark})/I_{dark}]$*100 as a function of potential.

Pt(110)

According to prior work the CV of Pt(110) typically shows one large current spike at 0.15 V vs. RHE (which is fully reversible) that has a smaller shoulder towards more positive potentials (which is not always fully reversible) and a small irreversible peak between 0 - 0.15 V vs. RHE in the anodic scan which is typically assigned to oxidation of hydrogen generated close to 0 V [124, 323, 325]. The size of this peak is expected to depend on rate and amount of generated hydrogen, but to be biggest on Pt(110) among the three basal planes of Pt under identical experimetal conditions, because Pt(110) is more active than Pt(100) and Pt(111) [24]. The exact meaning of the other two peaks is still under debate. Pt(110) has two stable reconstructions under atmospheric conditions, namely the (1x1) and the (1x2) missing row reconstruction. The reconstruction is a function of sample preparation, mostly of cooling atmosphere composition. As a consequence, the ratio of the two reversible peaks is also sensitive to sample preparation.

In Figure A.9 the cyclic voltammetry of Pt(110) is shown in the presence and absence of laser irradiation in the spectroelectrochemical cell (experimental details are given in the figure caption). The peak ratio is most consistent with the (1x2) reconstruction [122]. While the sign of the laser-induced changes to the main (110) H_{UPD} peak at around 0.15 V changes sign with scanning direction, this is not the case for the side peaks to either direction (as shown in the insets on the right). The most simple scenario explaining the

laser-induced changes to the side peaks is that at 0.05 V vs. RHE the illumination induces additional H_2 oxidation and anion desorption at 0.22 V.

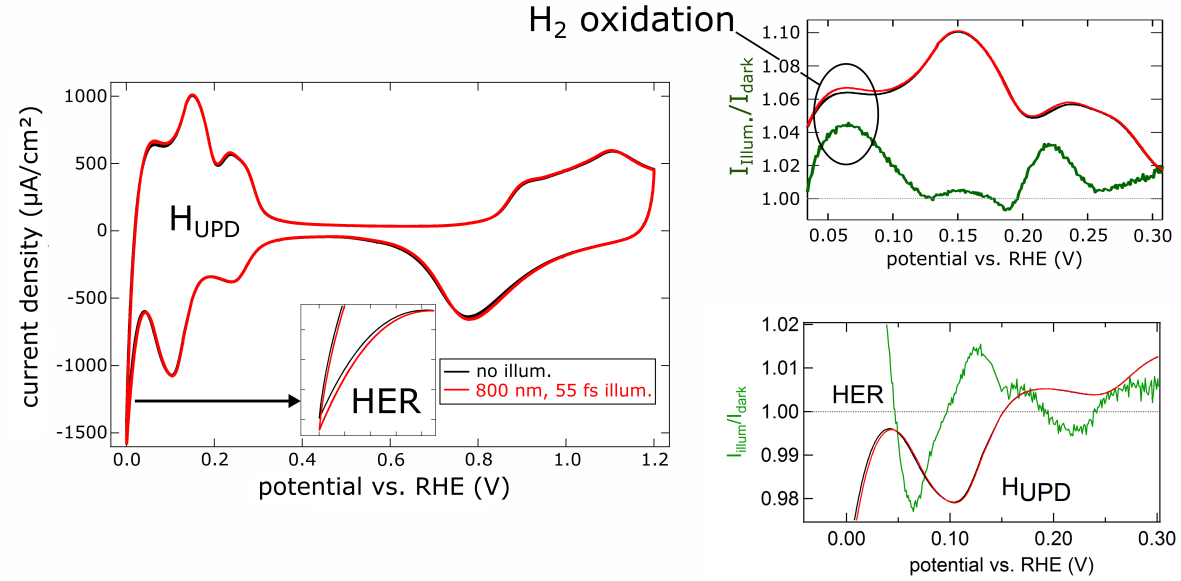

Figure A.9: CV of a Pt(110) electrode in the presence (red trace) and absence (black trace) of 800 nm, 55 fs, laser illumination with a fluence of 1.8 µJ/cm^2*pulse (1 kHz repitition rate). The scan rate was 500 mV/s, the electrolyte 0.5 M H_2SO_4. Insets show the HER region around 0 V vs. RHE and a magnification of the UPD region , here the green trace shows $[(I_{illum}\text{-}I_{dark})/I_{dark}]$*100 as a function of potential.

Normalizing the Laser-Induced Current vs. Substracting

In my analysis in the main text and here I have used $[(I_{illum}\text{-}I_{dark})/I_{dark}]$*100, the normalized laser-induced current, to quantify the laser-induced currents as a function of bias. It is not immediately obvious that this is the best choise for this purpose, one can imagine other possible metrics like $I_{illum}\text{-}I_{dark}$. I demonstrate in Figure A.10 that using the difference as metric for comparison of the laser-induced currents at the same potentials does not change the relative trends. The most apparent difference is that the laser-induced current difference on the microelectrode is significantly larger than on the single crystals. This is a consequence of much higher current densities with decreasing electrode size due to improved mass transport. If the illumination changes the measured current by a few % on both single crystals and microelectrode, then the difference $I_{illum}\text{-}I_{dark}$ will be much bigger for the microelectrode, just because I_{dark} is already substantially bigger.

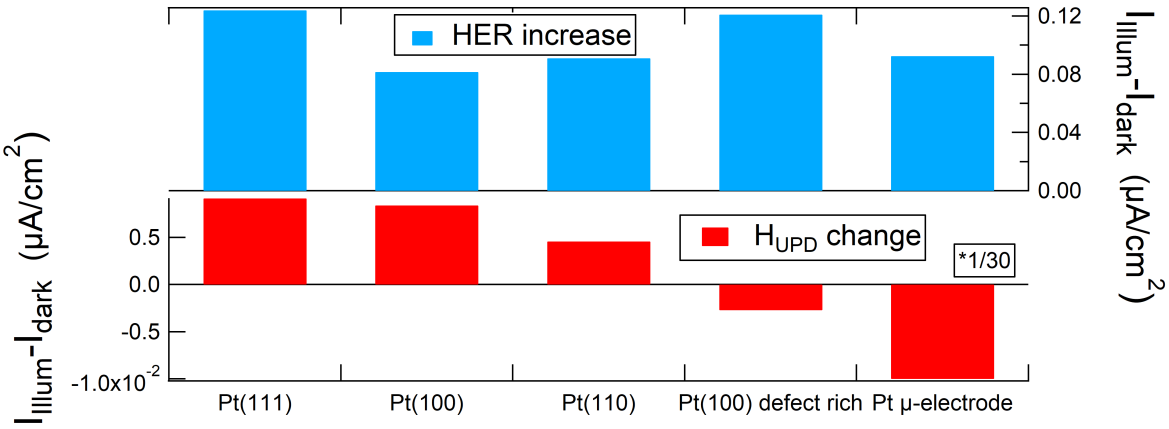

Figure A.10: I_{illum}-I_{dark} extracted for the HER at 0 V vs. RHE (top panel) and for H_{UPD} in the anodic scan (bottom panel) on four different Pt surfaces. For the single crystal measurements, 0.5 M H_2SO_4 was used as electrolyte and the laser fluence was 1.8 µJ/cm^2*pulse. For the microelectrode, 0.05 M H_2SO_4 was used as electrolyte and the laser fluence was 2.4 µJ/cm^2*pulse (800 nm, 55 fs, radiation at 1 kHz repitition rate was used in both cases).

Spectroelectrochemical Cell

A cartoon of the spectroelectrochemical cell that was used the measurements of section 4.2 is displayed in Figure A.11. In contrast to the spectroscopic measurements, this is an all glass cell without IR transparent window. This enables a cleaner environment for the electrodes, because neither a spacer (with possible organic contaminants), nor a IR transmissive window (contamination by dissolution) is needed. Unfortunately, it leads to a larger amount of defects when the single crystal electrodes are pushed against the window, because glass is substantially harder than, *e.g.*, CaF_2 and the used glass is not optically flat (in contrast to the IR transmissive windows). The electrodes were pushed against the window to create a thin electrolyte film analogous to the measurement conditions of the optical measurements under potential control. This ensures comparability of the results due to identical mass transport conditions.

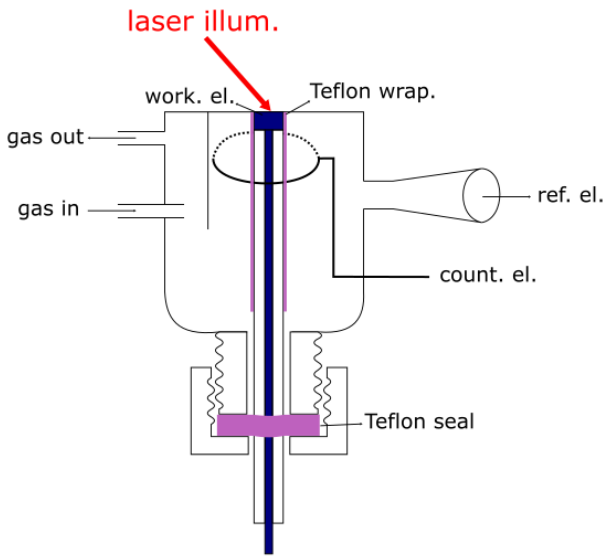

Figure A.11: All glass cell that was used for the measurements of section 4.2.

Optical Excitation Induced Pt-H Femtochemistry Monitored by SFG

Time Resolution

The time resolution of the experiments described in section 4.3 of the main text are as follows: -1000 to -500 fs in steps of 250 fs, -500 to +2000 fs in steps of 100 fs and +2000 to +8000 fs in steps of 1000 fs.

Reference Measurement on Au

The results from measuring the nonresonant background off of a gold mirror buried under a CaF_2 window as a function of pump-probe delay under identical conditions for the optical measurement as for the experiment at the Pt(111)/electrolyte interface are shown in Figure A.12 (bottom panel) together with the unperturbed spectrum (top panel). As mentioned in the main text, the pump-induced changes to the nonresonant background are only a few percent of the unperturbed signal. It is important to mention here that Au and Pt have substantially differing electronic structures (filled and deep lying vs. only partially occupied d-levels that lie at the Fermi level) and that no direct comparison is possible based only on these two measurements. However, together with the above mentioned transient reflectivity measurements at the Pt/electrolyte interface that only show a minute dependence of Pt's reflectivity on a 780 nm pump [153], I conclude that the pump induced changes to the nonresonant background of Au and Pt are comparable and that the results

of Figure 4.10 in the main text can be interpreted purely as changes to χ_R: as resonant changes to Pt-H that I interpret as changes in Pt-H population.

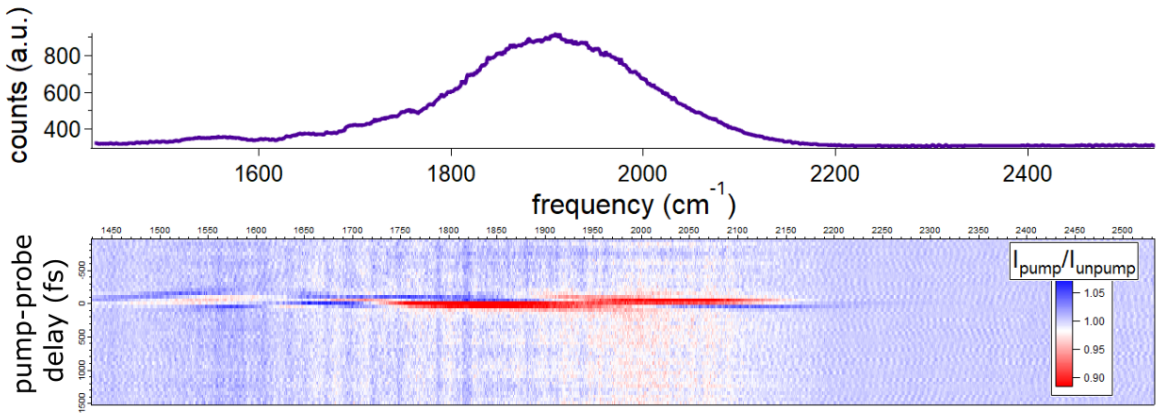

Figure A.12: Top panel: Unperturbed SFG spectrum of a Au mirror under a CaF_2 window. Bottom panel: I_{pu}/I_{unpu} ratio vs. frequency as a function of pump-probe delay from -950 to 1500 fs in 50 fs steps. Spectra were recorded with 2 μJ pulse energy for upconversion and IR pulses and 9 μJ pulse energy for the 800 nm, 35 fs pump; the repitition rate was 1 kHz.

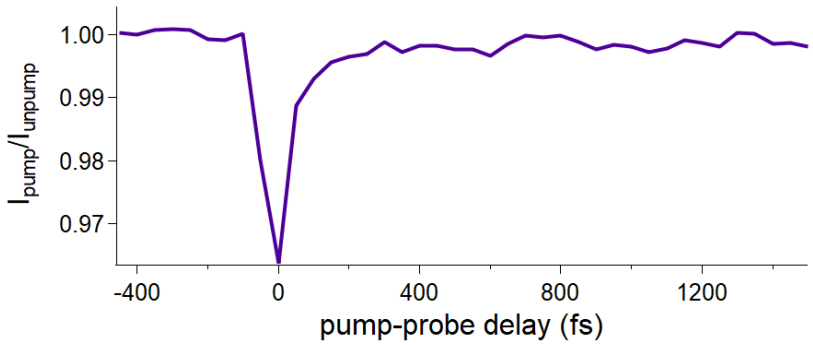

Figure A.13: SFG intensity integrated over the entire measured frequency range for the date of Figure A.12 plotted vs. pump-probe delay.

Optically pumping Pt(111)-H at 0.1, 0.5 and 0.8 V vs. RHE

The datasets recorded at 0.025 and 0.2 V vs. RHE can be seen in the main text.

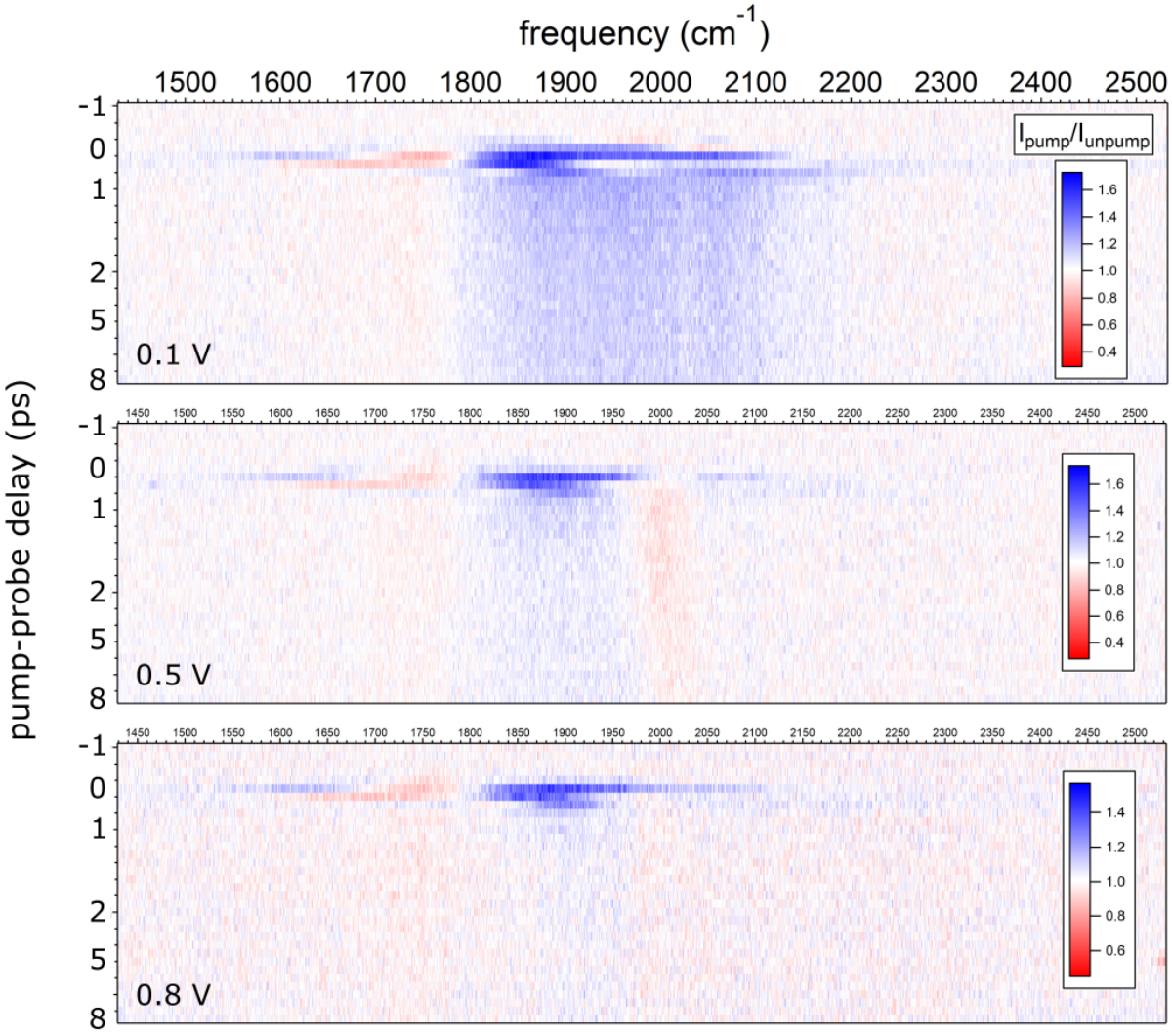

Figure A.14: I_{pu}/I_{unpu} ratio vs. frequency as a function of pump-probe delay at a Pt(111)/electrolyte interface at 0.1 (top), 0.5 (middle) and 0.8 V vs. RHE (bottom). The time resolution is finer around time zero and coarser at delays >3000 fs. Spectra were recorded with 2 μJ pulse energy for upconversion and IR pulses and 9 μJ pulse energy for the 800 nm, 35 fs pump; the repitition rate was 1 kHz and the electrolyte 0.5 M $HClO_4$.

Correcting for scattered light at delay times > 3 ps

A frequency and potential independent increase in SFG intensity at delay times > 3 ps was apparent in every dataset (see Figure A.15) and attributed to scattered light. The frequency range from 2350 to 2550 cm^{-1} was used to assess the contribution of the scattered light, because no SFG photons were created there (due to a lack of IR photons at this frequency). This frequency range was integrated and plotted for every potential in Figure

A.15. The average at delays > 3 ps (bold red curve) was subtracted from the raw data at every potential to account for the scattered light.

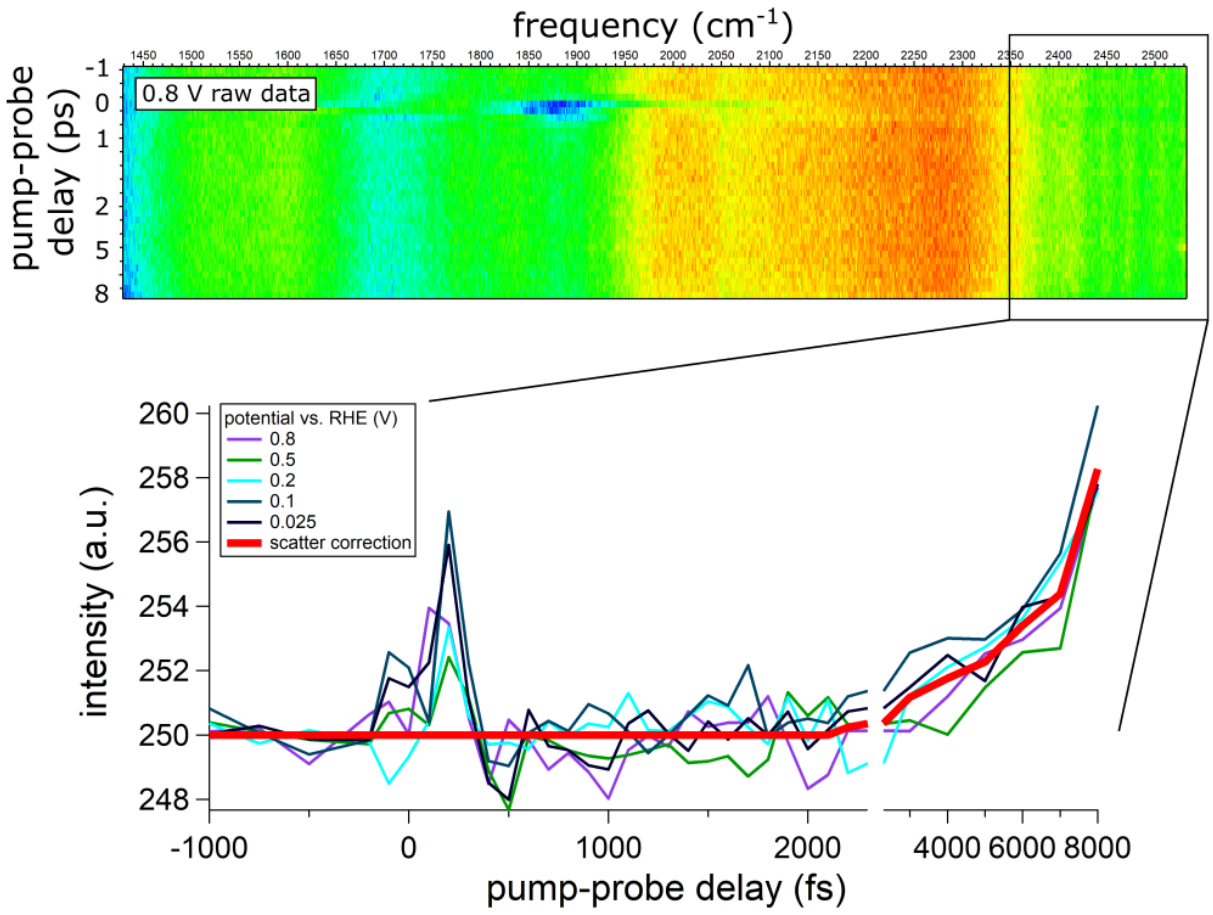

Figure A.15: Raw data at 0.8 V (top panel) highlighting the frequency range from 2350 to 2550 cm^{-1} that was used for the correction of the scattered light and integration over this frequency window for all potentials (bottom panel). The bold red curve is constant up to 3 ps and the average of all other curves after. In the top panel, red (blue) indicates high (low) SFG intensity.

Appendix B

Operando Insights into the OER: Activity is Highly Local on Au_{poly}; on Pt Higher Oxidation States are Inactive

The sections concerning SH imaging of Au electrodes have been modified from the supporting informations of my own publications [33, 184].

Mapping Heterogeneity in Au Surface Electrooxidation and its Potential-Induced Surface Reconstruction *Operando*

SEM Micrographs of the Working Electrodes

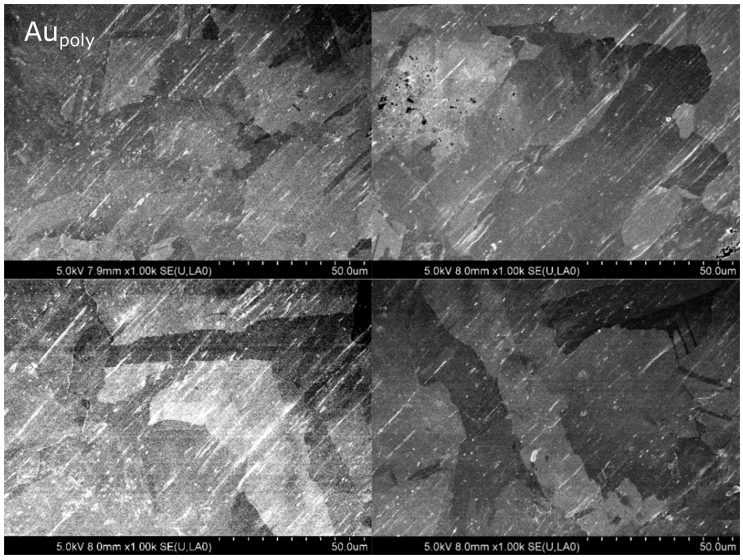

Figure B.1: Scanning Electron Microscopy (SEM) image of the polycrystalline working electrode after annealing at 500°C for 2 hours. The scale bar on the right hand bottom of each image is 50 µm. These images clearly show that the grain facets have length scales of 10s of µm. The image shown is of the electrode before any cleaning steps.

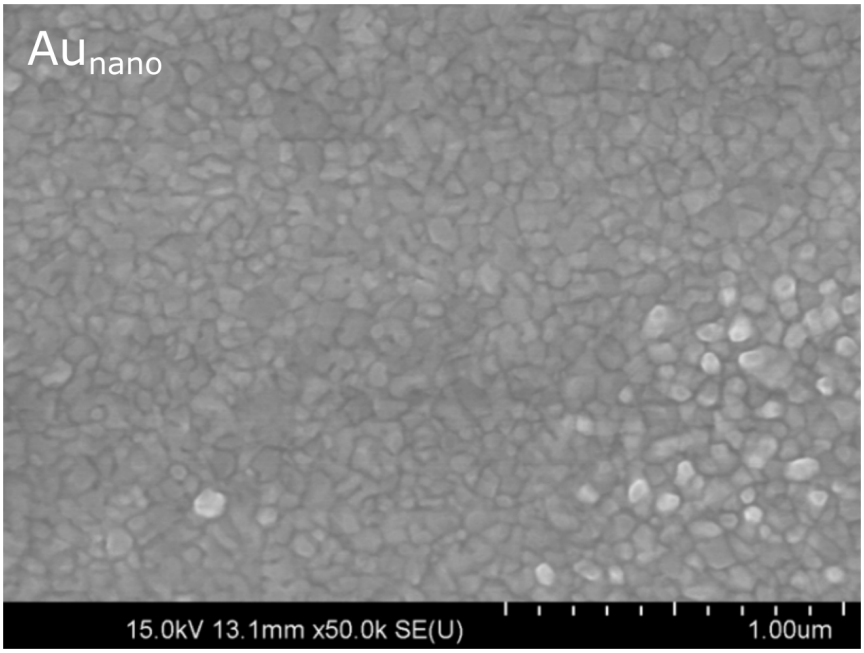

Figure B.2: SEM micrograph of the physical vapour deposited (nanocrystalline) gold film working electrode. As described in the manuscript, these electrodes are created starting with an optically smooth borofloat glass substrate, then depositing 3 nm of Cr, and finally depositing 200 nm of Au. The length of the scale bar in the lower right hand corner of the image is 1 µm. Clearly the crystallites apparent in the image are structurally heterogeneous on length scales of 10-100 nanometers.

Processing of the Second Harmonic Images

Measured second harmonic data in form of videos were first stabilized in ImageJ with the plugin "Image Stabiliser" using the Lucas-Kanade algorithm, the parameters that were used are: Transformation: Translation; Maximum Pyramid Levels: 1; Template Update Coefficient: 0.99; Maximum Iterations: 200; Error Tolerance 0.0000001. The stabilisation was used as the sample displayed random movements in the lateral plane on the order of a few hundreds of nanometers over the course of a measurement.

After image stabilisation I performed a flat-fielding procedure in MATLAB. The SH data in this paper is collected by a wide-field SH microscope. As opposed to a rastering SH microscope, where every pixel is illuminated with the same laser fluence, here I illuminate and collect the SH intensity from the whole imaged area at the same time. The benefits of the wide-field approach are: i) I can effectively deliver more laser power to the sample during the time equal to one rastering cycle, which enables this approach to be orders of magnitude faster; ii) SH intensity from all pixels are comparable in real time in every image as there is no rastering delay between different pixels. The downside of the wide-field illumination is that the illumination has a Gaussian like intensity distribution in the x and y direction, i.e. in the plane of the surface, and therefore does not deliver the

same laser fluence to every pixel of the field of view. To compensate for this I use a flat-fielding procedure to simulate a homogeneous illumination so I can directly compare the SH intensity pixel to pixel. For this reason, I acquire the SH beam profile immediately before every experiment. The flat-fielding procedure is then a simple division of acquired SH images with the SH beam profile image.

SH Imaging of the Nanocrystalline Au Electrode

As mentioned in the main text, the SH-V behavior across the surface of the nanocrystalline gold electrode is very homogeneous: Figure B.3 D) shows an identical SH-V behavior for three different pixels during three successive potential cycles.

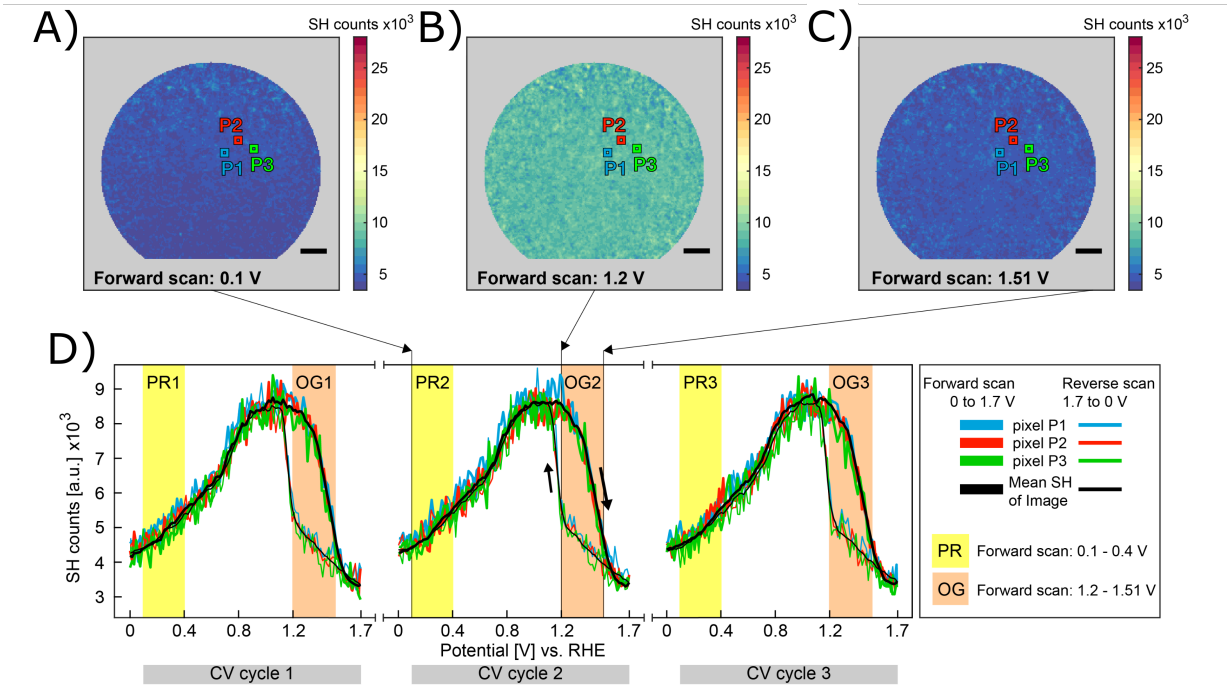

Figure B.3: SH images of the nanocrystalline electrode recorded at 0.1 (A), 1.2 (B) and 1.51 (C) V vs. RHE in PPP polarization combination during cyclic voltammetry (60 mV/s, 0.5 M NaH_2PO_4). P1 - P3 indicate the position of pixels whose SH-V behavior is plotted in blue (1), red (2) and green (3) in panel D) together with the FOV average in black for three successive CV cycles. The black arrows in the second image of panel D) indicate the scanning direction. The polarization region (PR, 0.1 - 0.4 V vs. RHE) is highlighted in yellow, the oxide generation region (OG, 1.2 - 1.51 V vs. RHE) in orange. All potential values are given with respect to the RHE. The range of the color scale is identical to the one of Figure 5.3 of the main text and the scale bar measures 10 µm.

Parabolic Model Analysis of the Nanocrystalline Au Electrode

The results from fitting the SH-V curve of every pixel of the nanocrystalline electrode with the parabolic model is displayed in Figure B.4. The most important difference to the results obtained with the data of the polycrystalline electrode is the fraction and distribution of areas with a negative Q coefficient. Only 8.8 % of the nanocrystalline surface have a negative Q coefficient and the spots with $Q < 0$ are distributed with increasing abbundance towards the fringe of the image, but almost no $Q < 0$ spots can be found in the centre of the FOV. The spatial distribution of $Q < 0$ spots coincides with the spatial distribution of error bars, which also get increasingly larger towards the fringe (Gaussian like intensity distribution of the illuminating beam). It is therefore likely that the majority of $Q < 0$ spots towards the fringe are a consequence of a lower signal to noise ratio. The error bars increase going from the centre to the fringe, which is in support of this argument. The calculation of error bars is discussed below.

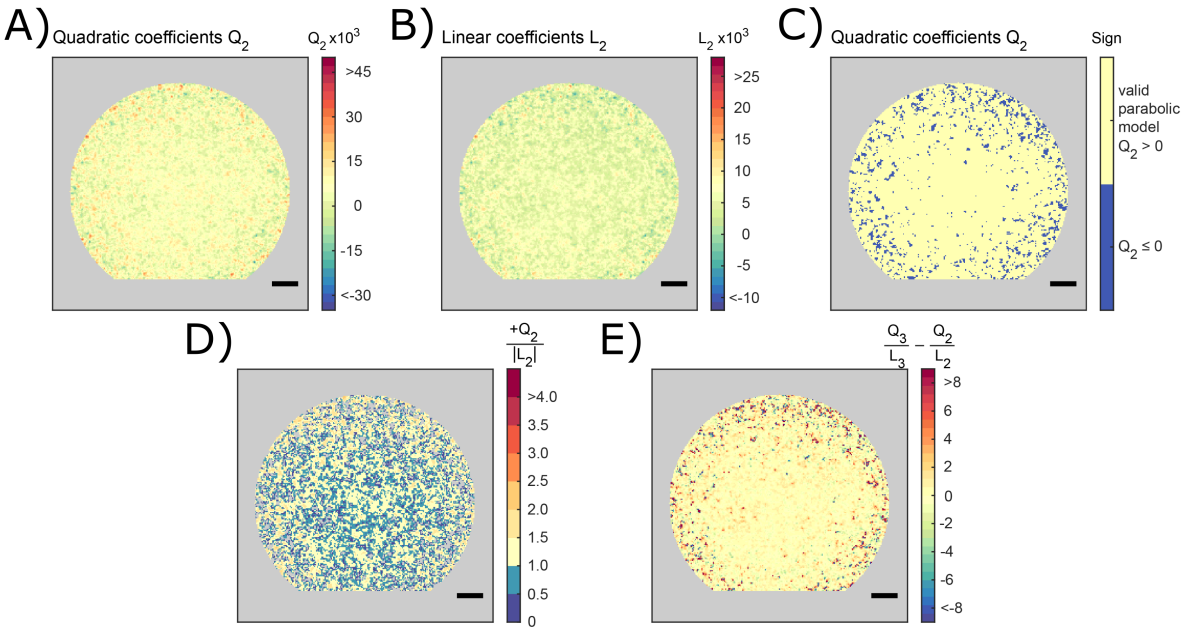

Figure B.4: Fitting the SH-V curve (details of the measurement are described in the caption of Figure B.3) at every pixel with the parabolic model. The index '2/3' denotes that the quantity was extracted from fitting of the second/third CV cycle in a series of three consecutive cycles. A) and B) show maps of the quadratic (Q) and linear (L) coefficients. C) shows a map of areas with $Q > 0$ in yellow and areas with $Q < 0$ in blue. D) shows a map of Q over the absolute of L for $Q > 0$ areas. E) Q/L difference map of the third and second CV cycle. The scale bar measures 10 µm.

Correlation Coefficient Analysis of the Nanocrystalline Au Electrode

As a reference for the correlation coefficient analysis of the polycrystalline electrode I also performed it with the data of the nanocrystalline electrode and plot the results for the correlation coefficient differences in the PR and OG region of the third and second CV cycle in Figure B.5. As argued for Q < 0 spots above, here the increasing amount of pixels with a nonzero $\mid \Delta CorrCoeff \mid$ towards the fringe are likely the consequence of a declining signal to noise ratio due to a Gaussian like intensity distribution of the beam.

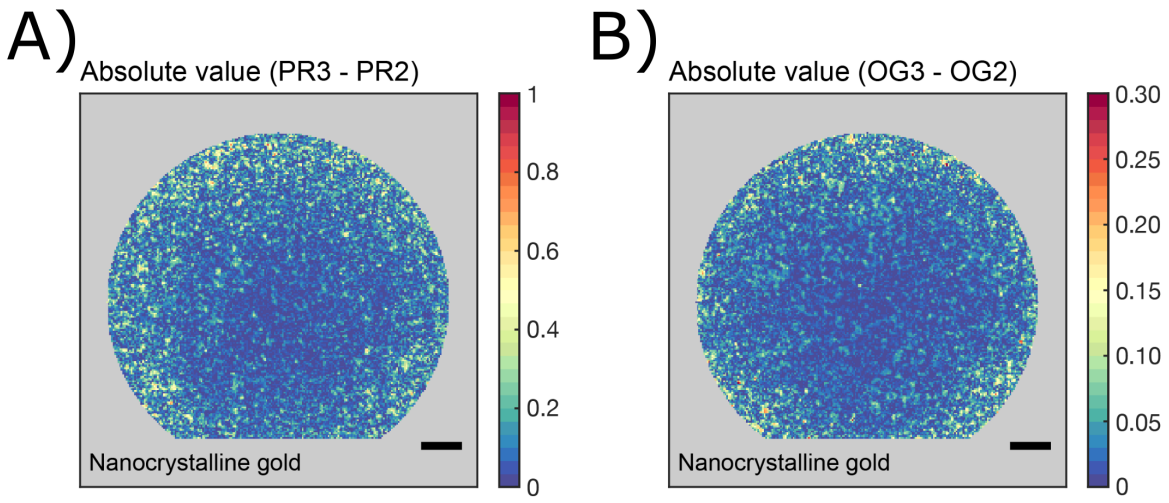

Figure B.5: A) and B) map the correlation coefficient differences from cycle 2 and 3 in the PR and OG region, respectively. The scale bar measures 10 µm.

Estimating the Third Order Susceptibility of Au

For a broad range of materials, Miller's rule can be used to estimate the second-order nonlinear optical properties. It can also be generalized to predict optical third-order nonlinear interactions of the form:

$$\chi^{(3)}(\omega_2, \omega_1, \omega_1, \omega_1) = B\chi^{(1)}(\omega_2)\chi^{(1)}(\omega_1)\chi^{(1)}(\omega_1)\chi^{(1)}(\omega_1) \tag{B.1}$$

Where $\omega_2, = \omega_1 + \omega_1 + \omega_1$ and B is a frequency independent constant that is almost the same for all materials [96]. This allows for an estimate of the ratio of real over imaginary part of the nonlinear third-order susceptibility according to:

$$\frac{Re(\chi^{(3)})}{Im(\chi^{(3)})} = \frac{(\varepsilon_2^{'} - 1)(\varepsilon_1^{'} - 1)(\varepsilon_1^{'} - 1)(\varepsilon_1^{'} - 1)}{\varepsilon_2^{''}\varepsilon_1^{''}\varepsilon_1^{''}\varepsilon_1^{''}} \tag{B.2}$$

where $\varepsilon'_{1/2}$ is the real part of the dielectric permittivity at frequencies $\omega_{1/2}$ and $\varepsilon''_{1/2}$ is the corresponding imaginary part.

Miller's rule predicts the correct order of magnitude for the third-order susceptibility: Calculated values for $\omega_1 = 600$ nm and $\omega_1 = 630$ nm are twice as high as the measured ones [191]. The $Re(\chi^{(3)})/Im(\chi^{(3)})$ ratio derived from experiment at $\omega_1 = 600$ nm is around 12, while for $\omega_1 = 630$ nm a ratio of about 18 is obtained. Extrapolating this to a fundamental wavelength of 1036 nm yields a $Re(\chi^{(3)})/Im(\chi^{(3)})$ ratio of 1180 and I therefore expect that $Im(\chi^{(3)})$ is negligible compared to $Re(\chi^{(3)})$.

Calculation of Error Bars

Error bars were obtained by taking the SH-V curve at every pixel and calculating its standard deviation with respect to itself after it was smoothed by a moving average method in MATLAB with a span of 10 neighboring data points. The error is smallest in the centre (around 1.3 % of the SH signal on average) of the FOV and increases towards the fringe (around 2.6 % of the SH signal on average).

Calculation of Error Bars for the Correlation Coefficient Analysis

The error of $\mid \Delta CorrCoeff \mid$ for (PR3 - PR2) and (OG3 - OG2) was calculated as follows. The error bars are calculated for the PR and OG region of cycle 3 and 2 as described above and these error bars are used to generate a random noise for every pixel. The upper and lower bound for the noise (that is either added, or subtracted) is given by the error bar of each respective pixel. This map with pixel-specific noise (that is lower in the middle and higher towards the fringe, see above) is then added to the original SH-V maps of the PR and OG region for cycles 2 and 3 to create a new dataset $\mid \Delta CorrCoeff \mid (PR/OG3 - PR/OG2)_{noise}$. The error for the correlation coefficient analysis (of both potential windows) is then calculated by:

$$\Delta = \mid \Delta CorrCoeff \mid - \mid \Delta CorrCoeff \mid_{noise} \tag{B.3}$$

The values for the error of the correlation coefficient analysis quoted in the main text (0.04 for the PR and 0.02 for the OG region) are an average over the centre of the FOV where the $\mid \Delta CorrCoeff \mid$ values are smaller compared to the values at the fringe and not artificially increased by the Gaussian like intensity distribution of the illuminating beam. I then quantify significant changes to the surface structure by only considering changes to the correlation coefficient from cycle to cycle that are 2.5 times, or more, larger than the error.

Imaging the OER Activity on Gold Electrodes *Operando*: it is Highly Local

Full Cyclic Voltammogram and Spatially Integrated SH Intensity vs. Potential Curve

The full CVs shown in section 5.1.1 the main text were recorded in 0.5 M NaH_2PO_4, pH = 2.9. Here I show the full CV of Au_{poly} in the 0.5 M Na_2HPO_4, pH = 9, solution used in section 5.1.2. The major differences to the CV in acidic electrolyte are pointed out below.

Prior work on the oxygen reduction reaction (ORR) on gold has shown that this reaction leads to a cathodic current starting at 0.9 V vs. RHE that increases with decreasing potentials in alkaline media in the absence of mass transfer limitations. This reaction is irreversible at 0.9 V and below and thus is expected to add a negative "tilt" to all CVs on Au in which O_2 is present in the electrolyte [326]. I see such a 'tilt' at potentials 0.7 V vs. RHE and below suggesting that our electrochemical cell contains dissolved O_2 (see the lower panel of Figure B.6 for data). Between 0.7 V vs. RHE and the start of oxidation at $\approx$ 1.3 V the CV appears to show small current features. Similar features have been observed previously – they are generally more pronounced in alkaline electrolyte than acid [327, 328] – and attributed to surface defects, or non-equilibrated surface domains [218, 219].

The spatially integrated SH-V curve is plotted (along with the CV) in Figure B.6. Clearly with increasing potential the SH intensity increases up to 0.85 V vs. RHE, is relatively stable between 0.85 and 1.1 and drops abruptly at potentials above 1.3: the onset of oxidation. The signal recovers at 1.15 V vs. RHE (with the reduction of the oxide) and is afterward reversible. This general behaviour of the integrated SH signal is in agreement with previous reports [113, 186] (and the respective work of this thesis in acidic electrolyte): at comparable fundamental wavelengths, these and other authors also found an approximately linear increase of SH intensity with increasing potential until the oxidation of the surface where a sharp drop in intensity was reported.

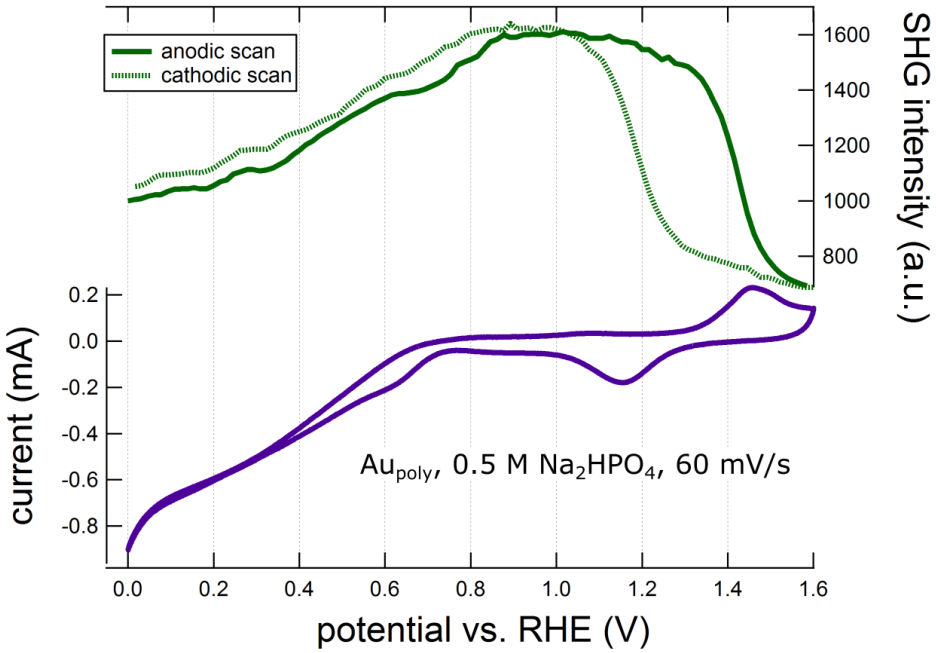

Figure B.6: Top panel: SH intensity integrated over the entire field of view versus potential during the potential sweep. Bottom panel: CV of the polycrystalline gold surface in 0.5 M Na_2HPO_4, pH = 9, at 60 mV/s.

Appearance, Growth and Detaching of Oxygen Bubbles and Calculating their Volume

As described in the main text, increasing the potential positive of 2 V vs. RHE leads to the formation of oxygen bubbles on the electrode surface. I monitor this formation by observing the bubbles and their shadows. In most cases the bubble itself is hardly visible because it extends well above the focal plane (which we place on the Au/electrolyte interface) and is thus out of focus. In contrast, the shadow is always in focus, because it lies in the plane of the electrode surface. An example where bubble and shadow can be seen together is the image showing bubble formation at the defect on the nanocrystalline electrode in the main text.

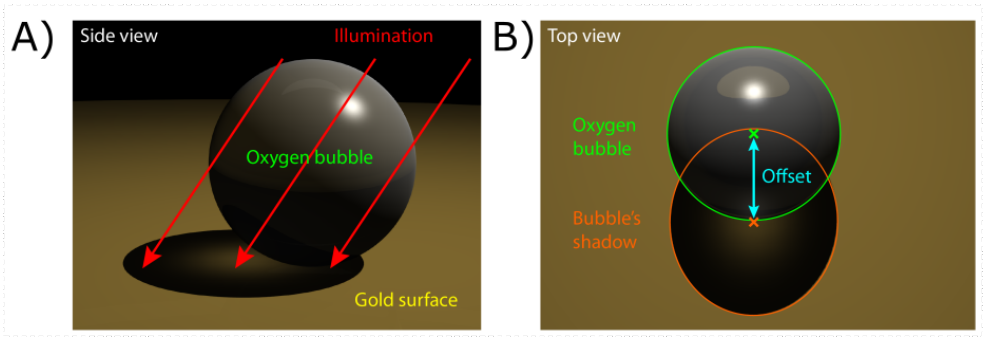

Figure B.7: Illustration of an oxygen bubble on the gold surface. Panel A) shows a bubble and its shadow in side view along with the collimated illumination at 34°. In panel B), the surface, bubble and shadow are seen from above. It is apparent that the real centre of the oxygen bubble is shifted from the centre of the shadow by a size specific offset.

The offset between an oxygen bubble and its shadow was taken into account by determining the centre of a bubbles shadow and then correcting in MATLAB assuming a spherical bubble and accounting for the 34° angle of incidence.

The shadows are slightly elliptical due to illuminating at 34°, therefore the shadow diameter perpendicular to the direction of illumination was used for calculating the bubble volume.

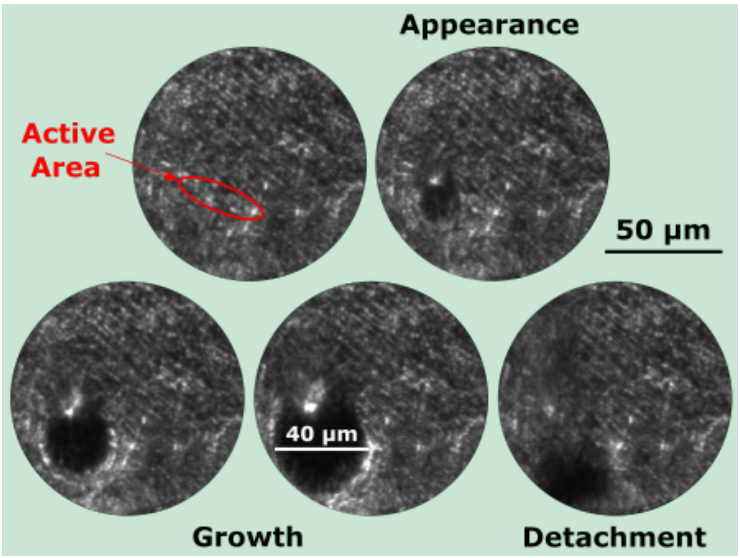

Figure B.8: The life-cycle of an oxygen bubble from appearance to detachment. The same FOV is shown as in Figure 5.7 of the main text. The last frame before the oxygen bubble detached from the surface was used to determine its diameter, which was taken perpendicular to the direction of the illumination.

The amount of charge that is passed in order to form a bubble was calculated as follows. Given the measured diameter of a bubble we calculate its (assumed spherical)

volume. The volume is then used to calculate the amount of oxygen molecules inside the bubble assuming pure oxygen and a pressure of 1 atm. It is worth noting that 1 atm is a lower bound of bubble pressure: bubbles with a radius of $\approx$ 10 µms (the average size of the bubbles evaluated for Figure 5.7 of the main text) will have slightly higher due to Laplace pressure. However, this additional pressure is only 0.14 atm (with larger bubbles having still lower pressures). From the amount of oxygen molecules I calculated the number of electrons consumed per bubble and then convert this number into a current. The conversion from current into a current density requires calculation of a size of the active area and is discussed further below.

Is Bubble Growth Dominated by Diffusion, or the Activity of the Active Site?

As discussed in the main text, it is not immediately apparent that the formation of bubbles exclusively in the active area is actually a consequence of its superior activity compared to the surroundings. One might alternatively imagine that bubble nucleation occurs from a supersaturated solution at nucleation sites that are particularly active because of roughness, or a specific composition. In this scenario bubble growth would be dictated by mass transport, i.e. convection or diffusion, of dissolved O_2 to the forming bubble. In such a scenario, the growth rate of the bubble is expected to be a function of bubble surface area. Evaluating the growth rate of a bubble over the course of 26 s during the linear sweep experiment of Figure 5.7 of the main text clarifies that this is not the case: within experimental error the growth rate is relatively insensitive to bubble size (see Figure B.9 and note that the possible slight increase in growth rate for large bubbles may be the result of the increase in bias during the course of bubble growth. As it is a linear sweep experiment with a sweep rate of 1 mV/s the potential at the end of the bubble growth will be 26 mV higher than at the start). I take this argument to suggest that the growth of bubbles, and the activity of the active area, are a consequence of the high intrinsic OER activity of the active area.

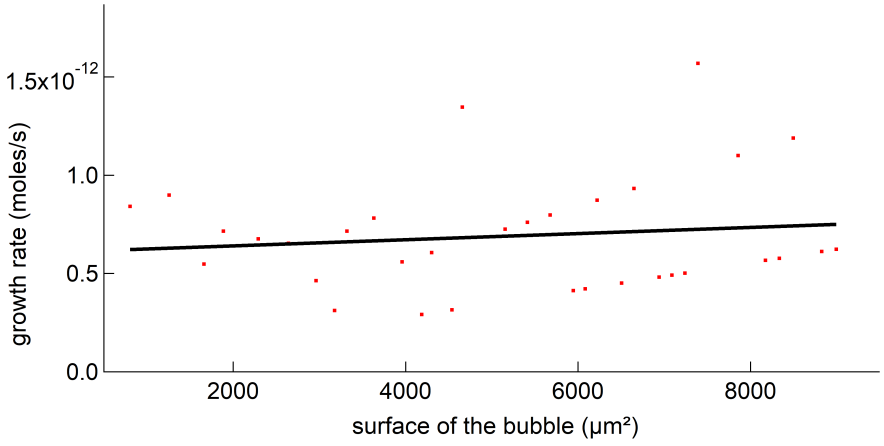

Figure B.9: Growth rate of a bubble versus its surface area during bubble growth. The bubble was part of the linear sweep depicted in Figure 5.7 of the main text, nucleated at around 2.08 V vs. RHE and grew for about 26 s before detaching. The experiment was conducted in 0.5 M Na_2HPO_4, the sweep rate was 1 mV/s.

Estimation of the Current Associated with Formation of Further Oxide and the Dissolution of Gold

It is in principle possible that the current features I observe may result from Au oxidation, the OER, double layer charging or some combination of all three [329]. Because current due to double layer charging should be small relative to Au oxidation, I address only the first two possible contributions. The amount of oxide that is formed during the linear sweep is estimated to be 330 $\frac{\mu C}{cm^2}$ from the CV. Prior workers have argued that 390 $\frac{\mu C}{cm^2}$ produces one monolayer of Au oxide from cyclic voltammetry experiments with upper potential limits of 1.75 and 2.1 V. This is a slight underestimate of the amount of oxide formed in the experiment reported in Figure 5.7 due to the lower potential limit. Linear sweep voltammetry experiments described in the manuscript were performed at 1 mV/sec. The rate of gold dissolution at this scan rate is estimated to be 0.5 $\frac{ng}{cm^2}$ [215] (the lowest scan rate measured by the authors was 2 mV/s and extrapolation to 1 mV/s suggests 0.5) which translates to a gold dissolution current of 1.67 microamps (assuming oxidation of Au^0 to Au^{3+}) for the sample.

The combined currents of oxide formation (assuming one monolayer) over the course of the experiment and gold dissolution are compared to the measured current in Figure B.10. It is apparent that the great majority of the current measured above 2 V vs. RHE comes from the OER.

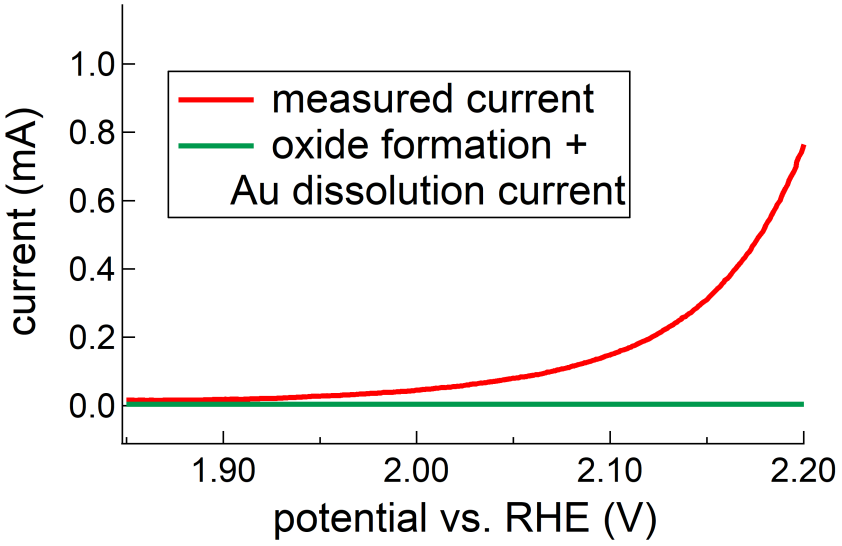

Figure B.10: Comparison of the measured current (red curve) with the combined currents of oxide formation and gold dissolution (green curve) during a linear sweep experiment. The experiment was conducted in 0.5 M Na_2HPO_4, the sweep rate was 1 mV/s.

Determination of the Size of the Active Area

Nucleation initially leads to bubbles that are only a few nanometers large [199], well below the resolution limit of the microscope. While such bubbles cannot be resolved I can identify their presence by intensity fluctuations of a few pixels against an otherwise static background. As might be expected, these fluctuations are spread over a circular area with a radius of 1-2 µms, but at this stage no clearly spherical shape can be identified and the centre of the bubble can not be determined reliably. The bubbles grow further and at around 3 µm in radius, the bubbles appear spherical. The centre of each bubble's nucleation sphere was then marked with a red dot in Figure 5.7 of the main text and a yellow cross here in Figure B.11. In the early stages of bubble growth (before it can be discerned as spherical), the bubbles geometry is ill defined and it is reasonable to assume an area for the bubble nucleation. For this purpose, I assume a circular nucleation area around the centre (blue circle), whose radius is defined by the standard deviation of a bubbles radius. This standard deviation was determined by fitting the the size of bubbles nine times by hand and then calculating the standard deviation from these nine values (the standard deviation obtained in this fashion is 1.8 µms). All nucleation sites lie in close vicinity, most nucleation areas overlap with neighbouring ones. This area was termed "active area", because, with few exceptions, every bubble originated there. An estimate for the geometrical area of this active area is then obtained by choosing an envelope that contains all nucleation areas for which it appears sensible to be grouped together. This envelope is shown in black in Figure B.11. For the present case, 69.6 square µm resulted.

The size of the *active area* determined in this manner is presumably not a function of the size of the actual active sites of the OER, rather this active area is determined by the effect spatial resolution of the images.

It is obvious that the calculated active area will linearly affect the current densities that are plotted in Figure 5.7 of the main text and that it depends to some degree on this choice of envelope (black line). However, this does not effect the argumentation in the manuscript for two reasons: i) the assumption of a spherical nucleation area with a radius of 1.8 µms is an overestimate that I am using because the microscope does not resolve the bubble nucleation on the submicron scale; ii) choice of a different envelope with the same nucleation areas (blue circles) would result in an active area that varies by ± 10 %, which would in turn alter the current density by a similar percentage. However, this can not explain the two orders of magnitude difference between the current densities of active areas and the average electrode.

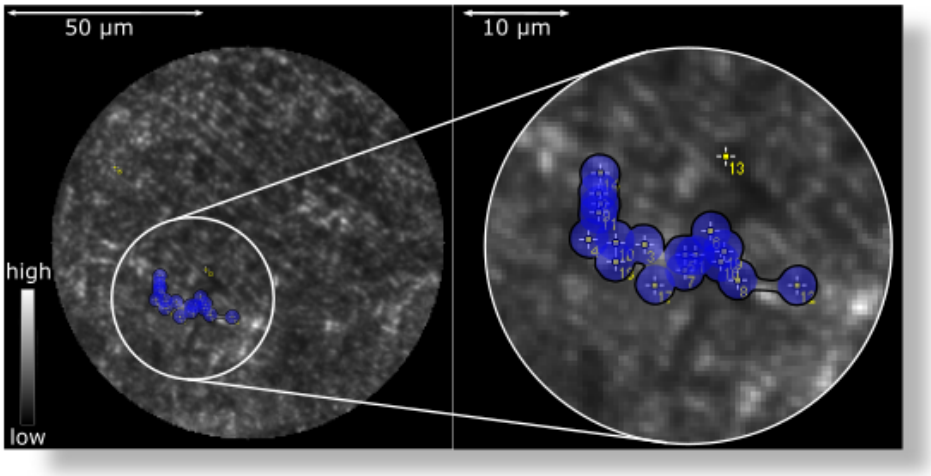

Figure B.11: The size of the active areas was determined by assuming a radius of bubble nucleation of 1.8 µms around every nucleation center (yellow crosses), overlapping these areas (blue circles) and taking the envelope (black). The radius of nucleation was determined from the standard deviation of how precisely we can determine a bubbles size.

Can the Outstanding OER Activity of Active Areas be Explained by SHM Data Alone?

In an effort to explain the outstanding activity of active areas, I performed a correlation coefficient analysis on SH-V data recorded from 0 - 1.9 V vs. RHE at 60 mV/s in 0.5 M Na_2HPO_4, pH = 9, in ppp polarization combiation with an acquisition time of 0.25 s. If a pixel has a value close to 1, then it performs like the average FOV and has a yellow hue. The farther the value is from one, the more it deviates from the average behaviour and is coloured blue. As detailed in section 5.1.1 of the main text, these maps identify areas

that perform like the average FOV and areas that deviate from the average behaviour and should therefore highlight areas with distinctive surface chemistry. This analysis was done using the MATLAB function corrcoef().

The spatial correlation map for the potential range 1.5 - 1.9 V vs. RHE shows spatial features on a tens of μm scale that resemble the grains in the SEM images. This potential range was chosen, because the oxidation of the surface leading up to the onset of the OER is believed to be more influential on OER activity, than for example spatial differences in ion sorption before surface oxidation. The map demonstrates a distinctive oxidation behaviour of large portions of the surface, where most of it is mostly either yellow, or either blue.

The nucleation sites for oxygen bubbles in a subsequent experiment (linear sweep from 1.8 - 2.2 V at 1 mV/s) are overlaid onto the map in red circles. It is striking that most of the nucleation sites lie either directly in a transition region (from yellow to blue), or close by. However, some lie in a clearly blue, or yellow region far from a transition region. More importantly, transitions from yellow to blue (or vice versa) exist over the entirety of the FOV, but oxygen bubble nucleation only occurs in a very confined area. So far there is no straightforward explanation for the elevated OER activity of some active areas from the optical SHM data alone, but this is work in progress.

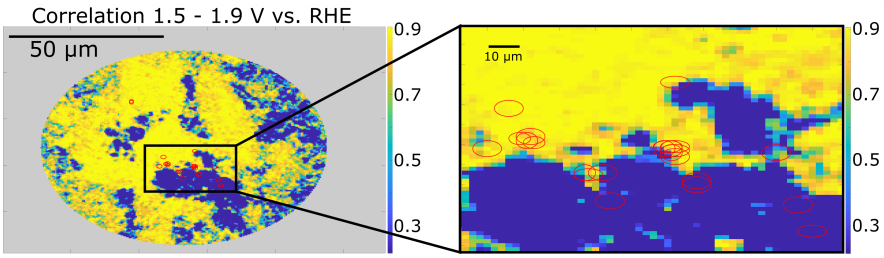

Figure B.12: Left panel: Spatial correlation map from 1.5 - 1.9 V vs. RHE at a scanning speed of 60 mV/s in 0.5 M Na_2HPO_4, pH = 9. The red circles designate nucleation sites in a subsequent linear sweep experiment from 1.8 - 2.2 V at a speed of 1 mV/s. The right panel shows a magnified excerpt of the image on the left.

SHM Data for the Second Type of Active Area that is not Stable with Respect to Surface Atom Rearrangement, Corresponding to Figure 5.9 of the Main Text

The SH intensity of the area in which the bubble(s) was nucleated was integrated and displayed vs. time.

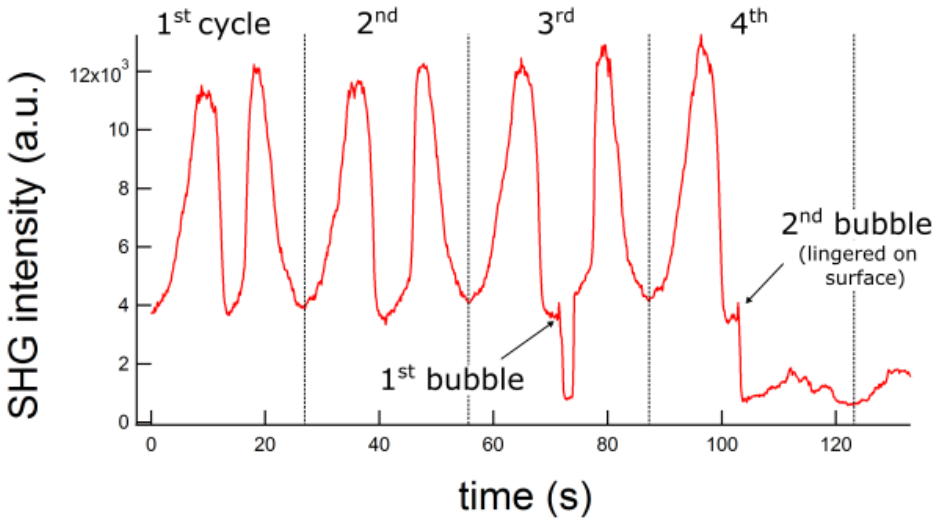

Figure B.13: Observation of the second type of active site under potential cycling conditions, corresponding to experiment one of Figure 5.9 in the main text. The scanning speed was 60 mV/s, the electrolyte 0.5 M Na_2HPO_4, pH = 9.

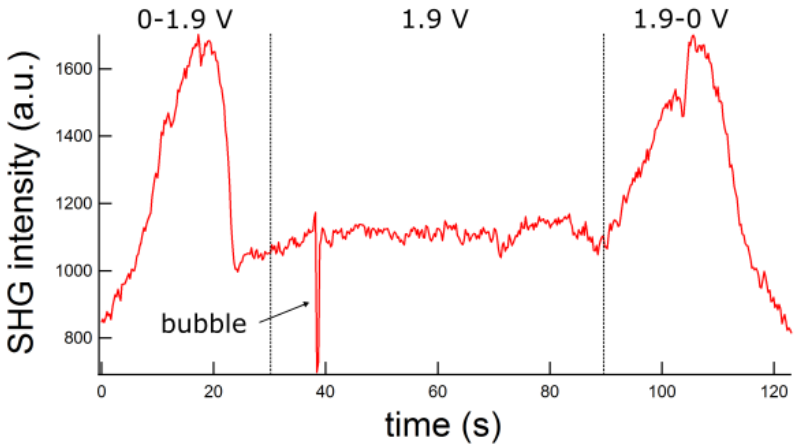

Figure B.14: Observation of second type of active site under constant potential conditions, as mentioned prior to Figure 5.9 in the main text. The electrolyte was 0.5 M Na_2HPO_4, pH = 9. The scanning speed prior to and after the potentiostatic period was 60 mV/s.

Switching Oxidation States of Pt *operando* with near-IR Femtosecond Radiation: High Valent Oxides do not Catalyze the OER

Oxide Reduction Peaks in the Reverse Scan of the Pt Microelectrode Experiment Under Illumination

The reverse scans (oxide reduction peaks) of the experiments displayed in Figure 5.11 of the main text are shown in Figure B.15.

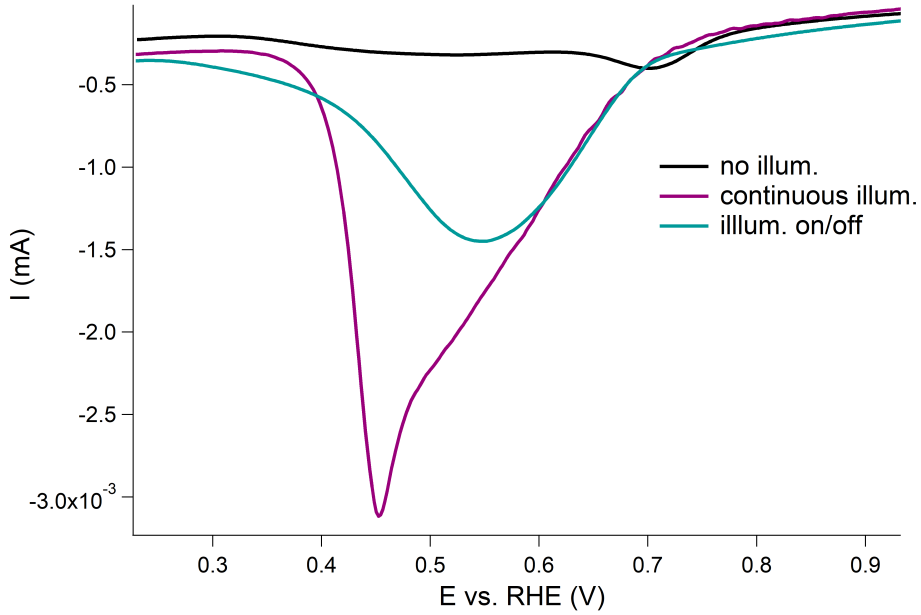

Figure B.15: Reverse sweeps of the OER illumination experiment on the Pt microelectrode. Experimental details can be found in the caption of Figure 5.11 in the main text. "continuous" illum. denotes the reverse scan corresponding to the experiment that is displayed in the left panel of Figure 5.11, while "illum. on/off" correspods to the experiment displayed in the right panel, respectively. The black curve shows a reverse scan in the absence of illumination.

Full Dataset of the Potentiostatic Pt Microelectrode Experiment Under Illumination

The full dataset for the potentiostatic experiments of the Pt microelectrode under illumination can be seen in Figures B.16 - B.18. The dataset is split up into three figures for a clearer visualization, focussing on mildly, more and highly anodic potentials. The electrode position was not changed during the experiment, only the potential was modulated and the illumination turned on/off.

The current response to the illumination is highly potential dependent. I argued in the main text that this is because of the state of the surface: as long as the surface is metallic, the holes that are excited by the 800 nm, 55 fs illumination are too short lived to participate in chemistry. As the surface gets oxidized with increasing potential, however, the lifetime of holes can be substantially higher and participation in chemistry becomes possible. Before 1.2 V vs. RHE, only a small influence of the illumination on the measured current is apparent. The amplitude of the laser-induced current oscillations grow substantially at 1.2 V vs. RHE and continue to grow until 1.5 V.

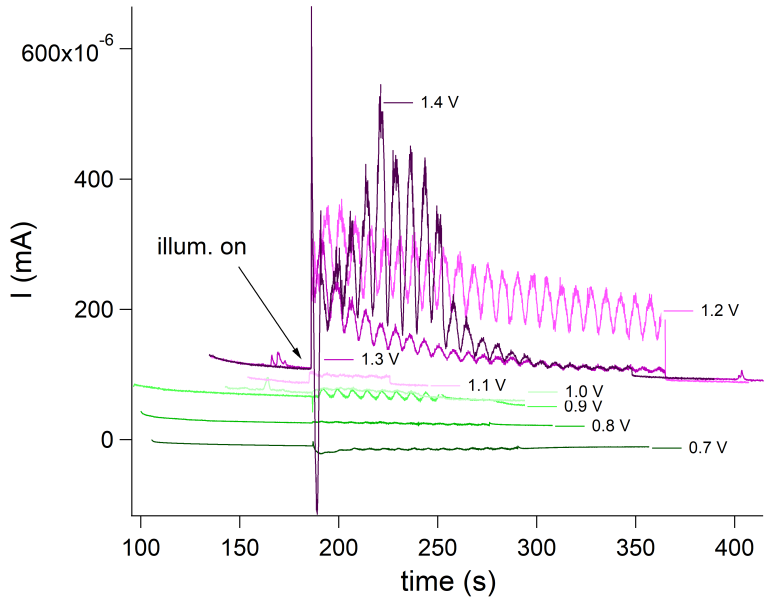

Figure B.16: Potentiostatic experiments of a Pt microelectrode with 100 micrometer diameter in 0.5 M $HClO_4$ in a spectroelectrochemical cell before, during and after illumination with 55 fs, 800 nm light at a repitition rate of 1 kHz. The illumination was turned off at different times for the different potentials. Mildly anodic potentials are shown here. Potentials are quoted vs. the RHE.

The oscillations that so far appeared to consist of only one reoccuring and disappearing peak develop a shoulder at 1.5 V vs. RHE. This shoulder likely indicates the periodic formation and depletion of a second, instable species. Until 1.5 V vs. RHE the oscillations are stable over many periods, but at 1.6 V and higher the bigger peak disappears after a few periods and a single feature oscillation with a smaller amplitude remains. At even more positive potentials also these oscillations with smaller amplitude disappear and the oscillations stop altogether, see Figure B.18.

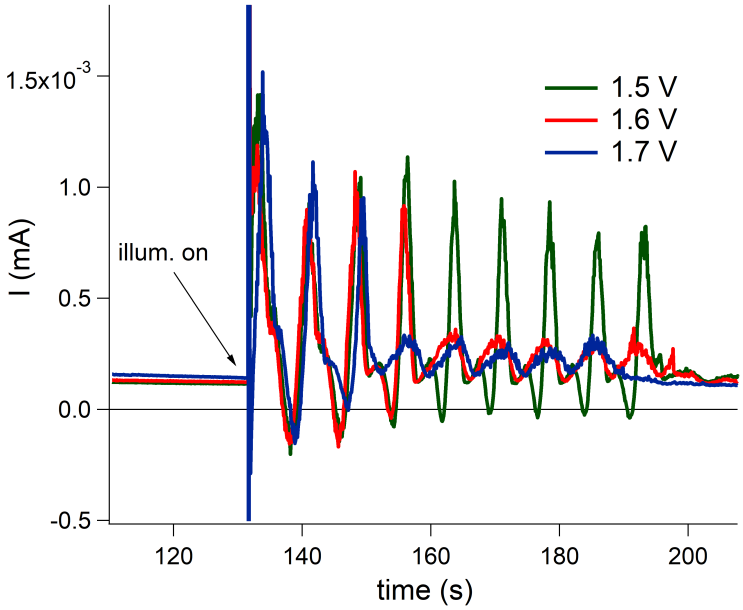

Figure B.17: Potentiostatic experiments analogous to the experiment of Figure B.16, but at more anodic potentials. The OER is slowly running at 1.7 V vs. RHE, as indicated by the offset of the blue curve from the red and green curve around 120 s. Potentials are quoted vs. the RHE.

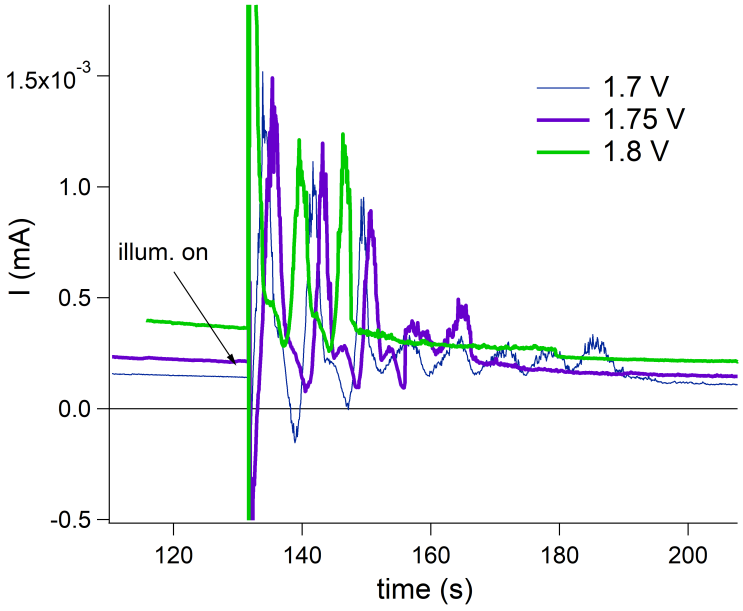

Figure B.18: Potentiostatic experiments analogous to the experiment of Figure B.16, but at highly anodic potential with ongoing OER. Potentials are quoted vs. the RHE.

XPS Analysis of a Pt_{poly} Electrode After Electrooxidation in the Presence and Absence of Illumination

For the XPS analysis of the oxide that is grown during Pt surface electrooxidation with and without 800 nm, 55 fs illumination, a macroscopic Pt_{poly} was used. The employed commercial laboratory XP spectrometer has a probe spot of approximately 2 mm diameter and samples of a similar size are needed to produce a sufficient signal to noise ratio. Consequently, the Pt microelectrode was not suited for this measurement. Therefore a 5 mm diameter Pt_{poly} was used. The electrode potential was cycled from 0.9 - 1.65 V vs. RHE (including the onset of the OER at the higher potential) 7 times with and without illumination (two separate experiments). The potential was cycled repeatedly at oxidizing potential to increase the oxide layer thickness. This was done to increase the signal of the oxide compared to the strong signal of the metal (the information depth of this measurement is 3.5 nm, which is not particularly surface sensitive). The scanning speed in this experiment was 10 mV/s, because the characteristic oxide peak due to laser illumination was smeared out at higher scanning speeds due to mass transport limitations on the macroscopic electrode. Figure B.19 shows the experiment with illumination (for clarity only one cycle under illumination is shown). The black curve shows the CV without illumination, the red curve the CV with illumination.

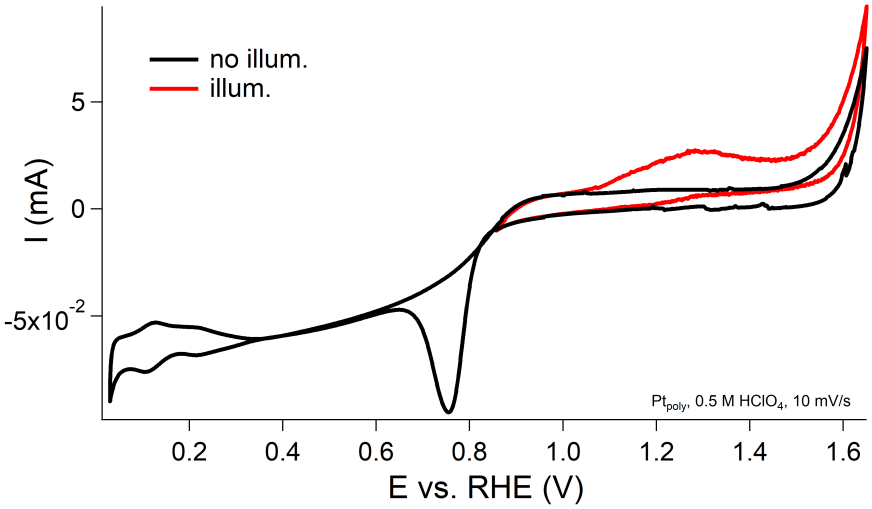

Figure B.19: CV of Pt_{poly} with and without illumination during electrooxidation. 10 mV/s scanning speed, 0.5 M $HClO_4$. The fluence was identical to the microelectrode experiment: 3 mJ/cm^2 (a larger area was illuminated in this case, though).

After potential cycling (with and without illumination), the electrode was pulled out of the electrolyte (0.5 M $HClO_4$) under potential control at 1.3 V vs. RHE (to prevent oxide reduction), rinsed thoroughly with and transported to the UHV chamber in Millipore water (to avoid salting out of the electrolyte when the electrode is placed inside the vacuum and to prevent surface contamination). The XPS measurements were conducted without

further surface preparation such as plasma cleaning after the samples had dried in the vacuum chamber. The measurements were conducted by Detre Teschner at the Inorganic Chemistry Department of the Fritz-Haber-Institute.

Spectra were collected at room temperature with non-monochromatized Al K_α radiation (1486.6 eV) using a hemispherical analyzer (Phoibos 150, SPECS). The binding energy scale was calibrated a few months before the experiment with the standard Au $4f_{7/2}$ and Cu $2p_{3/2}$ procedure. There is a slight offset (approximately -0.15 eV), both the Fermi edge in the valence band (not shown) and the main Pt $4f_{7/2}$ peak was slightly shifted negatively. This was not corrected, but could be accounted for by rigidly shifting all spectra by +0.15 eV. The elemental composition was calculated using theoretical cross sections from Yeh and Lindau [330] for O 1s and Pt 4p. These peaks are very close in binding energy (and partially overlap) and therefore the respective photoelectrons have an almost identical escape depth. The inelastic mean free path of these photoelectrons is around 1.2 nm, the information depth is 3.5 nm (the information depth of Pt 4f is 4.6 nm).

Figure B.20 shows the O 1s and Pt 4p peaks of the electrode recorded in two subsequent experiments. The red curve "EC with light" shows the XP spectrum that has been recorded after Pt electrooxidation in the presence of the illumination. "Dark EC" denotes the spectrum recorded after purely electrochemical electrode pretreatment without illumination. The Pt peak of the "EC with light" spectrum is notably smaller, which indicates a more oxidized sample. Core level quantification suggests the following O/Pt ratio: 0.97 (Dark EC) and 1.16 (EC with light).

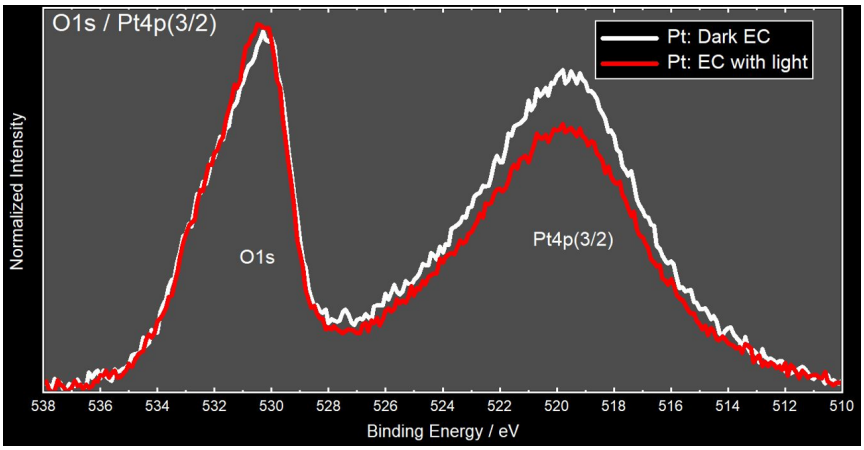

Figure B.20: XP spectra of a Pt electrode after electrooxidation in the presence ("EC with light", red curve) and absence ("Dark EC", white curve).

In accord with the argumentation in the main text, detail spectra of the Pt 4f peak suggest that the higher degree of oxidation (after electrooxidation in the presence of the illumination) is a consequence of a higher amount of PtO_2, see Figures B.21 and B.22.

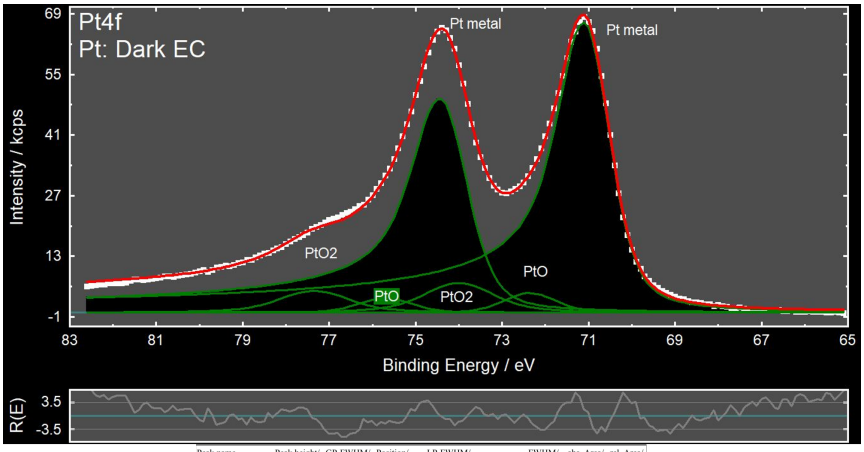

Peak name Pt4f_3	Peak height/ cps	GP-FWHM/ eV	Position/ eV	LP-FWHM/ eV	Asymmetry	FWHM/ eV	abs. Area/ cps eV	rel. Area/ %
Pt metal	66999.6	1	70.9737	0.53406	1.604	0.20237	196316	51.68
Pt metal_2	49201	1.1	74.2968	0.5	1.695	0.20463	141792	37.33
PtO	4500.7	1.24	72.3628	0.31	1.417	0	7339	1.93
PtO_2	3304.5	1.27	75.7	0.33	1.457	0	5553	1.46
PtO2	6799.9	1.4	74	0.9	1.944	0	16454	4.33
PtO2_2	5006.7	1.4	77.35	0.9	1.947	0	12123	3.19
Peak 7	165.748	0.94988	79.0501	0.5	1.251	0	254.64	0.07

Figure B.21: Pt 4f XPS peak after electrode oxidation without illumination including a fit assuming two peaks each for metallit Pt, PtO and PtO_2. Below the spectrum the residual of the fit and the fit parameters are displayed.

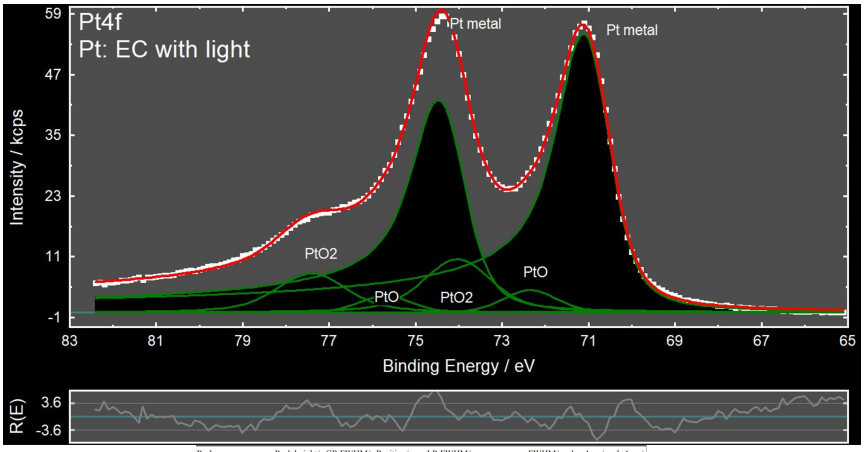

Peak name Pt4f_2	Peak height/ cps	GP-FWHM/ eV	Position/ eV	LP-FWHM/ eV	Asymmetry	FWHM/ eV	abs. Area/ cps eV	rel. Area/ %
Pt metal	55088.4	1	70.9775	0.54537	1.607	0.19877	160853	48.08
Pt metal_2	41951.6	1.01724	74.3222	0.5	1.611	0.21	117540	35.13
PtO	4417.1	1.27	72.35	0.31	1.448	0	7351	2.2
PtO_2	3284.3	1.24	75.7	0.32	1.42	0	5382	1.61
PtO2	10500	1.35	74.03	0.86724	1.875	0	24538	7.33
PtO_2	7678.4	1.4	77.4096	0.9	1.944	0	18556	5.55
Peak 7	164.798	1.4	79.4505	0.62919	1.771	0	349.78	0.1

Figure B.22: Pt 4f XPS peak after electrode oxidation with illumination including a fit assuming two peaks each for metallit Pt, PtO and PtO_2. Below the spectrum the residual of the fit and the fit parameters are displayed.

Appendix C

Identifying the Chemical Nature and Modelling the SFG Response of H_2SO_4 Derived Anions on Pt(111)

Isotope Exchange SFG Measurements Clarify the Chemical State of the Anions: they are SO_4^{2-}

Potential Dependent SFG Spectra of Sulfate on Pt(111) in D_2O

Figure C.1 shows the full data set of potential dependent sulfate/Pt(111) SFG spectra recorded in D_2O analog to Figure 6.2 of the main text.

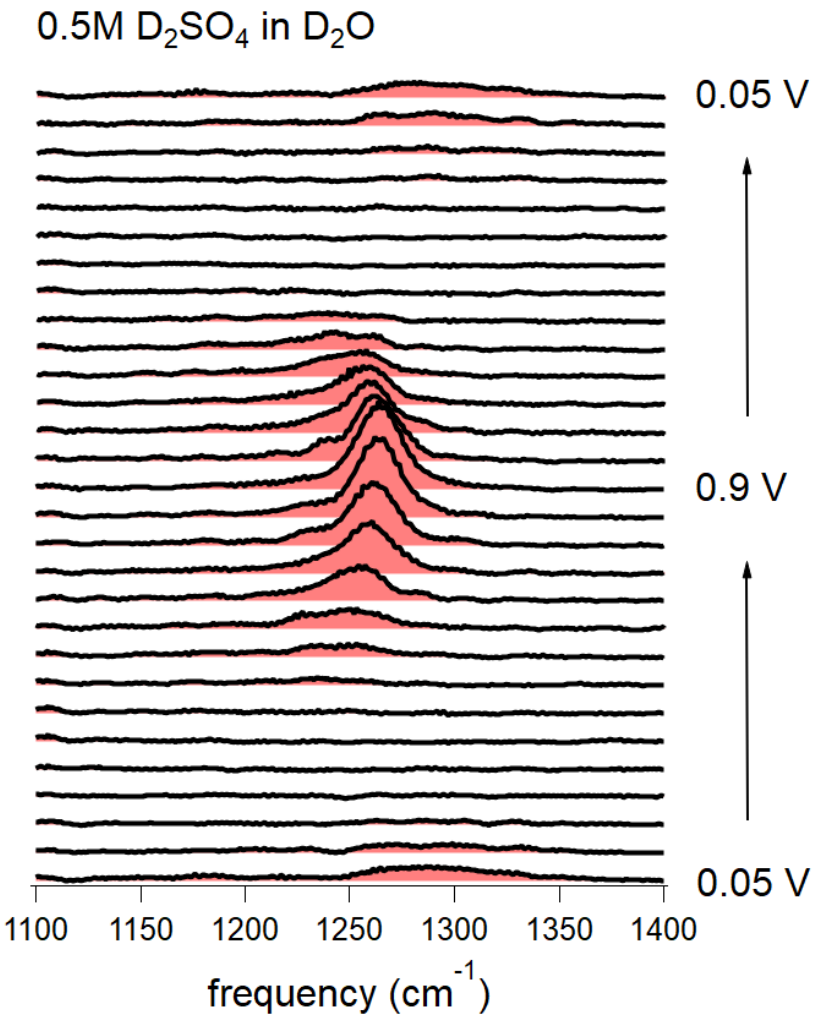

Figure C.1: Pt(111)/$SO_4^{(2)-}$ SFG spectra as a function of potential recorded in 0.5 M D_2SO_4 in D_2O. The potential in this measurement is defined by a reversible deuterium electrode (Pt wire in D_2 saturated 0.5 M D_2SO_4 in D_2O).

Cyclic Voltammetry of Pt(111) in D_2SO_4/D_2O

The CVs of the Pt(111) electrode in measurement configuration can be seen in Figure C.2 for protonic and deuteronic electrolytes. The small asymmetry of the H_{UPD} current features in forward and reverse scan likely is the result of trace amounts of O_2 being reduced in the ORR. Even though the electrolyte has been thoroughly degassed before the experiment, trace amounts of O_2 can diffuse into the spectroelectrochemical cell that is not being continuously purged throughout the optical measurement. Trace impurities in the D_2O likely are responsible for the smaller anion adsorption feature (butterfly) in the deuteronic, as compared to the protonic solution.

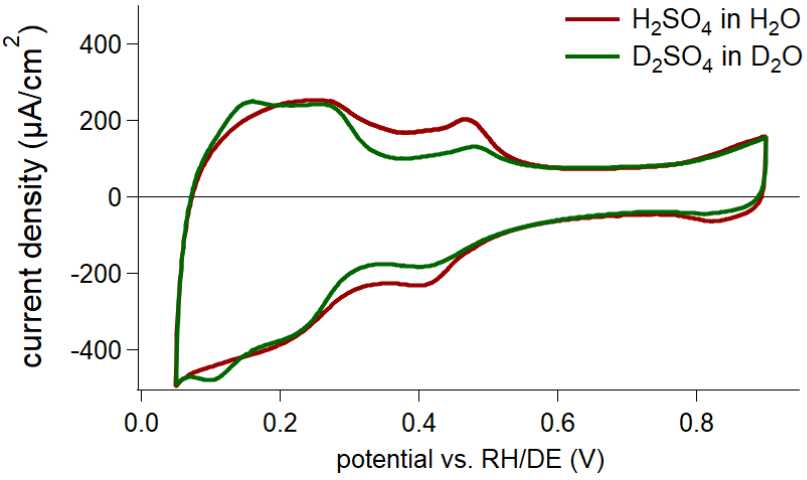

Figure C.2: Pt(111) CVs in D_2SO_4/D_2O and H_2SO_4/H_2O. The CVs were recorded in the spectroelectrochemical cell at a scanning speed of 500 mV/s and an electrolyte layer thickness of about 1 µm between the working electrode and the CaF_2 window.

Influence of IR Absorption on the Measured Spectral Features in D_2SO_4/D_2O vs. H_2SO_4/H_2O

While SFG is an interface specific process and SFG spectra disclose the desired interfacial information without prior subtraction of a reference spectrum to account for the bulk signal, IR absorption of the bulk electrolyte may influence the spectrum, because the number of generated SFG photons at a certain frequency is proportional to the available IR photons at said frequency. While no specific IR absorption occurs in H_2O from 1100 - 1400 cm^{-1}, D_2O's bending vibration may distort SFG spectra in this frequency window. In the main text I have shown that the sulfate resonances recorded in protonic and deuteronic solution are quantitatively identical after accounting for the intensity loss due to IR absorption in D_2O. In Figure C.4 I show that the nonresonant background at 0.05 V, where no sulfate resonance is present, is nearly identical for both electrolytes, thus clarifying that IR absorption does not influence the SFG line shape at any potential. For reference, the sulfate resonance at 0.9 V vs. RDE recorded in D_2O is plotted.

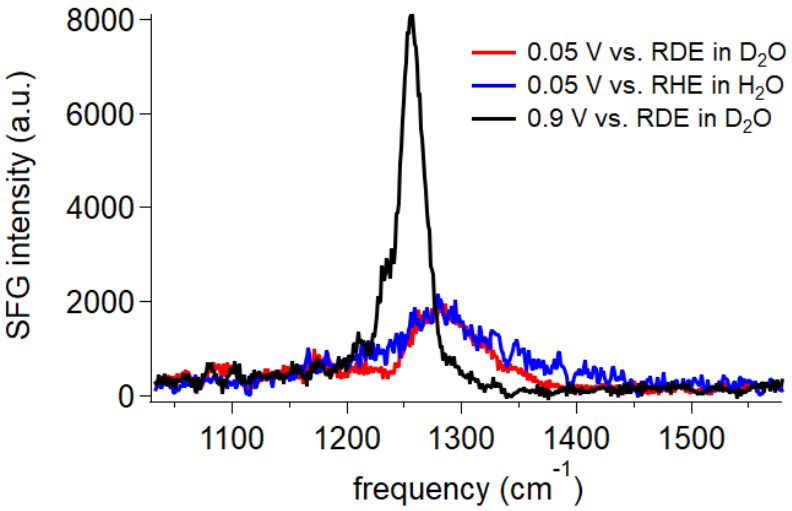

Figure C.3: SFG nonresonant background of Pt(111) in D_2SO_4/D_2O vs. H_2SO_4/H_2O. The sulfate resonance at 0.9 V vs. RDE recorded in D_2O is plotted for reference.

Details of the DFT calculation

The following two paragraphs have been modified from my own publication reference [286].

First-principles electronic-structure calculations were done employing the *FHI-aims* package [331]. The ion-electron interactions were represented in an all-electron/full-potential treatment and the atomic zeroth order regular approximation (ZORA) was modified to capture the effect of near-nuclear relativity on valence- and semicore-like electrons. The basis set utilized a set of numerical atom-centered orbitals (NAO) with the recommended setting 'tight'. The DFT calculations were performed in the generalized gradient approximation employing the extended Perdew-Burke-Ernzerhof (xPBE) functional [332], which has been proven to preserve the accuracy of PBE [333] for H-bond interactions but considerably improve the description of atomization energies of small molecules. The force convergence criterion in the self-consistency cycle was put to $10^{-5} eV/Å$. Together with the maximum residual force criterion of $10^{-4} eV/Å$ in the geometry relaxation precedure and a finite displacement of 0.0002 Å for calculating the Hessian matrix, it guarantees a precise vibrational calculation by finite differences within *FHI-aims*.

In order to model the Pt(111) surface, 55 Pt atoms were taken from a five-layer slab with an experimentally measured lattice constant of 3.92 Å. All other Pt atoms were fixed in the calculation of geometry relaxation and vibrations, except for the six platinum atoms that are closer to the adsorbate. Surface charging was shown to only have a small effect on the calculated vibrational frequencies by comparing the results acquired from the neutral adsorption model of SO_4 on the Pt(111) cluster and a model with an overall charge of -2 (see below). As differences in relative frequencies between the models are minimal, and experimental measurements of electrosorption valency find the adsorbed sulfuric acid derived anions are continuously discharged during the potential sweep, in the main text

the structures and frequencies of the charged model are reported. Here, in Figure C.4, the normal mode frequencies of the uncharged adsorbates on the same Pt(111) surface are displayed. While the modes are shifted towards higher frequencies with respect to the charged model, isotope exchange yields the same result: bisulfate and sulfate modes are clearly distinguishable. This implies that the choice of anion charge in the DFT calculation does not affect the reported conclusions.

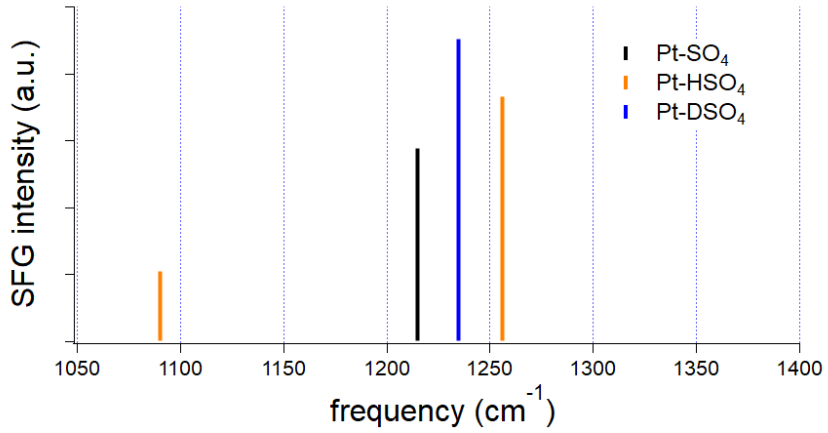

Figure C.4: Vibrational normal modes of SO_4, HSO_4 and DSO_4 on Pt(111). The adsorbate geometries were calculated by DFT.

Orientations of Transition Dipole Moments of Sulfate and Bisulfate on Pt(111)

The transition dipole moments of sulfate and bisulfate on Pt(111) are indicated by arrows in Figure C.5. Only modes with a transition dipole moment component normal to the surface (modes around 1250 cm^{-1}) can be probed by SFG.

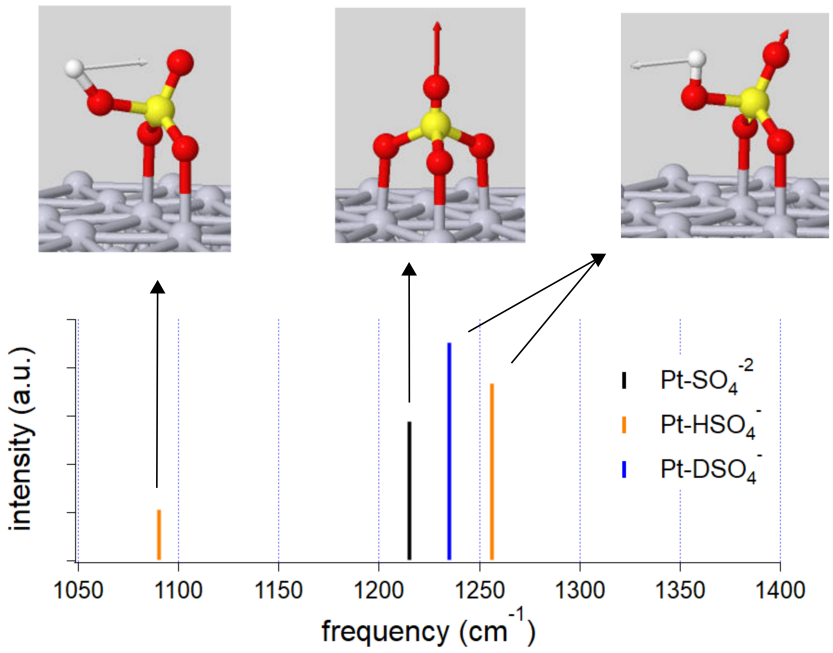

Figure C.5: Schematic representation of the transition dipole moment of SO_4^{2-} and H/DSO_4^- vibrations on Pt(111) by arrows. The adsorbate geometries were calculated by DFT.

A Microscopic Model of the Electrochemical Vibrational Stark Effect of SO_4^{2-} on Pt(111): Understanding the SFG Response

This section was modified from the supporting information of my own publication reference [52].

Fitting parameters

Derivation of Equation 6.9

Equation 6.9 was derived by evaluating the maximum of Equation 6.7, i.e., the maximum value of $\chi^{(2)}$ as a function of ω_{IR}. First, I substitute $\beta^{(2)}$ and α_{IR} in Equation 6.7 with Equations 6.4 and 6.8, respectively. To simplify the total expression, I let $L_{ext}\Delta V = U_0$, and assume the nonresonant amplitude to be zero (the line shape model discussed above suggests the resonant amplitude is 2 orders of magnitude higher than that of the

Table C.1: Parameters of the Lorentzian used to fit the resonance in the SFG data. The data was first normalized with the nonresonant background to account for the intensity distribution of the IR beam. This description of the data assumes that both nonresonant parameters are potential independent - the phase is -2, and the amplitude 1. However, because the nonresonant $\chi^{(2)}$ of Pt is small, the values of these parameters have little correlation with those describing the resonance.

E (V)	$\beta_r^{(2)}$ (a.u.)	ω_{S-O} (cm^{-1})	ω_{S-O} (cm^{-1})
0.48	4.85	1225.5	23
0.5	4.83	1229.23	29
0.52	5.35	1231.95	25
0.54	5.42	1235.5	23
0.56	5.56	1236.85	23
0.58	5.79	1240.08	22
0.6	6.01	1241.49	11
0.62	6.48	1243.61	19
0.64	6.53	1244.43	20
0.66	6.72	1247.93	19
0.68	7.16	1248.11	17
0.7	7.2	1249.96	17
0.72	7.56	1251.67	16
0.74	7.96	1252.06	15
0.76	8.24	1253.72	14
0.78	8.56	1255.49	13
0.8	8.8	1255.96	12
0.82	8.82	1257.4	13
0.84	8.95	1258.42	13
0.86	9.26	1258.86	13
0.88	9.57	1260.04	12
0.9	9.65	1260.29	12

nonresonant). Expanding the modulus of Equation 6.7 gives:

$$\frac{\beta^{(2)}_{r,pzc}U_0^n}{(\alpha_e U_0+1)^2\sqrt{\frac{\Gamma^2}{\omega^2_{pzc}}+(1-\frac{\omega_{IR}}{\omega_{pzc}})^2}\sqrt{(1+U_0(\alpha_e+\frac{\alpha_\nu(1-\frac{\omega^2_{IR}}{\omega^2_{pzc}})}{\frac{\Gamma^2\omega^2_{IR}}{\omega^4_{pzc}}+(1-\frac{\omega^2_{IR}}{\omega^2_{pzc}})^2}))^2+\frac{\alpha^2_\nu\Gamma^2U_0^2\omega^2_{IR}}{\omega^4_{pzc}(\frac{\Gamma^2\omega^2_{IR}}{\omega^4_{pzc}}+(1-\frac{\omega^2_{IR}}{\omega^2_{pzc}})^2)^2}}} \tag{C.1}$$

For this expression to reach a minimum, the quadratic term under the second root in the denominator must be zero. That is,

$$(1+U_0(\alpha_e+\frac{\alpha_\nu(1-\frac{\omega^2_{IR}}{\omega^2_{pzc}})}{\frac{\Gamma^2\omega^2_{IR}}{\omega^4_{pzc}}+(1-\frac{\omega^2_{IR}}{\omega^2_{pzc}})^2}))^2=0 \tag{C.2}$$

Since $\Gamma << \omega_{pzc}$, the terms $\frac{\Gamma^2}{\omega^2_{pzc}}$ and $\frac{\Gamma^2\omega^2_{IR}}{\omega^4_{pzc}}$ are close to zero and can be ignored. Rearranging the above equation, one obtains Equation 6.9. Note that in the full treatment described here and above I have not explicitly accounted for the potential dependence of the measured Γ on the external bias.

The Nonlinearity of the VSE and the Corresponding Conditions

Given that most of the previous VSE studies reported a linear relationship [289, 297, 275, 295] between the Stark frequency shift and the external bias, it is necessary to discuss the nonlinearity of this relationship according to Equation 6.9. Figure C.6 shows the simulated Stark shift of the peak centre frequency as a function of the local field ($L = L_{pzc} + L_{ext}\Delta V$, see main text for the definition). Figure 6.6 of the main text is reproduced in panel B); A) uses the same parameters but takes the value of L_{ext} to be one order of magnitude smaller than in B); the calculation shown in (C) is with all parameters the same as those in B), but L_{pzc} increased by 5 $Å^{-3}$. This exercise clarifies that the measured potential dependent shift in resonance centre frequency will appear linear in external field if the value of L_{pzc} is large relative to L_{ext}, or the ΔV is not sufficiently large. This explains why in previous studies mostly linear relationships were reported.

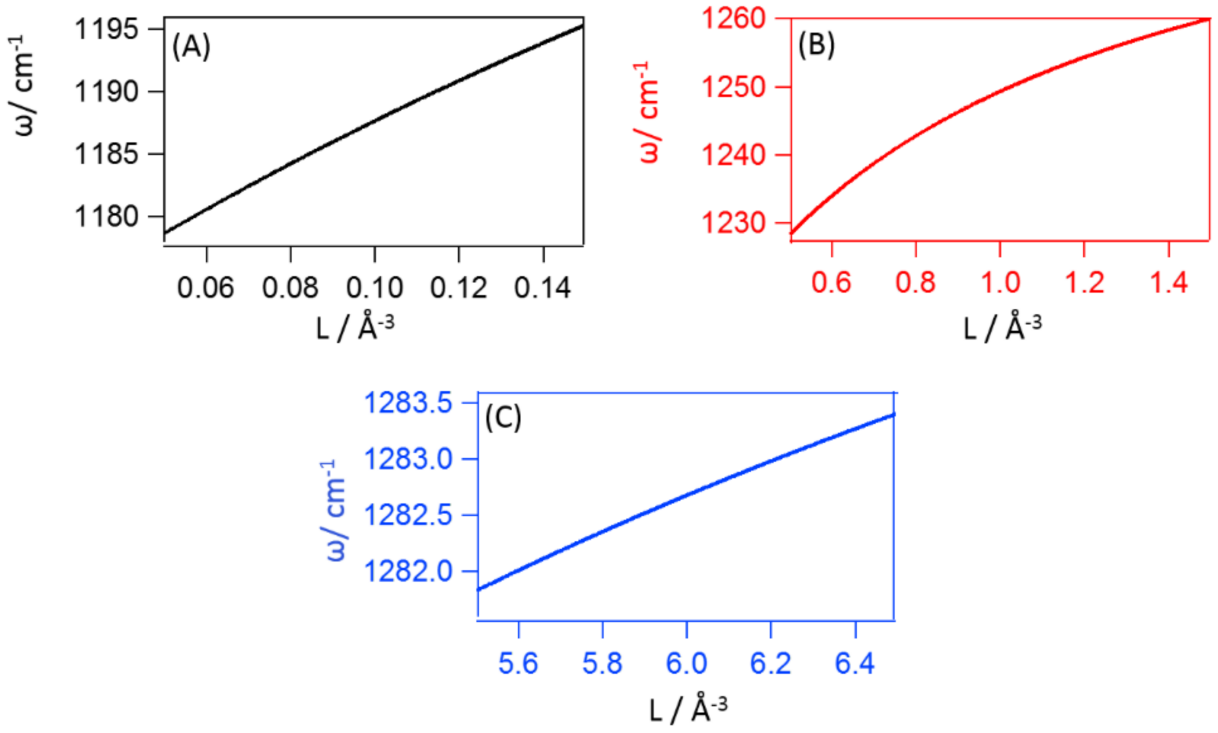

Figure C.6: Simulated Stark frequency shift as a function of local field. A), with L_{ext} 1 order of magnitude smaller than the real system of this experiment that is shown in B); C), with L_{pzc} offset by 5 $Å^{-3}$ with respect to the real system.

Laser Power Dependent VSE

During the experiment I found that the Stark frequency shifting was laser power dependent if the laser power is higher than a certain threshold. Figure C.7 shows one of the examples, as the IR power is raised from 3.6 to 4.2 mW, a clear decrease of the Stark frequency shift is observed. While I did not systematically investigate the cause of this effect - for purposes of this study I am largely interested in finding conditions where the measured parameters are independent of laser fluence - these results are consistent with a scenario in which IR powers above 3.6 mW are sufficient to induce sulfate desorption, which leads to a new, dynamic steady state equilibrium coverage under laser illumination that depends on the laser power. As has been described in the main text, coverage dependent shifts in measured frequency are well known [298, 299, 301]. It is therefore expected that if the laser modifies surface coverage, it would also modify the slope of the Stark shift.

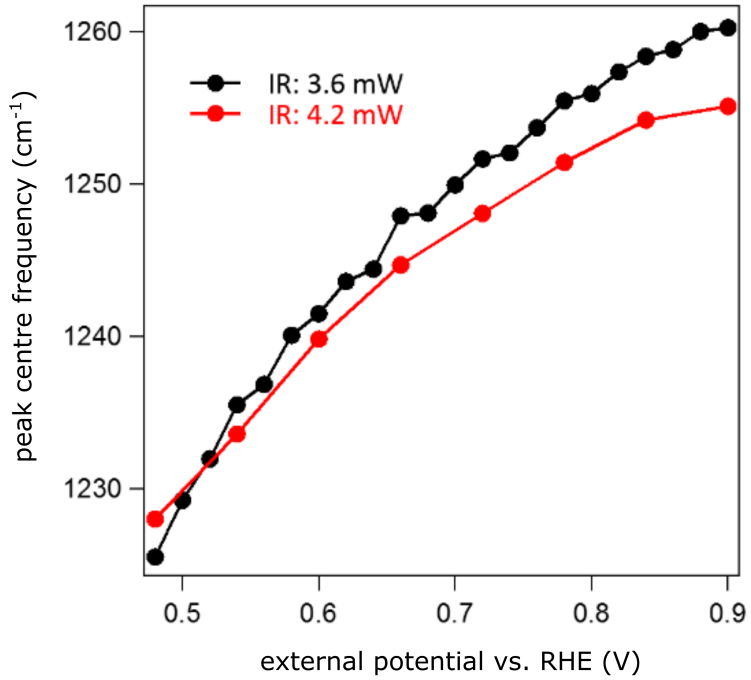

Figure C.7: Peak centre frequency as a function of applied external potential for different IR powers: black and red traces for IR powers 3.6 and 4.2 mW, respectively.

Perchlorate/Phosphate Adsorption to A Pt(111) Electroe

The frequency window 1100 - 1400 cm^{-1} was monitored with SFG while the potential of a Pt(111) electrode was cycled between 0.05 - 0.9 V vs. RHE in 0.5 M H_3PO_4 at 2 mV/s.

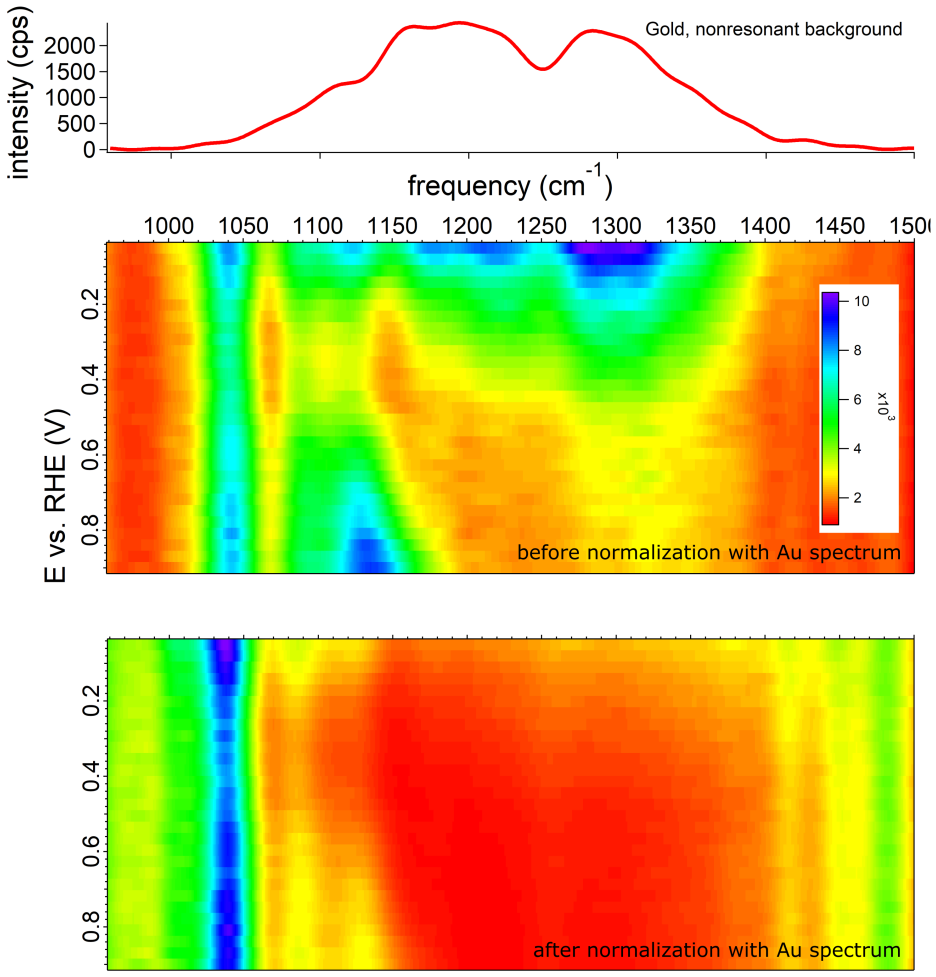

Figure C.8: Top: nonresonant background of Au that was used for signal normalization. Middle: raw data after subtraction of the background signal (acquired with blocked IR beam). Bottom: data after normalization (division) with the Au nonresonant background.

Bibliography

[1] AL Hodgkin and AF Huxley. A quantitative description of membrane current and its application to conduction and excitation in nerve. *The Journal of Physiology*, 117(4):500, 1952.

[2] PY Julien. *Erosion and Sedimentation*. Cambridge University Press, 2010.

[3] AN Gloess, B Schönbächler, B Klopprogge, D Lucio, K Chatelain, A Bongartz, A Strittmatter, M Rast, and C Yeretzian. Comparison of nine common coffee extraction methods: instrumental and sensory analysis. *European Food Research and Technology*, 236(4):607–627, 2013.

[4] WR Revie. *Corrosion and corrosion control: an introduction to corrosion science and engineering*. John Wiley & Sons, 2008.

[5] RA Marcus. Chemical and Electrochemical Electron-Transfer Theory. *Annual Review of Physical Chemistry*, 15(1):155–196, 1964.

[6] RA Nicodemus, SA Corcelli, JL Skinner, and A Tokmakoff. Collective Hydrogen Bond Reorganization in Water Studied with Temperature-Dependent Ultrafast Infrared Spectroscopy. *The Journal of Physical Chemistry B*, 115(18):5604–5616, 2011.

[7] AH Zewail. Femtochemistry: Ultrafast Dynamics of the Chemical Bond: Volume I. In *Femtochemistry: Ultrafast Dynamics of the Chemical Bond: Volume I*, pages 3–22. World Scientific, 1994.

[8] MM Martin and JT Hynes. *Femtochemistry and femtobiology: ultrafast events in molecular science*. Elsevier, 2004.

[9] SB King, K Broch, A Demling, and J Stähler. Multistep and multiscale electron transfer and localization dynamics at a model electrolyte/metal interface. *The Journal of Chemical Physics*, 150(4):041702, 2019.

[10] G Ertl. *Reactions at Solid Surfaces*. John Viley & Sons, 2009.

[11] GE Dieter and DJ Bacon. *Mechanical Metallurgy*, volume 3. McGraw-hill New York, 1986.

[12] AD Rollett, G Gottstein, LS Shvindlerman, and DA Molodov. Grain boundary mobility–a brief review. *Zeitschrift für Metallkunde*, 95(4):226–229, 2004.

[13] RG Mariano, K McKelvey, HS White, and MW Kanan. Selective increase in CO_2 electroreduction activity at grain-boundary surface terminations. *Science*, 358(6367):1187–1192, 2017.

[14] PCK Vesborg, B Seger, and I Chorkendorff. Recent Development in Hydrogen Evolution Reaction Catalysts and their Practical Implementation. *The Journal of Physical Chemistry Letters*, 6(6):951–957, 2015.

[15] R O'Hayre, S-W Cha, W Colella, and FB Prinz. *Fuel Cell Fundamentals*. John Wiley & Sons, 2016.

[16] JO'M Bockris. The origin of ideas on a Hydrogen Economy and its solution to the decay of the environment. *International Journal of Hydrogen Energy*, 27(7-8):731–740, 2002.

[17] MM Rashid, MK Al Mesfer, H Naseem, and M Danish. Hydrogen Production by Water Electrolysis: A Review of Alkaline Water Electrolysis, PEM Water Electrolysis and High Temperature Water Electrolysis. *International Journal of Engineering and Advanced Technology*, 4(3):2249–8958, 2015.

[18] U Eberle, B Müller, and R Von Helmolt. Fuel cell electric vehicles and hydrogen infrastructure: status 2012. *Energy & Environmental Science*, 5(10):8780–8798, 2012.

[19] M Carmo, DL Fritz, J Mergel, and D Stolten. A Comprehensive Review on PEM Water Electrolysis. *International Journal of Hydrogen Energy*, 38(12):4901–4934, 2013.

[20] U Babic, M Suermann, FN Büchi, L Gubler, and TJ Schmidt. Review–Identifying Critical Gaps for Polymer Electrolyte Water Electrolysis Development. *Journal of The Electrochemical Society*, 164(4):F387, 2017.

[21] A Buttler and H Spliethoff. Current status of water electrolysis for energy storage, grid balancing and sector coupling via power-to-gas and power-to-liquids: A review. *Renewable and Sustainable Energy Reviews*, 82:2440–2454, 2018.

[22] KE Ayers, EB Anderson, C Capuano, B Carter, L Dalton, G Hanlon, J Manco, and M Niedzwiecki. Research advances towards low cost, high efficiency PEM electrolysis. *ECS Transactions*, 33(1):3, 2010.

[23] E Kemppainen, A Bodin, B Sebok, T Pedersen, B Seger, B Mei, D Bae, PCK Vesborg, J Halme, Ole Hansen, D Lund, and I Chorkendorff. Scalability and feasibility of photoelectrochemical H_2 evolution: the ultimate limit of Pt nanoparticle as an HER catalyst. *Energy & Environmental Science*, 8(10):2991–2999, 2015.

[24] NM Marković and Philip N Ross. Surface science studies of model fuel cell electrocatalysts. *Surface Science Reports*, 45(4):117–229, 2002.

[25] CCL McCrory, S Jung, JC Peters, and TF Jaramillo. Benchmarking Heterogeneous Electrocatalysts for the Oxygen Evolution Reaction. *Journal of the American Chemical Society*, 135(45):16977–16987, 2013.

[26] JH Russell, LJ Nuttall, and AP Fickett. Hydrogen generation by solid polymer electrolyte water electrolysis. *American Chemical Society Division of Fuel Chemistry Prepr.*, 18:24–40, 1973.

[27] G Ertl and J Küppers. *Low energy electrons and surface chemistry*. VCH Weinheim, 1985.

[28] D Sanchez-Portal, J Stähler, and X Zhu. Basic theory of heterogeneous electron transfer. *Dynamics at Solid State Surfaces and Interfaces: Volume 2: Fundamentals*, pages 155–180, 2012.

[29] AM Funtikov, U Linke, U Stimming, and R Vogel. An in-situ STM study of anion adsorption on Pt(111) from sulfuric acid solutions. *Surface Science*, 324(1):L343–L348, 1995.

[30] NM Marković, ST Sarraf, HA Gasteiger, and PN Ross. Hydrogen electrochemistry on platinum low-index single-crystal surfaces in alkaline solution. *Journal of the Chemical Sociecty, Faraday Transactions*, 92(20):3719–3725, 1996.

[31] NM Markovic, BN Grgur, and PN Ross. Temperature-dependent hydrogen electrochemistry on platinum low-index single-crystal surfaces in acid solutions. *The Journal of Physical Chemistry B*, 101(27):5405–5413, 1997.

[32] N-T Suen, S-F Hung, Q Quan, N Zhang, Y-J Xu, and HM Chen. Electrocatalysis for the oxygen evolution reaction: recent development and future perspectives. *Chemical Society Reviews*, 46(2):337–365, 2017.

[33] G Zwaschka, I Nahalka, A Marchioro, Y Tong, S Roke, and RK Campen. Imaging the Heterogeneity of the Oxygen Evolution Reaction on Gold Electrodes Operando: Activity is Highly Local. *ACS Catalysis*, 2020.

[34] DV Tripkovic, D Strmcnik, D Van Der Vliet, VR Stamenkovic, and NM Markovic. The role of anions in surface electrochemistry. *Faraday Discussions*, 140:25–40, 2009.

[35] D Strmcnik, M Escudero-Escribano, K Kodama, VR Stamenkovic, A Cuesta, and NM Marković. Enhanced electrocatalysis of the oxygen reduction reaction based on patterning of platinum surfaces with cyanide. *Nature Chemistry*, 2(10):880–885, 2010.

[36] T Shinagawa, MT-K Ng, and K Takanabe. Electrolyte Engineering towards Efficient Water Splitting at Mild pH. *ChemSusChem*, 10(21):4155–4162, 2017.

[37] D Gao, IT McCrum, S Deo, Y-W Choi, F Scholten, W Wan, JG Chen, MJ Janik, and B Roldan Cuenya. Activity and Selectivity Control in CO_2 Electroreduction to Multicarbon Products over CuO_x Catalysts via Electrolyte design. *ACS Catalysis*, 8(11):10012–10020, 2018.

[38] MA Lopez-Bote and S Montero. Raman intensities, vibrational eigenvectors, electro-optical parameters and force constants of SO_4^{2-}, ClO_4^-, PO_4^{3-}, CO_3^{2-} and NO_3^- anions in polycrystalline samples. *Journal of Raman spectroscopy*, 9(6):386–392, 1980.

[39] AP dos Santos, A Diehl, and Y Levin. Surface Tensions, Surface Potentials, and the Hofmeister Series of Electrolyte Solutions. *Langmuir*, 26(13):10778–10783, 2010.

[40] AJ Bard, LR Faulkner, J Leddy, and CG Zoski. *Electrochemical methods: fundamentals and applications*, volume 2. Wiley New York, 2 edition, 2001.

[41] U Nickel. *Lehrbuch der Thermodynamik: eine verständliche Einführung*, volume 2. PhysChem Verlag, 2011.

[42] S Schnur and A Groß. Properties of metal–water interfaces studied from first principles. *New Journal of Physics*, 11(12):125003, 2009.

[43] LR Faulkner. Understanding electrochemistry: Some distinctive concepts. *Journal of Chemcial Education*, pages 262–264, 1983.

[44] J Tafel. Über die Polarisation bei kathodischer Wasserstoffentwicklung. *Zeitschrift für physikalische Chemie*, 50(1):641–712, 1905.

[45] JAV Butler. Studies in heterogeneous equilibria. Part II.—The kinetic interpretation of the Nernst theory of electromotive force. *Transactions of the Faraday Society*, 19(March):729–733, 1924.

[46] T Erdey-Grúz and M Volmer. Zur Theorie der Wasserstoff Überspannung. *Zeitschrift für physikalische Chemie*, 150(1):203–213, 1930.

[47] T Shinagawa, AT Garcia-Esparza, and K Takanabe. Insight on Tafel slopes from a microkinetic analysis of aqueous electrocatalysis for energy conversion. *Scientific Reports*, 5:13801, 2015.

[48] P-O Eggen. A Simple Hydrogen Electrode. *J. Chem. Educ*, 86(3):352, 2009.

[49] JM Feliu, JM Orts, R Gomez, A Aldaz, and J Clavilier. New information on the unusual adsorption states of Pt(111) in sulphuric acid solutions from potentiostatic adsorbate replacement by CO. *Journal of Electroanalytical Chemistry*, 372(1-2):265–268, 1994.

[50] A Cuesta, M Kleinert, and DM Kolb. The adsorption of sulfate and phosphate on Au(111) and Au(100) electrodes: an in situ STM study. *Physical Chemistry Chemical Physics*, 2(24):5684–5690, 2000.

[51] GA Attard, A Brew, K Hunter, J Sharman, and E Wright. Specific adsorption of perchlorate anions on Pt{hkl} single crystal electrodes. *Physical Chemistry Chemical Physics*, 16(27):13689–13698, 2014.

[52] G Zwaschka, M Wolf, RK Campen, and Y Tong. A Microscopic Model of the Electrochemical Vibrational Stark Effect: Understanding VSF Spectroscopy of (bi)Sulfate on Pt(111). *Surface Science*, 678:78–85, 2018.

[53] KJP Schouten, MJTC Van Der Niet, and MTM Koper. Impedance spectroscopy of H and OH adsorption on stepped single-crystal platinum electrodes in alkaline and acidic media. *Physical Chemistry Chemical Physics*, 12(46):15217–15224, 2010.

[54] K Krischer and ER Savinova. Handbook of heterogeneous catalysis. *Wiley-VCH*, 9:1873–1905, 2008.

[55] S Trasatti. Work function, electronegativity, and electrochemical behaviour of metals: III. Electrolytic hydrogen evolution in acid solutions. *Journal of Electroanalytical Chemistry and Interfacial Electrochemistry*, 39(1):163–184, 1972.

[56] OA Petrii and GA Tsirlina. Electrocatalytic Activity Prediction for Hydrogen Electrode Reaction: Intuition, Art, Science. *Electrochimica Acta*, 39(11):1739–1747, 1994.

[57] H Gerischer. Mechanismus der elektrolytischen Wasserstoffabscheidung und Adsorptionsenergie von atomarem Wasserstoff. *Bulletin des Sociétés Chimiques Belges*, 67(7-8):506–527, 1958.

[58] R Parsons. The rate of electrolytic hydrogen evolution and the heat of adsorption of hydrogen. *Transactions of the Faraday Society*, 54:1053–1063, 1958.

[59] J Greeley, JK Nørskov, LA Kibler, AM El-Aziz, and DM Kolb. Hydrogen evolution over bimetallic systems: Understanding the trends. *ChemPhysChem*, 7(5):1032–1035, 2006.

[60] AR Zeradjanin, J-P Grote, G Polymeros, and KJJ Mayrhofer. A Critical Review on Hydrogen Evolution Electrocatalysis: Re-exploring the Volcano-relationship. *Electroanalysis*, 28(10):2256–2269, 2016.

[61] P Quaino, F Juarez, E Santos, and W Schmickler. Volcano plots in hydrogen electrocatalysis–uses and abuses. *Beilstein Journal of Nanotechnology*, 5(1):846–854, 2014.

[62] BE Conway and L Bai. Determination of the adsorption behaviour of overpotential-deposited hydrogen-atom species in the cathodic hydrogen-evolution reaction by analysis of potential-relaxation transients. *Journal of the Chemical Society, Faraday Transactions 1: Physical Chemistry in Condensed Phases*, 81(8):1841–1862, 1985.

[63] BE Conway. Electrochemical proton transfer and cathodic hydrogen evolution. *Science Progress (1933-)*, pages 479–509, 1987.

[64] RJ Nichols and A Bewick. Spectroscopic identification of the adsorbed intermediate in hydrogen evolution on platinum. *Journal of Electroanalytical Chemistry and Interfacial Electrochemistry*, 243(2):445–453, 1988.

[65] BE Conway and L Bai. State of adsorption and coverage by overpotential-deposited H in the H_2 evolution reaction at Au and Pt. *Electrochimica Acta*, 31(8):1013–1024, 1986.

[66] L Bai. Behaviour of a hydride phase formed in the hydrogen evolution reaction at a rotating Pt electrode: analysis of potential relaxation transients from a kinetic approach. *Journal of Electroanalytical Chemistry*, 355(1-2):37–55, 1993.

[67] H Lei, B Wu, and C Cha. The adsorbed intermediate of the hydrogen evolution reaction at Pt in acid solution. *Journal of Electroanalytical Chemistry*, 332(1-2):257–264, 1992.

[68] L Bai, DA Harrington, and BE Conway. Behavior of overpotential–deposited species in Faradaic reactions–II. ac Impedance measurements on H_2 evolution kinetics at activated and unactivated Pt cathodes. *Electrochimica Acta*, 32(12):1713–1731, 1987.

[69] E Protopopoff and P Marcus. Effect of chemisorbed sulfur on the electrochemical hydrogen adsorption and recombination reactions on Pt(111). *Journal of Vacuum Science & Technology A*, 5(4):944–947, 1987.

[70] E Protopopoff and P Marcus. Effects of chemisorbed sulphur on the hydrogen adsorption and evolution on metal single crystal surfaces. *Journal de Chimie Physique*, 88(7-8):1423–1452, 1991.

[71] S Chen and A Kucernak. Electrocatalysis under conditions of high mass transport: Investigation of hydrogen oxidation on single submicron Pt particles supported on carbon. *The Journal of Physical Chemistry B*, 108(37):13984–13994, 2004.

[72] J Durst, C Simon, A Siebel, PJ Rheinländer, T Schuler, M Hanzlik, J Herranz, F Hasché, and HA Gasteiger. Hydrogen oxidation and evolution reaction (HOR/HER) on Pt electrodes in acid vs. alkaline electrolytes: Mechanism, activity and particle size effects. *ECS Transactions*, 64(3):1069–1080, 2014.

[73] R Subbaraman, D Tripkovic, K-C Chang, D Strmcnik, AP Paulikas, P Hirunsit, M Chan, J Greeley, VR Stamenkovic, and NM Markovic. Trends in activity for the water electrolyser reactions on 3d M (Ni, Co, Fe, Mn) hydr(oxy) oxide catalysts. *Nature Materials*, 11(6):550–557, 2012.

[74] D Strmcnik, M Uchimura, C Wang, R Subbaraman, N Danilovic, D van der Vliet, AP Paulikas, VR Stamenkovic, and NM Markovic. Improving the hydrogen oxidation reaction rate by promotion of hydroxyl adsorption. *Nature Chemistry*, 5(4):300–306, 2013.

[75] D Strmcnik, PP Lopes, B Genorio, VR Stamenkovic, and NM Markovic. Design principles for hydrogen evolution reaction catalyst materials. *Nano Energy*, 29:29–36, 2016.

[76] I Ledezma-Yanez, WDZ Wallace, P Sebastián-Pascual, V Climent, JM Feliu, and MTM Koper. Interfacial water reorganization as a pH-dependent descriptor of the hydrogen evolution rate on platinum electrodes. *Nature Energy*, 2(4):17031, 2017.

[77] FJ Sarabia, P Sebastián-Pascual, MTM Koper, V Climent, and JM Feliu. Effect of the Interfacial Water Structure on the Hydrogen Evolution Reaction on Pt(111) Modified with Different Nickel Hydroxide Coverages in Alkaline Media. *ACS Applied Materials & Interfaces*, 11(1):613–623, 2018.

[78] J Rossmeisl, K Chan, E Skúlason, M E Björketun, and V Tripkovic. On the pH dependence of electrochemical proton transfer barriers. *Catalysis Today*, 262:36–40, 2016.

[79] Y Zheng, Y Jiao, A Vasileff, and S-Z Qiao. The Hydrogen Evolution Reaction in Alkaline Solution: From Theory, Single Crystal Models, to Practical Electrocatalysts. *Angewandte Chemie International Edition*, 57(26):7568–7579, 2018.

[80] C Hu, L Zhang, and J Gong. Recent Progress of Mechanism Comprehension and Design of Electrocatalysts for Alkaline Water Splitting. *Energy & Environmental Science*, 2019.

[81] N Dubouis and AJL Grimaud. The Hydrogen Evolution Reaction: From Material to Interfacial Descriptors. *Chemical Science*, 2019.

[82] J Barber, S Morin, and BE Conway. Specificity of the kinetics of H_2 evolution to the structure of single-crystal Pt surfaces, and the relation between opd and upd H. *Journal of Electroanalytical Chemistry*, 446(1):125–138, 1998.

[83] BE Conway, J Barber, and S Morin. Comparative evaluation of surface structure specificity of kinetics of UPD and OPD of H at single-crystal Pt electrodes. *Electrochimica Acta*, 44(6):1109–1125, 1998.

[84] BE Conway and G Jerkiewicz. Relation of energies and coverages of underpotential and overpotential deposited H at Pt and other metals to the volcano curve for cathodic H_2 evolution kinetics. *Electrochimica Acta*, 45(25):4075–4083, 2000.

[85] BE Conway and BV Tilak. Interfacial processes involving electrocatalytic evolution and oxidation of H_2, and the role of chemisorbed H. *Electrochimica Acta*, 47(22):3571–3594, 2002.

[86] S Xue, B Garlyyev, S Watzele, Y Liang, J Fichtner, MD Pohl, and AS Bandarenka. Influence of Alkali Metal Cations on the Hydrogen Evolution Reaction Activity of Pt, Ir, Au, and Ag Electrodes in Alkaline Electrolytes. *ChemElectroChem*, 5(17):2326–2329, 2018.

[87] S Watzele, J Fichtner, B Garlyyev, JN Schwämmlein, and AS Bandarenka. On the dominating mechanism of the hydrogen evolution reaction at polycrystalline Pt-electrodes in acidic media. *ACS Catalysis*, 2018.

[88] K Kunimatsu, T Senzaki, G Samjeské, M Tsushima, and M Osawa. Hydrogen adsorption and hydrogen evolution reaction on a polycrystalline Pt electrode studied by surface-enhanced infrared absorption spectroscopy. *Electrochimica Acta*, 52(18):5715–5724, 2007.

[89] G Zwaschka, Y Tong, M Wolf, and RK Campen. Probing the Hydrogen Evolution Reaction and Charge Transfer on Platinum Electrodes on Femtosecond Timescales. *ChemElectroChem*, 6(10):2675–2682, 2019.

[90] CG Zoski. *Handbook of Electrochemistry*. Elsevier, 2007.

[91] C Frischkorn and M Wolf. Femtochemistry at metal surfaces: nonadiabatic reaction dynamics. *Chemical Reviews*, 106(10):4207–4233, 2006.

[92] E Knoesel, A Hotzel, and M Wolf. Ultrafast dynamics of hot electrons and holes in copper: Excitation, energy relaxation, and transport effects. *Physical Review B*, 57(20):12812, 1998.

[93] D Diesing, G Kritzler, M Stermann, D Nolting, and A Otto. Metal/insulator/metal junctions for electrochemical surface science. *Journal of Solid State Electrochemistry*, 7(7):389–415, 2003.

[94] AG Krivenko, J Krüger, W Kautek, and VA Benderskii. Subpicosecond-Pulse-Laser-Induced Electron Emission from Mercury and Silver into Aqueous Electrolytes. *Berichte der Bunsengesellschaft für physikalische Chemie*, 99(12):1489–1494, 1995.

[95] RR Nazmutdinov, IR Manyurov, and W Schmickler. The effect of hot electrons on heterogeneous adiabatic charge transfer reactions. *Chemical Physics Letters*, 429(4-6):457–463, 2006.

[96] RW Boyd. *Nonlinear optics*. Academic Press, 2008.

[97] YR Shen. The Principles of Nonlinear Optics. *New York, Wiley-Interscience, 1984, 575 p.*, 1984.

[98] YR Shen and V Ostroverkhov. Sum-Frequency Vibrational Spectroscopy on Water Interfaces: Polar Orientation of Water Molecules at Interfaces. *Chemical Reviews*, 106(4):1140–1154, 2006.

[99] YR Shen. *Fundamentals of Sum-Frequency Spectroscopy*. Cambridge University Press, 2016.

[100] M Buck and M Himmelhaus. Vibrational spectroscopy of interfaces by infrared–visible sum frequency generation. *Journal of Vacuum Science & Technology A: Vacuum, Surfaces, and Films*, 19(6):2717–2736, 2001.

[101] GL Richmond. Molecular Bonding and Interactions at Aqueous Surfaces as Probed by Vibrational Sum Frequency Spectroscopy. *Chemical Reviews*, 102(8):2693–2724, 2002.

[102] XD Zhu, Hajo Suhr, and YR Shen. Surface vibrational spectroscopy by infrared-visible sum frequency generation. *Physical Review B*, 35(6):3047, 1987.

[103] YR Shen. A few selected applications of surface nonlinear optical spectroscopy. *Proceedings of the National Academy of Sciences*, 93(22):12104–12111, 1996.

[104] X Zhuang, PB Miranda, D Kim, and YR Shen. Mapping molecular orientation and conformation at interfaces by surface nonlinear optics. *Physical Review B*, 59(19):12632, 1999.

[105] F Vidal and A Tadjeddine. Sum-frequency generation spectroscopy of interfaces. *Reports on Progress in Physics*, 68(5):1095, 2005.

[106] H Arnolds and M Bonn. Ultrafast surface vibrational dynamics. *Surface Science Reports*, 65(2):45–66, 2010.

[107] D Strickland and G Mourou. Compression of Amplified Chirped Optical Pulses. *Optics Communications*, 56(3):219–221, 1985.

[108] YR Shen. Surface properties probed by second-harmonic and sum-frequency generation. *Nature*, 337(6207):519, 1989.

[109] X Zhao, S Ong, H Wang, and KB Eisenthal. New method for determination of surface pKa using second harmonic generation. *Chemical Physics Letters*, 214(2):203–207, 1993.

[110] A Wieckowski. *Interfacial electrochemistry: theory: experiment, and applications*. CRC Press, 1999.

[111] CH Lee, RK Chang, and N Bloembergen. Nonlinear Electroreflectance in Silicon and Silver. *Physical Review Letters*, 18(5):167, 1967.

[112] AA Tamburello-Luca, Ph Hébert, PF Brevet, and HH Girault. Surface Second Harmonic Study of Anion Adsorption at the Mercury — Electrolyte Interface. *Journal of Electroanalytical Chemistry*, 409(1-2):123–129, 1996.

[113] P Guyot-Sionnest and A Tadjeddine. Study of Ag(111) and Au(111) Electrodes by Optical Second-Harmonic Generation. *The Journal of Chemical Physics*, 92(1):734–738, 1990.

[114] FX Wang, FJ Rodríguez, WM Albers, R Ahorinta, JE Sipe, and M Kauranen. Surface and bulk contributions to the second-order nonlinear optical response of a gold film. *Physical Review B*, 80(23):233402, 2009.

[115] A Bewick and AM Tuxford. Studies of Adsorbed Hydrogen on Platinum Cathodes Using Modulated Specular Reflectance Spectroscopy. *Journal of Electroanalytical Chemistry and Interfacial Electrochemistry*, 47(2):255–264, 1973.

[116] K Christmann. Interaction of hydrogen with solid surfaces. *Surface Science Reports*, 9(1):1–163, 1988.

[117] IT McCrum and MJ Janik. Deconvoluting Cyclic Voltammograms to Accurately Calculate Pt Electrochemically Active Surface Area. *The Journal of Physical Chemistry C*, 121(11):6237–6245, 2017.

[118] H Ogasawara and M Ito. Hydrogen adsorption on Pt(100), Pt(110), Pt(111) and Pt(1111) electrode surfaces studied by in situ infrared reflection absorption spectroscopy. *Chemical Physics Letters*, 221(3-4):213–218, 1994.

[119] A Peremans and A Tadjeddine. Electrochemical deposition of hydrogen on platinum single crystals studied by infrared-visible sum-frequency generation. *The Journal of Chemical Physics*, 103(16):7197–7203, 1995.

[120] B Ren, X Xu, XQ Li, WB Cai, and ZQ Tian. Extending surface Raman spectroscopic studies to transition metals for practical applications: II. Hydrogen adsorption at platinum electrodes. *Surface Science*, 427:157–161, 1999.

[121] K Kunimatsu, T Senzaki, M Tsushima, and M Osawa. A combined surface-enhanced infrared and electrochemical kinetics study of hydrogen adsorption and evolution on a Pt electrode. *Chemical Physics Letters*, 401(4):451–454, 2005.

[122] NM Markovic, BN Grgur, CA Lucas, and PN Ross. Surface electrochemistry of CO on Pt(110)-(1x2) and Pt(110)-(1x1) surfaces. *Surface Science*, 384(1-3):L805–L814, 1997.

[123] IT McCrum and MJ Janik. pH and Alkali Cation Effects on the Pt Cyclic Voltammogram Explained Using Density Functional Theory. *The Journal of Physical Chemistry C*, 120(1):457–471, 2015.

[124] J Clavilier, R Faure, G Guinet, and R Durand. Preparation of monocrystalline Pt microelectrodes and electrochemical study of the plane surfaces cut in the direction of the {111} and {110} planes. *Journal of Electroanalytical Chemistry and Interfacial Electrochemistry*, 107(1):205–209, 1979.

[125] G Anger, HF Berger, M Luger, S Feistritzer, A Winkler, and KD Rendulic. Microfacets of the (1×2) reconstructed Pt(110) surface seen in the adsorption dynamics of H_2. *Surface Science*, 219(3):L583–L589, 1989.

[126] M Minca, S Penner, T Loerting, A Menzel, E Bertel, R Zucca, and J Redinger. Chemisorption of hydrogen on the missing-row Pt(110)-(1×2) surface. *Topics in Catalysis*, 46(1-2):161–167, 2007.

[127] S Gudmundsdóttir, E Skúlason, K-J Weststrate, L Juurlink, and H Jónsson. Hydrogen adsorption and desorption at the Pt(110)-(1×2) surface: experimental and theoretical study. *Physical Chemistry Chemical Physics*, 15(17):6323–6332, 2013.

[128] ŞC Bădescu, P Salo, T Ala-Nissila, S-C Ying, K Jacobi, Y Wang, K Bedürftig, and G Ertl. Energetics and Vibrational States for Hydrogen on Pt(111). *Physical Review Letters*, 88(13):136101, 2002.

[129] PS Rice, Y Mao, C Guo, and P Hu. Interconversion of hydrated protons at the interface between liquid water and platinum. *Physical Chemistry Chemical Physics*, 21(11):5932–5940, 2019.

[130] N Chen, P Blowers, and RI Masel. Formation of hydronium and water–hydronium complexes during coadsorption of hydrogen and water on Pt(110)-(2×1). *Surface Science*, 419(2-3):150–157, 1999.

[131] DT Limmer, AP Willard, P Madden, and D Chandler. Hydration of metal surfaces can be dynamically heterogeneous and hydrophobic. *Proceedings of the National Academy of Sciences*, 110(11):4200–4205, 2013.

[132] K Christmann, G Ertl, and T Pignet. Adsorption of hydrogen on a Pt(111) surface. *Surface Science*, 54(2):365–392, 1976.

[133] Y Kim, C Noh, Y Jung, and H Kang. The Nature of Hydrated Protons on Platinum Surfaces. *Chemistry–A European Journal*, 23(69):17566–17575, 2017.

[134] G Hussain, L Pérez-Martínez, J-B Le, M Papasizza, G Cabello, J Cheng, and A Cuesta. How cations determine the interfacial potential profile: Relevance for the CO_2 reduction reaction. *Electrochimica Acta*, page 135055, 2019.

[135] IT McCrum and MJ Janik. First Principles Simulations of Cyclic Voltammograms on Stepped Pt(553) and Pt(533) Electrode Surfaces. *ChemElectroChem*, 3(10):1609–1617, 2016.

[136] X Chen, IT McCrum, KA Schwarz, MJ Janik, and MTM Koper. Co-adsorption of Cations as the Cause of the Apparent pH Dependence of Hydrogen Adsorption on a Stepped Platinum Single-Crystal Electrode. *Angewandte Chemie International Edition*, 56(47):15025–15029, 2017.

[137] M Thämer, L De Marco, K Ramasesha, A Mandal, and A Tokmakoff. Ultrafast 2D IR spectroscopy of the excess proton in liquid water. *Science*, 350(6256):78–82, 2015.

[138] N Agmon, HJ Bakker, RK Campen, RH Henchman, P Pohl, S Roke, M Thämer, and A Hassanali. Protons and Hydroxide Ions in Aqueous Systems. *Chemical Reviews*, 116(13):7642–7672, 2016.

[139] NM Markovic, HA Gasteiger, and PN Ross Jr. Oxygen Reduction on Platinum Low-Index Single-Crystal Surfaces in Sulfuric Acid Solution: Rotating Ring-Pt(hkl) Disk Studies. *The Journal of Physical Chemistry*, 99(11):3411–3415, 1995.

[140] B Hammer and JK Norskov. Why gold is the noblest of all the metals. *Nature*, 376(6537):238, 1995.

[141] JR Kitchin, JK Norskov, MA Barteau, and JG Chen. Modification of the surface electronic and chemical properties of Pt(111) by subsurface 3d transition metals. *The Journal of Chemical Physics*, 120:10240, 2004.

[142] K Ataka, T Yotsuyanagi, and M Osawa. Potential-Dependent Reorientation of Water Molecules at an Electrode/Electrolyte Interface Studied by Surface-Enhanced Infrared Absorption Spectroscopy. *The Journal of Physical Chemistry*, 100(25):10664–10672, 1996.

[143] Y Tong, F Lapointe, M Thämer, M Wolf, and RK Campen. Hydrophobic Water Probed Experimentally at the Gold Electrode/Aqueous Interface. *Angewandte Chemie International Edition*, 56(15):4211–4214, 2017.

[144] W Schmickler and R Guidelli. The partial charge transfer. *Electrochimica Acta*, 127:489–505, 2014.

[145] VA Marichev. Partial Charge Transfer During Anion Adsorption Methodological Aspects. *Surface Science Reports*, 56:277–324, 2005.

[146] BB Damaskin and OA Petrii. Historical Development of Theories of the Electrochemical Double Layer. *Journal of Solid State Electrochemistry*, 15:1317–1334, 2011.

[147] JW Schultze and D Rolle. The partial discharge of electrosorbates and its influence in electrocatalysis. *Canadian Journal of Chemistry*, 75(11):1750–1758, 1997.

[148] J Durst, A Siebel, C Simon, F Hasche, J Herranz, and HA Gasteiger. New insights into the electrochemical hydrogen oxidation and evolution reaction mechanism. *Energy & Environmental Science*, 7(7):2255–2260, 2014.

[149] RA Marcus. On the Theory of Oxidation-Reduction Reactions Involving Electron Transfer. *The Journal of Chemical Physics*, 24(5):966–978, 1956.

[150] AR Kucernak and C Zalitis. General models for the electrochemical hydrogen oxidation and hydrogen evolution reactions: theoretical derivation and experimental results under near mass-transport free conditions. *The Journal of Physical Chemistry C*, 120(20):10721–10745, 2016.

[151] F Fournier, W Zheng, S Carrez, H Dubost, and B Bourguignon. Vibrational dynamics of adsorbed molecules under conditions of photodesorption: Pump-probe SFG spectra of CO/Pt(111). *The Journal of Chemical Physics*, 121(10):4839–4847, 2004.

[152] C Frischkorn. Microscopic understanding of an ultrafast photochemical surface reaction: H_{ads}+H_{ads} to H_2 gas on Ru(001). *Surface Science*, 593(1):67–78, 2005.

[153] A Harata, T Edo, and T Sawada. Analysis of hydrogen on a platinum electrode using sub-picosecond time-resolved transient reflectivity measurements under electrochemical potential control. *Chemical Physics Letters*, 249(1):112–116, 1996.

[154] MJ Weaver. Potentials of zero charge for platinum (111)-aqueous interfaces: a combined assessment from in-situ and ultrahigh-vacuum measurements. *Langmuir*, 14:3932–3936, 1998.

[155] V Climent, Nuria García-Araez, E Herrero, and JM Feliu. Potential of zero total charge of platinum single crystals: A local approach to stepped surfaces vicinal to Pt(111). *Russian Journal of Electrochemistry*, 42(11):1145–1160, 2006.

[156] O Diaz-Morales, F Calle-Vallejo, C de Munck, and MTM Koper. Electrochemical Water Splitting by Gold: Evidence for an Oxide Decomposition Mechanism. *Chemical Science*, 4(6):2334–2343, 2013.

[157] J Durst, C Simon, F Hasché, and HA Gasteiger. Hydrogen oxidation and evolution reaction kinetics on carbon supported Pt, Ir, Rh, and Pd electrocatalysts in acidic media. *Journal of The Electrochemical Society*, 162(1):F190–F203, 2015.

[158] J Suntivich, KJ May, HA Gasteiger, JB Goodenough, and Y Shao-Horn. A Perovskite Oxide Optimized for Oxygen Evolution Catalysis from Molecular Orbital Principles. *Science*, 334(6061):1383–1385, 2011.

[159] CC Pavel, F Cecconi, C Emiliani, S Santiccioli, A Scaffidi, S Catanorchi, and M Comotti. Highly Efficient Platinum Group Metal Free Based Membrane-Electrode Assembly for Anion Exchange Membrane Water Electrolysis. *Angewandte Chemie International Edition*, 53(5):1378–1381, 2014.

[160] J Suntivich, HA Gasteiger, N Yabuuchi, H Nakanishi, JB Goodenough, and Y Shao-Horn. Design principles for oxygen-reduction activity on perovskite oxide catalysts for fuel cells and metal–air batteries. *Nature Chemistry*, 3(7):546–550, 2011.

[161] HS Taylor. A Theory of the Catalytic Surface. *Proceedings of the Royal Society of London. Series A, Containing Papers of a Mathematical and Physical Character*, 108(745):105–111, 1925.

[162] MTM Koper. Structure Sensitivity and Nanoscale Effects in Electrocatalysis. *Nanoscale*, 3(5):2054–2073, 2011.

[163] AP O'Mullane. From Single Crystal Surfaces to Single Atoms: Investigating Active Sites in Electrocatalysis. *Nanoscale*, 6(8):4012–4026, 2014.

[164] MJS Farias and JM Feliu. Determination of Specific Electrocatalytic Sites in the Oxidation of Small Molecules on Crystalline Metal Surfaces. *Topics in Current Chemistry*, 377(1):5, 2019.

[165] JHK Pfisterer, Y Liang, O Schneider, and AS Bandarenka. Direct instrumental identification of catalytically active surface sites. *Nature*, 549(7670):74, 2017.

[166] J Solla-Gullón, P Rodríguez, E Herrero, A Aldaz, and JM Feliu. Surface characterization of platinum electrodes. *Physical Chemistry Chemical Physics*, 10(10):1359–1373, 2008.

[167] R Schlögl. Heterogeneous catalysis. *Angewandte Chemie International Edition*, 54(11):3465–3520, 2015.

[168] SC Warren, K Voïtchovsky, H Dotan, CM Leroy, M Cornuz, F Stellacci, C Hébert, A Rothschild, and M Grätzel. Identifying champion nanostructures for solar water-splitting. *Nature Materials*, 12(9):842, 2013.

[169] C Macias-Romero, I Nahalka, HI Okur, and S Roke. Optical imaging of surface chemistry and dynamics in confinement. *Science*, 357(6353):784–788, 2017.

[170] H Angerstein-Kozlowska, BE Conway, A Hamelin, and L Stoicoviciu. Elementary steps of electrochemical oxidation of single-crystal planes of Au. Chemical basis of processes involving geometry of anions and the electrode surfaces. *Electrochimica Acta*, 31(8):1051–1061, 1986.

[171] H Angerstein-Kozlowska, BE Conway, A Hamelin, and L Stoicoviciu. Elementary steps of electrochemical oxidation of single-crystal planes of Au Part II. A chemical and structural basis of oxidation of the (111) plane. *Journal of Electroanalytical Chemistry and Interfacial Electrochemistry*, 228(1-2):429–453, 1987.

[172] U Zhumaev, AV Rudnev, J-F Li, A Kuzume, T-H Vu, and T Wandlowski. Electrooxidation of Au(111) in contact with aqueous electrolytes: New insight from in situ vibration spectroscopy. *Electrochimica Acta*, 112:853–863, 2013.

[173] K Yoshida, A Kuzume, P Broekmann, IV Pobelov, and T Wandlowski. Reconstruction and electrochemical oxidation of Au(110) surface in 0.1 M H_2SO_4. *Electrochimica Acta*, 139:281–288, 2014.

[174] T Kondo, J Morita, K Hanaoka, S Takakusagi, K Tamura, M Takahasi, J Mizuki, and K Uosaki. Structure of Au(111) and Au(100) Single-Crystal Electrode Surfaces at Various Potentials in Sulfuric Acid Solution Determined by In Situ Surface X-ray Scattering. *The Journal of Physical Chemistry C*, 111(35):13197–13204, 2007.

[175] MA Schneeweiss and DM Kolb. Oxide formation on Au(111): An in situ STM study. *Solid State Ionics*, 94(1-4):171–179, 1997.

[176] N Weiher. *Combined in situ and ex situ studies of an electrochemical interface: investigation of anodic oxide layers on Gold*. PhD thesis, Freie Universitaet Berlin, 2003.

[177] SJ Xia and VI Birss. A multi-technique study of compact and hydrous au oxide growth in 0.1 M sulfuric acid solutions. *Journal of Electroanalytical Chemistry*, 500(1-2):562–573, 2001.

[178] T Binninger, R Mohamed, K Waltar, E Fabbri, P Levecque, R Kötz, and TJ Schmidt. Thermodynamic explanation of the universal correlation between oxygen evolution activity and corrosion of oxide catalysts. *Scientific Reports*, 5:12167, 2015.

[179] LD Burke and PF Nugent. The electrochemistry of gold: II the electrocatalytic behaviour of the metal in aqueous media. *Gold Bulletin*, 31(2):39–50, 1998.

[180] M Wohlfahrt-Mehrens and J Heitbaum. Oxygen Evolution on Ru and RuO_2 Electrodes Studied using Isotope Labelling and on-line Mass Spectrometry. *Journal of Electroanalytical Chemistry and Interfacial Electrochemistry*, 237(2):251–260, 1987.

[181] S Fierro, T Nagel, H Baltruschat, and C Comninellis. Investigation of the oxygen evolution reaction on Ti/IrO_2 electrodes using isotope labelling and on-line mass spectrometry. *Electrochemistry Communications*, 9(8):1969–1974, 2007.

[182] K Macounova, M Makarova, and P Krtil. Oxygen evolution on nanocrystalline RuO_2 and $Ru_{0.9}Ni_{0.1}O_{2-\delta}$ electrodes–DEMS approach to reaction mechanism determination. *Electrochemistry Communications*, 11(10):1865–1868, 2009.

[183] C Macias-Romero, MEP Didier, P Jourdain, P Marquet, P Magistretti, OB Tarun, V Zubkovs, A Radenovic, and S Roke. High throughput second harmonic imaging for label-free biological applications. *Optics Express*, 22(25):31102–31112, 2014.

[184] I Nahalka, G Zwaschka, RK Campen, A Marchioro, and S Roke. Mapping Electrochemical Heterogeneity at Gold Surfaces: A Second Harmonic Imaging Study. *The Journal of Physical Chemistry C*, Submitted.

[185] G Niaura, AK Gaigalas, and VL Vilker. Surface-Enhanced Raman Spectroscopy of Phosphate Anions: Adsorption on Silver, Gold, and Copper Electrodes. *The Journal of Physical Chemistry B*, 101(45):9250–9262, 1997.

[186] SMA Baten, AG Taylor, and CP Wilde. Second Harmonic Generation studies of the oxidation of metal electrodes: Compact and hydrous oxide growth at gold electrodes in acid solutions. *Electrochimica Acta*, 53(23):6829–6834, 2008.

[187] B Pettinger, S Mirwald, and J Lipkowski. In-situ SHG Studies of Ionic and Molecular Adsorption on Surface Structure of Au(111)-Electrodes. *Berichte der Bunsengesellschaft für physikalische Chemie*, 97(3):395–398, 1993.

[188] B Pettinger, S Mirwald, and J Lipkowski. Microfacetting of Au(110) electrodes: An optical second-harmonic generation study. *Applied Physics A*, 60(2):121–125, 1995.

[189] BE Conway, ER White, and JO Bockris. *Modern Aspects of Electrochemistry*. Plenum Press, 1985.

[190] A Hamelin, Z Borkowska, and J Stafiej. A double layer study of the (210) and (111) faces of gold in aqueous $NaBF_4$ solutions. *Journal of Electroanalytical Chemistry and Interfacial Electrochemistry*, 189(1):85–97, 1985.

[191] RW Boyd, Z Shi, and I De Leon. The third-order nonlinear optical susceptibility of gold. *Optics Communications*, 326:74–79, 2014.

[192] J Rodríguez-Fernández, AM Funston, J Pérez-Juste, RA Álvarez-Puebla, LM Liz-Marzán, and P Mulvaney. The effect of surface roughness on the plasmonic response of individual sub-micron gold spheres. *Physical Chemistry Chemical Physics*, 11(28):5909–5914, 2009.

[193] X Lang, L Qian, P Guan, J Zi, and M Chen. Localized surface plasmon resonance of nanoporous gold. *Applied Physics Letters*, 98(9):093701, 2011.

[194] B Pettinger, J Lipkowski, and S Mirwald. In situ SHG studies of adsorption induced surface reconstruction of Au(111)-electrodes. *Electrochimica Acta*, 40(1):133–142, 1995.

[195] L Luo and HS White. Electrogeneration of Single Nanobubbles at Sub-50-nm-Radius Platinum Nanodisk Electrodes. *Langmuir*, 29(35):11169–11175, 2013.

[196] Q Chen, HS Wiedenroth, SR German, and HS White. Electrochemical Nucleation of Stable N_2 Nanobubbles at Pt Nanoelectrodes. *Journal of the American Chemical Society*, 137(37):12064–12069, 2015.

[197] Q Chen, L Luo, and HS White. Electrochemical Generation of a Hydrogen Bubble at a Recessed Platinum Nanopore Electrode. *Langmuir*, 31(15):4573–4581, 2015.

[198] H Ren, SR German, MA Edwards, Q Chen, and HS White. Electrochemical Generation of Individual O_2 Nanobubbles via H_2O_2 Oxidation. *The Journal of Physical Chemistry Letters*, 8(11):2450–2454, 2017.

[199] SR German, MA Edwards, H Ren, and HS White. Critical Nuclei Size, Rate, and Activation Energy of H_2 Gas Nucleation. *Journal of the American Chemical Society*, 140(11):4047–4053, 2018.

[200] Q Chen, L Luo, H Faraji, SW Feldberg, and HS White. Electrochemical Measurements of Single H_2 Nanobubble Nucleation and Stability at Pt Nanoelectrodes. *The Journal of Physical Chemistry Letters*, 5(20):3539–3544, 2014.

[201] DE Westerheide and JW Westwater. Isothermal Growth of Hydrogen Bubbles During Electrolysis. *American Institute of Chemical Engineers Journal*, 7(3):357–362, 1961.

[202] JP Glas and JW Westwater. Measurements of the Growth of Electrolytic Bubbles. *International Journal of Heat and Mass Transfer*, 7(12):1427–1443, 1964.

[203] JRT Seddon, ES Kooij, B Poelsema, HJW Zandvliet, and D Lohse. Surface Bubble Nucleation Stability. *Physical Review Letters*, 106(5):056101, 2011.

[204] M Guan, W Guo, L Gao, Y Tang, J Hu, and Y Dong. Investigation on the Temperature Difference Method for Producing Nanobubbles and Their Physical Properties. *ChemPhysChem*, 13(8):2115–2118, 2012.

[205] T Zambelli, J Wintterlin, J Trost, and G Ertl. Identification of the "Active Sites" of a Surface-Catalyzed Reaction. *Science*, 273(5282):1688–1690, 1996.

[206] S Dahl, A Logadottir, RC Egeberg, JH Larsen, I Chorkendorff, E Törnqvist, and JK Nørskov. Role of steps in N_2 activation on Ru(0001). *Physical Review Letters*, 83(9):1814, 1999.

[207] K Amakawa, S Wrabetz, J Kröhnert, G Tzolova-Müller, R Schlögl, and A Trunschke. In Situ Generation of Active Sites in Olefin Metathesis. *Journal of the American Chemical Society*, 134(28):11462–11473, 2012.

[208] BJ Plowman, AP O'Mullane, and SK Bhargava. The active site behaviour of electrochemically synthesised gold nanomaterials. *Faraday Discussions*, 152:43–62, 2011.

[209] S Cherevko, N Kulyk, and C-H Chung. Utilization of surface active sites on gold in preparation of highly reactive interfaces for alcohols electrooxidation in alkaline media. *Electrochimica Acta*, 69:190–196, 2012.

[210] BJ Plowman, MR Field, SK Bhargava, and AP O'Mullane. Exploiting the Facile Oxidation of Evaporated Gold Films to Drive Electroless Silver Deposition for the Creation of Bimetallic Au/Ag Surfaces. *ChemElectroChem*, 1(1):76–82, 2014.

[211] PL Hansen, JB Wagner, S Helveg, JR Rostrup-Nielsen, BS Clausen, and H Topsøe. Atom-Resolved Imaging of Dynamic Shape Changes in Supported Copper Nanocrystals. *Science*, 295(5562):2053–2055, 2002.

[212] T Lunkenbein, J Schumann, M Behrens, R Schlögl, and MG Willinger. Formation of a ZnO Overlayer in Industrial $Cu/ZnO/Al_2O_3$ Catalysts Induced by Strong Metal–Support Interactions. *Angewandte Chemie*, 127(15):4627–4631, 2015.

[213] A Wieckowski. *Interfacial Electrochemistry*. Marcel Dekker Inc., 1999.

[214] W Ruettinger and O Ilinich. *Encyclopedia of Chemical Processing*, volume 5. Taylor & Francis, 2006.

[215] S Cherevko, AA Topalov, AR Zeradjanin, I Katsounaros, and KJJ Mayrhofer. Gold dissolution: towards understanding of noble metal corrosion. *RSC Advances*, 3(37):16516–16527, 2013.

[216] LD Burke, VJ Cunnane, and BH Lee. Unusual postmonolayer oxide behavior of gold electrodes in base. *Journal of The Electrochemical Society*, 139(2):399–406, 1992.

[217] LD Burke, JA Collins, and MA Murphy. Redox and electrocatalytic activity of copper in base at unusually low, premonolayer potentials. *Journal of Solid State Electrochemistry*, 4(1):34–41, 1999.

[218] LD Burke and AP O'Mullane. Generation of active surface states of gold and the role of such states in electrocatalysis. *Journal of Solid State Electrochemistry*, 4(5):285–297, 2000.

[219] LD Burke, AJ Ahern, and AP O'Mullane. High Energy States of Gold and their Importance in Electrocatalytic Processes at Surfaces and Interfaces. *Gold Bulletin*, 35(1):3–10, 2002.

[220] N Danilovic, R Subbaraman, K-C Chang, SH Chang, YJ Kang, J Snyder, AP Paulikas, D Strmcnik, Y-T Kim, D Myers, VR Stamenkovic, and NM Markovic. Activity–stability trends for the oxygen evolution reaction on monometallic oxides in acidic environments. *The Journal of Physical Chemistry Letters*, 5(14):2474–2478, 2014.

[221] K Yamamoto, DM Kolb, R Kötz, and G Lehmpfuhl. Hydrogen adsorption and oxide formation on platinum single crystal electrodes. *Journal of Electroanalytical Chemistry and Interfacial Electrochemistry*, 96(2):233–239, 1979.

[222] Y-F Huang, PJ Kooyman, and MTM Koper. Intermediate stages of electrochemical oxidation of single-crystalline platinum revealed by in situ Raman spectroscopy. *Nature Communications*, 7(1):1–7, 2016.

[223] A Björling, E Ahlberg, and JM Feliu. Kinetics of surface modification induced by submonolayer electrochemical oxygen adsorption on Pt(111). *Electrochemistry Communications*, 12(3):359–361, 2010.

[224] A Björling and JM Feliu. Electrochemical surface reordering of Pt(111): A quantification of the place-exchange process. *Journal of Electroanalytical Chemistry*, 662(1):17–24, 2011.

[225] L Jacobse, Y-F Huang, MTM Koper, and MJ Rost. Correlation of surface site formation to nanoisland growth in the electrochemical roughening of Pt(111). *Nature Materials*, 17(3):277, 2018.

[226] JT Lundquist and P Stonehart. Platinum crystallite size effects on oxide formation and reduction parameters – II. *Electrochimica Acta*, 18(5):349–354, 1973.

[227] KJJ Mayrhofer, BB Blizanac, M Arenz, VR Stamenkovic, PN Ross, and NM Markovic. The Impact of Geometric and Surface Electronic Properties of Pt-Catalysts on the Particle Size Effect in Electrocatalysis. *The Journal of Physical Chemistry B*, 109(30):14433–14440, 2005.

[228] RR Adžić and NM Marković. Optical and electrochemical study of cation adsorption on oxide layers on gold and platinum electrodes. *Electrochimica Acta*, 30(11):1473–1479, 1985.

[229] D Strmcnik, K Kodama, D Van der Vliet, J Greeley, VR Stamenkovic, and NM Marković. The role of non-covalent interactions in electrocatalytic fuel-cell reactions on platinum. *Nature Chemistry*, 1(6):466, 2009.

[230] R Gisbert, G García, and MTM Koper. Adsorption of phosphate species on poly-oriented Pt and Pt(111) electrodes over a wide range of pH. *Electrochimica Acta*, 55(27):7961–7968, 2010.

[231] AKN Reddy, MA Genshaw, and JO'M Bockris. Ellipsometric Study of Oxygen-Containing Films on Platinum Anodes. *The Journal of Chemical Physics*, 48(2):671–675, 1968.

[232] ME van der Geest, NJ Dangerfield, and DA Harrington. An AC voltammetry study of Pt oxide growth. *Journal of Electroanalytical Chemistry*, 420(1-2):89–100, 1997.

[233] DA Harrington. Simulation of anodic Pt oxide growth. *Journal of Electroanalytical Chemistry*, 420(1-2):101–109, 1997.

[234] A Sun, J Franc, and DD Macdonald. Growth and properties of oxide films on platinum I. EIS and X-ray photoelectron spectroscopy studies. *Journal of the Electrochemical Society*, 153(7):B260–B277, 2006.

[235] F Mao, S Sharifi-Asl, J Yu, and DD Macdonald. Diagnosis of the mechanism of anodic oxide film growth on platinum in H_2SO_4. *Journal of the Electrochemical Society*, 161(5):C254–C260, 2014.

[236] VA Saveleva, V Papaefthimiou, MK Daletou, WH Doh, C Ulhaq-Bouillet, M Diebold, S Zafeiratos, and ER Savinova. Operando Near Ambient Pressure XPS (NAP-XPS) Study of the Pt Electrochemical Oxidation in H_2O and H_2O/O_2 Ambients. *The Journal of Physical Chemistry C*, 120(29):15930–15940, 2016.

[237] K Al Jaaf-Golze, DM Kolb, and D Scherson. On the voltammetry of curves of Pt(111) in aqueous solutions. *Journal of Electroanalytical Chemistry and Interfacial Electrochemistry*, 200(1-2):353–362, 1986.

[238] VI Birss, M Chang, and J Segal. Platinum oxide film formation – reduction: an in-situ mass measurement study. *Journal of Electroanalytical Chemistry*, 355(1-2):181–191, 1993.

[239] G Jerkiewicz, G Vatankhah, J Lessard, MP Soriaga, and Y-S Park. Surface-oxide growth at platinum electrodes in aqueous H_2SO_4: Reexamination of its mechanism through combined cyclic-voltammetry, electrochemical quartz-crystal nanobalance, and Auger electron spectroscopy measurements. *Electrochimica Acta*, 49(9-10):1451–1459, 2004.

[240] M Alsabet, M Grden, and G Jerkiewicz. Comprehensive study of the growth of thin oxide layers on Pt electrodes under well-defined temperature, potential, and time conditions. *Journal of Electroanalytical Chemistry*, 589(1):120–127, 2006.

[241] G Jerkiewicz, M Alsabet, M Grden, H Varela, and G Tremiliosi-Filho. Erratum to: "Comprehensive study of the growth of thin oxide layers on Pt electrodes under well-defined temperature, potential, and time conditions" [Journal of Electroanalytical Chemistry, 589 (2006) 120–127]. *Journal of Electroanalytical Chemistry*, 2(625):172–174, 2009.

[242] S Cherevko, N Kulyk, and KJJ Mayrhofer. Durability of platinum-based fuel cell electrocatalysts: Dissolution of bulk and nanoscale platinum. *Nano Energy*, 29:275–298, 2016.

[243] A Kongkanand and JM Ziegelbauer. Surface Platinum Electrooxidation in the Presence of Oxygen. *The Journal of Physical Chemistry C*, 116(5):3684–3693, 2012.

[244] J Drnec, M Ruge, F Reikowski, B Rahn, F Carla, R Felici, J Stettner, OM Magnussen, and DA Harrington. Initial stages of Pt(111) electrooxidation: dynamic and

structural studies by surface X-ray diffraction. *Electrochimica Acta*, 224:220–227, 2017.

[245] D Fantauzzi, JE Mueller, L Sabo, ACT van Duin, and T Jacob. Surface buckling and subsurface oxygen: Atomistic insights into the surface oxidation of Pt(111). *ChemPhysChem*, 16(13):2797–2802, 2015.

[246] MJ Eslamibidgoli and MH Eikerling. Atomistic Mechanism of Pt Extraction at Oxidized Surfaces: Insights from DFT. *Electrocatalysis*, 7(4):345–354, 2016.

[247] KJ Vetter and JW Schultze. The kinetics of the electrochemical formation and reduction of monomolecular oxide layers on platinum in 0.5 M H_2SO_4: Part i. Potentiostatic pulse measurements. *Journal of Electroanalytical Chemistry and Interfacial Electrochemistry*, 34(1):131–139, 1972.

[248] SJ Xia and VI Birss. In situ mass and ellipsometric study of hydrous oxide film growth on Pt in alkaline solutions. *Electrochimica Acta*, 45(22-23):3659–3673, 2000.

[249] R Arrigo, M Hävecker, ME Schuster, C Ranjan, E Stotz, A Knop-Gericke, and R Schlögl. In Situ Study of the Gas-Phase Electrolysis of Water on Platinum by NAP-XPS. *Angewandte Chemie International Edition*, 52(44):11660–11664, 2013.

[250] EL Redmond, BP Setzler, FM Alamgir, and TF Fuller. Elucidating the oxide growth mechanism on platinum at the cathode in PEM fuel cells. *Physical Chemistry Chemical Physics*, 16(11):5301–5311, 2014.

[251] M Favaro, C Valero-Vidal, J Eichhorn, FM Toma, PN Ross, J Yano, Z Liu, and EJ Crumlin. Elucidating the alkaline oxygen evolution reaction mechanism on platinum. *Journal of Materials Chemistry A*, 5(23):11634–11643, 2017.

[252] G Tremiliosi-Filho, G Jerkiewicz, and BE Conway. Characterization and Significance of the Sequence of Stages of Oxide Film Formation at Platinum Generated by Strong Anodic Polarization. *Langmuir*, 8(2):658–667, 1992.

[253] G Jerkiewicz, G Tremiliosi-Filho, and BE Conway. Significance of the apparent limit of anodic oxide film formation at Pt: saturation coverage by the quasi two-dimensional state. *Journal of Electroanalytical Chemistry*, 334(1-2):359–370, 1992.

[254] JO'M Bockris and AKM Shamshul Huq. The mechanism of the electrolytic evolution of oxygen on platinum. *Proceedings of the Royal Society of London. Series A. Mathematical and Physical Sciences*, 237(1209):277–296, 1956.

[255] A Damjanovic, A Dey, and Bockris JO'M. Kinetics of oxygen evolution and dissolution on platinum electrodes. *Electrochimica Acta*, 11(7):791–814, 1966.

[256] BE Conway and TC Liu. Characterization of electrocatalysis in the oxygen evolution reaction at platinum by evaluation of behavior of surface intermediate states at the oxide film. *Langmuir*, 6(1):268–276, 1990.

[257] J Rossmeisl, A Logadottir, and JK Nørskov. Electrolysis of water on (oxidized) metal surfaces. *Chemical physics*, 319(1-3):178–184, 2005.

[258] IC Man, H-Y Su, F Calle-Vallejo, HA Hansen, JI Martínez, NG Inoglu, J Kitchin, TF Jaramillo, JK Nørskov, and J Rossmeisl. Universality in oxygen evolution electrocatalysis on oxide surfaces. *ChemCatChem*, 3(7):1159–1165, 2011.

[259] CR Churchill and DB Hibbert. Kinetics of the Electrochemical Evolution of Isotopically Enriched Gases. Part 1 – $^{18}O^{16}O$ Evolution on Platinum in Acid and Alkaline Solution. *Journal of the Chemical Society, Faraday Transactions 1: Physical Chemistry in Condensed Phases*, 78(10):2937–2945, 1982.

[260] T Reier, M Oezaslan, and P Strasser. Electrocatalytic oxygen evolution reaction (OER) on Ru, Ir, and Pt catalysts: a comparative study of nanoparticles and bulk materials. *ACS Catalysis*, 2(8):1765–1772, 2012.

[261] X Cui, C Wang, A Argondizzo, S Garrett-Roe, B Gumhalter, and H Petek. Transient excitons at metal surfaces. *Nature Physics*, 10(7):505–509, 2014.

[262] M Kuwata-Gonokami, M Kubouchi, R Shimano, and A Mysyrowicz. Time-resolved excitonic Lyman spectroscopy of Cu_2O. *Journal of the Physical Society of Japan*, 73(4):1065–1069, 2004.

[263] CR Aita. Optical behavior of sputter-deposited platinum-oxide films. *Journal of applied physics*, 58(8):3169–3173, 1985.

[264] J Zhensheng, X Chanjuan, Z Qingmei, Y Feng, Z Jiazheng, and X Jinzhen. Catalytic behavior of nanoparticle α-PtO_2 for ethanol oxidation. *Journal of Molecular Catalysis A: Chemical*, 191(1):61–66, 2003.

[265] Y Yang, O Sugino, and T Ohno. Band gap of β-PtO_2 from first-principles. *AIP Advances*, 2(2):022172, 2012.

[266] K-T Park, DL Novikov, VA Gubanov, and Arthur J Freeman. Electronic structure of noble-metal monoxides: PdO, PtO, and AgO. *Physical Review B*, 49(7):4425, 1994.

[267] J Drnec, DA Harrington, and OM Magnussen. Electrooxidation of Pt(111) in acid solution. *Current Opinion in Electrochemistry*, 4(1):69–75, 2017.

[268] MC Figueiredo, D Hiltrop, R Sundararaman, KA Schwarz, and MTM Koper. Absence of diffuse double layer effect on the vibrational properties and oxidation of chemisorbed carbon monoxide on a Pt(111) electrode. *Electrochimica Acta*, 281:127–132, 2018.

[269] M Favaro, B Jeong, PN Ross, J Yano, Z Hussain, Z Liu, and EJ Crumlin. Unravelling the electrochemical double layer by direct probing of the solid/liquid interface. *Nature Communications*, 7(1):1–8, 2016.

[270] PW Faguy, NS Marinković, and RR Adžić. An in situ Infrared Study on the Effect of pH on Anion Adsorption at Pt(111) Electrodes from Acid Sulfate Solutions. *Langmuir*, 12(2):243–247, 1996.

[271] AM Funtikov, U Stimming, and R Vogel. Anion adsorption from sulfuric acid solutions on Pt(111) single crystal electrodes. *Journal of Electroanalytical Chemistry*, 428(1-2):147–153, 1997.

[272] A Kolics and A Wieckowski. Adsorption of bisulfate and sulfate anions on a Pt(111) electrode. *The Journal of Physical Chemistry B*, 105(13):2588–2595, 2001.

[273] E Herrero, J Mostany, JM Feliu, and J Lipkowski. Thermodynamic studies of anion adsorption at the Pt(111) electrode surface in sulfuric acid solutions. *Journal of Electroanalytical Chemistry*, 534(1):79–89, 2002.

[274] T Pajkossy and DM Kolb. Anion-adsorption-related frequency-dependent double layer capacitance of the platinum-group metals in the double layer region. *Electrochimica Acta*, 53(25):7403–7409, 2008.

[275] B Braunschweig, P Mukherjee, DD Dlott, and A Wieckowski. Real-time Investigations of Pt(111) Surface Transformations in Sulfuric Acid Solutions. *Journal of the American Chemical Society*, 132(40):14036–14038, 2010.

[276] N Garcia-Araez, V Climent, P Rodriguez, and JM Feliu. Elucidation of the Chemical Nature of Adsorbed Species for Pt(111) in H_2SO_4 Solutions by Thermodynamic Analysis. *Langmuir*, 26(14):12408–12417, 2010.

[277] T Kondo, T Masuda, N Aoki, and K Uosaki. Potential-Dependent Structures and Potential-Induced Structure Changes at Pt(111) single-crystal Electrode/Sulfuric and Perchloric Acid Interfaces in the Potential Region between Hydrogen Underpotential Deposition and Surface Oxide Formation by in situ Surface X-ray Scattering. *The Journal of Physical Chemistry C*, 120(29):16118–16131, 2016.

[278] A Lachenwitzer, N Li, and J Lipkowski. Determination of the acid dissociation constant for bisulfate adsorbed at the Pt(111) electrode by subtractively normalized interfacial Fourier transform infrared spectroscopy. *Journal of Electroanalytical Chemistry*, 532(1-2):85–98, 2002.

[279] Y Shingaya and M Ito. Comparison of a bisulfate anion adsorbed on M(111) (M = Pt, Rh, Au, Ag and Cu). *Journal of Electroanalytical Chemistry*, 467(1-2):299–306, 1999.

[280] N Hoshi, A Sakurada, S Nakamura, S Teruya, O Koga, and Y Hori. Infrared Reflection Absorption Spectroscopy of Sulfuric Acid Anion Adsorbed on Stepped Surfaces of Platinum Single-Crystal Electrodes. *The Journal of Physical Chemistry B*, 106(8):1985–1990, 2002.

[281] Z Su, V Climent, J Leitch, V Zamlynny, JM Feliu, and J Lipkowski. Quantitative SNIFTIRS studies of (bi)sulfate adsorption at the Pt(111) electrode surface. *Physical Chemistry Chemical Physics*, 12(46):15231–15239, 2010.

[282] B Braunschweig and W Daum. Superstructures and Order-Disorder Transition of Sulfate Adlayers on Pt(111) in Sulfuric Acid Solution. *Langmuir*, 25(18):11112–11120, 2009.

[283] A Comas-Vives, J Bandlow, and T Jacob. Ab initio study of the electrochemical H_2SO_4/Pt(111) interface. *Physical Chemistry Chemical Physics*, 15(3):992–997, 2013.

[284] C Nishihara and H Nozoye. Note on the hydrogen adsorption-desorption voltammogram on Pt(111) in sulfuric acid solution. *Journal of Electroanalytical Chemistry (1992)*, 379(1-2):527–530, 1994.

[285] N Garcia-Araez, V Climent, P Rodriguez, and JM Feliu. Thermodynamic analysis of (bi)sulphate adsorption on a Pt(111) electrode as a function of pH. *Electrochimica Acta*, 53(23):6793–6806, 2008.

[286] IY Zhang, G Zwaschka, Z Wang, M Wolf, RK Campen, and Y Tong. Resolving the chemical identity of H_2SO_4 derived anions on Pt(111) electrodes: they're sulfate. *Physical Chemistry Chemical Physics*, 21(35):19147–19152, 2019.

[287] R Jinnouchi, T Hatanaka, Y Morimoto, and M Osawa. First principles study of sulfuric acid anion adsorption on a Pt(111) electrode. *Physical Chemistry Chemical Physics*, 14(9):3208–3218, 2012.

[288] MJ Weaver and SA Wasileski. Influence of Double-Layer Solvation on Local versus Macroscopic Surface Potentials on Ordered Platinum-Group Metals as Sensed by the Vibrational Stark Effect. *Langmuir*, 17(10):3039–3043, 2001.

[289] A Ge, PE Videla, GL Lee, B Rudshteyn, J Song, CP Kubiak, VS Batista, and T Lian. Interfacial Structure and Electric Field Probed by in Situ Electrochemical Vibrational Stark Effect Spectroscopy and Computational Modeling. *The Journal of Physical Chemistry C*, 121(34):18674–18682, 2017.

[290] JA Santana, CR Cabrera, and Y Ishikawa. A density-functional theory study of electrochemical adsorption of sulfuric acid anions on Pt(111). *Physical Chemistry Chemical Physics*, 12(32):9526–9534, 2010.

[291] K-Y Yeh, NA Restaino, MR Esopi, JK Maranas, and MJ Janik. The adsorption of bisulfate and sulfate anions over a Pt(111) electrode: A first principle study of adsorption configurations, vibrational frequencies and linear sweep voltammogram simulations. *Catalysis Today*, 202:20–35, 2013.

[292] V Briega-Martos, E Herrero, and JM Feliu. Pt(hkl) surface charge and reactivity. *Current Opinion in Electrochemistry*, 2019.

[293] E Tyrode and R Corkery. Charging of Carboxylic Acid Monolayers with Monovalent Ions at Low Ionic Strengths: Molecular Insight Revealed by Vibrational Sum Frequency Spectroscopy. *The Journal of Physical Chemistry C*, 122(50):28775–28786, 2018.

[294] I Villegas and MJ Weaver. Infrared spectroscopy of model electrochemical interfaces in ultrahigh vacuum: roles of solvation in the vibrational stark effect. *The Journal of Physical Chemistry B*, 101(30):5842–5852, 1997.

[295] V Climent, N García-Araez, and JM Feliu. Influence of alkali cations on the infrared spectra of adsorbed (bi)sulphate on Pt(111) electrodes. *Electrochemistry Communications*, 8(10):1577–1582, 2006.

[296] R Jinnouchi, T Hatanaka, Y Morimoto, and M Osawa. Stark effect on vibration frequencies of sulfate on Pt(111) electrode. *Electrochimica Acta*, 101:254–261, 2013.

[297] JG Patrow, SA Sorenson, and JM Dawlaty. Direct spectroscopic measurement of interfacial electric fields near an electrode under polarizing or current-carrying conditions. *The Journal of Physical Chemistry C*, 121(21):11585–11592, 2017.

[298] M Scheffler. The influence of lateral interactions on the vibrational spectrum of adsorbed CO. *Surface Science*, 81(2):562–570, 1979.

[299] BNJ Persson and R Ryberg. Vibrational interaction between molecules adsorbed on a metal surface: The dipole-dipole interaction. *Physical Review B*, 24(12):6954, 1981.

[300] EHG Backus and M Bonn. A quantitative comparison between reflection absorption infrared and sum-frequency generation spectroscopy. *Chemical Physics Letters*, 412(1-3):152–157, 2005.

[301] M Cho, C Hess, and M Bonn. Lateral interactions between adsorbed molecules: Investigations of CO on Ru(001) using nonlinear surface vibrational spectroscopies. *Physical Review B*, 65(20):205423, 2002.

[302] JK Sass, D Lackey, J Schott, and B Straehler. Electrochemical double layer simulations by halogen, alkali and hydrogen coadsorption with water on metal surfaces. *Surface Science*, 247(2-3):239–247, 1991.

[303] I Villegas and MJ Weaver. Modeling electrochemical interfaces in ultrahigh vacuum: molecular roles of solvation in double-layer phenomena. *The Journal of Physical Chemistry C*, 49:10166–10177, 1997.

[304] P Jungwirth, JE Curtis, and DJ Tobias. Polarizability and aqueous solvation of the sulfate dianion. *Chemical Physics Letters*, 367(5-6):704–710, 2003.

[305] S Yang, H Noguchi, and K Uosaki. Broader energy distribution of CO adsorbed at polycrystalline Pt electrode in comparison with that at Pt(111) electrode in H_2SO_4 solution confirmed by potential dependent IR/visible double resonance sum frequency generation spectroscopy. *Electrochimica Acta*, 235:280–286, 2017.

[306] J Wang, M Xu, Z Huangfu, Y Wang, Y He, W Guo, and Z Wang. Observation of gold electrode surface response to the adsorption and oxidation of thiocyanate in acidic electrolyte with broadband sum-frequency generation spectroscopy. *Vibrational Spectroscopy*, 85:122–127, 2016.

[307] S Xu, S Xing, S-S Pei, V Ivanistsev, R Lynden-Bell, and S Baldelli. Molecular Response of 1-Butyl-3-Methylimidazolium Dicyanamide Ionic Liquid at the Graphene Electrode Interface Investigated by Sum Frequency Generation Spectroscopy and Molecular Dynamics Simulations. *The Journal of Physical Chemistry C*, 119(46):26009–26019, 2015.

[308] P Koelsch, MI Muglali, M Rohwerder, and A Erbe. Third-order effects in resonant sum-frequency-generation signals at electrified metal/liquid interfaces. *Journal of the Optical Society of America B*, 30(1):219–223, 2013.

[309] ZD Schultz, SK Shaw, and AA Gewirth. Potential Dependent Organization of Water at the Electrified Metal-Liquid Interface. *Journal of the American Chemical Society*, 127(45):15916–15922, 2005.

[310] BNJ Persson and M Persson. Vibrational lifetime for CO adsorbed on Cu(100). *Solid State Communications*, 36(2):175–179, 1980.

[311] ME Schmidt and P Guyot-Sionnest. Electrochemical tuning of the lifetime of the CO stretching vibration for CO/Pt(111). *The Journal of Chemical Physics*, 104(6):2438–2445, 1996.

[312] Y Tong, IY Zhang, and RK Campen. Experimentally quantifying anion polarizability at the air/water interface. *Nature Communications*, 9(1):1–8, 2018.

[313] MCd Santos, DWa Miwa, and SAS Machado. Study of anion adsorption on polycrystalline Pt by electrochemical quartz crystal microbalance. *Electrochemistry Communications*, 2(10):692–696, 2000.

[314] Y Sawatari, J Inukai, and M Ito. The Structure of Bisulfate and Perchlorate on a Pt(111) Electrode Surface Studied by Infrared Spectroscopy and Ab-Initio Molecular Orbital Calculation. *Journal of Electron Spectroscopy and Related Phenomena*, 64:515–522, 1993.

[315] G Herzberg. Molecular Spectra and Molecular Structure II. Infrared and Raman Spectra. *Beijing: Science Press*, 215:281, 1945.

[316] Y Chen, Y-H Zhang, and L-J Zhao. ATR-FTIR spectroscopic studies on aqueous $LiClO_4$, $NaClO_4$, and $Mg(ClO_4)_2$ solutions. *Physical Chemistry Chemical Physics*, 6(3):537–542, 2004.

[317] AF Holleman. *Lehrbuch der anorganischen Chemie*. Walter de Gruyter GmbH & Co KG, 2019.

[318] K Zeng and D Zhang. Recent progress in alkaline water electrolysis for hydrogen production and applications. *Progress in Energy and Combustion Science*, 36(3):307–326, 2010.

[319] PW Faguy, N Markovic, and PN Ross. Anion adsorption on Pt(100) from sulfuric acid: electrochemistry and fourier transform infrared spectroscopy. *Journal of The Electrochemical Society*, 140(6):1638–1641, 1993.

[320] G Jerkiewicz. Hydrogen sorption at in electrodes. *Progress in Surface Science*, 57(2):137–186, 1998.

[321] MTM Koper and JJ Lukkien. Modeling the Butterfly: Influence of Lateral Interactions and Adsorption Geometry on the Voltammetry at (111) and (100) Electrodes. *Surface Science*, 498(1-2):105–115, 2002.

[322] GS Karlberg, TF Jaramillo, E Skulason, J Rossmeisl, T Bligaard, and JK Nørskov. Cyclic voltammograms for H on Pt(111) and Pt(100) from first principles. *Physical Review Letters*, 99(12):126101, 2007.

[323] LA Kibler, A Cuesta, M Kleinert, and DM Kolb. In-situ STM characterisation of the surface morphology of platinum single crystal electrodes as a function of their preparation. *Journal of Electroanalytical Chemistry*, 484(1):73–82, 2000.

[324] J Clavilier, D Armand, and B L Wu. Electrochemical Study of the Initial Surface Condition of Platinum Surfaces with (100) and (111) Orientations. *Journal of Electroanalytical Chemistry*, 135:159–166, 1982.

[325] MJTC Van der Niet, N Garcia-Araez, J Hernández, JM Feliu, and MTM Koper. Water dissociation on well-defined platinum surfaces: The electrochemical perspective. *Catalysis Today*, 202:105–113, 2013.

[326] RW Zurilla, RK Sen, and E Yeager. The Kinetics of the Oxygen Reduction Reaction on Gold in Alkaline Solution. *Journal of the Electrochemical Society*, 125(7):1103–1109, 1978.

[327] A Hamelin, MJ Sottomayor, F Silva, S-C Chang, and MJ Weaver. Cyclic voltammetric characterization of oriented monocrystalline gold surfaces in aqueous alkaline solution. *Journal of Electroanalytical Chemistry and Interfacial Electrochemistry*, 295(1-2):291–300, 1990.

[328] A Hamelin. Cyclic voltammetry at gold single-crystal surfaces. Part 1. Behaviour at low-index faces. *Journal of Electroanalytical Chemistry*, 407(1-2):1–11, 1996.

[329] HA Laitinen and MS Chao. The Anodic Surface Oxidation of Gold. *Journal of The Electrochemical Society*, 108(8):726–731, 1961.

[330] JJ Yeh and I Lindau. Atomic Subshell Photoionization Cross Sections and Asymmetry Parameters: $1 \leq Z \leq 103$. *Atomic Data and Nuclear Data Tables*, 32(1):1–155, 1985.

[331] V Blum, R Gehrke, F Hanke, P Havu, V Havu, X Ren, K Reuter, and M Scheffler. Ab initio molecular simulations with numeric atom-centered orbitals. *Computer Physics Communications*, 180(11):2175–2196, 2009.

[332] X Xu and WA Goddard III. The extended Perdew-Burke-Ernzerhof functional with improved accuracy for thermodynamic and electronic properties of molecular systems. *The Journal of Chemical Physics*, 121(9):4068–4082, 2004.

[333] JP Perdew, K Burke, and M Ernzerhof. Generalized gradient approximation made simple. *Physical Review Letters*, 77(18):3865, 1996.

List of Publications

Publications in the Framework of this Thesis

Gregor Zwaschka, Martin Wolf, R. Kramer Campen, Yujin Tong, "A Microscopic Model of the Electrochemical Vibrational Stark Effect: Understanding VSF Spectroscopy of (bi)Sulfate on Pt(111)". *Surface Science* 678, 78-85 (2018).

Gregor Zwaschka, Yujin Tong, Martin Wolf, R. Kramer Campen, "Probing the Hydrogen Evolution Reaction and Charge Transfer on Platinum Electrodes on Femtosecond Timescales". *ChemElectroChem* 6, no. 10., 2675 - 2682 (2019).

Igor Ying Zhang, **Gregor Zwaschka**, Zhenhua Wang, Martin Wolf, R. Kramer Campen, Yujin Tong, "Resolving the chemical identity of H_2SO_4 derived anions on Pt(111) electrodes: they're sulfate". *Physical Chemistry Chemical Physics* 21, no. 35, 19147 - 19152 (2019).

Gregor Zwaschka, Igor Nahalka, Arianna Marchioro, Yujin Tong, Sylvie Roke and R. Kramer Campen, "Imaging the Heterogeneity of the Oxygen Evolution Reaction on Gold Electrodes Operando: Activity is Highly Local". *ACS Catalysis* 10, 11, 6084 - 6093 (2020).

Igor Nahalka, **Gregor Zwaschka**, R. Kramer Campen, Arianna Marchioro, Sylvie Roke "Mapping Electrochemical Heterogeneity at Gold Surfaces: A Second Harmonic Imaging Study". Submitted to *The Journal of Physical Chemistry C* (2020).

In Preparation

Gregor Zwaschka, Martin Wolf, Yujin Tong, Detre Teschner, R. Kramer Campen "High Valent Pt Oxides do not catalyze the OER: separating metal oxidation state and applied bias on Pt".

Gregor Zwaschka, Martin Wolf, R. Kramer Campen, Yujin Tong "Spectroscopically Resolving Underpotentially Deposited Hydrogen on Pt(111), Pt(110) and the Influence of Alkali Metal Cations on Interfacial Solvation and the Hydrogen Evolution Reaction".

Publications on other Topics

Andrew S. Crampton, Claron J. Ridge, Marian D. Rötzer, **Gregor Zwaschka**, Thomas Braun, Valerio D'Elia, Jean-Marie Basset, Florian F. Schweinberger, Sebastian Günther, Ueli Heiz "Atomic Structure Control of Silica Thin Films on Pt(111)". *The Journal of Physical Chemistry C* 119, 24, 13665 - 13669 (2015).

Manuel Rondelli, **Gregor Zwaschka**, Maximilian Krause, Marian D. Rötzer, Mohamed N. Hedhili, Manuel P. Högerl, Valerio D'Elia, Florian F. Schweinberger, Jean-Marie Basset, Ueli Heiz "Exploring the Potential of Different-Sized Supported Subnanometer Pt Clusters as Catalysts for Wet Chemical Applications". *ACS Catalysis* 7, 6, 4152 - 4162 (2017).

Jürgen Kraus, Lena Böbel, **Gregor Zwaschka**, Sebastian Günther "Understanding the Reaction Kinetics to Optimize Graphene Growth on Cu by Chemical Vapor Deposition". *Annalen der Physik* 529, 1700029 (2017).

Gregor Zwaschka, Manuel Rondelli, Maximilian Krause, Marian D. Rötzer, Mohamed N. Hedhili, Ueli Heiz, Jean-Marie Basset, Florian F. Schweinberger, Valerio D'Elia "Supported sub-nanometer Ta oxide clusters as model catalysts for the selective epoxidation of cyclooctene". *New Journal of Chemistry* 42, 3035 - 3041 (2018).

Acknowledgements

Despite showing only my name on the front page, this thesis could not have been written without the help of many others.

First I would like to thank Martin Wolf, the director of the Physical Chemistry Department of the Fritz Haber Institut (FHI) for enabling me to conduct my work in his department. From the limited understanding of a PhD student, part of Martin Wolf's success as a scientist comes from his ability to create an atmosphere of collegiality and openness in his department that, in turn, attracts many great and capable personalities. I have always felt treated fairly as a PhD student and I was never under the impression that PhD students are viewed as lifeless workhorses in his department (which does happen elsewhere). The yearly excursions and christmas parties that Martin Wolf financed from his personal funds were always spectacular and deserve mention.

I owe a very special thank you to Kramer Campen, who supervised my work at FHI from start to finish. I particularly value the freedom I enjoyed while working with Kramer. While, of course, I was supposed to work on certain subjects, I always felt that I had the freedom to do this as I imagined (but maybe this is just my imagination and Kramer was perpetually upset with my stubbornness). I was also free to start a few new projects and a collaboration that ultimately ended up as publications and chapters of my thesis. Perhaps Kramer was a bit too liberal with the freedoms I enjoyed which ultimately spoiled me: I felt free to suggest that it would increase the productivity of his group if I got a raise, because then I, as a part of his group, would be more motivated. As a humorous person that probably did not have to use his own grant for this, Kramer agreed. Thanks!

I am particularly grateful for all the help, guidance and support I received from Yujin Tong throughout my PhD career. It is not hyperbole to say that Yujin was my mentor during the time as a PhD student. When I first arrived at FHI I neither knew about ultrafast laser systems, nor electrochemistry, but Yujin managed to get me acquainted with both in a (relatively) short time. More than just the technical knowledge, I learned from Yujin the necessary mindset to master basically anything: patience, openness and, this can not be stressed enough if you want to measure anything meaningful in optics, frustration tolerance. Yujin is not just a good scientist and teacher, he is also very skilled in many sports and competing with him in bowling, table tennis and go-carting was always fun.

Pursuing a PhD is an endeavor with many ups and downs and, especially in the beginning of my PhD, Harald Kirsch often provided me with much needed advice and positivity.

He also “helped” me make some losing investment decisions and empty a few beers. Cheers Harald!

In the very first days at FHI, Sabine Wasle helped me take my first steps, showed me around, helped me perform my first electrochemical measurements and later often assisted with troubleshooting electrochemical problems. Thank you!

A special thank you goes to Reinhard Franke and Willie Kraus, who helped me with innumerable mechanical problems and CAD drawings of electrochemical cells.

Martin Thämer often helped me with small problems in Igor Pro and always provided useful input when discussing anything optics related. Thanks!

Of course, I also want to thank the remaining group members of the Campen group, my fellow PhD colleagues, for the time spent together.

Frequent support from the PC secretariat, Manuel Krüger, Daria Haberland and Ines Bressel is gratefully acknowledged. More generally, I want to thank the entire PC department for being great colleagues and creating an amazing atmosphere that I will certainly miss.

I want to thank Igor Nahalka, Arianna Marchioro and Sylvie Roke for our fruitful collaboration that allowed me to experience the lightless tristesse of yet another optical lab (but this time in beautiful Lausanne). All jokes aside, I am really grateful for the science, for my trip to Lausanne and the friendship formed during this collaboration.

I am deeply grateful for friendships, financial support, soft skill seminars and an amazing trip to castle Ringberg, all enabled by the International Max Planck Research School “Functional Interfaces in Physics and Chemistry”. In this context Alex Paarmann and Ines Bressel deserve special praise for being amazing organizers and great folks.

Further technical support is acknowledged from the FHI crystal lab that brought the single crystals used in this thesis back to life *many* times, and the FHI mechanical end electrical workshops.

My flatmates Lynh and Maggie often distracted me and were a highly appreciated source of constant positivity. Thank you!

This thesis would not have been possible without my parents who take credit for, well, if this is credit worthy, me, and for getting me interested in science at a young age. I am particularly grateful that they always supported me, no matter what I was doing (maybe again because of my stubbornness). My grandmother deserves mention as the sweetest old lady. My brothers take credit for exsisting. Thank you!

Finally, I want to thank my wonderful girlfriend Eva for all the love, support and friendship one could possibly ask for. Words fail me when I try to describe how precious you are and what you mean to me. Off to new adventures together!

Curriculum Vitae

Der Lebenslauf ist in der Online-Version aus Gründen des Datenschutzes nicht enthalten.

Declaration of Authorship

Name: Zwaschka
Vorname: Gregor

I declare to the Freie Universität Berlin that I have completed the submitted dissertation independently and without the use of sources and aids other than those indicated. The present thesis is free of plagiarism. I have marked as such all statements that are taken literally or in content from other writings. This dissertation has not been submitted in the same or similar form in any previous doctoral procedure.

I agree to have my thesis examined by a plagiarism examination software.

Berlin,

Gregor Zwaschka